THE UNIVERSITY
of EDINBURGH

Time-domain simulations of marine operations and their application to the offshore renewable energy sector

Ben Hudson

Engineering Doctorate

The University of Edinburgh (IDCORE)

2019

This thesis is submitted in partial fulfilment of the requirements for the award of an Engineering Doctorate, jointly awarded by the University of Edinburgh, the University of Exeter and the University of Strathclyde.

The work presented has been conducted under the industrial supervision of JBA Consulting as a project within the Industrial Doctoral Centre for Offshore Renewable Energy (IDCORE).

THE UNIVERSITY *of* EDINBURGH

For

MarSelly and Pile

Abstract

In the coming decades, offshore renewable energy is expected to play a crucial role in the decarbonisation of global electricity supply essential for limiting anthropogenic greenhouse gas emissions to an acceptable level. The cost of utilising expensive vessels to install and maintain these marine energy devices represents a significant proportion of their life-cycle cost and one of the major barriers to their continued development. It is vitally important to estimate accurately these costs and attempt to reduce them as much as possible. This thesis investigates the use of time-domain simulations of marine operations to estimate the likely duration and manage the inherent risks of an offshore project. The development and application of an original time-domain simulation software are described through a case study that supported construction of a Round 3 offshore wind farm. Analysis completed in advance of the project identified the most suitable installation strategy with a potential reduction in indicative cost of up to £6m. Simulations performed during the project enabled the early identification of significant deviations from initial estimates; such as the mean observed duration of a critical activity midway through the project being approximately 30% lower than initially specified, eventually leading to a 10.8% reduction in the estimated project duration. Detailed analysis of the operational data after project completion identified the importance of the learning phenomenon associated with repetitions of identical operations and the accurate representation of random delays and stoppages. Implementing the learning factor had the effect of reducing mean project duration by 10%, while accounting for technical downtime increased this estimate by 15%. The thesis shows that time-domain simulations are well-suited to the development of optimal strategies for the execution of marine operations and the subsequent minimisation of the duration and cost of offshore projects.

Lay Summary

The warming of the climate is undeniable and established beyond scientific doubt to have been caused by human related greenhouse gas emissions. To reduce the likelihood of the severe and irreversible impacts of global warming on people and ecosystems, it is imperative that the proportion of electricity generated from renewable sources is maximised. Offshore renewable energy refers to sustainable energy technologies located in the marine environment such as offshore wind turbines and devices that harness the energy of ocean waves or tides. The cost of constructing and maintaining these devices at sea represents a significant proportion of the total cost over their lifetime. If this promising new sector is to realise its large potential, it is vitally important to estimate accurately the cost of these installation and maintenance operations and try to reduce them as much as possible. This thesis proposes methods that simulate how an offshore project would have "played out" if it had been undertaken last year, the year before or over many historical years. These simulations use extensive records of weather data and algorithms that represent the project operations, their costs and their dependencies on weather and sea-state conditions. The development of a software package that incorporates these simulations methods is described and its application to the offshore renewable energy sector is highlighted through an industrial case study that provided continuous support to the construction of a large European offshore wind farm and showed that cost savings in the order of several million pounds are achievable. The results show that the developed software and simulation methods are suitable for estimating the likely duration of an offshore project, informing planning decisions and subsequently minimising the cost of installation and maintenance operations.

Acknowledgements

I would like to thank all those who have supported and encouraged me throughout this EngD process. Firstly, to my team of supervisors. Mark Lawless; for convincing me to move to Skipton, your constant support throughout my time at JBA and the interesting chats about music, life and home-made recording studios. I am extremely grateful for the guidance of Tom Bruce, particularly for his support while finalising this thesis. Your expert insights and suggestions have been hugely beneficial. Thanks also to my additional academic supervisors Helen Smith and Rafet Emek Kurt.

A sincere thank you to all the students and staff of IDCORE. I will forever have fond memories of everyone in the 2014 cohort—even of the many late nights spent in the "dungeon". I was also extremely lucky to work with such brilliant colleagues at JBA and to make so many dear friends over the last four years in Skipton. I cannot mention you all so must limit it to the past and present members of our small team; thank you to Richard Lines, Anthony Gray and Laurie Wilkinson. A special mention must go to Edward Kay—the better half of Bedward. I am enormously grateful for your support and friendship throughout our time at JBA. It was a pleasure working with you and I am immensely proud of what we achieved working on ForeCoast® Marine.

My greatest thanks must go to my family. To my brothers Ricky, Adam and Sam; thank you for your love, support and the endless amount of *craic*—fair job and snare the drum. To Gran and Granda; the thought of another celebration with you in Edinburgh and McEwan Hall was one of the biggest inspirations and driving forces for getting this thesis over the line—*maith agaibh*. A massive hug to Wowa and Nanna who I know are looking down and watching over me. To my fantastic partner Rachel, for filling my life with so much joy and providing a welcome distraction from this thesis. Fascinating discussions with an expert on light-hearted subjects such as time and death certainly helped to put things in perspective.

Finally, to Mum and Dad—*MarSelly* and *Pile*—to whom this thesis is dedicated. Words cannot express how grateful I am or how lucky I feel for the endless support, opportunities and love you have given me. I could not have done this without you. *Buíochas ó chroí libh*.

Declaration

I declare that this thesis was composed by myself, that the work contained herein is my own except where explicitly stated otherwise in the text, and that this work has not been submitted for any other degree or professional qualification except as specified.

Ben Hudson

Contents

Figures and Tables

Figures

Tables

Nomenclature

Acronyms and Abbreviations

AD	Anderson-Darling
AIC	Akaike Information Criterion
API	Application Programming Interface
BIC	Bayesian Information Criterion
C3S	Copernicus Climate Change Service
CAPEX	Capital Expenditure
CDF	Cumulative Distribution Function
CI	Confidence Interval
CSV	Comma Separated Variable
CTV	Crew Transfer Vessel
DES	Discrete-Event Simulation
DNV	Det Norske Veritas
DOE	Department of Energy
DP	Dynamic Positioning
DPR	Daily Progress Report
ECMWF	European Centre for Medium-range Weather Forecasts
EDA	Exploratory Data Analysis
ERA	European Re-Analysis
ERA5	5^{th}-generation European Re-Analysis
GBP	Great British Pound
IO&M	Installation, Operations and Maintenance
IQR	Inter-Quartile Range
LC	Learning Curve
LCOE	Levelised Cost of Energy
LÉ	Long Éireannach
M&E	Mechanical and Electrical
MAE	Mean Absolute Error
MC	Monte Carlo
MCS	Monte Carlo Simulations
ME	Mean Error
Mermaid	Marine Economic Risk Management Aid
MLE	Maximum Likelihood Estimation

NREAP	National Renewable Energy Action Plan
O&M	Operations and Maintenance
OAV	Offshore Access Vehicles
OE	Ocean Energy
OES	Ocean Energy Systems
ORE	Offshore Renewable Energy
OWC	Oscillating Water Column
OWF	Offshore Wind Farm
PDF	Probability Density Function
PERT	Programme Evaluation and Review Technique
PMF	Probability Mass Function
PNET	Probabilistic Network Evaluation Technique
POT	Peak Over Threshold
QA	Quality Assurance
RE	Renewable Energy
RMSE	Root Mean Square Error
SDA	Sequential Downtime Analysis
SEAI	Sustainable Energy Authority of Ireland
SI	Scatter Index
SOV	Service Operation Vessels
SWATH	Small Water-plane Area Twin Hull
TDMCS	Time-Domain Monte Carlo Simulation(s)
TDS	Time-Domain Simulation(s)
TIV	Turbine Installation Vessel
TP	Transition Piece
USD	United States Dollar
WEC	Wave Energy Converter
WES	Wave Energy Scotland
WTG	Wind Turbine Generator
XML	Extensible Markup Language

Roman Symbols

A.D.	Anderson-Darling statistic
A_p	Number of times an activity was performed; used in analysis of technical downtime
a	Location parameter of a parametric probability distribution
a_0	Suffix appended to the name of a parametric probability distribution whose location parameter is fixed at a value of 0

a_1	Location parameter for the probability distribution of the first iteration of an operation	
b	Scale parameter of a parametric probability distribution	
b_1	Scale parameter for the probability distribution of the first iteration of an operation	
b_s	Scale parameter for the probability distribution of the s^{th} iteration of an operation	
C	Additive constant that describes steady state performance in the Plateau learning curve model	time
C_1	Time required to produce the first unit or the duration to complete the first iteration of an operation	time
$C_{n\to 1}$	Performance time of the n^{th} unit transformed to the first unit ($s = 1$)	time
CV_{y_1}	Coefficient of variation of y_1	time
CV_{y_s}	Coefficient of variation of y_s	time
c	First shape parameter of a parametric probability distribution	
c_1	First shape parameter for the probability distribution of the first iteration of an operation	
c_p	Number of times the occurrences of technical downtime are equal to discrete integer k_p	
c_s	First shape parameter for the probability distribution of the s^{th} iteration of an operation	
D	Number of days in the specified time-interval	days
D_{ac}	Access days; number of access days in a given time-interval	days
$\mathrm{E}[y_1]$	Expected value of y_1	time
$\mathrm{E}[y_s]$	Expected value of y_s	time
$F_1(x)$	Cumulative distribution function for the first iteration of an operation	
F_j	Fitted cumulative distribution function when assessing the goodness of fit; ($F_j \triangleq F(x_j)$)	
$F_s(x)$	Cumulative distribution function for the s^{th} iteration of an operation	
F_X	Cumulative distribution function	
${F_X}^{-1}$	Inverse cumulative distribution function	
$F(x)$	Cumulative distribution function	
f	Expectation function characterising the relationship between y_i and x_i in the standard non-linear regression model	
f_1	Probability function for the first iteration of an operation	
f_a	Frame number of animation; used in animation algorithms	

f_s	Probability density function for the s^{th} iteration of an operation	
$f_y(y)$	Probability density function of y	
$f_{y_1}(y_1)$	Probability density function of y_1	
$f_{y_s}(y_s)$	Probability density function of y_s	
$f(x)$	Probability density function	
$f(.\|\theta)$	Probability density function of the parametric distribution analysed in the maximum likelihood estimation procedure	
$g(f_a)$	Artist function for animation algorithms	
$g(x)$	Function performed on a random variable x; used in the fundamental theorem proposed by Papoulis (1965)	
$g'(x)$	Derivative of $g(x)$	
H_{ac}	Access wave height; the upper limit of significant wave height required for access to an offshore location	m
H_s	Significant wave height	m
K	Number of parameters in a probability distribution	
k	Second shape parameter of a parametric probability distribution	
k_1	Second shape parameter for the Burr Type XII probability distribution of the first iteration of an operation	
k_p	Discrete integers defined as part of the Poisson distribution; used in the analysis and representation of technical downtime	
k_s	Second shape parameter for the Burr Type XII probability distribution of the s^{th} iteration of an operation	
L	Progress ratio; the constant proportional reduction in production time as cumulative production doubles	
$\mathcal{L}(\theta)$	Likelihood function; a function of the parameters of a parametric probability distribution	
$\hat{\mathcal{L}}$	The maximised value of the likelihood function	
M	Incompressibility factor; the factor that describes the fraction of the task executed using machinery in DeJong's learning curve model	
m	Learning slope; the slope of a learning curve when plotted on a log-scale	
N	Sample size; total number of observations in a sample	
$\mathcal{N}$	Implies that random variable follows a normal probability distribution	
N_{ac}	Number of accessible events in specified time-interval	
N_i	Total number of data-points in a sample	

N_t	Total number of wind turbine generators that need to be installed	
N_v	Wind turbine generator capacity of a vessel; the amount of turbines a vessel can carry	
n_r	Number of real roots of $g(x)$	
n_t	Total number of wind turbines installed in the simulation model	
n_v	Number of wind turbines currently on board the vessel in the simulation model	
O_i	Observed or measured values of selected parameter	
$\Pr(X)$	Probability of event X	
$P(c)$	Probability of occurrence of metocean condition c	
Q	Example constant 1 for demonstrating standard rules of integration	
q	Example constant 2 for demonstrating standard rules of integration	
q_p	Sample quantile; the number having the same units as the data which exceeds that proportion of the data given by the subscript p	
R	Pearson's product moment coefficient	
R^2	Coefficient of determination	
S	Task repetition number corresponding to the defined distribution parameters	
SI	Scatter index	%
S_i	Simulated or predicted values of selected parameter	
$S(\theta_v)$	Sum of the squared deviations between observed values and the non-linear curve fit in the standard non-linear regression model	
s	Unit number; the repetition or iteration number in the learning curve models	
s_1	Hypothetical iteration number used in the derivation of the learning rate; $s_2 = 2s_1$	
s_2	Hypothetical iteration number used in the derivation of the learning rate; $s_2 = 2s_1$	
$\mathcal{U}$	Implies that random variable follows a uniform distribution	
u	Random number generated from standard uniform distribution when performing inverse transform sampling	
v_w	Wind speed	m/s
x_i	Independent variable in standard non-linear regression model	

x_j	The n observations of variable X when performing maximum likelihood estimation	
y	In Crawford's learning curve model, the processing time of the s^{th} unit; in Wright's learning curve model, the average time of all units produced up to the s^{th} unit	time
y_1	Performance time of the first repetition; performance time is equivalent to the unit duration in Crawford's learning curve model	time
y_i	Response variable (dependent variable) in standard non-linear regression model	
y_n	Performance time of the n^{th} iteration	time
y_s	Performance time of the s^{th} iteration	time
y_{s_1}	Duration required to produce hypothetical iteration number s_1; used in the derivation of the learning rate	time
y_{s_2}	Duration required to produce hypothetical iteration number s_2; used in the derivation of the learning rate	time
y_t	Total time required to produce s units, based on Wright's learning curve model	time
y_u	Processing time of the s^{th} unit if using Wright's learning curve model	time

Greek Symbols

α	First shape parameter of Beta-PERT probability distribution
α_1	First shape parameter for the Beta-PERT probability distribution of the first iteration of an operation
α_s	First shape parameter for the Beta-PERT probability distribution of the s^{th} iteration of an operation
β	Second shape parameter of Beta-PERT probability distribution
β_1	Second shape parameter for the Beta-PERT probability distribution of the first iteration of an operation
β_s	Second shape parameter for the Beta-PERT probability distribution of the s^{th} iteration of an operation
Γ	Gamma function
γ	Shape parameter of Weibull probability distribution
γ_1	Shape parameter for the Weibull probability distribution of the first iteration of an operation

γ_s	Shape parameter for the Weibull probability distribution of the s^{th} iteration of an operation	
ϵ	Residual error term in standard non-linear regression model; assumed to be normally distributed centred around 0 with unknown variance	
η	Scale parameter of Weibull distribution	
η_1	Scale parameter for the Weibull distribution of the first iteration of an operation	
$\eta_i(\theta_v)$	Simplification made in the calculation of the sum of squared deviations in the non-linear regression model; $f(x_i;\theta_v) \equiv \eta_i(\theta_v)$	
η_s	Scale parameter for the Weibull distribution of the s^{th} iteration of an operation	
θ	The parameters of a theoretical probability distribution; used when performing maximum likelihood estimation	
θ_v	Vector of model parameters characterising the relationship between y_i and x_i, through the expectation function f, in the standard non-linear regression model	
κ	Arbitrary cycle number for transformation of data for learning curve fitting procedure	
λ	Rate parameter of an exponential distribution	
μ	Mean or expected value of a random variable	
μ_1	Mean value of y_1 assuming it is normally distributed	time
μ_L	Alternative scale parameter for Lognormal distribution	
μ_p	Average occurrence rate for Poisson distribution	
μ_s	Mean value of y_s assuming it is normally distributed	time
ν	Modal or most likely value for Beta-PERT and Triangular probability distributions	
ν_1	Modal or most likely value for the Beta-PERT and Triangular probability distributions of the first iteration of an operation	
ν_s	Modal or most likely value for the Beta-PERT and Triangular probability distributions of the s^{th} iteration of an operation	
σ	Shape parameter of Lognormal distribution	
σ_1	Shape parameter for the Lognormal probability distribution of the first iteration of an operation	
σ_s	Shape parameter for the Lognormal probability distribution of the s^{th} iteration of an operation	
σ^2	Variance of a random variable	
${\sigma_1}^2$	Variance of y_1 assuming it is normally distributed	time

${\sigma_s}^2$	Variance of y_s assuming it is normally distributed	time
${\sigma_{y_1}}^2$	Variance of y_1	time
${\sigma_{y_s}}^2$	Variance of y_s	time
τ_{ac}	Access time; the duration required for access	time
τ_d	Estimated metocean downtime	time
τ_{op}	Estimated total operation duration	time
ϕ	Learning rate; the percentage of labour hours required to double the units produced (to produce unit $2s$)	
ω	Scale parameter for Lognormal distribution	
ω_1	Scale parameter for the Lognormal probability distribution of the first iteration of an operation	
ω_s	Scale parameter for the Lognormal probability distribution of the s^{th} iteration of an operation	

List of Publications

Some of the work described in Chapter 3 is adapted from the peer-reviewed conference paper presented at the European Wave and Tidal Energy Conference 2017 (EWTEC) in Cork. See Hudson *et al.* (2017).

A preliminary version of the operation duration analysis and investigation of the learning phenomenon described in Chapter 7 can be found in the conference paper presented at the Asian Wave and Tidal Energy Conference 2018 (AWTEC) in Taiwan. See Hudson *et al.* (2018).

Chapter 1

Introduction

1.1 Background and Motivation

1.1.1 Offshore Renewable Energy and the Climate Crisis

Human-induced global warming is undeniable and represents an urgent threat to human societies and the planet (IPCC, 2014*a*,*b*, 2018). Anthropogenic greenhouse gas emissions are estimated to have already caused approximately 1.0°C of warming above pre-industrial levels (1850–1900) (IPCC, 2018). The effects of climate change on both natural and human systems are already evident around the globe and continued emission of greenhouse gases will cause further warming and a subsequent increase in the likelihood of extreme and irrevocable impacts on people and ecosystems (IPCC, 2014*b*). Pursuing efforts to restrict global temperature rise to 1.5°C, as agreed to by the majority of countries in signing the 2015 Paris Agreement, is essential for limiting the risk of heavy precipitation events; drought; local species extinction and heat-related human morbidity and mortality (IPCC, 2018).

In mitigation pathways that achieve this 1.5°C goal, renewable energy technologies are projected to supply 70–85% of electricity in 2050 (IPCC, 2018). For maritime nations such as the UK, *offshore renewable energy*—sourced from the marine environment and including offshore wind, wave and tidal energy technologies—can contribute significantly to the broad mix of renewable energy sources required if fossil fuel power generation is to be phased out entirely (ETI and UKERC, 2014; IPCC, 2014*a*). At the same time, the *energy trilemma* demands that supply is secure and affordable as well as sustainable, meaning that offshore renewable energy (ORE) technologies will need continued support, research and cost-reductions if their market shares are to be significantly increased (IPCC, 2014*a*).

1.1.2 Offshore Operations and Metocean Conditions

The common factor that impedes all marine operations, but also presents a significant opportunity for cost reduction and accelerating development in the ORE sector, is limited access to offshore locations due to adverse meteorological and oceanographic (*metocean*) conditions (Gintautas *et al.*, 2016; Morandeau *et al.*, 2013). The inherent risks associated with working in the harsh, complex and ever-changing marine environment are clear. These risks affect both the installation of ORE devices and the numerous scheduled and unscheduled maintenance tasks that have to be performed to keep the devices operational and to sustain power production (Dalgic *et al.*, 2015a).

The cost of these components—often grouped together and referred to as installation, operations and maintenance (IO&M) activities—is a major component of the life-cycle cost of an offshore wind farm, the most mature and established ORE technology, and is expected to be the same for the ORE sector in general. For offshore wind, O&M activities typically account for between 25% and 30% of the total levelised cost of energy (LCOE). It is estimated that the combined costs of IO&M will represent 35% and 46% of the lifetime cost of wave and tidal energy arrays respectively (see Section 2.4.1 for more details). It is vitally important to estimate these costs accurately and attempt to reduce them as much as possible (Gintautas *et al.*, 2016).

1.1.3 Time-domain Simulations and ForeCoast® Marine

Time-domain simulations (TDS) refer to the analysis of the time variation of metocean conditions and have been proposed as a method for estimating the likely duration of an offshore project. Indeed, their use is recommended by the DNV (Det Norske Veritas, 2010) and has been noted as the most straightforward and appropriate method for the estimation of downtime and the detailed design of marine operations strategies (Stallard *et al.*, 2010). This work describes the development of a time-domain simulation model and assesses its application to the planning, management and optimisation of operation strategies in the ORE sector.

Specifically, the work outlines a selection of the technical methods integrated within a metocean planning tool known as ForeCoast® Marine, a metocean risk management software developed by JBA Consulting. The software consists of two main modules; a metocean forecasting tool referred to as the *Mission Planner* and a metocean hindcasting and optimisation tool known as the *Gamer Mode*. The *Gamer Mode* simulates how a marine engineering project would have "played out" if it had been undertaken last year, the year before or over many historical years. The *Mission Planner* uses *forecast* metocean data to manage and track live weather risks, help anticipate adverse weather effects and determine the best time to undertake imminent marine operations. This project has focused on the development of the *Gamer Mode* module.

1.2 Hypothesis, Aim and Objectives

The hypothesis is that time-domain simulations can be used to estimate the likely duration of offshore operations and thus offer opportunity for project cost reduction. The aim of this thesis is to investigate this hypothesis and appraise the use of these simulation methods for informing planning strategies and managing the inherent risks of an offshore renewable energy project. Significant project cost reductions can play a critical role in the development of the promising offshore renewable energy sector and thus in the decarbonisation of global electricity supply.

To accomplish these goals, the objectives of this thesis are as follows:

- Validate the use of time-domain simulations for modelling offshore operations by comparing simulation results to observed operational data.
- Compare time-domain simulation theory to the alternative and well-known probabilistic methods of estimating the durations of offshore operations.
- Apply the simulation theory to real life examples to assess and appraise the suitability of time-domain simulation models for estimating accurately the likely duration of an offshore project and informing planning strategies.
- Perform exploratory data analysis on recorded operation data with the aim of identifying the key trends and phenomena that affect offshore operations.
- Expand the time-domain simulation theory by developing and incorporating additional functionality that models accurately any of the phenomena identified in the exploratory data analysis.

1.3 Thesis Outline

1.3.1 An "Analysis" Project

The industry-based research summarised in this thesis was slightly unusual as it coincided with the concurrent work of fellow IDCORE student Edward Kay. Both projects focused on the creation, development and application of the ForeCoast® Marine Gamer Mode. The main distinction between the two projects was originally in the field of application; this project aimed to apply the software to the wave and tidal energy sector while the other project was to focus on offshore wind. As it transpired, the majority of major ORE projects encountered over the placement period were in the offshore wind sector. Subsequently, an alternative and more significant deviation in the breakdown of work developed over time, one which allowed simultaneous work on the same projects, while keeping the research questions distinct.

Edward Kay's *development project* concentrated on the implementation and evolution of the simulation algorithms. Ben Hudson's *analysis project* focused on the quantitative

data analysis of the raw simulation outputs, the presentation of these results to clients and the application of the software to support the development of marine operation strategies. The *development project* discusses the creation of the algorithms[1] that take the two main inputs of the software—the metocean time-series and the sequence of tasks required to complete the offshore project—and perform the simulations that generate the list of raw output data. The *analysis project* focused on taking this long list of operation start and end times, analysing the data and producing the output graphs, animations and summary statistics.

Despite this distinct division of work, it should be noted that the software development was a concerted and iterative process, requiring significant collaboration and interaction between students. Indeed, this thesis discusses the development and incorporation of several additional methods within the Gamer Mode, including functionality for animating the outputs of the simulations; representing the random variation in operation durations; accounting for the learning that arises after consecutive repetitions of similar tasks and simulating random delays and stoppages that are independent of metocean conditions. Outside of these brief forays into the world of software development, this *analysis project* investigates the types of questions that time-domain simulations can be used to answer and the implications of results on operation strategies in the ORE sector.

1.3.2 Thesis Structure

The *Prologue* serves as an introduction to the theories of time-domain simulations. The main body of the thesis then focuses on their application and is divided into three parts—*Before*, *During* and *After*—that correspond to the types of analysis that can be performed in the planning stages *before* operations commence, *during* the operational phase of a marine project and *after* operation completion. Finally, the *Epilogue* describes the impacts of using the results of the operation duration and technical downtime analyses as inputs to the time-domain simulation model and summarises the major conclusions of the thesis.

While most of the analysis described in this thesis is similar to work carried out for a client in the offshore wind energy sector, the results are different due to changes made in the exact scenarios modelled, specific modelling assumptions (e.g. vessel charter rates, which were not provided by the client) and other factors which have been changed to ensure client confidentiality.

---

1. The state-of-the-art simulation algorithms developed as part of the *developer project* incorporate the theory of time-domain simulations and the modelling technique known as *Petri nets*, with appropriate representation of the stochastic weather effects. More information on *Petri nets* is given by Petri (1962) and Reisig (2013).

Prologue

A literature review is given in Chapter 2 that covers the need for renewable energy; a brief introduction to offshore renewable energy; the importance of installation, operations and maintenance for marine projects as well as methods of estimating weather windows.

Chapter 3 discusses time-domain simulations and alternative methods of estimating metocean downtime. This chapter describes a validation of time-domain simulation theory and provides a comparison of the theory to the common statistical methods.

Part I — Before

Chapter 4 describes the methods that enable the graphical animation of time-domain simulation outputs. The strengths, weaknesses and applications of the animations are discussed. It is shown that the animations are particularly useful for quality assurance during model development.

The exploratory data analysis methods that have been applied to extract key insights from the raw simulation outputs are discussed in Chapter 5. These are a selection of the methods that have been incorporated within the developed planning software and summarise the types of analysis that can be performed in the planning stages of a marine project, before operations commence.

Part II — During

The application of time-domain simulations during the execution phase of a marine operation is outlined in Chapter 6. The data analysis methods introduced in the previous chapter, particularly the proposed *progress plots*, enable the continuous monitoring of project performance and the early identification of significant deviations from baseline projections.

Part III — After

Chapter 7 aims to quantify the stochastic nature of the durations of offshore operations through the analysis of recorded data from a Round 3 offshore wind farm installation project. The concept of a *learning curve* is assessed for each operation in the data-set and the effect of this phenomenon on the representation of operation durations within time-domain simulations is investigated.

The implementation of the stochastic learning curve model within the developed time-domain simulation software is addressed in Chapter 8. The theory—which was only validated and applied explicitly for the Normal distribution—is expanded to seven

additional probability distributions. The chapter focuses on the the performance and processing speed of the implemented sampling methods that incorporate learning.

Chapter 9 is related to the analysis and implementation of the two previous chapters but focuses on *technical downtime*—the term given to unplanned and random interruptions to the operation schedule of an offshore project independent of the metocean conditions. The chapter assesses the viability of representing the technical downtime as the joint probability of downtime occurring, modelled by a Poisson distribution, and the downtime duration being equal to a certain value. The implementation and evaluation of technical downtime within the developed software are also described.

Epilogue

The combination of methods described in the preceding chapters is outlined in Chapter 10, which assesses the impacts of using the finalised, expanded time-domain simulation software for the planning and optimisation of marine operations in the offshore renewable energy sector.

Finally, the conclusions of the thesis are summarised in Chapter 11.

Prologue

Chapter 2

Literature Review

2.1 Introduction

Each chapter of this thesis begins with a review of the academic literature and theoretical background specific to that chapter. As such, the following review is restricted to giving a more general description of the context of the work within the offshore renewable energy sector and the current knowledge underpinning the stated motivations and objectives.

The requirement for sustainable forms of electricity generation and the important role that these technologies can play in reducing global greenhouse gas emissions are discussed in Section 2.2. Next, an introduction to offshore renewable energy (ORE) is provided and the four most mature ORE technologies—offshore wind, tidal range, tidal current and wave energy—are described. The current status of each technology is outlined in detail. Section 2.4 explains the importance of installation, operations and maintenance for the ORE sector, highlighting the large share of the life-cycle cost of ORE projects that is attributable to these activities. Existing methods for estimating weather downtime and weather windows are discussed in Section 2.5. Finally, Section 2.6 discusses the most recent academic and industrial applications of time-domain simulation theory. This final section summarises the current limitations and knowledge gaps that have been identified in the TDS literature.

2.2 The Need for Renewable Energy

Warming of the climate system is unequivocal; the atmosphere and ocean have warmed, the amounts of snow and ice have diminished and sea level has risen (IPCC, 2014*b*). Anthropogenic greenhouse gas emissions, which have been increasing since the beginning of the industrial era, are now higher than ever and the effects of these greenhouse gases are extremely likely to have been the dominant cause of observed warming since the mid-20$^{\text{th}}$ century (IPCC, 2014*b*). The latest estimates indicate that human-induced warming has already reached approximately 1.0°C above pre industrial levels (1850–1900), with a likely range of 0.8–1.2°C (IPCC, 2018).

Changes in climate have already caused impacts on natural and human systems on all continents and across the oceans. Continued emission of greenhouse gases will cause further warming and long-lasting changes in all components of the climate system, increasing the likelihood of severe, pervasive and irreversible impacts for people and ecosystems (IPCC, 2014*b*). In response to this urgent threat to human societies and the planet, an overwhelming majority of countries agreed to the 2015 Paris Agreement and to pursue efforts to limit global temperature rise to 1.5°C (IPCC, 2018). Restricting global warming to this level mitigates the likely increases in heavy precipitation events in several regions; reduces the probability of drought and associated water availability risks; lowers the likelihood of local species extinction and limits the risk to human health, heat-related morbidity and mortality (IPCC, 2018). If the current rate of warming of approximately 0.2°C per decade continues, global warming is likely to reach 1.5°C between 2030 and 2052 (IPCC, 2018).

Reducing the carbon intensity of electricity generation is an essential component of cost-effective mitigation strategies for limiting greenhouse gases to a level that restricts warming to 1.5°C (IPCC, 2014*a*). In pathways that achieve this critical goal, the proportion of low-carbon electricity supply is expected to increase from the current share of approximately 30% to between 70 and 85% by 2050 (IPCC, 2018), with fossil fuel power generation being phased out almost entirely by 2100 (IPCC, 2014*a*). Renewable energy (RE)—defined by Edenhofer *et al.* (2011) as any form of energy from solar, geophysical or biological sources that is replenished by natural processes at a rate that equals or exceeds its rate of use—is one of the main components of this low-carbon electricity supply. There has been a dramatic growth in RE in recent years; despite historic low oil prices between 2015 and 2017, RE technologies represented the largest capacity additions in 2017 (Bosch *et al.*, 2018). However, many of these RE sectors still need support if their market shares are to be significantly increased (IPCC, 2014*a*).

Simultaneously, society is faced with the imbalance between the competing aims of economics, politics and the environment, collectively known as the *energy trilemma* (Heffron *et al.*, 2015). Energy supply must be secure and affordable as well as sustainable. Increasing the penetration of renewable energy can help reduce greenhouse gas emissions and ensure reliable, timely and cost-efficient delivery of energy (Ellabban *et al.*, 2014).

For the UK, it is clear that the future energy system will require the deployment of significant quantities of low-carbon power generation plant if the UK government is to meet its legally binding carbon reduction targets for 2050 under the Climate Change Act (ETI and UKERC, 2014). For maritime nations similar to the UK, *offshore renewable energy* can play an important role in achieving the balanced portfolio of low-carbon

technologies required to deliver the capacity and security of supply required out to 2050 and beyond (ETI and UKERC, 2014).

2.3 Offshore Renewable Energy

Offshore renewable energy (ORE) refers to any sustainable energy technology located in the marine environment. The term encompasses both offshore wind energy and ocean energy (OE), which aims to generate electricity from sources such as tidal range; tidal currents; ocean currents; ocean waves; thermal differences; salinity gradients and biomass (Borthwick, 2016; Ellabban *et al.*, 2014). While offshore wind and tidal range energy technologies have reached a state where they are commercially competitive with conventional electricity sources, the remaining ORE technologies are in the pre-commercial prototype and early demonstration stages (Ellabban *et al.*, 2014). The following sections summarise the current status of the most mature ORE technologies; offshore wind, tidal range, tidal current and wave energy (Magagna *et al.*, 2018, 2016; Ellabban *et al.*, 2014).

2.3.1 Offshore Wind Energy

Wind power and wind energy refer to the conversion of the kinetic energy of moving air into electricity using wind turbine generators (WTGs). Offshore WTGs typically consist of three blades rotating about a hub—or *nacelle*—and are very similar to land-based wind turbines. In comparison to onshore wind, the offshore form of this technology competes less with other land uses and has faced less public opposition, but it also produces a less intermittent energy supply (Bosch *et al.*, 2018). Additionally, offshore farms can reach higher power densities with taller and larger turbines and fewer constraints on size and noise pollution (Bosch *et al.*, 2018). These reasons, together with a growth in nameplate WTG capacity and a fall in the cost of capital, have led to rapid developments in the now well-established offshore wind energy sector (Bosch *et al.*, 2018; Rodrigues *et al.*, 2015; Dalgic *et al.*, 2015*b*; Martini *et al.*, 2018; Colmenar-Santos *et al.*, 2016).

Current Status and Future Projections

The growth in global cumulative offshore wind capacity is highlighted in Figure 2.1. Between 2011 and 2017, the cumulative capacity of offshore wind grew from 4.1 GW to 18.8 GW (GWEC, 2017). The market in 2017 was dominated by European projects, which represented 15.8 GW of the total cumulative capacity (Wind Europe, 2018*a*). The total energy produced by offshore wind turbines in Europe for the year 2017 was

43 TWh (Wind Europe, 2018*b*). Globally, total offshore wind power generation in 2018 was 65.8 TWh (International Energy Agency, 2018).

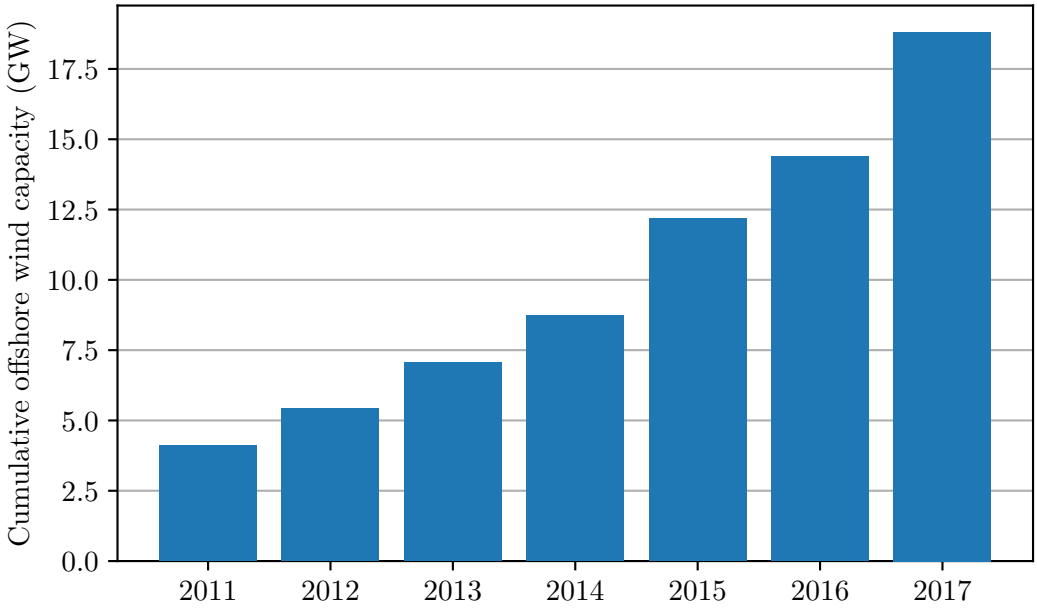

Figure 2.1: Growth of global cumulative offshore wind capacity (GW) since 2011. Data from GWEC (2017).

The rapid growth of the offshore wind energy sector is expected to continue. Global cumulative capacity is projected to reach 120 GW by 2030 (GWEC, 2017). The market will continue to be dominated by European offshore wind farms. It is estimated that cumulative capacity in Europe in 2020 will be 25 GW, accounting for 2.9 GW that are under construction and 13.2 GW that have been consented (Wind Europe, 2017). European projections for 2030 range between 50 and 99 GW with a central estimate of 70.2 GW (Wind Europe, 2017).

Floating Offshore

As shown in Table 2.1, the installation locations of offshore WTGs are typically classified under one of three categories according to the water depth and the corresponding foundation technologies. Although the offshore wind market has so far been dominated by countries with shallow water depths, falling costs and growing de-carbonisation incentives have resulted in several countries considering the potential of floating structures (Bosch *et al.*, 2018). As the "low-hanging fruit" of shallow near-shore sites is exhausted, there will be a need to develop farms further from shore and in deeper water (James and Ros, 2015). The associated technical challenges and cost implications of moving further offshore, together with the possibility of unlocking near-shore deep water sites

at a lower cost of energy than far-shore shallow water locations, have driven the interest in floating offshore wind energy (James and Ros, 2015).

Table 2.1: Typical water depth categories for offshore WTGs and suitable foundation technologies. Categorisation taken from Bosch *et al.* (2018).

Water depth range (m)	*Category*	*Suitable foundation technologies*
0–40	Shallow	Monopile, suction bucket, tripod, jacket
40–60	Transitional	Tripod, jacket, gravity base structure
60–1,000	Deep	Floating

Despite its promise, full-scale prototypes of offshore WTGs are still in the early production stage (Bosch *et al.*, 2018). Although several cost projections suggest that floating wind can achieve financial parity with fixed-bottom WTGs during the 2020s if supported adequately by government (James and Ros, 2015), floating offshore wind is likely to remain a niche sector throughout this period (GWEC, 2017).

Global Technical Potential

Several definitions of the potential energy available from RE sources and technologies have been put forward (see, for example, Verbruggen *et al.*, 2010). The following definitions are those put forward by Krewitt *et al.* (2008);

- *Theoretical* potential is derived from natural and climatic parameters and can be quantified with a reasonable accuracy but the information is of little relevance. The theoretical potential of renewable energy sources is huge compared to global energy demand and there are numerous constraints in their exploitation.
- *Technical* potential includes geographical restrictions as well as technical and structural constraints. The value for technical potential may change over time due to advancements in the energy conversion technologies.
- *Economic* potential is the technical potential that can be exploited at competitive costs. Due to rising fossil fuel prices and reducing RE generation costs, the break even point between RE and conventional fossil fuel technologies can change over time.

Section 2.3 of the thesis focuses on the *technical* potential of ORE technologies.

Estimates of the global technical wind energy potential vary significantly. The values range from 157,000 TWh per annum (Lu *et al.*, 2009) to 630,000 TWh per annum (Dupont *et al.*, 2018). A recent study by Bosch *et al.* (2018) used a bottom-up approach and characterised the capacity factors of offshore wind farms by estimating the available wind power from high resolution global wind speed data sets. The results suggested that the total global technical potential of approximately 330,000 TWh per annum could

be divided between 65,000 TWh in shallow waters; 35,000 TWh in transitional waters and 230,000 TWh in deep waters. Thus, Bosch *et al.* (2018) estimate that even in the unlikely event of the complete breakdown of the *floating* offshore wind industry, the technical potential is still about 100,000 TWh per annum.

Offshore Wind Energy Outlook

We have seen that the offshore wind sector has developed rapidly in the last decade, with several projects either under construction or scheduled for completion in the next 3–4 years. The growth in cumulative capacity has been accompanied by a significant reduction in cost. The weighted average strike price for offshore wind projects in the UK fell from £142/MWh in 2010/11 to £62.14/MWh in 2017, while even lower strike prices were awarded in Denmark and the Netherlands (Bosch *et al.*, 2018). Careful strategic planning of the installation and maintenance of these wind farms is essential for ensuring these increasingly complex projects are delivered on time and on budget. The management of these energy projects will become more difficult as both the physical size of individual WTGs and the number of turbines in each wind farm increase. Furthermore, offshore wind farms will tend to move further away from the coast and into deeper waters, thus introducing additional challenges for electricity transmission, installation, operations and foundation design (James and Ros, 2015). To ensure the continued growth of the offshore wind energy sector, it is imperative that both the financial and safety risks of these projects are managed adequately.

For the nascent *floating* offshore wind energy sector, the challenge for the industry is to reduce costs from today's expensive prototypes and demonstrators to a commercial model where designs can be optimised and the industry can benefit from the economies of scale needed to reduce costs (James and Ros, 2015). Leading floating concepts already expect costs of £85–95/MWh but require further investment, development and support mechanisms to ensure continued reductions over time (Bosch *et al.*, 2018; GWEC, 2017). In order for floating offshore wind technologies to be successful and the vast deep-water resource exploited, it is essential that these costs are reduced to a level comparable to the standard bottom-fixed configurations.

2.3.2 Tidal Range Energy

The existence of tides is due primarily to gravitational interactions between the Earth, the Moon and the Sun that, when combined with the rotation of the Earth, produce a twice-daily rise and fall in sea level at any particular point on the globe. Tidal range energy generation systems use the vertical difference between the water level at these low and high tides to generate electricity. In these systems, the water carried upstream by the tidal flow is trapped behind a *barrage* across an estuary. A head of water develops

when the tide turns and the water level on the downstream side of the barrage reduces. The head is then used to drive the water through turbine generators and generate electricity in much the same way as conventional hydroelectric power stations.

A variant of a tidal barrage is the concept of a tidal lagoon, which encloses a section of coastline with a high tidal range behind a breakwater (Waters and Aggidis, 2016). Offshore lagoons that form a complete circle are an alternative option (Waters and Aggidis, 2016). Due to their similar modes of operation and to distinguish them from systems using tidal *currents*, tidal barrage and tidal lagoon systems are often collectively labelled tidal range systems (Boyle, 2012).

Current Schemes, Proposed Schemes and Technical Potential

Worldwide, there are five tidal range power plants of significant scale, representing a combined installed capacity of 520 MW (Neill *et al.*, 2018). The majority of this power generating capacity is provided by the 240 MW La Rance tidal barrage in Brittany, which has been operational since 1966, and the 254 MW scheme at Lake Sihwa in South Korea, which was completed in 1994 (Neill *et al.*, 2018). According to Wyre Energy Ltd. (2013), the annual energy produced by these two tidal range schemes is approximately 1.1 TWh.

Several *proposed* tidal range energy projects have also been identified as being technically feasible. As outlined by Neill *et al.* (2018), the total capacity of these schemes is 125 GW, corresponding to an estimated annual output of approximately 220 TWh.

There are substantial variations in the estimates of tidal range energy potential (Neill *et al.*, 2018; Borthwick, 2016; Entec, 2007). Recently, Neill *et al.* (2018) have estimated the global theoretical potential to be 5,792 TWh per annum. The authors also suggest that approximately 37% of the theoretical resource is available for tidal range schemes, which corresponds to a technical potential of 2,143 TWh. A significantly smaller estimate for the global tidal range energy resource of between 386 and 560 TWh per annum is given by Entec (2007), who acknowledge the relative scarcity of sites suitable for development. The estimated annual output of 220 TWh from the aforementioned proposed schemes can be considered a conservative yet realistic estimate of the current technical potential of tidal range energy.

Tidal Range Energy Outlook

Future trends for the tidal range energy sector are difficult to predict. Physical constraints, costs and environmental impacts are the major barriers to development (Neill *et al.*, 2018). Environmental issues in particular have prevented numerous developments from being approved (Neill *et al.*, 2018).

Several of the proposed schemes mentioned previously are located in the UK, with the scheme closest to commercial viability being the Swansea Bay Tidal lagoon (Neill *et al.*, 2018). It is difficult to assess the true environmental impacts of a large scale tidal lagoon without observing an operational plant for an extended period of time. As such, the Swansea Bay Tidal Lagoon was considered by many to be a "pathfinder project", that would pave the way for the remaining proposed lagoons (Neill *et al.*, 2018). With this in mind, the UK government commissioned an independent review of tidal lagoons in February 2016. Despite the *Hendry Review*[1] strongly advocating the development of Swansea Bay and describing it as a "no regrets" option, the UK government decided in late June 2018 that it would not be supporting the project. The government review concluded that the proposed programme of lagoons did not meet the requirements for value for money[2]. Consequently, without significant reductions in capital and construction costs, it is unlikely that tidal range energy in the UK will prosper.

2.3.3 Tidal Current Energy

It is also possible to harness the kinetic energy in the horizontal movement of the tides. Although these tidal *currents* are quite low in the open sea, the speed of the tidal ebbs and floods can be much higher when the tidal movements are concentrated by passing through narrow channels or around islands, headlands or other topographical constraints. Tidal current or tidal stream energy refers to the extraction of this energy using relatively simple, submerged, wind turbine-like rotors (Boyle, 2012).

---

1. Charles Hendry's independent review of tidal lagoons, 2017. See https://hendryreview.wordpress.com [Accessed 18th January 2020]
2. Oral statement of the Rt Hon Greg Clark MP to Parliament on proposed Swansea Bay Tidal Lagoon, 25th June 2018. See https://www.gov.uk/government/speeches/proposed-swansea-bay-tidal-lagoon [Accessed 18th January 2020]

Current Status

The tidal current energy sector has made considerable progress in recent years and has now reached a pre-commercial state, with fourteen tidal energy projects grid connected and operational by the end of 2016 and an estimated installed capacity of approximately 13 MW (Magagna *et al.*, 2016). The deployment of these first demonstration farms was a significant milestone for the ocean energy sector and demonstrates the technological progression that has been achieved (Magagna *et al.*, 2016).

Scotland is currently the centre of tidal current energy development. The world's first grid-connected tidal array was installed by Nova Innovation in Shetland's Bluemull Sound (REN21, 2018; Magagna *et al.*, 2016). Two 100 kW, direct-drive turbines were constructed in 2016 with a third turbine added in 2017. The MeyGen tidal stream energy project, consisting of four 1.5 MW horizontal-axis turbines, was completed and grid-connected in early 2017 (REN21, 2018; Magagna *et al.*, 2016). By the end of that year, the project had generated 2.6 GWh of electricity and was close to entering its scheduled 25-year operational phase (REN21, 2018). Finally, Orbital Marine Power[3] installed their S2000 device off the coast of Orkney in 2016. This 2 MW floating tidal stream turbine operated at full power as it underwent a test programme in 2017 (REN21, 2018). The device generated more than 1.2 GWh over the course of the year, corresponding to 7% of the electricity demand of the Orkney Islands (REN21, 2018). An approximate value for the total energy production by tidal current energy technologies in 2017 can be obtained by adding the energy produced by the MeyGen project and the Orbital Marine Power device. This results in a value of 3.9 GWh.

Technical Potential and Consented Projects

Major tidal streams have been identified along the coastlines of every continent, but the site-specific nature of the resource makes it difficult to obtain reliable estimates for global technical energy potential (Hannon *et al.*, 2016). Charlier and Justus (1993) estimate a theoretical potential of 8,800 TWh per annum in shallow coastal basins but this includes both tidal range and tidal current resources. The European technical potential for tidal current energy has been calculated as 48 TWh per year (CEC, 1996) and is a more realistic estimate of practical potential.

Accounting for tidal energy projects that have obtained support through various public funding streams, the potential for tidal current energy is 71 MW of installed capacity by 2020 (Magagna *et al.*, 2016). Magagna *et al.* (2016) estimated that this value could increase to 600 MW if technological and financial barriers could be overcome but this is highly unlikely at present, as we shall see in the next section.

---

3. Scotrenewables re-branded to Orbital Marine Power Ltd on 15th October 2018. See https://orbitalmarine.com/news/114-press-release-rebrand [Accessed 18th January 2020]

Tidal Current Energy Outlook

Although the tidal current energy sector has developed significantly in recent years, the rate of progress is still lower than expected (Magagna *et al.*, 2016). For example, only 14 MW of ocean energy capacity had been installed in Europe by 2016. The expectation of EU member states by this time was approximately 400 MW of additional capacity (Magagna *et al.*, 2016).

Besides the technical and environmental challenges, the main barrier preventing large-scale tidal current energy uptake is the financial viability of the projects (Magagna *et al.*, 2018). Significant cost-reductions are therefore required in the next 10–15 years to achieve continued growth in this sector. Magagna *et al.* (2018) have estimated that the current cost of tidal energy technologies needs to be reduced by 75% to meet the ambitious targets set out in the European Strategic Energy Technology Plan.

The challenges facing the tidal current sector are exemplified by the recent decision of Naval Energies to cease investment in their tidal current energy company, OpenHydro[4]. A facility in Cherbourg for manufacturing the 2 MW open-centre turbines developed by OpenHydro, with a planned production capacity of 25 units per year, was completed in June 2018. This plant was expected to launch the commercialisation of the technology and seven of the turbines were expected for deployment at the Normandy Hydro Project at Raz Blanchard in 2018 (REN21, 2018).

In addition to existing support systems, innovative financial instruments and R&D programmes are required to support the deployment of additional pre-commercial projects and attract private investors (Magagna *et al.*, 2018, 2016).

2.3.4 Wave Energy

Ocean waves—generated when the wind blows across the surface of the ocean—are a huge, largely untapped energy resource (Drew *et al.*, 2009). Wave power refers to the transformation of this wave energy into useful forms such as electricity (Hussain *et al.*, 2017). Numerous wave energy converters (WECs) have been invented and it is estimated that over 50 types of device are currently under development (Borthwick, 2016). WECs can be categorised by location—converters can be defined as onshore, offshore and near-shore—and by the power take-off mechanism—categorisations include point absorber, attenuator, oscillating water column (OWC) and submerged pressure differential (Hussain *et al.*, 2017).

4. See https://marineenergy.biz/2018/07/26/tides-wash-away-openhydro/ [Accessed 18th January 2020]

Current Status

The development of wave energy has slowed down significantly in recent years and, apart from small-scale OWC concepts, no wave energy converter has thus far been able to deliver electricity to the grid on a continuous basis (i.e. for more than twelve consecutive months) (Magagna *et al.*, 2018, 2016). The commercial readiness of wave energy is still to be proven and most of the devices are still considered to be advanced prototypes (Magagna *et al.*, 2016).

Several wave energy developers have exited the sector in recent years, highlighting the risk associated with the full-scale demonstration of converters. In 2014, the sector experienced catastrophic setbacks when the two companies considered to be at the most advanced stage of development, Aquamarine Power and Pelamis Wave Power, went into administration (Magagna *et al.*, 2016). Subsequently, the present picture is not very different from 2014.

By the end of 2016, the total amount of installed wave energy capacity was less than 1 MW (Magagna *et al.*, 2016). Consequently, the current amount of grid-connected energy produced by wave energy devices is negligible. It is clear that the wave energy sector has underachieved.

Technical Potential and Consented Projects

There are various estimates of the practical wave energy resource that can be recovered. The values range from 2,000 TWh per annum (see Thorpe (1999) and Cornett (2008)) to approximately 5,500 TWh per annum (see Pelc and Fujita, 2002).

Accounting for wave energy projects that have obtained support through various public funding streams, the potential installed capacity for wave energy in 2020 is 37 MW (Magagna *et al.*, 2016). This value has the potential to increase to 65 MW if technological and financial barriers can be overcome (Magagna *et al.*, 2016).

Wave Energy Outlook

Following the setbacks of recent years, it is critical that methods for de-risking the demonstration phase of wave energy technologies are identified (Magagna *et al.*, 2016). Several national and international initiatives have been created to address this issue and ensure tangible progress is made in alignment with available funding. Examples of agencies that are driving these initiatives include Ocean Energy Systems (OES), Wave Energy Scotland (WES), the Sustainable Energy Authority of Ireland (SEAI) and the US Department of Energy (DOE) (Magagna *et al.*, 2016).

Technological progression is paramount for the future of the wave energy sector (Magagna *et al.*, 2016). Currently, wave energy developers and engineers are tasked with maximising power output; improving efficiency; reducing environmental impact; enhancing material robustness and durability; cutting capital costs and ensuring survivability (Borthwick, 2016). With this long list of technological deficiencies in mind, it is clear that for the wave energy sector to have any chance of future development, the cost of ancillary services such as installation and maintenance operations will also need to be minimised. This thesis appraises the suitability of time-domain simulations of offshore operations for achieving these cost reductions.

2.3.5 Offshore Renewable Energy Outlook

The estimates of global technical potential and current annual energy production for the four offshore renewable energy sectors discussed previously are summarised in Table 2.2. To put these values in perspective, total world electricity generation in 2015 was 24,255 TWh (International Energy Agency, 2017).

Table 2.2: Estimates of global technical potential and current annual energy production for offshore renewable energy technologies. Energy data unit is TWh/year.

Technology	*Technical potential*	*Current energy production*
Offshore wind	100,000–630,000	51
Tidal range	220–560	1.1
Tidal current	48	0.004
Wave energy	2,000–5,500	≈ 0
Total	102,268–636,108	52.1

Even if the lower estimates of technically accessible resource are assumed, the potential contribution of ORE technologies to the global energy mix is significant and considerably larger than current global energy demand. However, the current level of energy produced by ORE technologies is virtually non-existent compared to the huge potential resource. It is clear that rapid improvements need to be made if ORE is to make a significant contribution to global electricity supply.

The global challenge is in extracting the energy, bringing it to shore, storing it and exporting it cost-effectively (Borthwick, 2016). Section 2.3 has discussed the individual challenges facing each of the offshore wind, tidal range, tidal current and wave energy sectors. As offshore wind projects continue to move further away from the coast and into deeper waters, careful strategic planning is required to ensure these increasingly complex projects are delivered on time and on budget. For the developing floating offshore wind sector, the challenge is to reduce costs from expensive prototypes to a commercial model matching current near-shore wind energy converters. In the case

of tidal range energy, recent government decisions in the UK have shown that unless there are significant reductions in capital and construction costs, the sector is likely to fail completely. The main barrier preventing large-scale tidal current energy uptake is the financial viability of pre-commercial projects—the sector needs support to cross the infamous "valley of Death". For the wave energy sector that is showing some signs of life after its recent near-death experience, it is imperative that methods for de-risking the demonstration phase of wave energy technologies are identified. The need for reducing the lifetime cost across all four sectors is clear.

2.4 Installation, Operations & Maintenance

Installation methods are still developing for the nascent ORE technologies and are thus difficult to define. However, for the more mature offshore wind sector, the installation of foundations and turbines can be broken down into the following steps, as outlined by Lacal-Arántegui *et al.* (2018);

1. *Mobilisation*—the vessel is adapted for the upcoming operations,
2. *Loadout*—the turbines and/or foundations are loaded onto the installation vessel at port,
3. *Outward transit*—the vessel transports to the wind farm site,
4. *Installation*—the turbines and/or foundations are installed,
5. *Return transit*—the vessel returns to port and
6. *De-mobilisation*—the installation equipment is removed from the vessel.

Typically, the installation vessels can carry several items per trip and thus steps 2–5 are repeated several times per wind farm (Lacal-Arántegui *et al.*, 2018).

During the operational lifetime of an offshore wind farm, numerous scheduled and unscheduled maintenance tasks have to be performed to keep the turbines operational and to sustain power production (Dalgic *et al.*, 2015a). These tasks are collectively referred to as operations and maintenance (O&M). Installation, operations and maintenance are occasionally grouped together and referred to as IO&M.

2.4.1 The Cost of Installation, Operations and Maintenance

The lack of operational, commercial-scale devices and arrays for the nascent ORE technologies makes it difficult to obtain data on the cost of IO&M activities in these developing sectors. However, SI Ocean (2013) estimate that the combined costs of installation and O&M will represent 35% and 46% of the lifetime cost of wave and tidal energy arrays respectively. For the remaining technologies, and for the ORE sector in

general, the proportion of lifetime costs pertaining to IO&M is expected to be similar to that of offshore wind.

The installation of offshore WTGs and their foundations is estimated to contribute 10–20% of the total capital expenditure (CAPEX) of a wind farm (Gintautas and Sørensen, 2017). Improving this installation process can help achieve the cost reductions required to compete with conventional energy sources (Barlow *et al.*, 2015). O&M activities typically account for between 25 and 30% of the total levelised cost of energy (LCOE) (Gintautas and Sørensen, 2017; Dalgic *et al.*, 2015*a*; Blanco, 2009; Rodrigues *et al.*, 2015; Martini *et al.*, 2018; Maples *et al.*, 2013). The cost of O&M is estimated to be three times higher than that of onshore wind and the main cause of this substantial difference is the frequent need for utilising expensive transportation (Dalgic *et al.*, 2015*a*; Blanco, 2009). In fact, it has been suggested that costs associated with transportation systems can amount to 73% of total O&M costs of an offshore wind farm (Dalgic *et al.*, 2015*a*,*b*). Furthermore, transportation system costs can represent up to 50% of the total installation expenditure (Gintautas and Sørensen, 2017). As wind farms begin to move further offshore and into deeper water, these costs can be expected to rise because of the longer travel times and harsher weather conditions that limit accessibility (Gintautas and Sørensen, 2017).

2.4.2 Vessels for Offshore Operations

For minor maintenance tasks, current transportation options to offshore locations include small workboats such as mono-hull boats, small catamaran vessels and small water-plane area twin hull (SWATH) vessels (Dalgic *et al.*, 2015*b*). These vessels are commonly referred to as crew transfer vessels (CTVs) (Dalgic *et al.*, 2015*b*). Offshore access vessels (OAVs) and service operation vessels (SOVs) are larger than CTVs, have better operational capability and are typically equipped with dynamic positioning (DP) systems and motion-compensating gangways (Dalgic *et al.*, 2015*b*).

In the case of major component failures and maintenance tasks, these small maintenance vessels are not adequate and alternative vessels are required (Dalgic *et al.*, 2015*a*). Jack-up vessels and barges currently dominate the offshore wind market (Dalgic *et al.*, 2015*a*). These vessels consist of a buoyant hull with a number of legs and are capable of stationing their legs on the sea floor, raising their hulls above the sea-surface, thus providing a stable platform for operations (Dalgic *et al.*, 2015*a*). Leg-stabilised vessels are similar to jack-up vessels, but do not lift the hull above the sea-surface; they instead use their legs to stabilise the hull (Dalgic *et al.*, 2015*a*). Heavy-lift vessels are designed for the installation of pre-assembled modules for the offshore oil and gas industry and therefore possess the highest crane capabilities in the offshore sector (Dalgic *et al.*, 2015*a*).

The construction and installation of offshore wind farms require similar vessels to those involved in the major maintenance tasks (Lacal-Arántegui *et al.*, 2018). These include jack-up barges; crane barges; cargo barges and tug boats (Lacal-Arántegui *et al.*, 2018). Sophisticated jack-up vessels designed specifically for the installation of offshore wind farms are alternatively classified as turbine installation vessels (TIVs) (Lacal-Arántegui *et al.*, 2018).

2.4.3 Cost Reduction Opportunities

IO&M expenditure is clearly a major component of the life-cycle cost of an offshore wind farm. A similar phenomenon can be expected for the other ORE technologies. Reducing these costs can therefore lead to significant reductions in the overall cost of an offshore project and consequently help to accelerate development in the ORE sector. As noted by Barlow *et al.* (2018), improved management of installation logistics has been identified as an area where substantial cost reductions can be achieved through innovation.

Detailed and accurate estimates of the durations of offshore projects would enable identification of the most cost-effective strategies for installing or maintaining ORE technologies. Scenario testing, sensitivity analysis and similar methods could be used to assess and select from a multitude of operational scenarios with the aim of reducing the projected charter length—and thus total charter cost—of these expensive and sophisticated vessels.

Lacal-Arántegui *et al.* (2018) suggest that the daily rate of a turbine installation vessel is between 150,000 and 250,000 USD. Assuming a conversion rate of 0.76 GBP/USD, this range corresponds to 114,000–190,000 GBP/day. For example, if it was possible to reduce the charter length of one of these vessels for an offshore wind farm installation project by a single week, the savings would be between approximately 800,000 and 1.3m GBP. The potential cost savings are further highlighted by the fact that the campaign durations of these large installations are often in the order of years and will only increase as wind farms move into deeper waters or further offshore. Consequently, methods of reducing these costs represent a significant opportunity for accelerating development in the ORE sector.

2.4.4 Quantifying Uncertainty

The percentages of life-cycle costs attributable to IO&M quoted in Section 2.4.1 are either estimated or mean values based on the ORE sector as a whole. In reality, there is huge uncertainty in the duration and cost estimates for a specific project or operation. A negligible amount of offshore wind farms have reached the end of their life-cycle (Wind Europe, 2017). Thus, it is almost impossible to know the total life-cycle cost of O&M with great certainty. Furthermore, the duration of an installation campaign is affected by the metocean conditions that prevail during construction and their relative severity in comparison to the mean conditions at the project location. The installation and maintenance cost will of course be different for every ORE project.

It would be hugely beneficial to quantify accurately these uncertainties in project duration and cost. Stochastic estimates of campaign duration could inform planning strategies and decision making processes, improve financial projections and help mitigate against the risks of working in the offshore environment. Without appropriate probabilistic ranges of project cost, there is an increased risk of financial failure for projects that were originally considered profitable and viable. Scenario testing methods, similar to those mentioned in the previous section for informing strategic planning decisions, that could also be used for the accurate quantification of uncertainty in financial projections and project length would therefore be highly advantageous.

2.5 Weather Downtime and Weather Windows

The inherent risks associated with working in the harsh, complex and ever-changing marine environment are clear. Limited access to offshore locations due to adverse meteorological and oceanographic (*metocean*) conditions is a common factor that impedes all marine operations (Gintautas *et al.*, 2016; Morandeau *et al.*, 2013). The critical importance of metocean conditions to the duration and success of an offshore project is a consequence of the high weather sensitivity of the equipment and vessels used for transportation and IO&M (Gintautas *et al.*, 2016).

Typically, the accessibility of offshore locations is expressed in terms of weather windows, during which operations can be performed, and the *downtime* spent waiting for these weather windows (Gintautas *et al.*, 2016). The subsequent sections summarise several methods for estimating weather windows; occurrence and persistence statistics, Markov theory, time-domain simulations, vessel response simulations and optimisation methods.

2.5.1 Occurrence and Persistence

Background

Historically, weather windows and weather downtime were calculated using occurrence and persistence statistics of accessible conditions (Stallard *et al.*, 2010; Walker *et al.*, 2013; Anastasiou and Tsekos, 1996; O'Connor *et al.*, 2013). *Occurrence* is the probability that an environmental parameter will be less than a threshold level (Stallard *et al.*, 2010). *Persistence* refers to the duration for which a metocean variable remains continuously below the required threshold level (Stallard *et al.*, 2010). Detailed definitions and examples of these two parameters are provided in Section 3.2.

Several methods for the estimation of downtime based on the probability of occurrence and persistence of metocean conditions are available. The method proposed by Stallard *et al.* (2010) and Walker *et al.* (2013) is outlined and assessed in Chapter 3.

Estimating Persistence

The calculation of persistence probabilities requires a long-term metocean data-set, typically greater than 5 years (Graham, 1982). In the past, recorded metocean time-series would have been the primary source of this data and obtaining recorded data-sets of sufficient duration was difficult. Furthermore, persistence statistics obtained from analysing these records can sometimes produce a misleading and inaccurate representation of the metocean climate, due to gaps in the recorded data and the relative severity of the measurement period against the long term norm (Graham, 1982). Consequently, several statistical methods were developed to estimate the duration of persistence intervals from available short-term metocean data records.

Initially, empirical relationships for a basic Weibull equation were derived to predict persistence statistics (Graham, 1982). This method was developed by Kuwashima and Hogben (1986), who used cumulative distribution functions of significant wave height to generate corresponding distributions of mean duration of persistence, expressed in terms of a two-parameter Weibull distribution.

A modified version of the Weibull method was proposed by Mathiesen (1994), who used the long-term distribution of significant wave height together with the absolute rate of change of significant wave height. However, as the rate of change of wave height can only be obtained from a time-series, it can be argued that the original data should be analysed directly, using time-domain methods such as those discussed in subsequent sections (Stallard *et al.*, 2010).

Persistence estimation methods are particularly useful when only short-term metocean data records are available (Stallard *et al.*, 2010). As described in the recent application

by Walker *et al.* (2013), these methods enable efficient and straightforward comparisons of site accessibility between separate project locations and seasons (Walker *et al.*, 2013).

Recent developments in sophisticated atmospheric and ocean models—combined with improvements in physical data measurement, collation and accessibility—have improved the quantity, extent and quality of available metocean data-sets, thus negating the main advantage of using persistence estimation methods. For example, the 5^{th} generation re-analysis (ERA5) produced by the European Centre for Medium-range Weather Forecasts (ECMWF) periodically uses its forecast models and data assimilation methods to 'reanalyse' archived observations, creating accurate global data-sets that describe recent history of the atmosphere and oceans (Copernicus Climate Change Service (C3S), 2017). This data-set is freely accessible online and contains data on a regular $0.25° \times 0.25°$ latitude-longitude grid for the entire globe. Data is currently available between 2000 and the present day. By mid 2019, the data-set will cover the period 1950–present (Copernicus Climate Change Service (C3S), 2017).

Because there are numerous available data-sets with similar geographic coverage that provide accurate representations of historic metocean conditions, it is preferable to calculate the persistence statistics directly—for example, using the methods described by O'Connor *et al.* (2013)—rather than use persistence estimation methods. Research in this area should instead focus on investigating the best use of the state-of-the-art metocean models and data-sets.

Limitations

The use of occurrence and persistence methods to estimate weather windows and expected durations of offshore operations is not well-suited for analysing projects consisting of sequential operations (Walker *et al.*, 2013). These methods only provide estimates of the expected value of weather downtime for a single operation. As such, the pattern of transitions between operable sea states for successive operations that comprise an entire project is not taken into consideration (Anastasiou and Tsekos, 1996).

Additionally, it is difficult to account for the joint probability of more than one metocean variable (Stallard *et al.*, 2010). A statistical approach is straightforward to apply to a single metocean variable, but marine operations are often strongly dependent on several metocean parameters. For example, installing a tidal turbine in an energetic tidal stream will require benign wave and tidal current conditions. If any heavy lifting operations are required, the project will also be dependent on wind speed.

2.5.2 Markov Theory

Background

An alternative approach for estimating the duration of offshore operations has been proposed by Anastasiou and Tsekos (1996) that generates probability distributions of persistence statistics using the assumption that the sea states behave as a first order Markov process. The Markov method establishes a transition matrix describing the probabilities of changing from one sea state to another and uses this matrix to estimate the persistence statistics (Stallard *et al.*, 2010). The methodology differs from the time-domain based Monte Carlo techniques (discussed in Section 2.5.3) because it establishes analytically, not through simulation, the probability distribution of the operations (Anastasiou and Tsekos, 1996).

Crucially, Markov methods are applied for a single operation, i.e. a single task or component of a marine project. The durations of individual activities are then combined according to the Probabilistic Network and Evaluation Technique (PNET), a method well-established in the probabilistic project scheduling subject area. For a clear introduction to the detail of the method, the reader is referred to Ang *et al.* (1975). The method assumes that the duration of each critical path in an operations scenario is normally distributed and that the mean and variance of the total duration of each is obtained through the addition of the mean values and variances of the activities that comprise that path (Anastasiou and Tsekos, 1996).

Advantages

One of the main advantages of the proposed Markov methodology is that it provides a better understanding of the key factors that influence the duration of the execution of an activity (Anastasiou and Tsekos, 1996). This is achieved by defining several "efficiency states" that are dependent on the prevailing metocean conditions and affect the duration required to complete an operation. For example, an efficiency state of 0.5 implies that any operation performed in the environmental conditions defined by that efficiency state will take twice as long to complete.

A practical advantage of the Markov methodology is that the computational time is significantly shorter in comparison to time-domain methods (Anastasiou and Tsekos, 1996). For time-domain simulations, Anastasiou and Tsekos (1996) suggest that the duration of an activity and vessel performance are the determining factors for the computational speed and the required length of environmental data. The Markov methods are not applied in the time-domain and so avoid these issues.

Finally, the requirements of the Markov methodology in terms of environmental input data are limited to a relatively short record of the wave height and wind speed (Anasta-

siou and Tsekos, 1996). However, as mentioned previously, the availability of accurate and extensive environmental data is not as problematic now as it was in the past.

Limitations

The most significant limitation of the Markov method is that it is performed for individual operations and it relies upon the PNET methodology to obtain estimates of total project duration. Using the *Central Limit Theorem*, PNET assumes a normal distribution for each representative path within an operations scenario. Anastasiou and Tsekos (1996) mention that this assumption may not be accurate in certain cases, for instance; if there are only a small number of tasks, their probability distributions are considerably skewed or the duration of a particular activity dominates the path duration (Anastasiou and Tsekos, 1996). In these cases, an alternative approach is suggested where the probability distribution of the path duration is expressed in terms of the central moments of the probability distributions of its individual activities.

Regardless of whether the basic PNET methodology or the improved central moments method is employed, there is uncertainty in the validity of combining sequential operations in this manner and assuming that their expected durations are statistically independent. This ignores the temporal auto-correlation of metocean conditions. In a period of particularly favourable metocean conditions, several sequential operations may be completed in quick succession, highlighting an example when the expected durations of successive operations are not independent. Conversely, an extensive spell of unfavourable weather can have the opposite effect on progress. This is exaggerated by the impact of seasonality on weather windows throughout a typical year. For example, several subsequent instances of unexpected downtime in the calm summer months could delay an offshore project into the more extreme weather of the winter months. As such, although the combined use of Markov theory and PNET produces accurate estimates of mean project duration, there is a doubt about their ability to capture the extreme results (see Anastasiou and Tsekos, 1996). The impact of only considering the mean values of individual operations is assessed in Chapter 3, where this strategy is compared to the time-domain simulation methods that can consider every possible eventuality and are thus expected to be able to capture these extreme cases more accurately.

Additionally, although the Markov method takes into account the effect of weather on the *efficiency* of operations (through the pre-defined efficiency states), the random variations in operation duration that can occur independently of metocean conditions are not considered. Natural variations in the time required to complete a task, ignoring weather effects, should be considered separately to the impact of weather on progress efficiency. The Markov-PNET methodology described by Anastasiou and Tsekos (1996) cannot account for this subtle difference. Furthermore, the methodology does not seem

to be able to account for random instances of downtime (e.g. due to failure of equipment or the late arrival of equipment) that can occur at any stage during an offshore project. Conversely, it is possible to represent these phenomena within a time-domain simulation model. Indeed, Chapters 7, 8 and 9 describe methods that enable natural variations in task duration independent of weather effects and random instances of downtime to be modelled.

2.5.3 Time-domain Simulations

Background

Time-domain Monte Carlo simulations have been proposed as an alternative method for estimating weather windows and the likely duration of an offshore project (see Det Norske Veritas, 2010; Beamsley *et al.*, 2007; Ballard and Evans, 2014; Stallard *et al.*, 2010; Anastasiou and Tsekos, 1996; van der Wal and de Boer, 2004; Anastasiou and Tsekos, 1996). Several names for the same theory can be found in the literature;

- sequential downtime analysis (SDA) (Beamsley *et al.*, 2007; Ballard and Evans, 2014),
- time-domain simulations (TDS) (Stallard *et al.*, 2010; Det Norske Veritas, 2010; Morandeau *et al.*, 2013),
- Monte Carlo simulations (MCS) (Anastasiou and Tsekos, 1996),
- time-domain Monte Carlo simulations (TDMCS) (Dalgic *et al.*, 2015a,*b*),
- discrete-event simulation (DES) (Barlow *et al.*, 2015, 2018; Muhabie *et al.*, 2018) and
- the scenario approach (van der Wal and de Boer, 2004).

The theory will be referred to as *time-domain simulations* (TDS) throughout this thesis.

TDS are powerful numerical techniques that enable the determination of the likely duration of an offshore project. These simulations are run on a long time-series of metocean data, defining at each time-step whether the critical conditions which allow an activity to proceed are met or not, in which case the particular time interval counts as *downtime* (Anastasiou and Tsekos, 1996). The algorithms analyse sequential activities in this manner until the entire project is complete. An estimate of the probability distribution of project duration is then determined after the execution of an adequate number of simulation runs (Anastasiou and Tsekos, 1996). Further explanations regarding the methodology and application of TDS are discussed in Section 3.2.

Advantages

The limitations of the probabilistic and Markov methods described above do not apply to the use of TDS for the analysis of offshore operations. In contrast to other weather window analysis techniques, this method considers the sequential nature of marine operations and the effect of small cumulative delays on the overall project completion date (Beamsley *et al.*, 2007). Analysing records of the time variation of metocean conditions is the most straightforward and appropriate method for the estimation of downtime and the detailed design of marine operation strategies (Stallard *et al.*, 2010).

The use of TDS for the modelling and analysis of offshore operations is recommended by the DNV (Det Norske Veritas, 2010), who note several advantages over the standard probabilistic methods. Crucially, they emphasise the ease with which complex thresholds involving several metocean parameters can be combined. Furthermore, TDS can be easily adapted to complex operation scenarios (Anastasiou and Tsekos, 1996)

Limitations

A selection of the earliest examples of TDS methods are described by Anastasiou and Tsekos (1996), where the main weaknesses of the technique are identified as the relatively slow computational time and the requirement for extensive metocean time-series. The increase in easily accessible and accurate weather data (Copernicus Climate Change Service (C3S), 2017; Olauson, 2018; van der Wal and de Boer, 2004) and the continued exponential growth in processing power of modern computers have addressed these limitations. However, there is still no clear consensus on the minimum amount of metocean data or the required number of simulation runs that need to be performed to ensure convergence is achieved. One of the objectives of this thesis is to investigate these TDS convergence issues. Studies are provided in Chapters 5 and 10 that assess quantitatively the effect of both the amount of metocean data and the number of simulations performed on the output results.

Stallard *et al.* (2010) also suggest that TDS are appropriate for detailed design but may be overly complicated for the purposes of site comparison. They argue that TDS are too time-consuming and that simpler methodologies may be more appropriate for the purpose of site evaluation. Again, with modern computer processing power and bespoke, efficient algorithms for applying TDS theory—such as those described in this thesis—these speed and complexity constraints are not expected to be critical issues.

2.5.4 Vessel Response Simulations

The methods proposed by Gintautas *et al.* (2016) and Gintautas and Sørensen (2017) use a similar approach to the time-domain simulation methodology, but focus on the simulated *response* of installation equipment. It is argued that the actual limitations of offshore operations are physical in nature and related to the response of equipment rather than simple environmental thresholds (Gintautas *et al.*, 2016). The proposed model presents a novel approach to weather window estimation that performs statistical analyses on parameters such as crane wire tension and rotor assembly motions while lifting (Gintautas *et al.*, 2016). A hydrodynamic multi-body motion simulator is used to generate the equipment response for a given offshore operation and the input metocean time-series (Gintautas *et al.*, 2016; Gintautas and Sørensen, 2017). The peak over threshold (POT) method is then used to estimate the probability of operation failure (Gintautas *et al.*, 2016; Gintautas and Sørensen, 2017). The methods use ensemble forecast metocean data and are thus focused on the estimation of weather window immediately prior to their execution (Gintautas *et al.*, 2016; Gintautas and Sørensen, 2017), but the methods are equally applicable to longer hindcast data-sets.

Acero *et al.* (2016) suggest a similar methodology to Gintautas *et al.* (2016) that can be used to determine the operational limits of an arbitrary installation procedure by identifying critical events and their respective response parameters through numerical simulation. The determined operation limits for installation operations are still simple metocean parameters, even though critical events and response parameters are identified through numerical simulations (Gintautas and Sørensen, 2017; Acero *et al.*, 2016). In a similar manner to the time-domain simulation methodology, the operational limits of a complete marine operation are determined by taking into account several activities, their durations, continuity, and sequential execution (Acero *et al.*, 2016). The developed methodology is applicable to any marine operation for which operational limits need to be established and used on-board as a basis for decision-making towards safe execution of operations (Acero *et al.*, 2016).

Time-domain simulations of the physical motions of vessels and the resulting response of installation equipment are likely to produce more accurate results than the standard method of using relatively simple metocean weather limits. However, the intermediate step of performing hydrodynamic multi-body motion simulations will have a significant impact on overall run-time and computational performance. Most of the software packages capable of performing these hydrodynamic simulations will also incur significant financial costs. Furthermore, the hydrodynamic motion simulators require detailed geometric models of the operations vessels being assessed. The difficulty in obtaining these geometric vessel representations from vessel owners will introduce additional complications.

2.5.5 Optimisation Methods

An alternative approach often applied in the assessment of the likely cost of offshore operations is to use optimisation methods. The aim of these models is to formulate mathematical representations of the numerous variables and constraints associated with an offshore project and then use numerical methods to find the optimal solution to the formulated model. Optimisation models are used extensively for analysing various O&M strategies over the lifetime of an ORE project and sometimes used in the investigation of potential installation strategies (Dalgic *et al.*, 2015*a*,*b*; Barlow *et al.*, 2018; Sarker and Faiz, 2017). For example, an optimisation model is proposed by Sarker and Faiz (2017) to analyse the transportation and installation costs for turbines in an offshore wind farm. The objective function of this model is to minimise these transportation and installation costs (Sarker and Faiz, 2017).

In general, optimisation models are useful for providing an holistic representation of offshore operations but they tend to simplify the effect of weather downtime and if used in isolation do not consider the temporal, sequential nature of operations and metocean conditions. Using the same example as above, Sarker and Faiz (2017) note the possibility of adverse weather conditions delaying a project indefinitely but do not include these in the study. Instead, a simple multiplier for offshore lifting operations is applied. Sarker and Faiz (2017) also note the effect of adverse weather on the rate of lifting operations and vessel speed and recommend further investigation of these phenomena.

There is a class of optimisation methods that can be used in conjunction with simulation models—for example genetic algorithms or simulated annealing techniques (Paul and Chanev, 1998). In fact, the process of using simulation models to ask "what if" questions and analysing model behaviour when certain parameters are changed can be described as a rudimentary optimisation technique. Simulation models have specific features that make the application of classical optimisation methods difficult or even impossible (Paul and Chanev, 1998). For instance, the model behaviour is often very complex—a result of the highly non-linear interaction of the model parameters. Genetic algorithms are one of the few classical optimisation methods that can solve such demanding problems (Paul and Chanev, 1998). They can be used to find optimal solutions to the underlying problem; something that cannot be achieved using time-domain simulations along with a primitive trial and error optimisation method. In a similar manner, recent work by the *University of Strathclyde* (see section 2.6.1) led to the development of an integrated model that combines a simulation model and an optimisation model.

2.6 Current Status of Time-domain Simulations

2.6.1 Recent Applications

Mermaid

Mermaid (Marine Economic Risk Management Aid) is a software package that has been developed by Mojo Maritime Ltd. in collaboration with the University of Exeter (Morandeau *et al.*, 2013). The software uses the TDS approach and conforms to Det Norske Veritas (DNV) recommended practices (Det Norske Veritas, 2010). In addition to the accessibility of the site, Mermaid considers the severity of the metocean conditions and their impact on the working efficiency of a vessel and its crew (Morandeau *et al.*, 2013), in a similar manner to the Markov method proposed by Anastasiou and Tsekos (1996). Morandeau *et al.* (2013) state that the Mermaid software allows more informed planning of the marine operations by identifying critical tasks in order to avoid downtimes and minimize the overall cost.

While Morandeau *et al.* (2013) account for the impact that severe weather can have on the time required to complete an operation (e.g. a task with a 50% efficiency state will take twice as long to complete if that 50% weather threshold is exceeded), the underlying representation of the operation duration is still a simplified, deterministic value. This leads to a discrete probability distribution for the operation duration that is dependent on the prevailing metocean conditions. The lack of a stochastic representation that accounts for random variations in operation duration irrespective of weather conditions is a potential weakness. Chapters 7 and 8 describe methods for incorporating random variations in operation duration that are independent of prevailing metocean conditions.

Additionally, it is not clear whether the efficiency states are multiplicative. For example if the 50% threshold limits are exceeded for two of the metocean variables under consideration, it is unclear as to whether the efficiency is 0.25 or 0.5. Regardless, the scalar value operation duration assumption is overly-simplified and is not supported by any analysis of observed or recorded operational data.

Finally, the crucial effect that technical failures of vessels or equipment can have on a project is acknowledged by Morandeau *et al.* (2013), but is not included in their study. As such, this *technical downtime* phenomenon requires further investigation. An assessment of observed instances of technical downtime is provided in Chapter 9, along with a proposed method for representing the phenomenon within a TDS model.

Shoreline

Shoreline[5] is a software package that consists of an *O&M Design* tool for simulating and measuring the performance of maintenance strategies for offshore wind farms and a *Construction Design* tool for simulating the installation and commissioning of offshore WTGs. The simulation engine for both of these tools uses TDS technology, with an underlying model built on agent-based and discrete-event principles. Further information on the software, which has developed from academic research conducted at the University of Stavanger, and the multi-method approach combining discrete-event and agent-based modelling is provided by Endrerud *et al.* (2014) and Endrerud and Liyanage (2015).

Endrerud *et al.* (2014) and Endrerud and Liyanage (2015) apply the software to support the O&M regime of an established offshore wind farm. The software is used to conduct scenario tests and sensitivity analyses of the O&M regime, but the results presented are limited to tabular summaries of the mean, standard deviation and standard error of indicative metrics that are functions of the downtime results.

As with Mermaid and the work of Morandeau *et al.* (2013), Endrerud and Liyanage (2015) assume the "repair time" duration required for selected maintenance tasks can be represented appropriately by a triangular distribution. No justification for this assumption is provided, but the benefit of defining the distribution using the maximum, minimum and most likely values for duration is noted. Further, the potential effect of technical downtime on offshore operations is not considered. The present work assesses both the durations of observed offshore operation data (see Chapter 7) and recorded instances of technical downtime (see Chapter 9). The work presented in this thesis thus addresses this common limitation in the current literature by identifying the most appropriate model representations for these two phenomena, informed by the quantitative analysis of recorded operational data from an offshore project.

Endrerud and Liyanage (2015) acknowledge the scarcity of operational data and the difficulty this creates for attempting to validate their developed methods. As such, they rely on comparisons with similar simulation models and parameter-sensitivity analysis to check their model validity (Endrerud and Liyanage, 2015). Explicit validation studies for similar TDS models would thus be beneficial. Consequently, a targeted validation study is described in Chapter 3.

---

5. See Shoreline website at https://www.shoreline.no/ [Accessed 18th January 2020]

University of Strathclyde—Construction Model

Barlow *et al.* (2015) developed a simulation tool to model the logistics of the installation process and to identify the vessels and operations most sensitive to weather delays. Their software combines a logical discrete-event simulation model of the installation of an offshore wind farm and a synthetic weather time-series model and simulates the progress of the installation, given the defined installation scenario, subject to each synthetic weather series (Barlow *et al.*, 2015). The resulting analysis identified that loading operations contribute significantly to the overall delay of the installation process and that a non-linear relationship exists between vessel operational limits and the duration of installation (Barlow *et al.*, 2015).

Barlow *et al.* (2018) describe an integrated model that combines the simulation model developed by Barlow *et al.* (2015) with a separate optimisation model. The simulation component enables the impact of asset selection on the likely cost and duration of the installation process to be assessed (Barlow *et al.*, 2018). The optimisation component provides an installation schedule that is robust to changes in operation durations due to weather uncertainties (Barlow *et al.*, 2018). The combined framework enhances the individual capability of both models by feedback channels between the two, taking advantage of the benefits of either approach.

However, the TDS component of the combined model possesses some of the common weaknesses that have already been discussed above. Barlow *et al.* (2018) acknowledge that task durations are uncertain but do not discuss their representation within the model in detail. In Barlow *et al.* (2017), they recognise triangular distributions as suitable for modelling uncertain activity durations in project scheduling problems. Again, the intuitive definition of this distribution by the minimum, mean and maximum task durations is noted as an additional advantage. The authors do not support the selection of the triangular distribution with analysis of real operational data. They also state that factors such as contingency time and random vessel failures can be considered, but do not elaborate further.

The models developed and described by Barlow *et al.* (2015) and Barlow *et al.* (2018) have been validated using three methods. Firstly, the software code was assessed by an external mathematical software consultancy to ensure accuracy. Secondly, the model was benchmarked against an industry-standard tool. Finally, multiple case studies were performed by external industry organisations to ensure the model was fit for purpose. Again, bespoke studies with the sole purpose of validating the model, and TDS theory, have not been provided.

The presentation of output results in the work of Barlow *et al.* (2018), including multiple box-and-whisker plots and intuitive graphical summaries, is superior to the tabular

presentation provided by Endrerud and Liyanage (2015). Results presented in Barlow *et al.* (2018) demonstrate more appropriately the visualisation capabilities and potential applications of TDS output data.

University of Strathclyde—O&M Model

Dalgic *et al.* (2015a) use a time-domain Monte Carlo approach within an O&M model to investigate optimal jack-up vessel strategies. The models can be used to assist operators in developing long-term O&M plans and the results show that the optimal O&M cost can be achieved by selecting the optimal chartering strategy for the jack-up vessels (Dalgic *et al.*, 2015a).

The methodology is further developed by Dalgic *et al.* (2015*b*) to include analysis of environmental conditions, investigation of failures and simulation of repairs. The developed discrete-event simulation model allows the identification of favourable operating strategies for offshore wind O&M fleets (Dalgic *et al.*, 2015*b*).

The TDS components of the models developed by Dalgic *et al.* (2015a) and Dalgic *et al.* (2015*b*) are quite simplistic. The sequential operations are limited to; transit, jack-up (or crew transfer), perform O&M tasks, jack-down and return to port. Factors such as interactions between vessels and detailed modelling of the operations required at port are not considered. Further, single values for jack-up and replacement/repair time are assumed. A triangular distribution is chosen to represent the mobilisation time required for the large jack-up vessels as a stochastic variable, but no reference is made to the possible impacts of vessel or equipment failure. In short, the TDS components of these models are appropriate for the O&M scenarios to which they are applied, but are not suitable for detailed and exhaustive planning of more complex projects.

Deterministic and Probabilistic Approaches

A discrete-event simulation approach is also implemented by Muhabie *et al.* (2018) in their investigation of offshore wind farm installation strategies. Muhabie *et al.* (2018) use two approaches; the deterministic approach, which is similar to the classical time-domain simulation approach, and the probabilistic approach which calculates operability probability on a monthly basis for each transport resource and activity (Muhabie *et al.*, 2018). The results show good agreement between the two approaches and highlight the financial risks arising from the stochastic nature of the weather (Muhabie *et al.*, 2018).

Muhabie *et al.* (2018) note the stochastic nature of operation durations and assume they are normally distributed with a standard deviation equal to 10% of the mean. They also performed a sensitivity analysis on the standard deviation parameter, varying it

between 10% and 100% in steps of 10%. Results showed that this parameter had a negligible effect compared to the influence of the metocean data and it was proposed that future simulations could consider the standard deviation parameters modelling task duration to be constant.

The assumption that task durations are normally distributed is unfounded. Instead, it can be argued that asymmetric distributions for task duration would be more applicable, due to there being a minimum time in which that operation can be completed—a result of the mechanical and physical constraints associated with the operation, especially when machinery is required to perform that operation. On the other hand, one expects that there is no definite upper limit to how long an operation can take, thus making a distribution with a long right-hand tail more realistic. Consequently, the assumption of a symmetric normal distribution needs to be investigated. The investigation of task duration probability distribution described by Muhabie *et al.* (2018) could thus be expanded significantly. For example, analysing variations in the selected distributions or in all of the distribution parameters, not just the standard deviation parameter, would be beneficial.

Interestingly, the probabilistic approach discussed by Muhabie *et al.* (2018) is directly related to the monthly persistence approach discussed previously. This method uses time-series metocean data to calculate monthly persistence probabilities for each operation and then simulates these operations in turn by sampling randomly from these persistence probabilities. For consecutive operations that cannot be interrupted, the conditional probability of one event followed by the other is assumed.

The results of the analysis show good agreement between this probabilistic approach and the more standard TDS approach. However, it is suggested that the probabilistic approach may slightly underestimate the completion time of projects (Muhabie *et al.*, 2018). The probabilistic methods capture the mean and central values of project duration accurately but fail to represent the extreme durations. In other words, the *deterministic* TDS approach produces a larger spread of results. Although the probabilistic approach described by Muhabie *et al.* (2018) is slightly more sophisticated than the standard persistence calculation methods (see Stallard *et al.*, 2010; Morandeau *et al.*, 2013), the results suggest that TDS methods are more suited for capturing the full range of likely project durations. A similar comparison study between the TDS and standard persistence methods would thus be of interest. Such a study is provided in Chapter 3.

2.6.2 Limitations and Knowledge Gaps

The limitation common to all of the example TDS applications discussed above is the lack of a justified stochastic representation of operation durations. Example representations that have not been substantiated sufficiently include single values; triangular distributions and normal distributions. Several more modelling approaches for expected task duration variation can be found in the literature. For example, a percentage variation in task duration, either randomly assigned or based on a Rayleigh distribution, is used by Beamsley *et al.* (2007), as well as a randomly selected potential delay in the starting of a task. It is important to note the subtle difference here; a delay in starting the task simply shifts the operation later in time whereas the variation in task duration will increase or decrease the time required for access. Ballard and Evans (2014) define operations by their minimum completion time together with the likely increase in duration due to delays in carrying out the task. These delays are drawn from a half-normal distribution, under the assumption that the minimum time to complete the operation is the most likely and that delays are defined on top of the ideal task duration. Clearly, there is a need to assess and investigate the most suitable modelling representation for these tasks. This is the main objective of Chapter 7. Similarly, identifying an accurate representation of the frequency and duration of technical failures, and incorporating this into the TDS theory, are high priorities and thus the focus of the analysis presented in Chapter 9.

An additional feature that has so far not been mentioned is the phenomenon of *learning*. The results of the optimisation study described by Sarker and Faiz (2017), which simplifies the effect of weather and task duration, indicate that the learning rate of performing lifting and assembly operations has a significant impact on project duration. Sarker and Faiz (2017) assume a logarithmic learning rate and conclude that detailed studies on the effect of this learning phenomenon would be beneficial. Consequently, any investigations into modelling task durations should consider this learning effect. The analysis of operational data presented in Part III of this thesis has a strong focus on this learning phenomenon.

Finally, there is a paucity of research targeting the validation of time-domain simulation models. Most validation studies are described qualitatively and involve comparisons with results generated using industry-standard tools. Furthermore, while Muhabie *et al.* (2018) compares TDS results to a simulated version of the persistence method, there seems to be a lack of comparisons between TDS and the standard probabilistic methods of estimating downtime using occurrence and persistence statistics. The next chapter of this thesis, Chapter 3, describes both a targeted validation study of the TDS methods and a comparison of these methods with the standard occurrence and persistence methods.

Chapter 3

Time-domain Simulations

3.1 Introduction

Time-domain simulation (TDS) models can be used to estimate the durations of offshore operations and have been proposed as an alternative to the well-known statistical methods incorporating occurrence and persistence probabilities of metocean conditions. This chapter describes the theory and application of these two contrasting methodologies. Specifically, this chapter serves as an introduction to the field of TDS by addressing two of the major limitations highlighted in the Literature Review in Chapter 2.

Firstly, it has been shown that there is a lack of targeted validation studies of TDS methods in the academic and industrial literature. Several TDS implementations have been benchmarked against existing software tools, but explicit studies comparing observed and modelled results using TDS methods are non-existent. Thus, the first objective of this chapter is to describe a specific validation study of TDS methods. This is achieved using observed operation data from the construction phase of a Round 3 offshore wind farm.

Secondly, two case studies are provided that compare the standard probability of occurrence and persistence methods to the proposed simulation procedures. Comparisons of TDS and Markov-theory methods exist (see, for example, Anastasiou and Tsekos (1996) as referenced throughout Section 2.5.2), as well comparisons of TDS to advanced persistence-simulation methods (see Muhabie *et al.* (2018) as referenced in Section 2.6.1). However to the author's best knowledge, direct comparisons of TDS and the original occurrence and persistence methods are not available. The second objective is thus to assess the strengths and weaknesses of both methods.

Section 3.2 outlines the theory of the classical probabilistic methods and how they can be used in the estimation of expected downtime for a marine operation. This section also describes TDS and their application as an alternative estimation method, focussing on the required inputs and simulation logic of a TDS model. Metocean data validation methods are provided in Section 3.2.5. The reasons for choosing the Python programming language to implement TDS theory are outlined briefly at the

beginning of Section 3.3. Subsequently, the methodology of both the validation study and the two comparative case studies are discussed. Finally, the results of the validation and comparative studies are given in Section 3.4 before the main conclusions of this introductory analysis are summarised.

3.2 Theoretical Background

3.2.1 Occurrence and Persistence Statistics

Conventionally, the viability of an offshore operation is determined through the calculation of the *occurrence* and *persistence* of accessible conditions (Det Norske Veritas, 2010; Stallard *et al.*, 2010; Walker *et al.*, 2013; Anastasiou and Tsekos, 1996; O'Connor *et al.*, 2013). *Occurrence* is defined as the probability that an environmental parameter will be less than a threshold level (Stallard *et al.*, 2010). For example, the probability that the significant wave height H_s is less than a specified wave height required for access H_{ac} is denoted as

$$P(H_s < H_{ac})\,. \tag{3.1}$$

An empirical cumulative distribution function (CDF), or non-exceedance probability curve, is shown in Figure 3.1 and is based on a 10-year hindcast data-set of significant wave height, recorded at a 3 hour time-step, for a sheltered offshore location in the Orkney Islands (59°N, 3°W). The figure shows that the probability of achieving a significant wave height of less than 1 m is just below 80%.

Persistence is defined as the duration for which a metocean variable remains continuously below the required threshold level (Stallard *et al.*, 2010). The use of persistence statistics is recommended by Det Norske Veritas (DNV) (see Det Norske Veritas, 2010). Following the simple example above, the probability that the significant wave height H_s is continuously below an access wave height H_{ac} for an event duration greater than the required access time τ_{ac} is given by

$$P(H_s < H_{ac}\ ,\ t \geq \tau_{ac})\,. \tag{3.2}$$

Figure 3.2 shows the variation of the probability of persistence for access wave heights of 1.5 m, 1.0 m and 0.5 m. The persistence example shown in Figure 3.2 corresponds to the same data that was used for Figure 3.1. For a given access wave height, the probability of persistence was calculated as the sum of all the weather windows greater than the given event duration, divided by the total number of hours in the data-set (O'Connor *et al.*, 2013). The probability that the significant wave height will be less than 0.5 m for a period greater than 24 hours is approximately 40%.

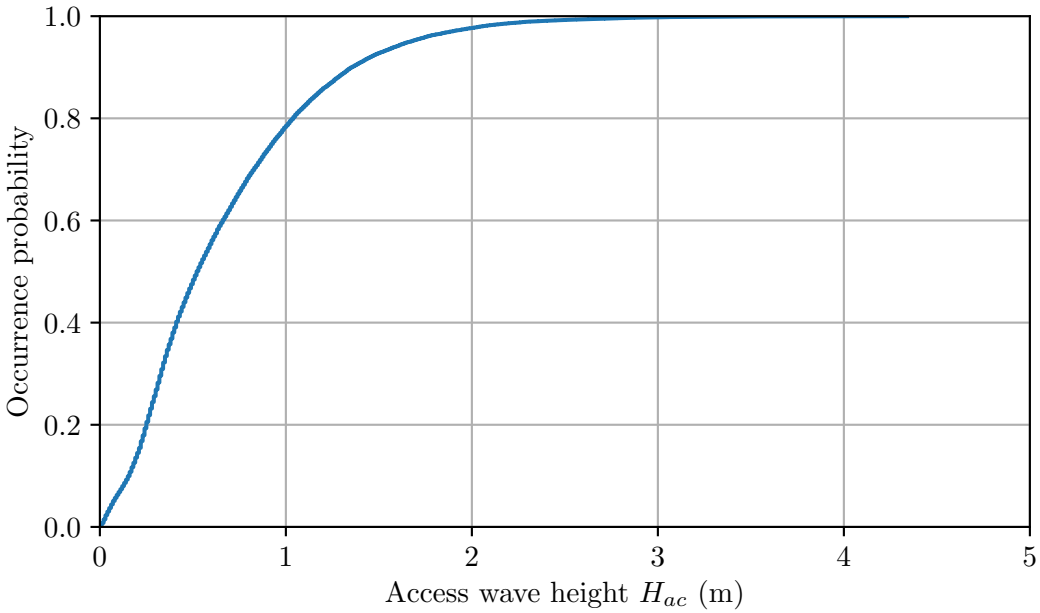

Figure 3.1: Example probability of occurrence plot for significant wave height H_s.

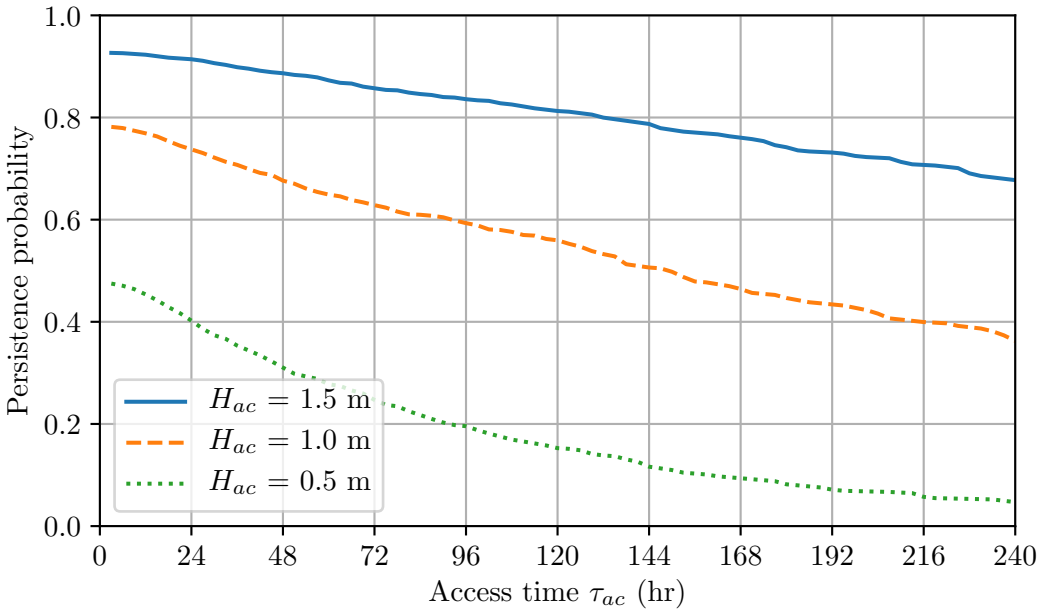

Figure 3.2: Example probability of persistence plot for significant wave height H_s.

3.2.2 Estimating Downtime using Occurrence and Persistence

A methodology for the estimation of downtime based on the probability of persistence of metocean conditions is outlined by Stallard *et al.* (2010) and Walker *et al.* (2013). The number of access days in a given time-interval is estimated as:

$$D_{ac} = D\,P(c,\ t \geq \tau_{ac})\,, \tag{3.3}$$

where $P(c,\ t \geq \tau_{ac})$ is the probability of persistence of a metocean condition c for an operation duration greater than or equal to τ_{ac} and D is the number of days in the time interval. For example, if annual persistence statistics were being assessed, the interval D would be set as 365 days.

An estimate of the number of accessible events with duration greater than τ_{ac} in this time interval D is given by;

$$N_{ac} = \frac{D_{ac}}{\tau_{ac}}\,, \tag{3.4}$$

noting that N_{ac} is a dimensionless quantity.

The estimated metocean downtime is obtained by calculating the mean number of days between the periods when the operation can be carried out;

$$\tau_d = \frac{D - N_{ac}\tau_{ac}}{N_{ac}} = \frac{D - D_{ac}}{N_{ac}}\,. \tag{3.5}$$

The total operation time is defined as the sum of the required access time and the mean metocean downtime;

$$\tau_{op} = \tau_{ac} + \tau_d\,. \tag{3.6}$$

Combining Equations 3.3–3.6 leads to the simplification;

$$\tau_{op} = \frac{\tau_{ac}}{P(c,\ t \geq \tau_{ac})}\,. \tag{3.7}$$

The above method can also be applied using the probability of *occurrence* of a given condition. In this case, the denominator of Equation 3.7 is the occurrence probability of a given condition, $P(c)$, and the method ignores the duration of the weather window, τ_{ac}. An example application of this alternative *occurrence* downtime equation can be found in the earlier work of van der Wal and de Boer (2004).

3.2.3 Limitations of Probabilistic Methods

The limitations of these probabilistic methods that have previously been discussed in Section 2.5.1 are re-iterated here to help illustrate the differences between the probabilistic approach and TDS methods. The probabilistic methods are not well-suited for analysing projects consisting of sequential operations (Walker *et al.*, 2013) because they only provide estimates of the expected value of weather downtime for a *single* operation, thus ignoring the transitions between operable or non-operable sea states for the successive operations that comprise an entire project (Anastasiou and Tsekos, 1996).

Furthermore, it is difficult to account for the joint probability of more than one metocean variable (Stallard *et al.*, 2010). A statistical approach is straightforward to apply to a single metocean variable, but marine operations are often strongly dependent on several metocean parameters. Using the same example described in Section 2.5.1, the installation of a tidal turbine in an energetic tidal stream that also requires heavy lifting operations will be constrained by wave, wind *and* tidal current conditions.

3.2.4 Time-domain Simulations

Background

As described in detail in Chapter 2, the limitations of the probabilistic methods described above do not apply to TDS. Analysing records of the time variation of metocean conditions is the most straightforward and appropriate method for the estimation of downtime and the detailed design of a marine project consisting of sequential operations (Stallard *et al.*, 2010). The use of TDS for the modelling and analysis of offshore operations is recommended by the DNV (Det Norske Veritas, 2010). Several advantages over the standard statistical methods are described by (Det Norske Veritas, 2010), including the ease with which the limits of several metocean parameters can be combined.

Simulating the marine operation over several years provides a robust statistical basis for the estimation of downtime and likely duration of an offshore project. In contrast to the other weather window analysis techniques discussed above, this method considers the sequential nature of marine operations and the effect of small cumulative delays on the overall project completion date (Beamsley *et al.*, 2007).

The two main inputs required for a TDS analysis are (*i*) a metocean data time-series and (*ii*) definitions of the *job sequence*.

Metocean Data

The application and validity of the TDS technique is determined by the availability of accurate and site-specific metocean data at a sufficient temporal resolution (Beamsley *et al.*, 2007). Temporal resolutions applied in the literature range from hourly (see Beamsley *et al.*, 2007) to 3-hourly (see Ballard and Evans, 2014). Most importantly, this resolution needs to compatible with the operation with the lowest duration in the model. For example, 3-hourly data will be unsuitable for a tidally-constrained operation that requires a strict tidal window of 15 minutes.

Furthermore, a TDS analysis requires a sufficiently extensive metocean data-set to ensure the validity of results (Ballard and Evans, 2014). A period of greater than 5–10 years is recommended by van der Wal and de Boer (2004), but they do not provide a quantitative justification for this number. It is particularly important to obtain a temporally extensive data-set capable of capturing longer-term oceanic and climate cycles such as the North Atlantic Oscillation or El Niño Southern Oscillation. It is also important to avoid the issue of using a metocean time-series history that was particularly severe or benign in comparison to the long-term norm (Graham, 1982). The analysis in Chapter 5 investigates this issue and attempts to identify the minimum acceptable length of metocean data for a TDS study.

Hindcast data-sets are typically used as the source for metocean data in a TDS study as they are often the only method of obtaining a suitably long time-series. Recorded metocean data can also be used but are generally too short in duration, only available for a limited number of locations and are difficult to obtain (Ballard and Evans, 2014). Re-analysis data such as the 5^{th} generation re-analysis (ERA5) produced by the European Centre for Medium-Range Weather Forecasts (ECMWF) are an alternative option. ERA5 periodically uses its forecast models and data assimilation methods to 'reanalyse' archived observations, creating accurate global data-sets that describe recent history of the atmosphere and oceans (Copernicus Climate Change Service (C3S), 2017). This data-set is freely available on a high-resolution latitude-longitude grid for the entire globe. At present, approximately 18 years of data are available but the data-set is expected to cover the period 1950–present by mid 2019 (Copernicus Climate Change Service (C3S), 2017).

Job Sequence

The next input requirement for a TDS model is the definition of the *job sequence*. This comprises a list of marine operations that must be completed in a specified order. A typical marine project naturally lends itself to this sequential breakdown of operations. Each individual operation is defined by;

- its duration (typically given in hours),
- an indication of the probability distribution of operation duration (see below),
- a time-series of metocean data that represents adequately the environmental conditions at the operation location,
- its metocean thresholds and
- its requirement for daylight working hours.

Probability Distribution of Operation Duration

Fluctuations in the durations of offshore operations due to unforeseen events, independent of metocean conditions, are typical. TDS are capable of quantifying these effects by employing a Monte Carlo approach (Ballard and Evans, 2014). Statistical probability distributions give an indication of the likely range in operation duration and are essential if a Monte Carlo analysis is required. Operation durations are determined by randomly sampling from the input probability distribution.

The input distributions are defined in several ways in the literature, several examples of which are given in Section 2.6. There has been no clear consensus on the best method of representing this variability in operation duration in TDS models. This is the main subject of investigation in Chapters 7–8.

Simulation Logic

Starting at a specified simulation start date, the TDS algorithms analyse the duration of each operation in sequence. Using the thresholds and duration of the operation and the associated metocean input data, the simulation model identifies when the operation can proceed, storing the end date of that operation as well as the downtime experienced. The system then moves through the subsequent sequential operations until the project is complete. The above simulation is repeated a number of times for each year in the metocean data-set.

Several recommendations on the required number of simulations are given in the literature. For example, Beamsley *et al.* (2007) suggest in excess of 1,000 iterations per year, while Ballard and Evans (2014) only use 500. Chapter 5 assesses the number of simulations per year that are required to achieve convergence of results.

3.2.5 Metocean Data Validation Methods

Several sources of metocean data were used in the validation study described in this chapter. It was necessary to validate a selection of these data-sets to ensure that they represented accurately the metocean conditions experienced at the project location for the time-interval in question. A combination of graphical and numerical statistical methods were used to perform these metocean data validations. Time-series plots comparing the two data-sets were the main graphical technique used in this chapter.

The numerical methods included the calculation of the following industry-standard statistics (see, for example, Olauson, 2018; Van Os *et al.*, 2011; Williams and Esteves, 2017; Boudière *et al.*, 2013; Shao *et al.*, 2018);

- Root-mean-square error (RMSE),
- Mean absolute error (MAE),
- Bias or mean error (ME),
- Correlation (Pearson's product-moment coefficient, R) and
- Scatter index (SI).

The formulae for these statistical metrics are given below, where O_i are the *observed* or measured values and S_i are the *simulated* or predicted values of the selected parameter. N_i is the total number of data-points in each sample.

$$\mathrm{RMSE} = \sqrt{\frac{1}{N_i}\sum_{i=1}^{N_i}\left(S_i - O_i\right)^2}\,. \tag{3.8}$$

$$\mathrm{MAE} = \frac{1}{N_i}\sum_{i=1}^{N_i}\left|S_i - O_i\right|\,. \tag{3.9}$$

$$\mathrm{Bias} = \frac{1}{N_i}\sum_{i=1}^{N_i}\left(S_i - O_i\right)\,. \tag{3.10}$$

$$\mathrm{R} = \frac{\sum_{i=1}^{N_i}\left(S_i - \overline{S_i}\right)\left(O_i - \overline{O_i}\right)}{\sqrt{\sum_{i=1}^{N_i}\left(S_i - \overline{S_i}\right)^2}\sqrt{\sum_{i=1}^{N_i}\left(O_i - \overline{O_i}\right)^2}}\,, \tag{3.11}$$

where

$$\overline{O_i} = \frac{1}{N_i}\sum_{i=1}^{N_i} O_i \tag{3.12}$$

and

$$\overline{S_i} = \frac{1}{N_i} \sum_{i=1}^{N_i} S_i \,. \tag{3.13}$$

$$\mathrm{SI} = 100 \times \frac{\sqrt{\frac{1}{N_i} \sum_{i=1}^{N_i} (S_i - O_i)^2}}{\frac{1}{N_i} \sum_{i=1}^{N_i} O_i} \,. \tag{3.14}$$

3.3 Methodology

The methodology for the initial exploration reported in this chapter is divided into three parts. Firstly, Section 3.3.1 outlines the reasons for choosing the Python programming language to implement the TDS algorithms described in this thesis. Secondly, the methodology of the validation study using observed operation data from the construction phase of a Round 3 European offshore wind farm is described. Finally, the procedure for comparing TDS and the previously described probabilistic methods is given.

3.3.1 Why Python?

The ForeCoast® Marine time-domain simulation software has been developed using the Python programming language. The following list, selected from the benefits of Python proposed by Oliphant (2007), outlines some of the reasons for choosing Python.

- The liberal open source licence allows the developers of Python-based applications to decide how the software is sold, used and distributed.
- The fact that Python runs on numerous platforms avoids issues with portability.
- The language's clean syntax allows code to be written in either a procedural or fully object-orientated fashion.
- Python can be embedded into an existing application.
- The large number of library modules enable the construction of sophisticated programs.

The final point listed above is crucially important. The Python-based *SciPy* eco-system of open-source software (Jones *et al.*, 2001–) for mathematics, science and engineering has been used extensively throughout the development process. This suite of software includes; *NumPy*, the fundamental package for scientific computing with Python (see Oliphant, 2006); *Matplotlib*, a 2D graphics package used for application development, interactive scripting and publication-quality image generation (see Hunter, 2007) and

Pandas, a library of robust, easy-to-use data structures and statistical tools, initially developed for quantitative financial applications, that help make scientific Python a more attractive and practical statistical computing environment (see McKinney, 2010). These packages, and several others, are referenced throughout this thesis.

3.3.2 Validating Time-domain Simulations

The validation section of this analysis compares the results of a TDS model to observed installation data for a Round 3 offshore wind farm. The developed TDS model was used to support the entire construction campaign but the following validation study assesses a subset of the marine operations. Specifically, the analysis concerns the foundation installation tasks for a selection of the wind turbine generator (WTG) locations.

Operational Data

The exact durations of the selected installation operations, omitting all weather downtime, were extracted from the observed operational data supplied by the client. Using realistic and representative input operation data is a pre-requisite for a successful TDS simulation—the uncertainty associated with these durations is what necessitates a Monte Carlo approach in a full analysis. This Monte Carlo approach is not necessary when exact operation durations are provided, as is the case for this validation study. If perfectly accurate metocean data were used as an input, together with the exact operational data used in this validation, and assuming that the on-board crew followed the prescribed metocean thresholds exactly, the TDS algorithms should produce near-identical results to the observed installation progress.

Metocean Data

The other major requirement for the validation study was to obtain accurate representations of the metocean conditions experienced at the key project locations and for the time-period coinciding with the operational data records. Three project locations were included in the TDS model; the *port*, a point representing the *transit* route and the *site*. There were different limiting metocean thresholds for operations performed at each project location and these are summarised in Table 3.1.

Table 3.1: Limiting metocean parameters for each project location.

Data-point	*Significant wave height*	*Wind speed*	*Tidal current*
Port		✓	
Transit	✓		
Site	✓	✓	✓

Telemetry data for the significant wave height and tidal current at the offshore site were provided by the client for the appropriate time-period. These measurements were the most accurate source of metocean data. As can be seen in Table 3.1, representations of significant wave height for the transit route and wind speed for port and site operations were still required.

Metocean time-series from a bespoke hydrodynamic model for the key project locations were also provided by the client. This extensive data-set was used in the full Monte Carlo analysis that supported the entire construction campaign and is also used in the comparison of the probabilistic and TDS methods described in Section 3.3.3. Unfortunately, the temporal range of the provided time-series did not overlap with the dates of the observed operational data. However, the highly accurate and location-specific *client model* data provided appropriate representations of the realised conditions at the key project locations. As such, these data could be used to verify alternative metocean data sources that did overlap with the operational period in question and could thus be used in the validation study.

Firstly, recorded onshore wind speeds were obtained from the online database of the national weather institute for the port location in question. In the client model, the transit route was divided into several intermediate locations. Transit location "A" of this model was the closest intermediate location to the port. The weather station data was thus compared to the wind speed data record at transit location A using the numerical and graphical techniques discussed in Section 3.2.5.

A representation of the wave conditions experienced on the transit route was obtained from the interim European Reanalysis data-set (ERA-Interim) (see Dee *et al.*, 2011). ERA-Interim, created and maintained by the European Centre for Medium-Range Weather Forecasts (ECMWF), was the predecessor to the recently published ERA5 data-set mentioned previously (see Copernicus Climate Change Service (C3S), 2017). There was only one ERA-Interim data point in the vicinity of the transit route for this project. Data obtained for this location were compared to the nearest location available in the client model data-set, using the same techniques as before.

Finally, representative wind-speeds for the site location were also obtained from the ERA-Interim data-set. The ECMWF *Site* location was chosen as the closest available point in this data-set to the actual site and the same graphical and numerical comparison techniques were also applied to these two data-sets.

For all three of the alternative metocean sources, data were extracted for a time period that coincided approximately with the actual construction period but from a randomly chosen historical year. In this case, data were extracted for 2010 and compared to the corresponding interval from the client model data.

Running the Simulation

Using the extracted job sequence data and the metocean data informed by the results of the metocean validation analysis as inputs to the developed TDS model, a single simulation of the TDS was performed. Only one simulation was required because the exact durations and weather conditions were specified. The simulation results were then compared to the observed data provided by the client.

3.3.3 Comparing Time-domain Simulation and Probabilistic Methods

The next section of this analysis describes two case studies that compare the results for estimated project duration using the probabilistic methods and the TDS methods. It has been suggested that TDS simulations are well-suited for analysing offshore projects consisting of sequential tasks and that this is a main advantage over the standard probabilistic methods. However, a direct comparison between these two methods has not yet been performed. Consequently, this section aims to compare the two approaches and analyse quantitatively the differences between the results generated by each method. The first case study describes a hypothetical test activity and the second example uses the operational data from the validation study described previously.

Test Activity

Details of the hypothetical test activity comprised of 5 operations are given in Table 3.2. Metocean data obtained from the client's bespoke hydrodynamic model were used. The data consisted of 18 years of significant wave height (H_s), wind speed (v_w) and tidal velocity for the site location.

Table 3.2: Operation durations and thresholds for test activity comparison

Operation	*Duration (days)*	*H_s limit (m)*	*v_w limit (m/s)*
Op 1	0.42	1.25	14
Op 2	0.25	1.5	-
Op 3	1	1	8
Op 4	0.75	1.25	10
Op 5	0.5	2	18
Total	2.92	-	-

Using the above operation thresholds and durations, together with the 18 years of metocean data, the total operation time τ_{op} was calculated for each operation using Equation 3.7. Note that for the occurrence probability, the denominator of Equation 3.7 is the probability of occurrence $P(c)$. The total activity duration based on the probabilistic methods was then calculated as the sum of each total operation time. For the

TDS model, a simulation of the hypothetical activity was performed starting on each day of the metocean time-series. This struck a balance between omitting sequences of metocean data—if, for example, simulations were performed at intervals of a week—and repeated counting of the same metocean data—for instance, if simulations were performed starting at every hour of the metocean data-set.

Validation Activity

The metocean data output from the bespoke hydrodynamic model was also used for the validation activity. However, rather than using the entire 18 years of data, time-series for the 10 week period corresponding to the dates of the observed data-set were extracted from each of the 18 years. The mean duration, *excluding* weather downtime, of each operation in one of the main activities from the observed data-set described in Section 3.3.2 was obtained and used as the input job sequence. Once more, Equation 3.7 was used to calculate the expected activity duration using the probability of occurrence and persistence techniques. For the TDS model, the activity was simulated on each day of the partitioned metocean data-set. As for the test activity, identical inputs were used for the three methods being compared. The selection of metocean data also enabled a viable comparison to be made with the observed data.

3.4 Results and Discussion

3.4.1 Validating Time-domain Simulations

Metocean Data Validation

The numerical results of the metocean data validation for each of the three data-set are shown in Table 3.3. Graphical results are shown in Figures 3.3–3.5.

Table 3.3: Statistical validation results for metocean time-series comparison.

	Wind speed—port	*Significant wave height—transit*	*Wind speed—site*
RMSE	2.25 m/s	0.53 m	1.67 m/s
MAE	1.77 m/s	0.43 m	1.31 m/s
Bias	0.03 m/s	-0.36 m	0.21 m/s
R	0.81	0.64	0.86
SI (%)	30.95	52.62	20.28

The observed weather station data and the wind speed data from the client model at the port location showed good agreement. The bias between the client model and the weather station data was 0.03 m/s. The high correlation factor, low scatter index and

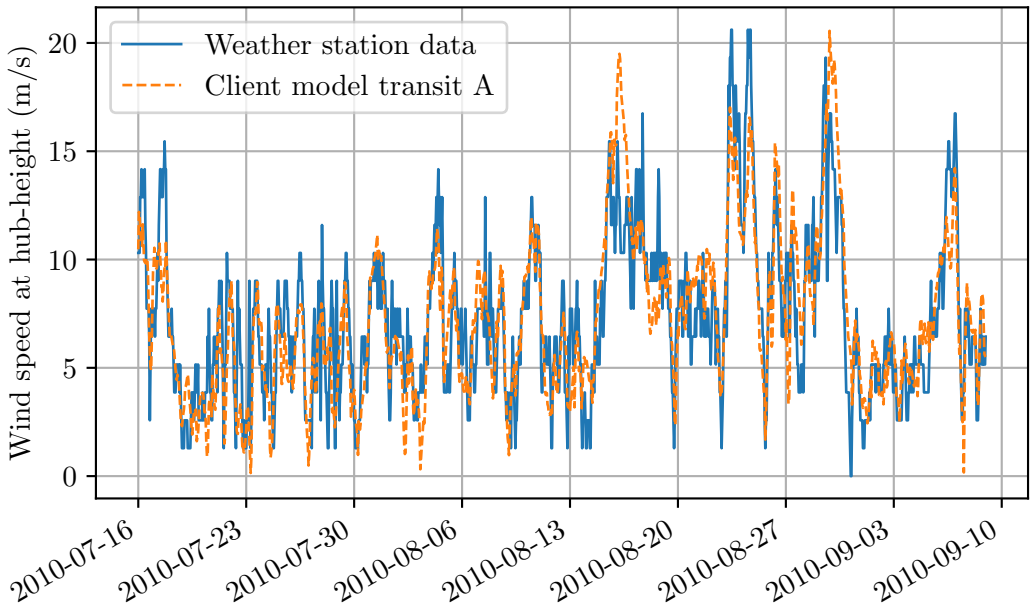

Figure 3.3: Comparison of weather station and client model wind speeds for the port.

visual agreement evident in Figure 3.3 suggest that the weather station data represent adequately the wind conditions at port and can be used in the TDS model.

Similarly, the results for the wind speed at the site location show an acceptable agreement. The numerical results show an even lower scatter index of 20.3% and a higher correlation coefficient of 0.86. The graphical comparison in Figure 3.4 supports the numerical results and shows that the ECMWF wind speed data for the site is appropriate.

Conversely, the results for significant wave height at the transit location highlight a large discrepancy between the client model data and the ECMWF wave data. The large negative bias statistic of -0.36 m, together with the visual comparison in Figure 3.5, show that the ECMWF data underestimate the client model data they are modelling. The numerical validation results for significant wave height are lower in absolute terms (0.53 m for RMSE and 0.43 m for MAE) in comparison to the wind speed results but this is attributable to the long-term absolute values of both variables. More importantly in this case, the statistics for correlation of the wave data are much lower (0.64) and the scatter index is significantly higher (over 50%), indicating a more substantial discrepancy.

The discrepancy in results is thought to be attributable to the nature of the transit route between port and site, which consisted of a sheltered section and an exposed section. The closest ECMWF data point to the transit route was located in the sheltered section of this transit. Transit location B in the client model is also located in the sheltered

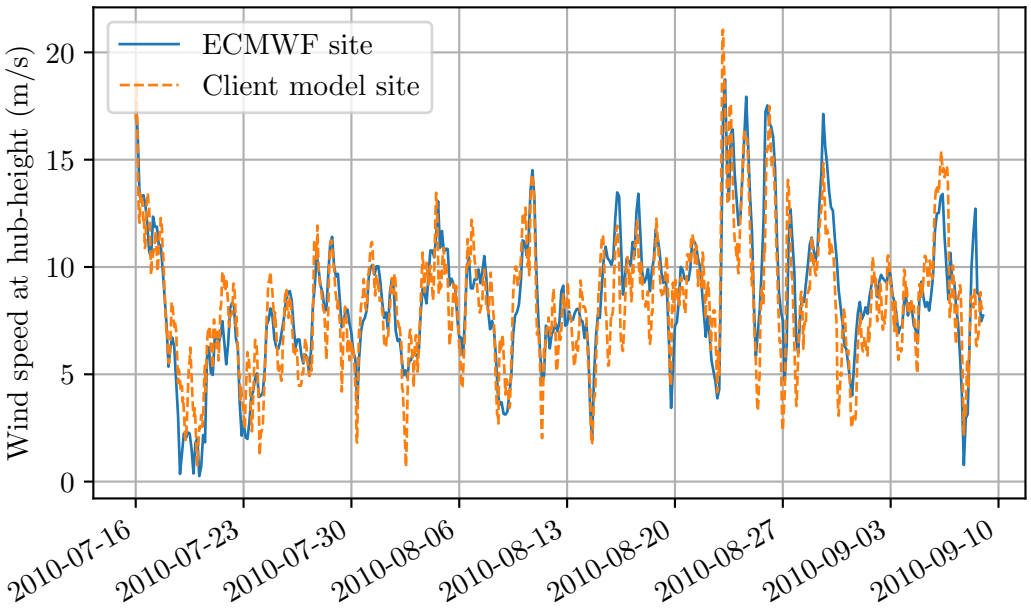

Figure 3.4: Comparison of ECMWF and client model wind speeds for the site.

section of the transit, but is slightly more exposed than the ECMWF transit location. It is thus understandable that using this point and the ECMWF data would have underestimated the metocean conditions experienced on the sheltered section of the transit.

Furthermore, a representation of the more energetic wave climate of the exposed section of the transit was also required. The wave climate in this second leg of the route was expected to be very similar to the wave regime at the site. Consequently, the transit operation in the TDS validation model was split into two legs. The first data-point used the wave heights and wind speeds of the ECMWF transit location and the second data-point used the telemetry data for the site location.

The four data-points used in the validation model are shown in Table 3.4, along with the source of metocean data for each of the three metocean parameters. The representation of the metocean conditions for the transit operation is not as accurate as the other locations, due to the slight mismatches between the ECMWF data location and the actual point it represents. However, the described metocean data was the most accurate data available. Additionally, the representation of the site conditions is the critical location—because the majority of operations, and those with the most stringent metocean thresholds, all take place at the site—and there is high confidence in these metocean data-sets.

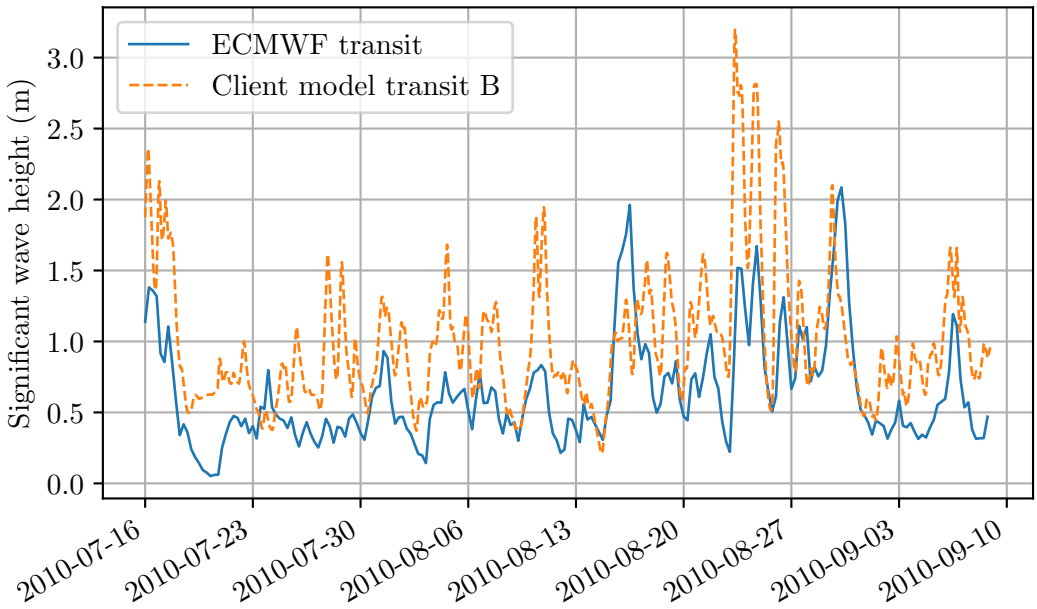

Figure 3.5: Comparison of ECMWF and client model significant wave heights speeds for the transit.

Table 3.4: Selected sources of metocean data for validation study.

Data-point	*Significant wave height*	*Wind speed*	*Tidal current*
Port	-	Weather station data	-
Transit 1	ECMWF transit	-	-
Transit 2	Telemetry site	-	-
Site	Telemetry site	ECMWF site	Telemetry site

TDS Validation

Figure 3.6 shows the durations required to complete successive project milestones for the observed operational data and the results produced by the TDS model. The comparison shows good agreement between the two data-sets, with the simulation results predicting slightly more optimistic progress than the observed data. By the end of the validation period, with a duration of just under 8 weeks, the deviation between the observed data and the simulated results was 1.5 days. Figure 3.7 shows the variation of the deviation between the observed and modelled results. The deviation is calculated as the simulated milestone completion date minus the observed milestone completion date, i.e. a negative deviation indicates that the simulation completed a milestone earlier than the actual data. The maximum deviation result over the entire validation period was -4.6 days. The mean deviation over the entire period was -1.7 days. Importantly, the random scatter of the deviation values implies that there is no systematic error being introduced in

the simulation model; there is no evidence for progressive underestimation of the time taken to complete successive milestones. The results show an acceptable validation of the TDS theory; if accurate metocean and operational data are provided, the simulation will generate precise estimates of project duration.

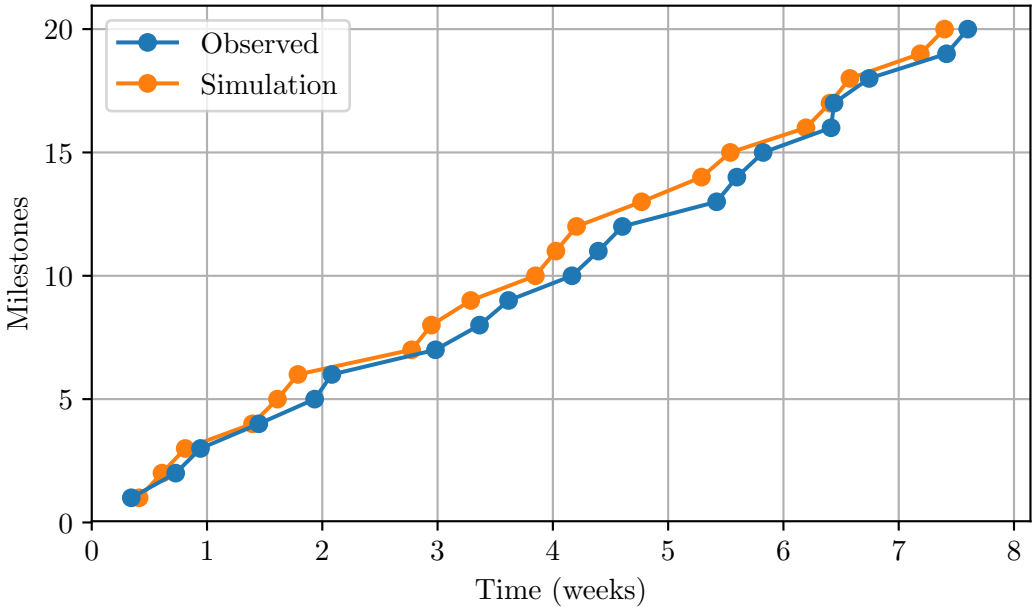

Figure 3.6: Validation curve showing progression of milestones over time.

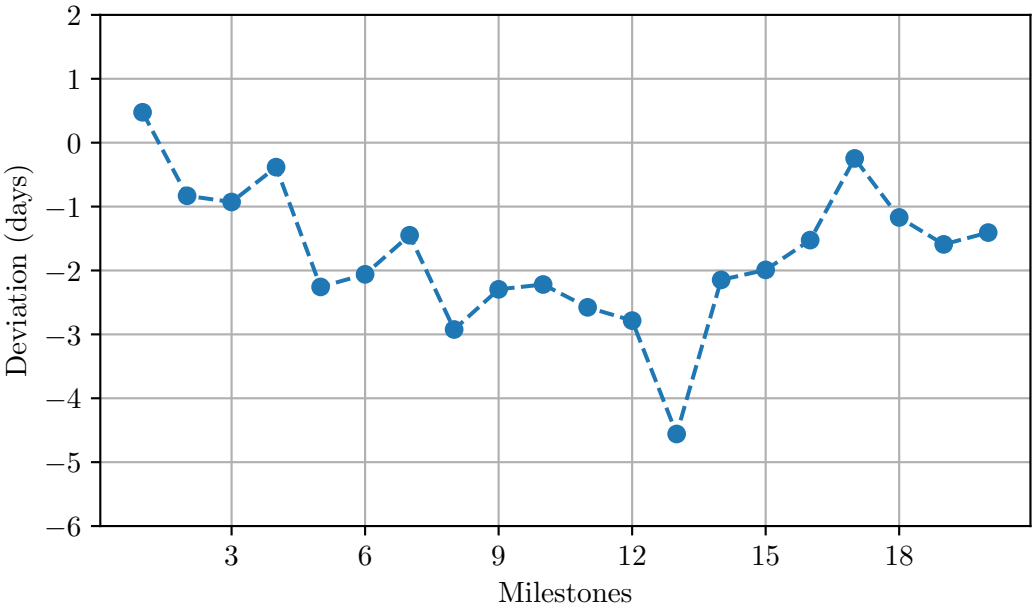

Figure 3.7: Deviation between simulation results and observations for validation study.

There are several probable explanations for the small discrepancies that can be seen in the results. The most obvious is that the metocean data used in the simulation was not perfectly representative of the actual metocean conditions. As outlined previously, the metocean data used for the transit location was not perfectly representative.

The other explanation is related to one of the major limitations of the current TDS model. Currently, operational decisions are based on the input metocean data, typically hindcast data, which is also assumed to be the actual representation of the metocean conditions. As such, the system essentially has perfect knowledge of future metocean conditions and it never makes a "wrong" decision. In reality, operational decisions are based on metocean forecasts and there will be times when the decision is made to halt operations based on the most recent forecast data, but the actual metocean conditions that arise would have allowed operations to continue. Conversely, the decision may be made to proceed with operations and the realised weather results in the operation failing. The latter of these two scenarios is accounted for in the model. Interruptible operations can proceed until adverse metocean conditions are encountered and recommence after the conditions have passed. For non-interruptible operations, the entire duration of adverse weather is counted as downtime. However, the former scenario is not considered in the current TDS implementation. Consequently, the simulation model can be viewed as being slightly optimistic. This offers a possible explanation for the discrepancies shown in Figures 3.6 and 3.7. Future work should incorporate archived forecast data in the model, in addition to the hindcast data that represents the realised weather. Operational decisions would then be based on the imperfect archived forecast data. This functionality would account for the human element that arises when making important decisions in the marine environment.

3.4.2 Comparing Time-domain Simulation and Probabilistic Methods

Test Activity

Figure 3.8 shows a box-and-whisker plot of activity duration for the two probabilistic methods and the results from the TDS model. The box represents the inter-quartile range (IQR). The whiskers represent the minimum and maximum observed values. Box-and-whisker plots are discussed in detail in Section 5.2.2.

As expected, the persistence method is predicting larger activity durations than the occurrence method because of the additional duration constraint. More importantly, both methods produce lower mean duration estimates than the TDS model. The mean simulation value is over double that predicted by the probability of occurrence. Also, the median TDS projection is slightly greater than the mean duration obtained from persistence methods. The results support the theory proposed by Beamsley *et al.* (2007) that the standard probabilistic methods ignore the sequential nature of marine

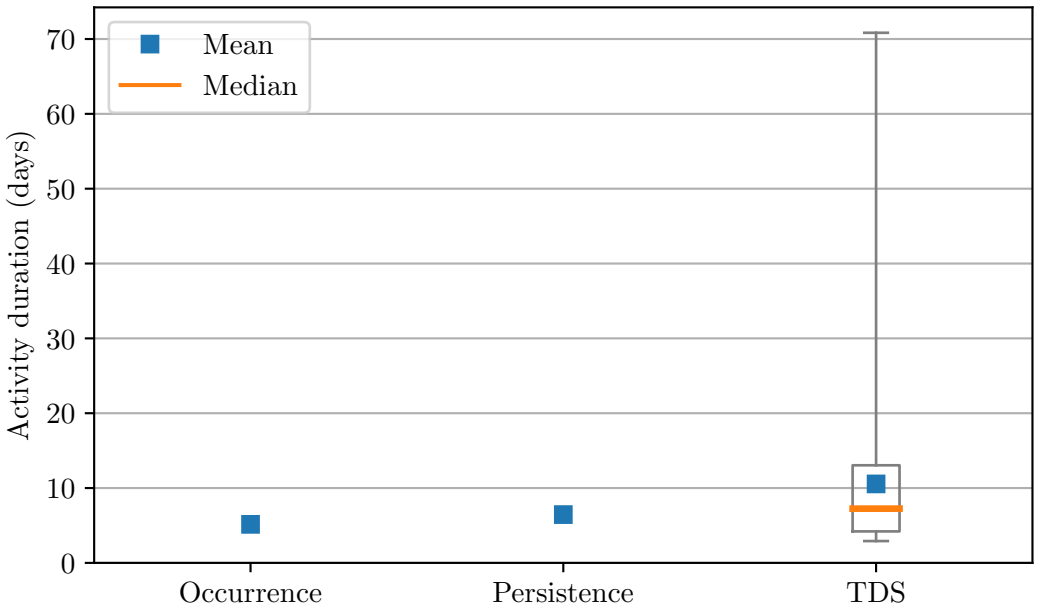

Figure 3.8: Comparison of probabilistic and TDS methods—test activity. Whiskers represent the minimum and maximum simulated values of the TDS results.

operations and the effect of small cumulative delays on the overall project completion date.

Additionally, the TDS model is capable of identifying the range in activity durations, rather than returning a single estimate of the mean value. The TDS results imply that there is just over a 25% chance that the duration of the activity will be less than that predicted by the probability of occurrence. Conversely, the worst case scenario, corresponding to the maximum value returned by the simulation results, indicates that an activity that should take just under 3 days could take approximately 70 days if the worst possible start date was chosen.

Validation Activity

Figure 3.9 shows a similar box-and-whisker plot of activity duration for the three analysis methods, with the data normalised to the mean activity duration of the observed results *including* metocean downtime. The comparison shows similar results to the test activity. The occurrence and persistence methods are predicting activity durations that are approximately 20% less than the observed value, while the mean result from the TDS model is approximately equal to the observed mean.

The figure also includes a box-and-whisker plot of the observed data. This plot shows the spread of recorded activity durations for the specific period in which the operations

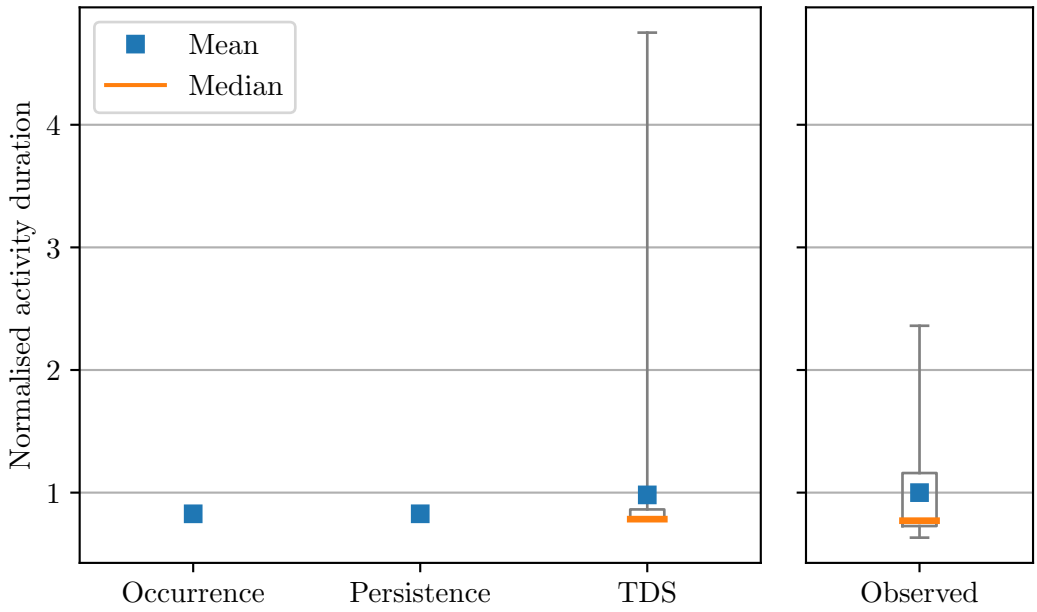

Figure 3.9: Comparison of probabilistic and TDS methods—validation activity. Whiskers represent the minimum and maximum values. The observed data shows the variation in the actual activity duration extracted from the observed installation data obtained over the 10-week campaign. The left-hand plot shows the results of the three methods using 18 instances of the equivalent 10-week period extracted from the metocean re-analysis data.

took place, while the calculated results show the estimates based on the partitioned re-analysis metocean data-set. In other words, the observed results show the variation in the actual activity duration as measured during the construction campaign. The calculated results are based on 18 instances of the equivalent 10-week period extracted from the historic re-analysis metocean data-set. As such, the underlying metocean data for the left- and right-hand side plots are different. The purpose of including the observed data is not to make a direct comparison between the two sets of results, but to show the variation that occurred in a single campaign and how this compares to the results produced by each calculation method when using an extensive metocean data-set. The TDS model yields a stochastic set of results that encloses the spread in observed activity duration while the probabilistic methods only offer a single mean value that gives no indication of the likely range of possible durations.

The operations involved in the chosen activity were all relatively short (in the order of hours) and had relatively lenient thresholds. This explains why the occurrence and persistence results are nearly identical. It also explains why the P0, P25 and P50 activity durations calculated by the TDS analysis are all equal to a value of 0.784, which is equal to the mean activity duration *excluding* metocean downtime.

The validation activity results reaffirm one of the major benefits of using TDS for estimating project durations of offshore operations. Half of the simulated activities are predicting durations slightly lower than the occurrence and persistence methods. However the maximum simulated value shows that the duration could be almost 5 times the observed mean duration. The results show that TDS models can be used to obtain realistic, probabilistic estimates of project duration and thus contribute to the quantification of the inherent risks of working in the offshore environment.

3.5 Conclusions

The aim of this chapter was to address two of the major limitations associated with TDS theory; firstly, to perform a specific validation analysis of the TDS methods using observed data and, secondly, to assess the differences between the standard probabilistic methods for estimating downtime and the results obtained from a TDS model.

The validation study in this chapter compared the results of a bespoke TDS model to observed operation data from an offshore wind farm construction project. For the 8 week validation period of this study, the mean deviation between simulated and observed milestone completion dates was 1.7 days. By the end of this 8 week period, the difference between simulated and observed results was 1.5 days. The validation study showed that if accurate metocean and operational data are provided, TDS models can produce precise estimates of project duration.

The results of two comparative case studies that assessed the differences between standard statistical methods and TDS theory support the idea that the classical probabilistic methods ignore the sequential nature of marine operations and the effect that small cumulative delays can have on the overall progression of the project. Results from both scenarios have shown that the conventional methods tend to underestimate metocean downtime and mean project duration.

Crucially, the analysis in this chapter has shown that TDS models can be used to generate probabilistic estimates of the duration of offshore operations. For a hypothetical test activity, occurrence and persistence methods predicted a mean duration of approximately 5 and 6.5 days respectively. A quarter of the TDS simulations resulted in an activity duration less than that estimated using the occurrence downtime method. Conversely, the mean TDS result of approximately 10 days was almost double the mean occurrence result and the maximum value returned by the TDS model indicated that an activity that should take 3 days (without weather downtime) could take up to 70 days. These probabilistic estimates of downtime that can be obtained from a TDS model are useful in the planning stages of a marine project and help assess the inherent risks of working in the harsh and complex marine environment.

PART I

Before

Chapter 4

Animating the Outputs of Time-domain Simulations

4.1 Introduction

Time-domain simulation (TDS) models are not exempt from George Box's well-known statistical aphorism that *"all models are wrong but some are useful"*. It is crucially important to ensure that the developed simulation models are as representative of the planned offshore operations as possible. Reducing the possibility of model error and significant misinterpretation of model logic and results is imperative. Ensuring the model is fit for purpose is a particularly difficult task when using the standard TDS outputs which typically consist of extensive lists of activity completion times. This chapter describes methods that enable for the first time the graphical animation of TDS outputs. Typical outputs from the developed animation module are provided that aid the visualisation of a hypothetical offshore wind farm construction project. The possibility of incorporating the animation functionality within quality assurance (QA) procedures is also discussed. One of the aims of this chapter is to provide a quantitative indication of the impact that TDS animations can have on the TDS modelling process.

Section 4.2.1 provides the overall strategy behind the development of the animation module and describes the two Python tool-kits that have been integrated within the TDS animation module; the *basemap* and *animation* packages. The specific methods required to convert TDS output data into an animated video are then discussed in Section 4.2.2. Typical animation outputs are described in Section 4.3 using results from a hypothetical offshore wind farm simulation. Finally, Section 4.4 provides a discussion on the animation module, focussing on the potential incorporation of TDS animations within QA procedures and the quantification of the scale and impact of the developed methodology.

4.2 Methodology

The methodology described in this chapter is divided into two parts. Section 4.2.1 discusses the general strategy for animating TDS, specifically the two software packages that are used within the animation module. The methods developed for converting the standard tabular output of TDS into an animated video are then described in Section 4.2.2.

4.2.1 Strategy

Matplotlib is a 2D graphics package for the Python programming language that is used for application development, interactive scripting and publication-quality image generation across user interfaces and operating systems (Hunter, 2007). It is one of the most important libraries in the *SciPy* ecosystem of open-source software for mathematics, science and engineering (Jones *et al.*, 2001–).

Two "sub-packages" within the *Matplotlib* library have been used in the development of the animation functionality for TDS. The *basemap*[1] tool-kit is a library for plotting 2D data on map projections in Python. The *animation*[2] functionality enables the creation of videos based on the standard plotting techniques within the library. As shown in Figure 4.1, the developed animation functionality combines these two packages with the standard outputs obtained from TDS.

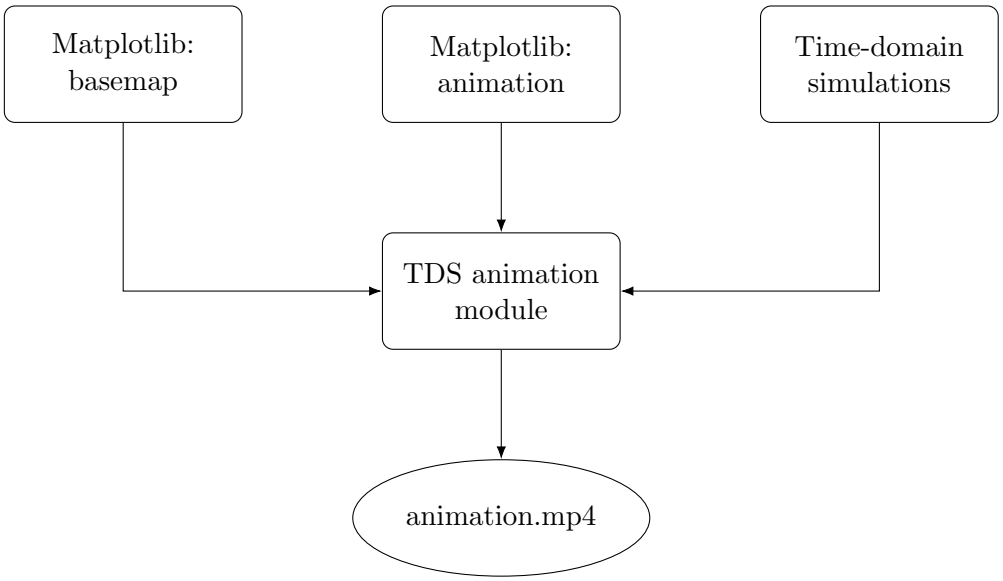

Figure 4.1: Structure of the time-domain simulation animation module.

1. see https://matplotlib.org/basemap/. Accessed 18th January 2020.
2. see https://matplotlib.org/api/animation_api.html. Accessed 18th January 2020.

Basemap

The *basemap* tool-kit enables data to be plotted on several map projections using the standard *Matplotlib* plotting techniques. It allows coastlines, political boundaries and rivers to be drawn in several resolutions and also supports annotations (Hunter, 2007).

Figure 4.2 shows an example figure generated using the *basemap* tool-kit. To produce this figure, the *Mercator* projection was chosen and the lower left and upper right coordinates were specified for the desired extent of the map. The coastline resolution was set to *intermediate*. Additionally, the latitude and longitude of four locations were specified and plotted on the map.

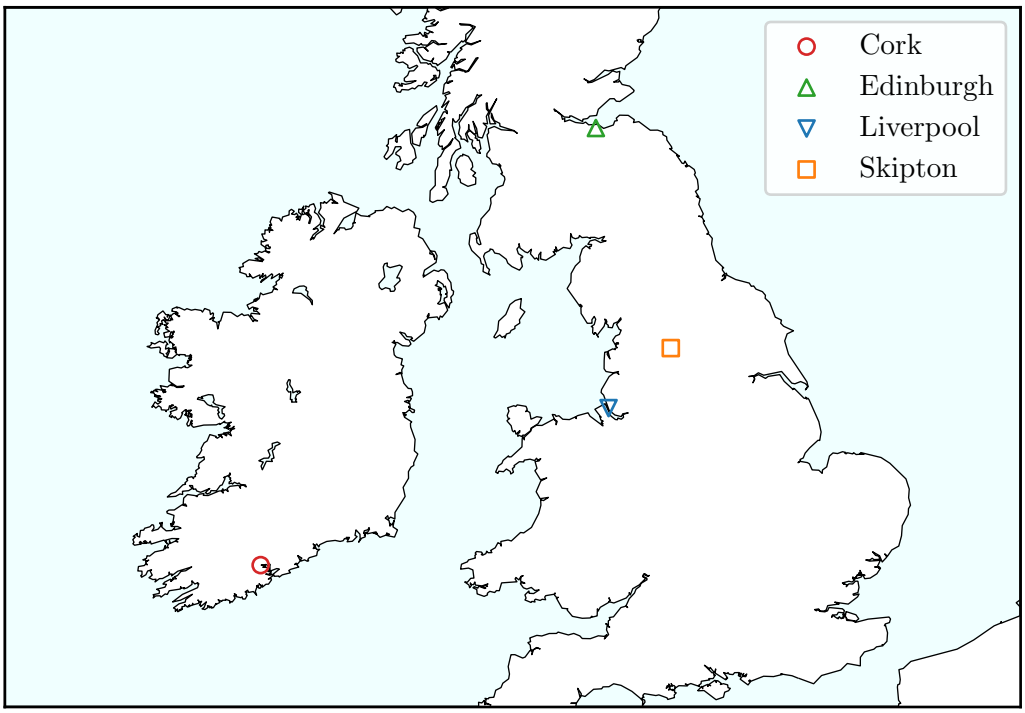

Figure 4.2: Example basemap figure.

Animation

In its simplest form, the Matplotlib animation algorithm is a simple *for-loop* that creates several successive plots and adds these together to generate the output animation. The methodology is shown in the flowchart in Figure 4.3. The *artist function* takes the frame number, f_a, as an argument and returns information on every *artist* that is being animated. An *artist* refers to any component of the plot that will change during the animation. The total number of frames must also be specified.

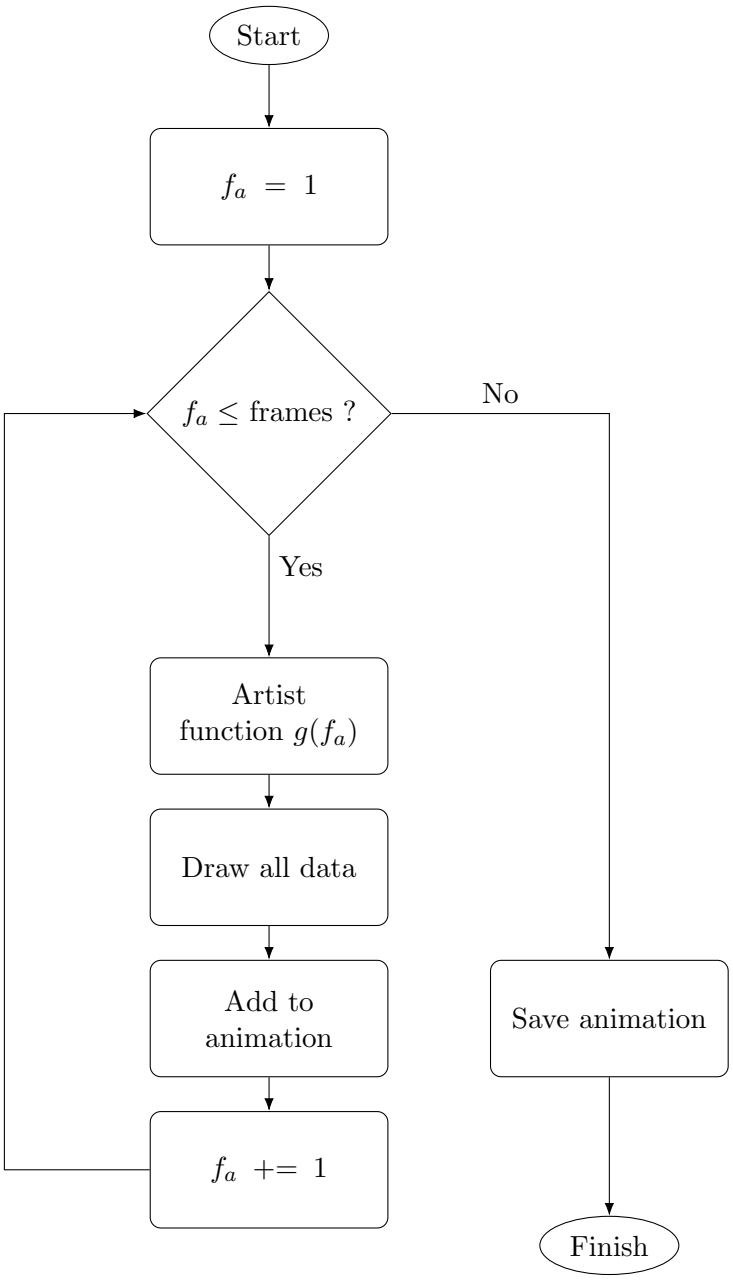

Figure 4.3: Simple form of animation algorithm.

In reality, most animations will use *blitting* to dramatically improve computational performance. Blitting is an old technique in computer graphics that takes an existing figure and *blits* artists on top of the original image (Sanchez and Canton, 2007). The flowchart in Figure 4.4 describes the animation algorithms used when *blitting* is enabled.

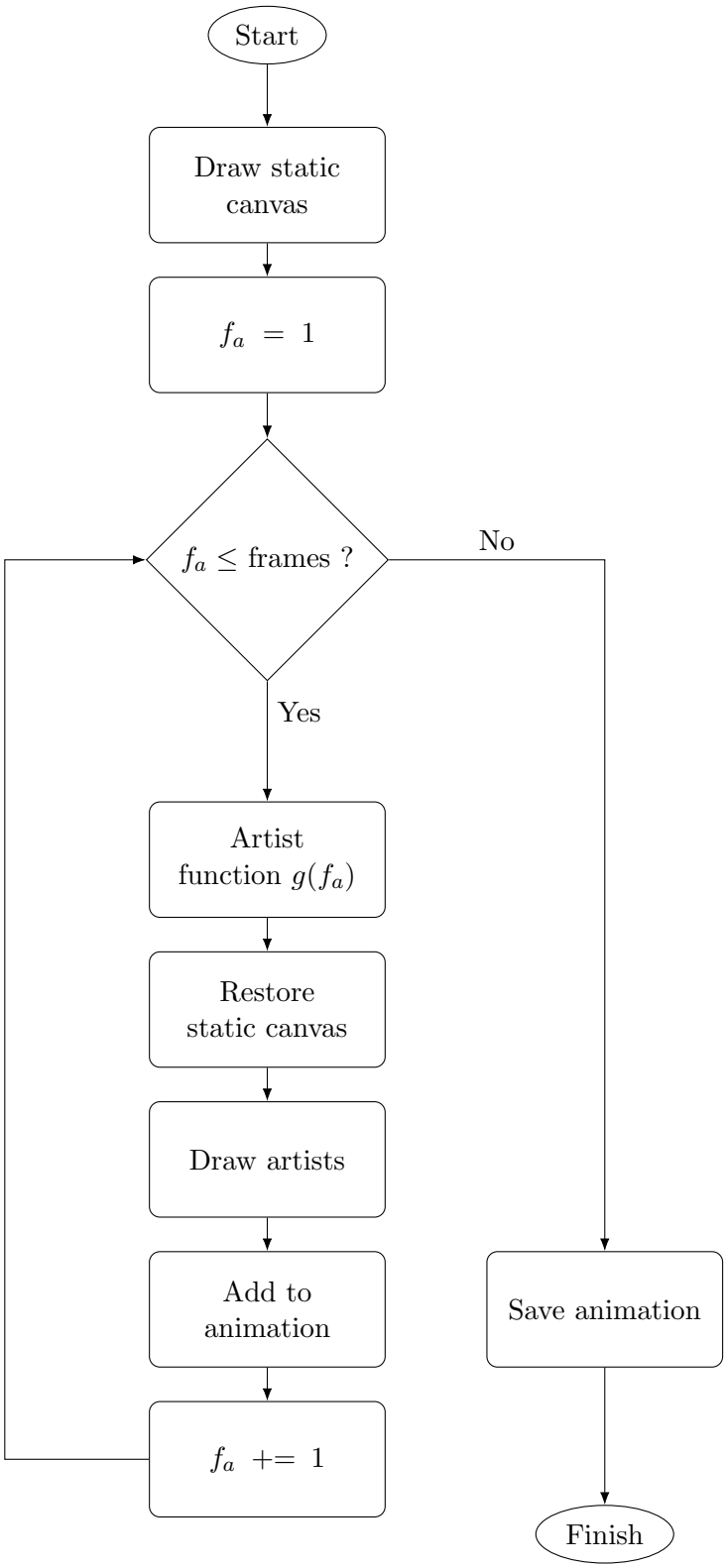

Figure 4.4: Animation algorithm when *blitting* is enabled.

The static canvas that is generated at the start of the animation loop includes all the *stationary* features of the animation—the features that do not change. For each frame, this static canvas is restored before the *dynamic* or *animated* artists are drawn on top of these stationary features. Thus, with *blitting* enabled, the animation algorithm only re-draws the features that are changing at each frame, leading to dramatic improvements in performance (Hunter, 2007). This is particularly important for the TDS animation module due to the combination of the *basemap* and *animation* tool-kits. Plotting the detailed coastlines, which typically are drawn at the maximum resolution, requires significant processing time. Re-drawing the basemap for every frame of the TDS animations would significantly increase the processing time of the animation scripts.

Example Animation

To demonstrate the application of the animation algorithm, consider a simple example of a vessel transiting from Cork to Liverpool. The static canvas in this case is the example basemap shown previously in Figure 4.2. The vessel, assumed to be the LÉ *Niamh*[3], is the dynamic feature and is represented as an annotated circular marker. The artist function returns the latitude and longitude of four intermediate points on the transit route, corresponding to the four frames that will be plotted to demonstrate the animation functionality. The coordinates for this example transit operation are given in Table 4.1. The table also shows the corresponding figure reference for each frame.

Table 4.1: Latitude and longitude coordinates of each frame in example animation.

Frame	*Latitude*	*Longitude*	*Figure*
1	51.67 N	7.89 W	Figure 4.5
2	52.08 N	6.00 W	Figure 4.6
3	53.61 N	4.88 W	Figure 4.7
4	53.50 N	3.45 W	Figure 4.8

The resulting animation can be imagined as the progression of images from Figure 4.5 to Figure 4.8. Although not shown in the process flowchart in Figure 4.4, the *frame-rate*—the number of frames shown per second of the animation—is an important input parameter to the Matplotlib animation function. To obtain a "smooth" animation, the number of frames—and thus the number of intermediate locations—and the frame-rate should be increased. As such, Figures 4.5–4.8 can be seen as "snapshots" of the full output animation.

3. LÉ stands for Long Éireannach, which is the Gaelic term for 'Irish ship' and is the designation given to ships in the Irish Naval Service.

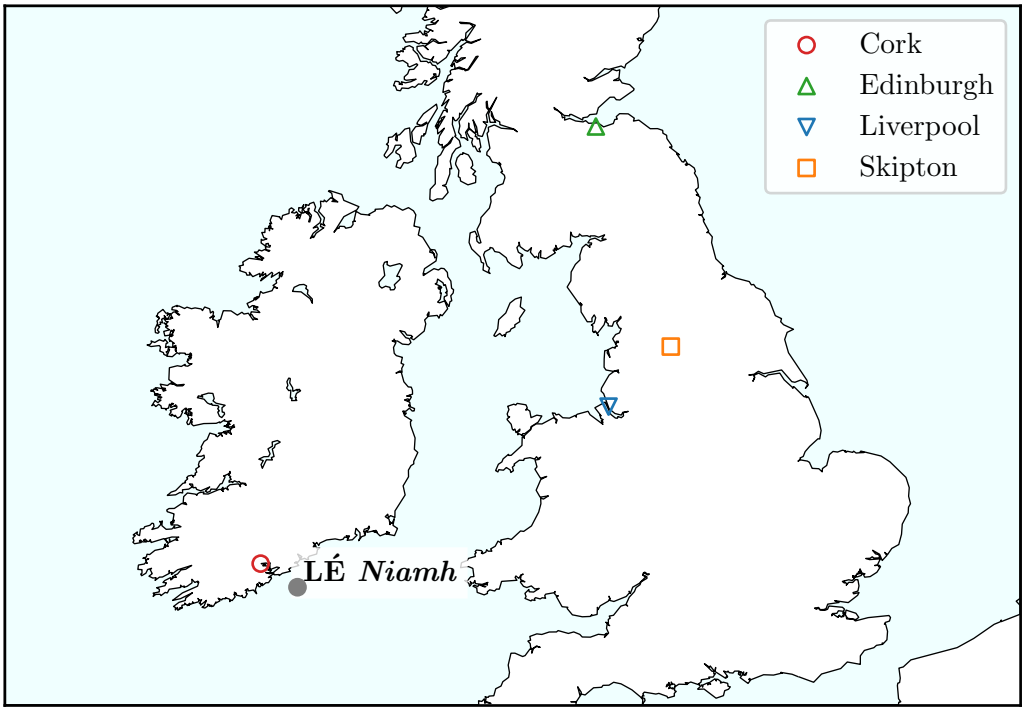

Figure 4.5: Example animation—frame 1.

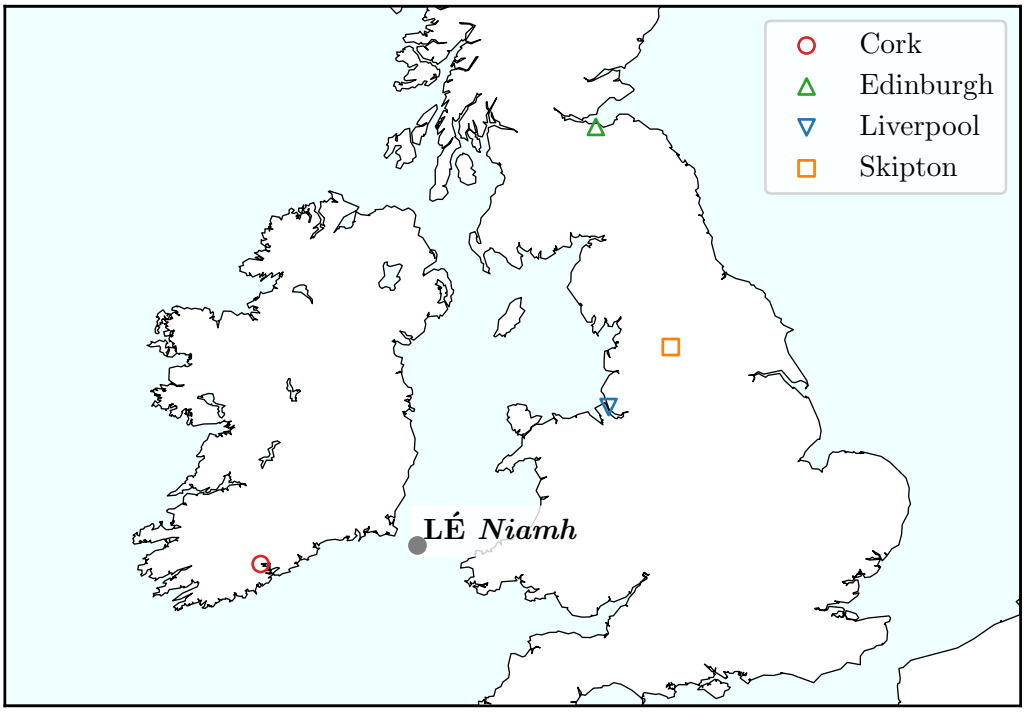

Figure 4.6: Example animation—frame 2.

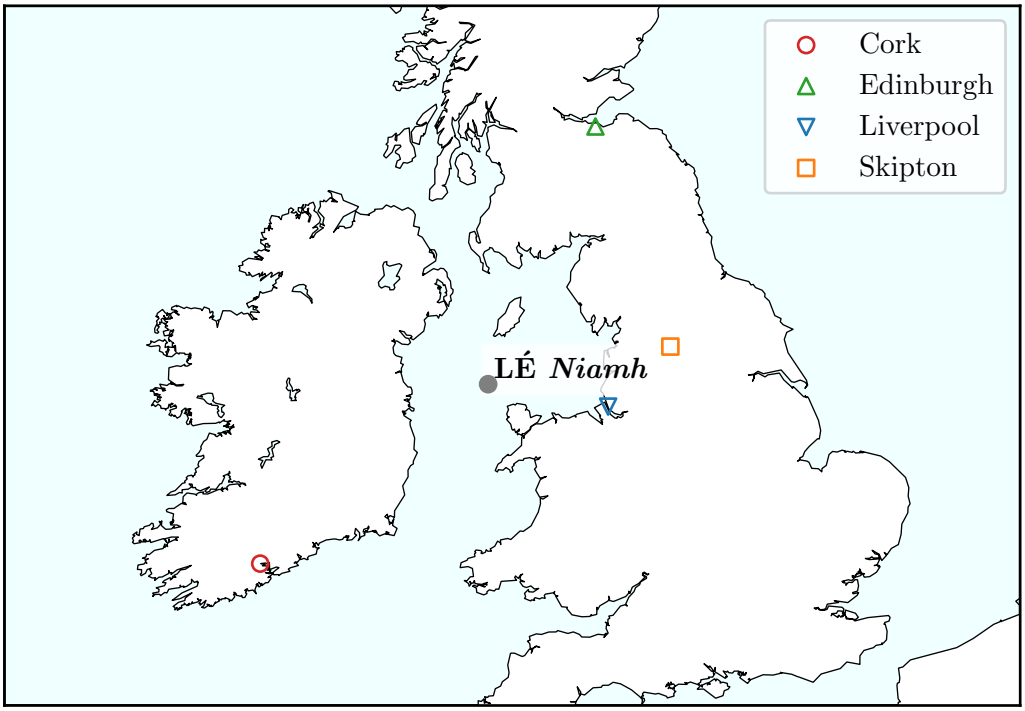

Figure 4.7: Example animation—frame 3.

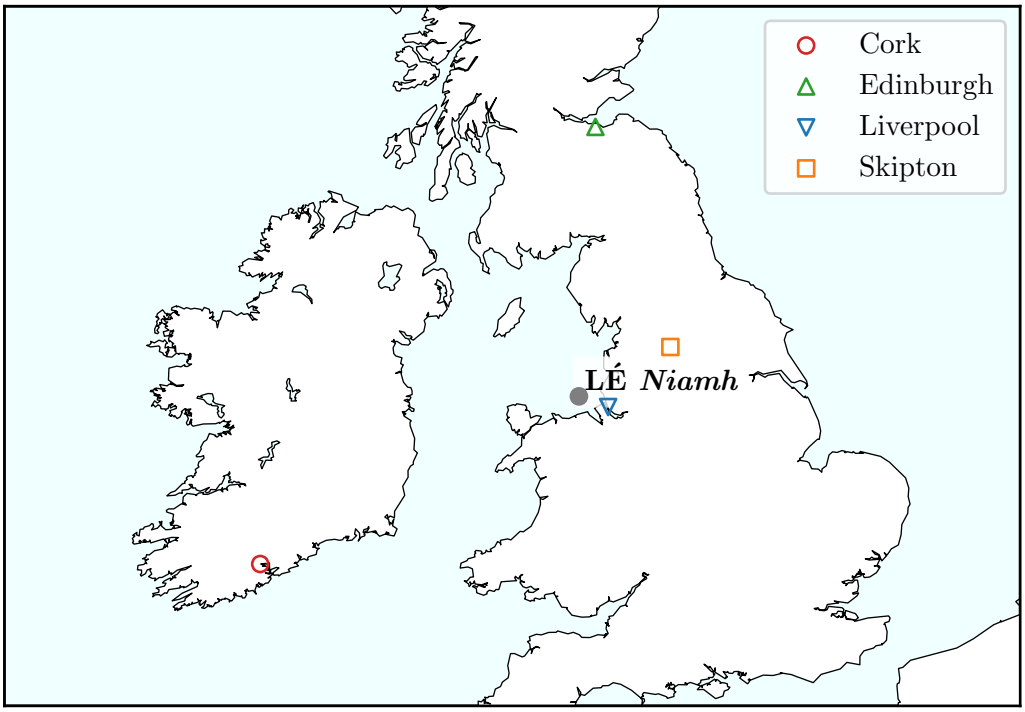

Figure 4.8: Example animation—frame 4.

4.2.2 Time-domain Simulation Animation Methods

This section describes the three critical methods required to create an animated video of an offshore operation using the tabular output data of TDS. These methods involve (*i*) mission selection, (*ii*) data processing and (*iii*) creating the background maps.

Mission Selection

A typical TDS model will run multiple iterations of a project simulation. Most of the data analysis is performed on the entire *ensemble* of mission results. However, as the animations are typically used for quality assurance (QA) purposes and because the animations are trying to capture accurately the sequential nature of the operations, the animation module requires iterations to be analysed independently.

Thus, one of the required inputs to the animation module is the desired percentile of the simulation results that is to be animated. The total duration of each iteration is calculated and the iteration with a total duration *closest* to the specified percentile is extracted. This single mission iteration is then used as the main input file to the animation methods.

Data Processing

The raw output data from a TDS model summarise the *milestone activities* completed by each vessel. A simplified example of a typical TDS output file is shown in Table 4.2. Note that a full analysis can include multiple vessels performing separate or concurrent operations. Therefore, a full output list will contain an additional column specifying the vessel that is performing each activity. Alternatively, each vessel—also referred to as a *resource*—can be viewed as having an associated output data file similar to that shown in Table 4.2.

Table 4.2: Example of typical TDS output data in tabular form.

Activity	*Start date*	*End date*	*Location*
Mobilise	10/07/2020 07:30	10/07/2020 09:00	Port
Transit to site	10/07/2020 09:00	10/07/2020 11:43	WTG 1
Inspect turbine	10/07/2020 11:43	10/07/2020 14:32	WTG 1
Re-locate	10/07/2020 14:32	10/07/2020 14:47	WTG 2
Inspect turbine	10/07/2020 14:47	10/07/2020 17:31	WTG 2
⋮	⋮	⋮	⋮
Transit to port	12/09/2020 17:07	12/09/2020 19:53	Port
Demobilise	12/09/2020 19:53	12/09/2020 20:29	Port

The objective of the artist function in the TDS animation module is to return the coordinates of each vessel as a time-series. The frames of the animation correspond to

successive entries in the time-series. Consequently, the data must be converted from the standard TDS output format, shown in Table 4.2, to a time-series for each vessel, an example of which is shown in Table 4.3.

Table 4.3: TDS output data converted to time-series format required for animation module.

	Vessel 1			*Vessel 2*		
Date-time	*Activity*	*Lat*	*Lon*	*Activity*	*Lat*	*Lon*
10/07/2020 07:30	Mobilise	51.67 N	7.89 W	Mobilise	53.50 N	3.45 W
10/07/2020 07:45	Transit	51.68 N	7.88 W	Transit	53.49 N	3.46 W
10/07/2020 08:00	Transit	51.69 N	7.87 W	Transit	53.48 N	3.47 W
10/07/2020 08:15	Transit	51.70 N	7.86 W	Transit	53.47 N	3.48 W
⋮	⋮	⋮	⋮	⋮	⋮	⋮
12/09/2020 20:30	Demobilise	53.50 N	3.45 W	Demobilise	51.67 N	7.89 W

Further complications arose due to the potential difference in duration of *transiting* activities and *operational* activities. For marine operations, a transit duration in the order of several hours leading to an operation that requires a number of days or weeks to complete is quite probable. Assuming there is a constant interval between successive time-series entries (15 minutes in Table 4.3, for example), it is likely that the animation will play too quickly to capture the transit activities or too slowly to demonstrate progress for the operational activities. Thus, it was important to be able to re-sample the time-series data by one of two separate intervals; one corresponding to transit activities and the other corresponding to operational activities.

Another important step in the methodology is the processing of *feature data*. A feature is any important location that will be included in the animation, e.g. the port and site locations and the positions of individual wind turbine generators (WTG). Features can be *static* or *dynamic*, depending on whether their visual representation can change throughout an animation. Dynamic feature data are also given a *status*. For an offshore wind construction project, the WTG features may have three statuses—planned, in construction and constructed—and each of these statuses will have an associated marker symbol, colour and size. Dynamic feature data are processed by identifying the completion time of key milestone activities in the TDS output data.

Creating the Background Map

The typical relative distance between the port and site locations compared to the distances between the locations of interest at the site itself necessitated two maps to be drawn for the animations. The *main map* is the larger of the two and is a *zoomed-out* view of the total extent of the marine operation. The *mini map* is a *zoomed-in* view of the offshore site that shows the results of the simulation at a finer detail. The *zoomed inset axes* method in Matplotlib (Hunter, 2007) was used to create the *mini map*.

Additionally, the development of what is termed the *time-slider* enabled the clear visualisation of the progression of simulation time in the animations. Initial versions of the animation showed the simulation time as a dynamic legend outside of the main map boundary. It was difficult to observe simultaneously the animated resources and the simulation time as a dynamic text legend. The time-slider was developed to address this issue and enable a visual representation of the progression of simulation time. The time-slider moves along the date-time axis from left to right as the animation progresses.

An example background map that includes all three of the above components is shown in Figure 4.9. Hypothetical port, site and WTG locations are plotted as example features.

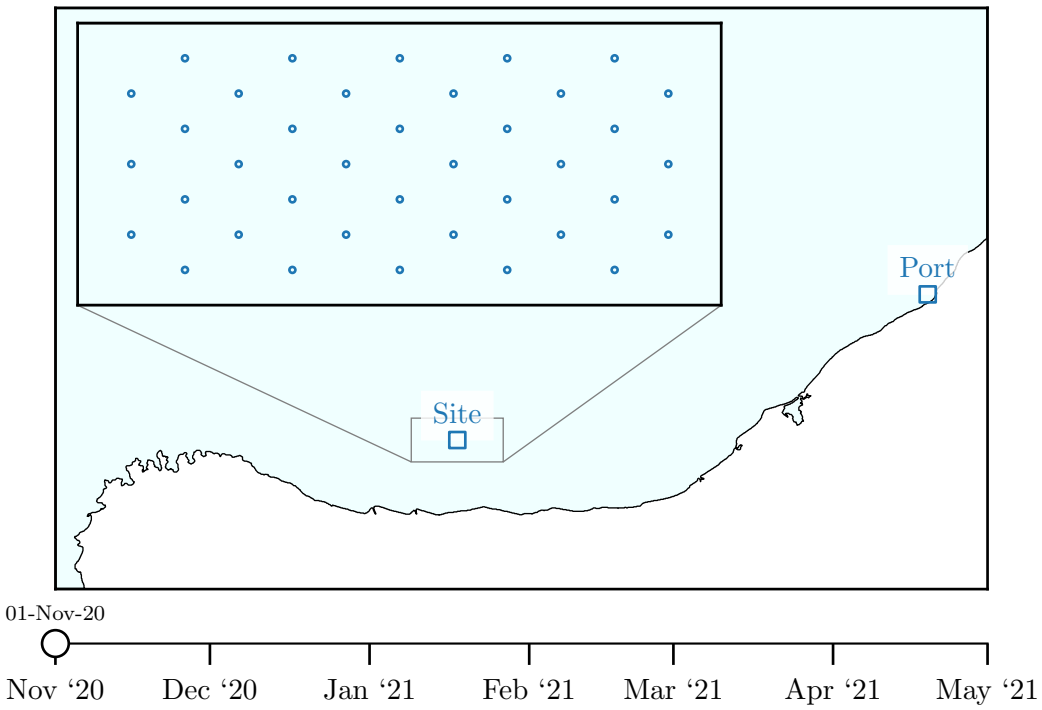

Figure 4.9: Example background map with main map, mini map and time slider below.

4.3 Animation Case Study

Typical outputs of the developed TDS animation module are presented in this section using simulated results for a hypothetical offshore wind farm construction project. The simulation model is based on completed analyses and results of a planned European wind farm but the number of vessels used, number of turbines and the project locations and coastlines have all been altered. In the project, a *heavy lift* vessel and a *barge* are used to install a wind farm consisting of 38 WTGs. The barge can carry a maximum of 4 WTGs, meaning that 10 loadouts are required. The background map and feature locations used in the project are the same as shown previously in Figure 4.9. Several frames have been selected from the animation to describe the animated output video. These screenshots are shown in Figures 4.10–4.18. They show how the animation module can provide clear and intuitive visualisations of the TDS results. The applications, strengths and weaknesses of these animations are discussed in the following sections.

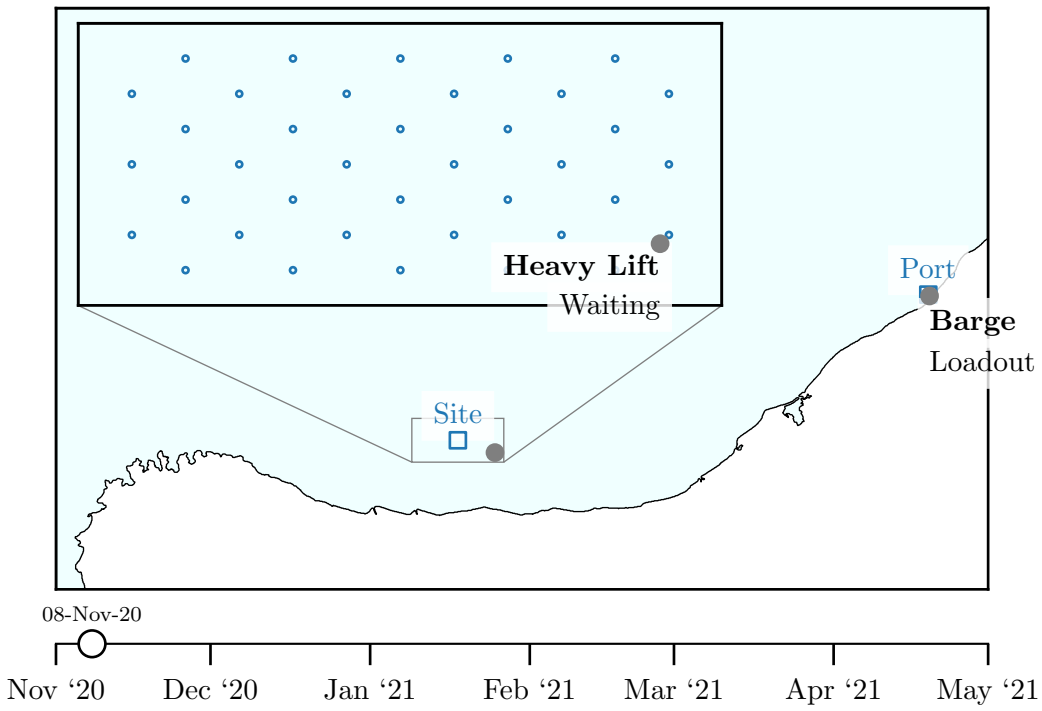

Figure 4.10: Animation case study frame 1—the animation begins on the 8th November 2020 with the *heavy lift* vessel waiting at the first WTG location and the *barge* finishing its first loadout at the hypothetical port.

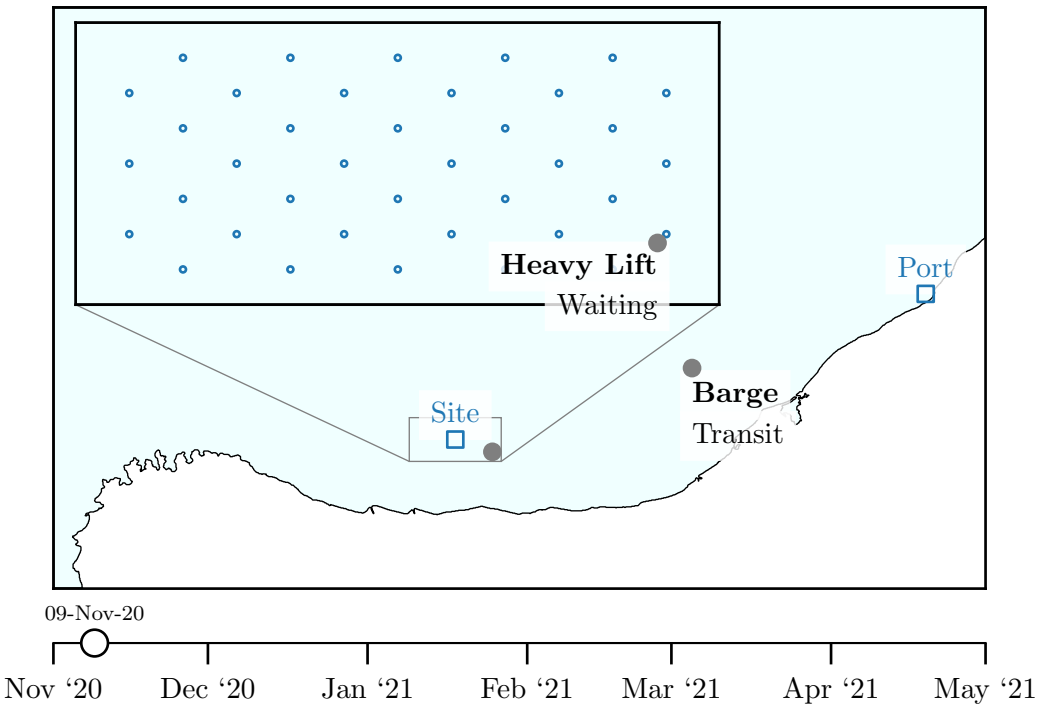

Figure 4.11: Animation case study frame 2—the barge is shown midway through its transit to site on the 9th November after completing its loadout operation.

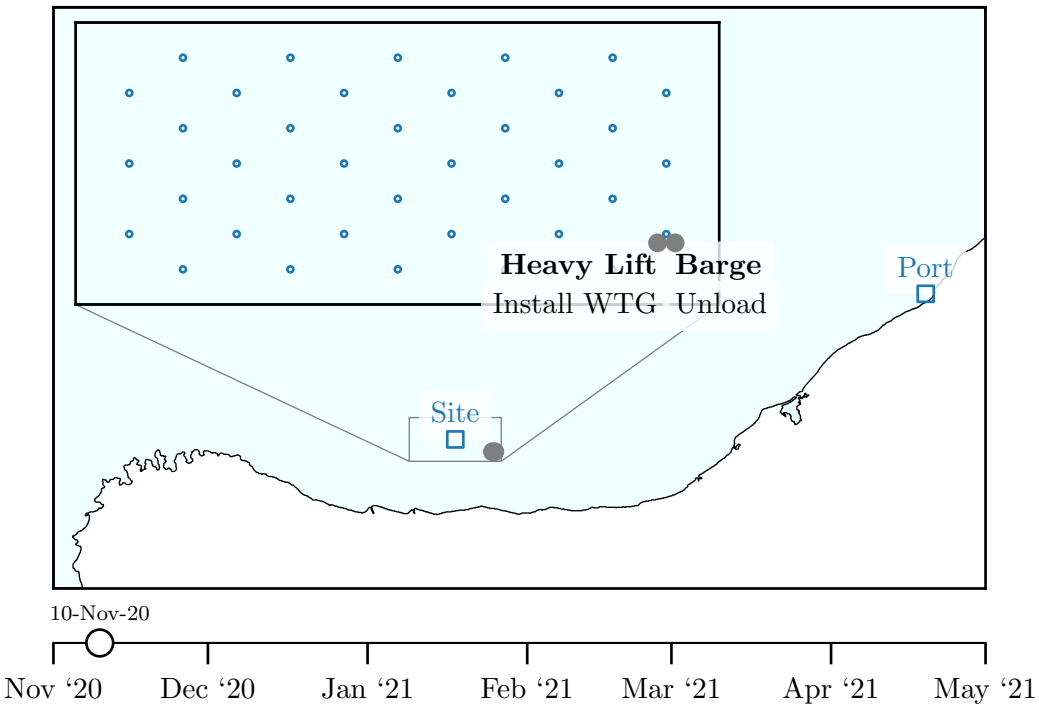

Figure 4.12: Animation case study frame 3—the barge unloads the first WTG at the first turbine location and the heavy lift vessel commences the installation process.

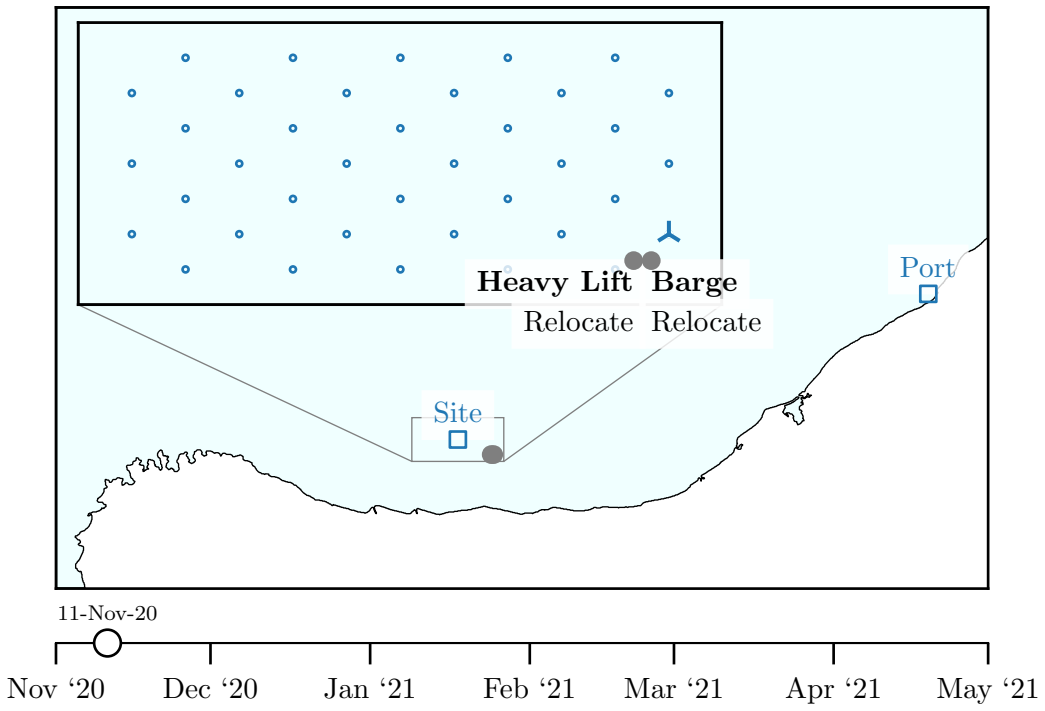

Figure 4.13: Animation case study frame 4—the symbol of the first WTG changes to a turbine once it is fully installed and both vessels relocate to the next turbine.

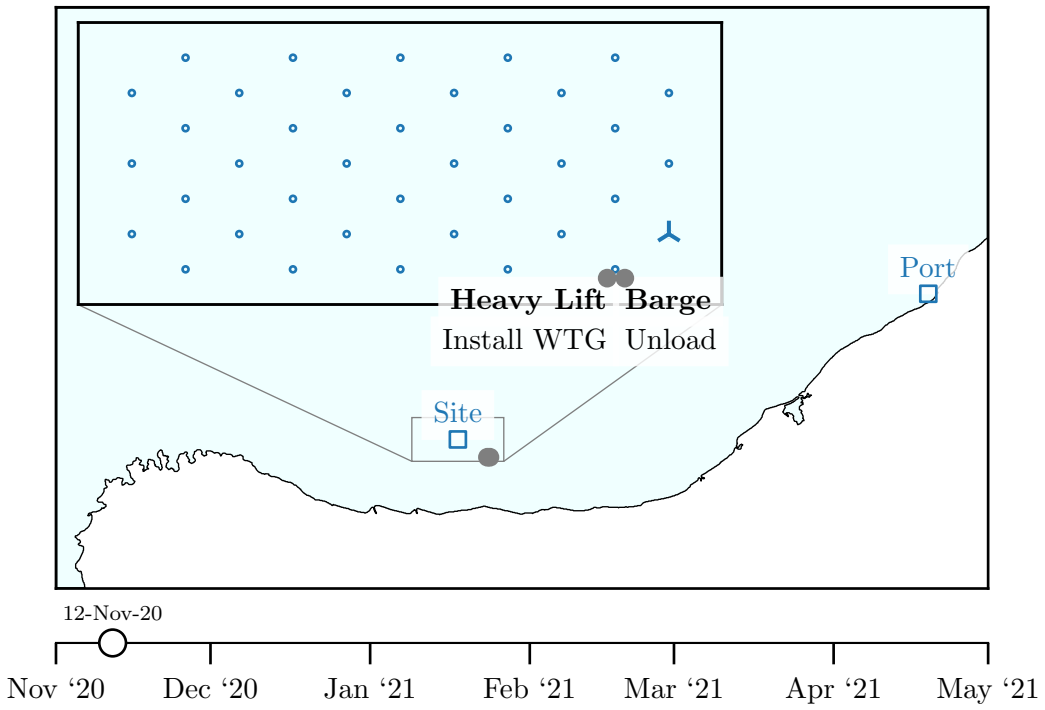

Figure 4.14: Animation case study frame 5—the vessels begin the installation of the second WTG.

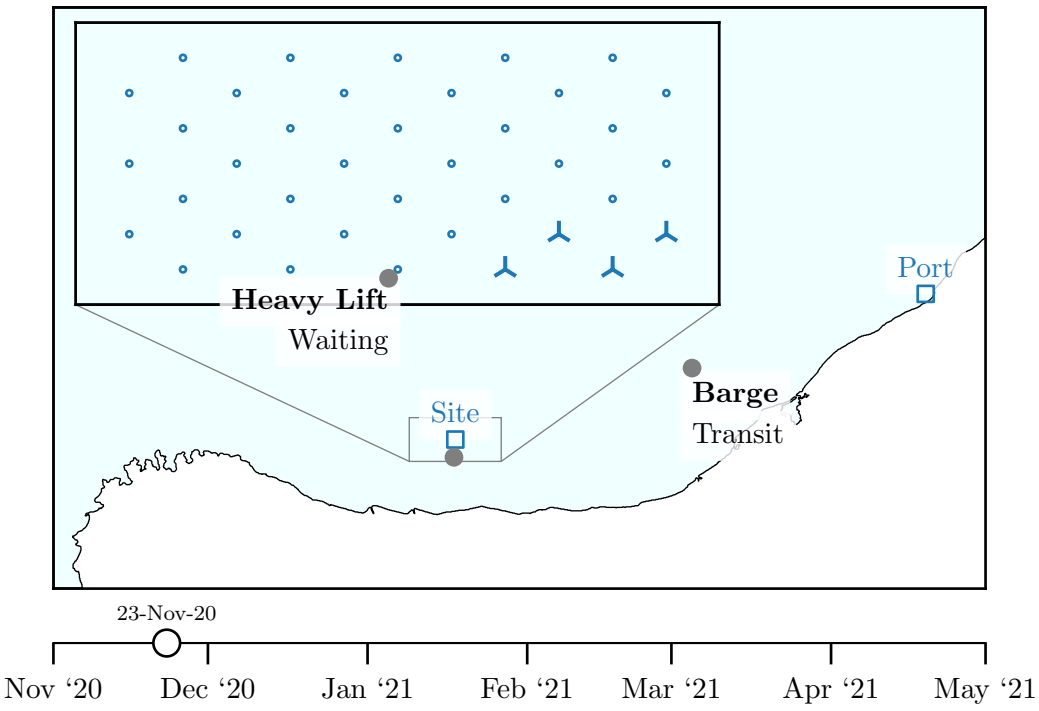

Figure 4.15: Animation case study frame 6—this frame skips forward to the 23rd November, when the first cycle is complete and the barge has to return to port to loadout the next 4 WTGs.

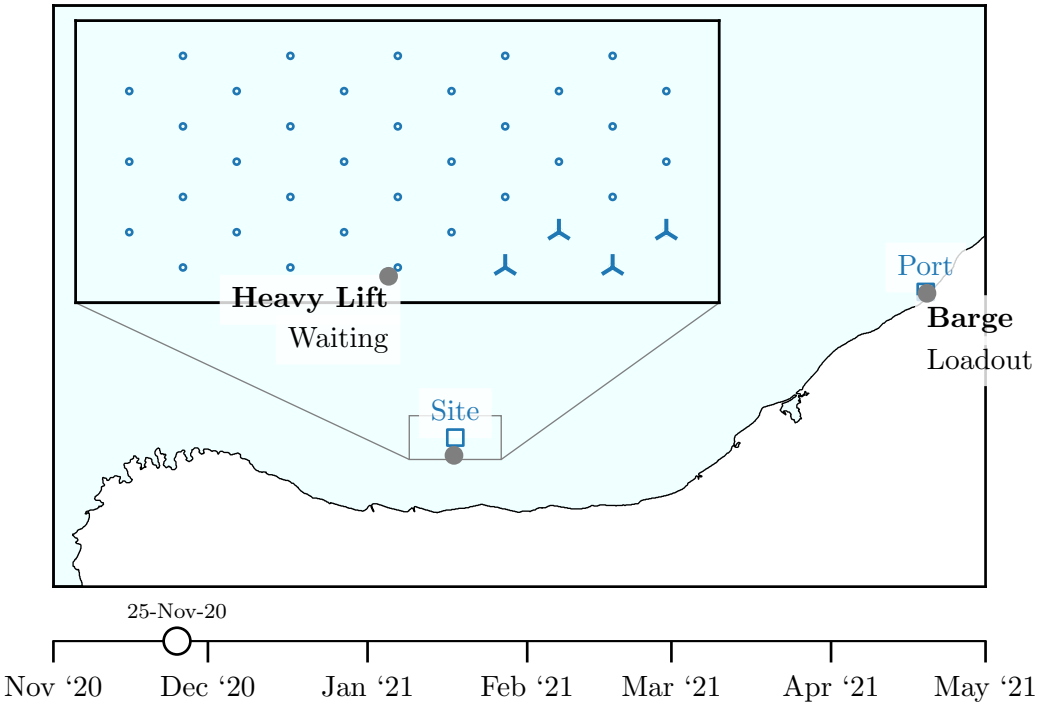

Figure 4.16: Animation case study frame 7—while the barge completes the second loadout, the heavy lift vessel remains at site at the fifth WTG location.

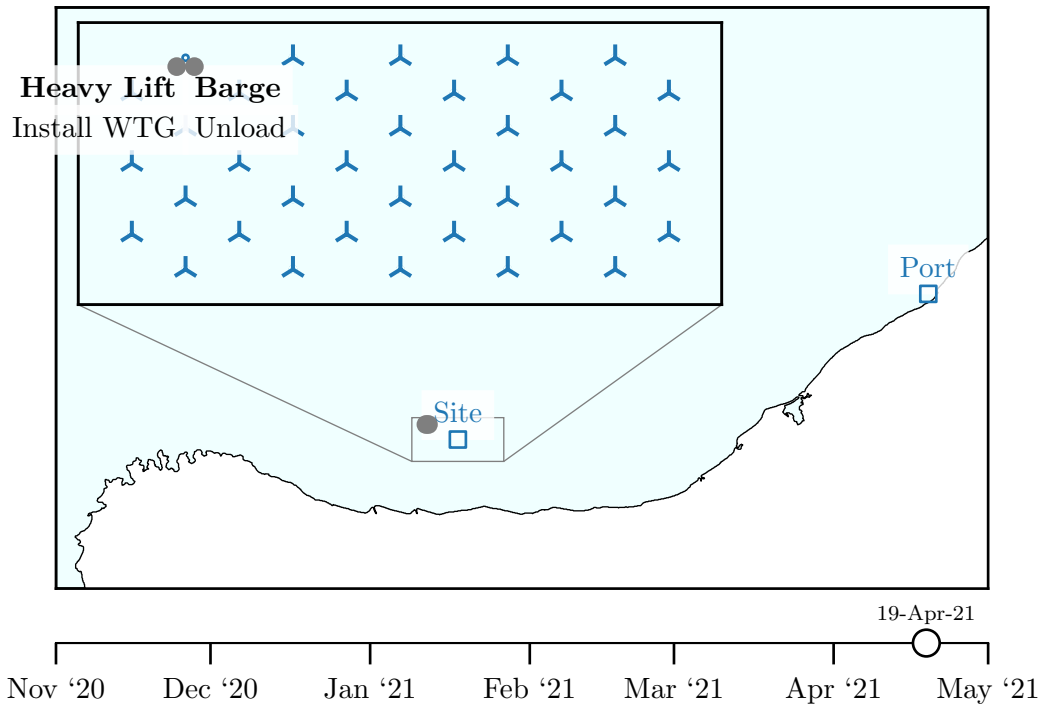

Figure 4.17: Animation case study frame 8—this frame skips forward several months to the end of the construction phase where both vessels are installing the final WTG.

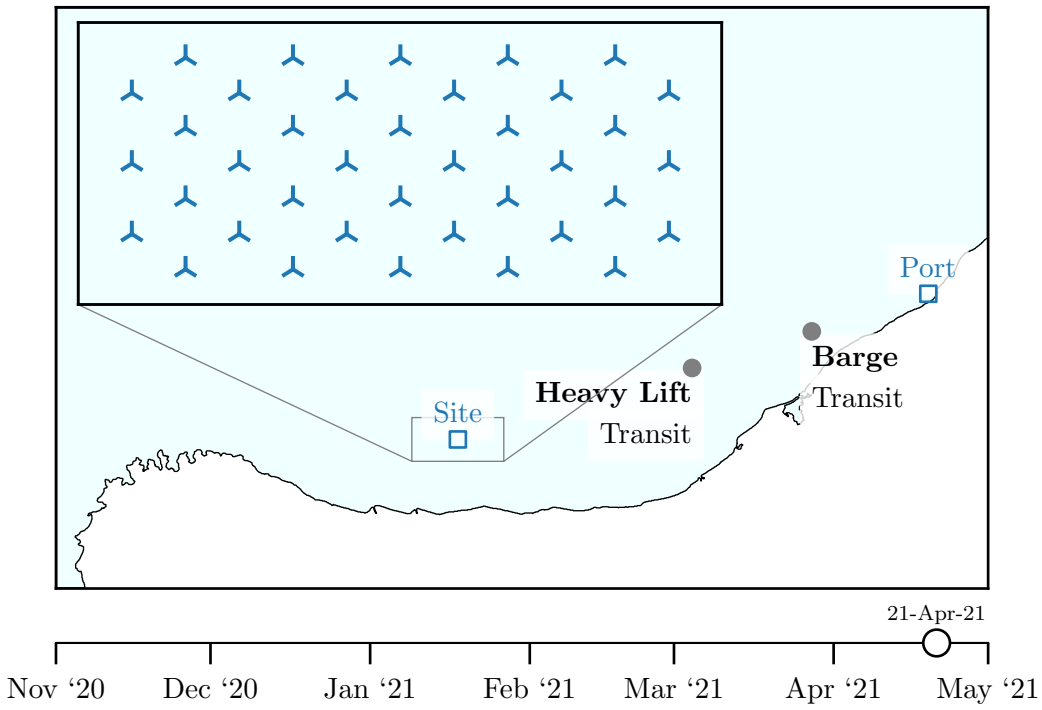

Figure 4.18: Animation case study frame 9—the heavy lift vessel and barge are shown on the final return transit with the wind farm fully constructed.

4.4 Discussion

4.4.1 Visualising Complex Projects

The genesis of the animation module stems from exchanges with a client involved in a major offshore construction project in the UK. This project involved the coordination of over 10 offshore vessels and several contractors for a construction period in the order of years. The timing of the project and organisation of the various construction team members were crucially important, both for the appropriate planning of concurrent operations and the financial implications of the charter length of each vessel. The animated TDS output results served as a sophisticated project management tool that incorporated weather downtime effects and highlighted bottlenecks and physical constraints that may otherwise have been missed.

Of major concern for this particular construction project was the physical space available at the port loadout berths. There were several limitations on the number and composition of vessels that could dock at the port simultaneously. For example, heavy lift vessel "A" may have been able to fit at the berth alongside two barges, but the larger, more sophisticated heavy lift vessel "B" may have only allowed space for one more additional vessel. In this way, the animations provided a clear visualisation of the causes that led to vessels having to *wait at port*, which were difficult to describe using standard graphical or tabular results.

After this proof of concept, the animation module was used for several offshore renewable energy projects. For example, the animation module has also been applied to several projects assessing potential O&M strategies for constructed offshore wind farms. In this case, the colours of the turbine symbols correspond to their status at each time step; WTGs can be *active*, scheduled for *preventative* maintenance or shut-down in the case of *corrective* maintenance. For certain projects, a *revenue counter* was added to the animated plots that showed the cumulative values of ideal revenue, lost revenue—from off-line turbines—and actual revenue at each time-step. For these O&M projects, the animations help to visualise clearly the relative benefits and weaknesses of alternative maintenance strategies.

Client feedback has revealed one of the major benefits of the animated TDS outputs is that they provide added confidence in the simulation models and the corresponding results. The animated visualisations of a project have helped assure clients that the simulation model is working correctly. The success of the animation module has led to the animations being included in the standard list of outputs provided to clients.

4.4.2 Quality Assurance

Perhaps the most important use of the animations is during the internal quality assurance (QA) process carried out for new projects. Typographical and work-flow errors are common during the initial configuration of a TDS model for an offshore project, due to the large quantity of .CSV files, text files and process flow-charts required as model inputs. While it can be difficult to discover errors in the extensive list of key milestone activities, these subtle mistakes, omissions and anomalies are clearly identifiable in the animated outputs. Consequently, the TDS animation module increases the efficiency and speed of the project configuration process, leading to subsequent improvements in accuracy and productivity. The animated TDS outputs have thus become an integral step in the QA procedure for every new project.

The animations can also be used as a QA process that links the developer of the model and the end-user. The incorporation of the animations module in this type of QA procedure is illustrated in the flow chart in Figure 4.19. Previously the model logic could only be checked via the manual calculation of the weather windows for all of the sequential operations within a randomly selected mission iteration. It is still necessary to perform this check of the simulation logic on the final output results, but the use of the animation module avoids the need for time-consuming manual checks throughout the initial project configuration process.

4.4.3 Impact of Animation Module

This section describes a case study partially informed by simulations completed for an offshore wind farm construction project. The objective is to provide indicative quantifications of the impact that the animations can have on the modelling process and on simulation results.

In offshore construction projects, it is common for there to be regulations on certain coincident operations. For example, the focus of one particular study assessed the impact of regulations that forbade multiple vessels from conducting piling operations at the same time. The reason for implementing this ban was to minimise the effect of noise pollution on marine animals. For projects located in the near-shore region, the effect of noise pollution on humans is another contributing factor.

Another example, previously mentioned in Section 4.4.1, is the constraint relating to the physical space available at port loadout berths. This can often lead to restrictions on coincident port operations. In this case, the size of the berths at one port meant that loadout operations could not be carried out concurrently by multiple vessels. This case study assesses the impact of both these types of coincident operation.

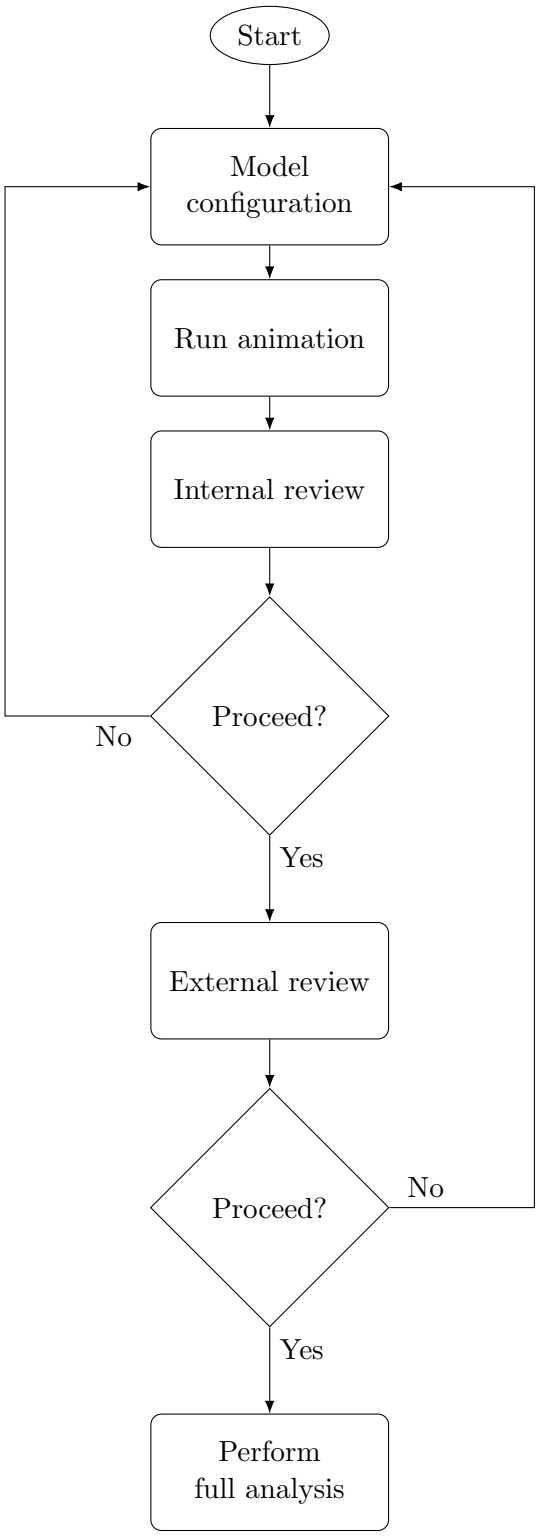

Figure 4.19: QA procedure showing the role of the animation module.

There are two ways in which the animation functionality described in this chapter can help to identify errors relating to these coincident operations. Firstly, a breakdown in communication between the developer of the TDS model and the client or end-user can often mean that these types of assumptions are omitted or forgotten. Secondly, errors can be introduced in the model configuration process through the typographical and work-flow errors mentioned previously. The incorporation of the animation module within the internal and external QA processes (see Figure 4.19) greatly increases the likelihood of finding these modelling errors before the final simulations are performed.

To obtain an indicative quantification of the effect that these errors can have on model results, a retrospective assessment of the impact of coincident operation constraints was performed. The results pertain to the piling installation phase for a European offshore wind farm. For this particular project, there was no ban on coincident operations. However, the impact of a potential ban on concurrent tasks was assessed by extracting the duration of coincident operations, for both piling operations and port loadout operations, from the simulation results. These durations are shown in Table 4.4 along with the duration of coincident operations expressed as a percentage of the total duration of the piling campaign. Finally, two indicative cost parameters are calculated based on the vessel day-rates suggested by Lacal-Arántegui *et al.* (2018). They suggest a range of 150,000–250,000 USD for a turbine installation vessel. Assuming a conversion rate of 0.76 GBP/USD, this range corresponds to a low estimate of 114,000 GBP/day and a high estimate of 190,000 GBP/day. These two day rates were used to obtain indicative cost estimates for coincident operations.

The results show that the duration of coincident operations is not substantial in relation to the total duration of the piling campaign. For the P50 results, the combined duration of coincident piling and port operations is 82 hours, which represents 2.73% of the total duration of the piling phase. In the P90 scenario, the combined duration is 144 hours; 4.8% of the total duration of this phase of the project. The results for absolute duration also suggest the model is more sensitive to the restriction on port operations than it is to coincident piling operations.

Crucially, the results also show the potential cost implications of failing to identify erroneous modelling assumptions or omissions. For instance, imagine if coincident operations were not allowed for this particular project but that this assumption had been excluded erroneously from the simulation model. In this case, the median value for project cost would have been underestimated by approximately £400,000–£650,000. In the worst-case scenario, the discrepancy in project cost would have been approximately £1m. Note that this retrospective analysis assumes that the delay that would have been introduced is identical to the duration of coincident operations. As will be discussed further in Section 6.3.1, this would not necessarily be the case and a more accurate anal-

Table 4.4: Indicative case study results for the duration and cost of coincident operations.

	P10	*P50*	*P90*
Duration of coincident operations (hours)			
Port operations	16	63	117
Piling operations	6	20	32
Combined	35	82	144
Percentage duration of piling phase (%)			
Port operations	0.53	2.10	3.89
Piling operations	0.19	0.67	1.06
Combined	1.16	2.73	4.79
Indicative cost of coincident operations Low vessel rate (thousand GBP)			
Port operations	76	299	555
Piling operations	27	95	152
Combined	166	390	684
Indicative cost of coincident operations High vessel rate (thousand GBP)			
Port operations	127	499	925
Piling operations	44	158	253
Combined	277	649	1,140

ysis would require simulations with and without the coincident operation constraint, but it does give an approximate indication of the impact of incorrect assumptions. The animation module enables easy identification of these modelling and configuration errors and omissions. It also improves communication between the model developers and end-users. The results of the case study quantify the scale and impact of model error that can be avoided through the use of the developed animation functionality.

4.4.4 Weaknesses and Future Work

Despite the use of *blitting*, the performance of the animation module is not optimal. The run-times required to generate the animated outputs can be quite long. For a moderately complex model, it can take between 5–10 minutes to generate an animated video with a duration of approximately 2–3 minutes. This performance is adequate when a subset of operations is being animated and the desired output animation is quite short, which is often the case. However, if a long animation is required, for example showing the entire O&M campaign for the lifespan of an offshore wind farm, then this performance is unsuitable.

The need to process the data before creating the animation does not have a significant

effect on performance but it can introduce new errors that are not present in the raw TDS outputs. This is particularly counter-productive when using the animations for the QA process. Minimal development is required to enable the outputs of the TDS to be formatted in the appropriate time-series structure. In fact, early versions of the software produced outputs in the required format. The increasing number of simulations required for the Monte Carlo method necessitated the re-structuring of the outputs into the key milestone activities described previously. Enabling the output results to be formatted as time-series would eliminate the need to process the data before running the animation module, thus greatly simplifying the methodology. It might even be possible to generate animations as the simulations are running, which would further improve the QA process.

Using a bespoke graphics and animation package would solve the performance issues mentioned above. Preliminary investigations have focussed on the use of *Blender*, which is an open-source software package for production quality 3D graphics, modelling and animation (Kent, 2013; Hess, 2010). Crucially, the software uses a Python application programme interface (API) for scripting (Kent, 2013; Hess, 2010) which would facilitate integration with the TDS software. Furthermore, using *Blender*, or an equivalent software package, would improve the visual appearance of the animations, which was not of primary concern during development.

4.5 Conclusions

A method for animating the outputs of a TDS model has been developed. Selected animation results from a hypothetical offshore wind farm construction project have been presented that show how the developed module can provide clear and intuitive visualisations of the simulated results.

The animation module has been used to support several marine projects, including construction and O&M campaigns for offshore renewable energy farms. The animated outputs enable clear comparisons to be made between various offshore strategies. Furthermore, the animations can be used to support the project management of complex projects involving multiple vessels and contractors.

TDS animations have been shown to enable easy identification of modelling and configuration errors and omissions. They also improve communication links between model developers and end-users. The incorporation of the animation functionality as a QA method within the model configuration process eliminates the need for time-consuming manual checks of tabular output data.

Finally, an indicative case study has highlighted the potential cost implications of failing to identify erroneous modelling assumptions or omissions. If the analysis in this chapter

described a model that mistakenly omitted restrictions on coincident piling and port operations, the median value for total project cost would have been underestimated by between £400,000 and £650,000. In the hypothetical worst-case scenario, the piling installation project was likely to have been about 5% longer and £1m more expensive than the simulation results suggested.

Chapter 5

Time-domain Simulation Outputs and Data Analysis Methods

5.1 Introduction

This chapter discusses the exploratory data analysis and visualisation methods that have been developed to extract key insights from the raw output of the TDS models. These methods are described through the scenario tests and associated analysis that informed the installation strategy for a Round 3 offshore wind farm construction project. The primary objective of this chapter is to describe and appraise the types of analysis that can be performed in the planning stages prior to the commencement of a marine project. A new graphical output technique referred to as a *progress plot* is described. An additional objective of the present analysis is to quantify the number of simulations and years of metocean data that are required to achieve satisfactory convergence of TDS results. As outlined in Chapter 2, there is no general consensus on convergence issues in the literature.

The technical background to the exploratory data analysis methods is given in Section 5.2, including discussions on classical box-and-whisker plots and rangefinder boxplots. A description of the Round 3 offshore wind farm construction project, the various scenarios that were tested, the configuration of the bespoke simulation model, the convergence tests and the quantitative data analysis methods can be found in Section 5.3. The results of the scenario testing and other analyses are described in Section 5.4, while the alternative scenarios that were tested and additional outputs omitted from the analysis are outlined in Section 5.5. Finally, Section 5.6 summarises the main conclusions of the chapter.

5.2 Technical Background

The following methods can be found in any introductory textbook on exploratory data analysis (EDA) and statistical analysis (e.g. see Wilks, 2011).

5.2.1 Quantiles and the Inter-quartile Range

Many summary statistical measures rely on the use of sample quantiles, sometimes referred to as fractiles, which are essentially equal to the more familiar term percentile. A sample quantile, q_p, is a number having the same units as the data, which exceeds that proportion of the data given by the subscript p, with $0 \leq p \leq 1$. Equivalently, the sample quantile q_p is identical to the $(p \times 100)^{\text{th}}$ percentile of the data-set.

Robust statistical methods are those that are insensitive to particular assumptions about the overall nature of the data (Wilks, 2011). A resistant method is not unduly influenced by a small number of outliers (Wilks, 2011). The inter-quartile range (IQR) is a common, simple, robust and resistant measure of the spread of a data sample. The IQR is the difference between the upper and lower *quartiles*;

$$\text{IQR} = q_{0.75} - q_{0.25}\,. \tag{5.1}$$

5.2.2 Box-and-whisker Plots

The box-and-whisker plot, also referred to simply as the boxplot, is a widely used tool introduced by Tukey (1977). The simplest form consists of a plot of five sample quantiles—the minimum, the lower quartile, the median, the upper quartile and the maximum—and presents a quick sketch of the distribution of the underlying data. An example of this form of the boxplot (labelled as the "min/max whiskers" method) is shown in Figure 5.1. The boxplot describes a set of 250 values sampled randomly from a standard normal distribution.

A shortcoming of the simple min/max whiskers boxplots is that they generalise the information about the tails of the data (Wilks, 2011). Several refinements of the simple boxplot exist that provide more detail in the tails of the distribution. For example, a schematic plot (Tukey, 1977) is identical to the simple boxplot except that extreme points considered to be sufficiently unusual are plotted individually. Four dividing lines for the classification of these sufficiently unusual extrema are defined:

$$\text{Upper outer fence} = q_{0.75} + 3\ \text{IQR} \tag{5.2}$$

$$\text{Upper inner fence} = q_{0.75} + 1.5\ \text{IQR} \tag{5.3}$$

$$\text{Lower inner fence} = q_{0.25} - 1.5\ \text{IQR} \tag{5.4}$$

$$\text{Lower outer fence} = q_{0.25} - 3\ \text{IQR}\,. \tag{5.5}$$

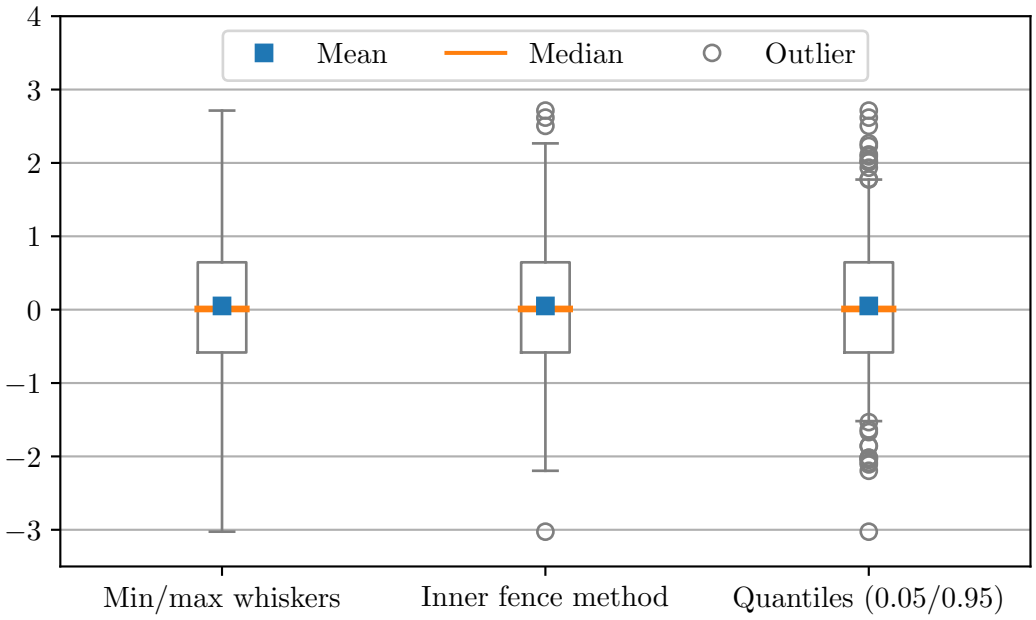

Figure 5.1: Example box-and-whisker plot variations for a normal distribution.

Typically, points between the inner and outer fences are plotted as circles, as shown in the middle boxplot of Figure 5.1. Data lying outside the outer fences are plotted with a different symbol, typically an asterisk, but examples of these data are not included in Figure 5.1. Alternatively, the whiskers can be set to extend to specific quantiles. For example, Figure 5.1 shows the common case of drawing the whiskers between $q_{0.05}$ and $q_{0.95}$.

Box-and-whisker plots can convey a surprisingly large amount of information at a glance (Wilks, 2011). For example, Figure 5.1 shows the data are clearly concentrated about 0, as expected for a standard normal distribution; visualises the full range of the data and indicates the data are nearly symmetrical—the median is near the centre of the box, the mean and median are approximately equal and the whiskers are of comparable length (Wilks, 2011).

To further illustrate the graphical box-and-whisker technique, the same three plots were re-created using 250 random samples from a Weibull distribution with a shape parameter of 1.5 (Chapters 7 and 8 focus on theoretical probability distributions and describe the Weibull distribution in more detail). The resulting boxplots are shown in Figure 5.2.

The data suggest a tendency towards *positive skewness* (i.e. the right tail of the data is longer) as indicated by the inequality of the upper and lower whisker lengths. The effect of this positive skewness on the sample mean is evident in the discrepancy between

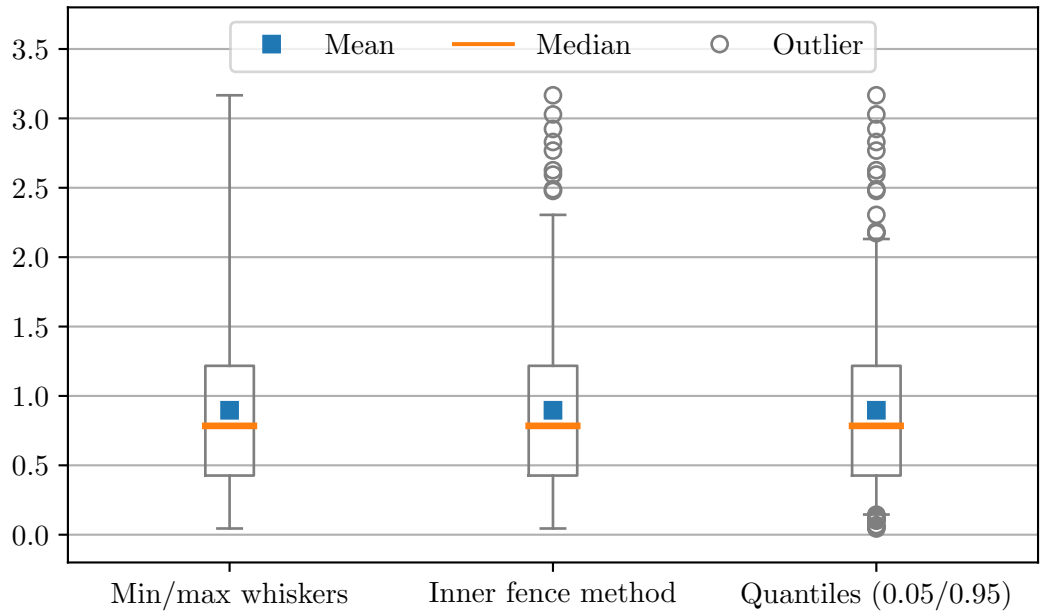

Figure 5.2: Example box-and-whisker plot variations for a Weibull distribution with a shape parameter of 1.5.

the mean and median values of the data-set. Figure 5.2 also highlights the difference between the boxplot variations. Values in the sampled data-set below the 5^{th} percentile (or $q_{0.05}$) are shown as outliers using the "quantiles" method but these data points fall within the lower inner fence as shown in the middle boxplot.

Identical data-sets have been used in each of Figures 5.1 and 5.2 to compare separate boxplot techniques. However, it is important to note that a primary use of box-and-whisker plots is in the simultaneous graphical comparison of several *distinct* batches of data (Wilks, 2011). As such, they are well-suited for comparing different scenarios that are being tested using TDS methods.

5.2.3 Rangefinder Boxplots

Bi-variate boxplots are an extension of the original box-and-whisker plots and are useful when analysing two-dimensional variability (Becketti and Gould, 1987). For the proposed *progress plots* discussed in Section 5.3.4, a method of dealing with these two-dimensional variables is crucial. Several bi-variate boxplots have been proposed; for example relplots and quelplots (Goldberg and Iglewicz, 1992), bagplots (Rousseeuw *et al.*, 1999) and the related theory of highest density regions (HDR) (Hyndman, 1996) *Rangefinder* boxplots are the easiest to construct and are used throughout this thesis.

The rangefinder boxplot contains precisely the same information as the standard box-

plots for both of the variables displayed (Becketti and Gould, 1987). Typically, the rangefinder boxplot is superimposed on a scatterplot and consists of six line segments. The two central line segments intersect at the cross-median values. The vertical line segments cover the IQR of the variable measured on the vertical axis. Similarly, the horizontal line segments cover the IQR of the variable measured on the horizontal axis. Finally, the upper and lower horizontal line segments are drawn at the upper and lower adjacent values of the vertical axis—that is, at the points where the whiskers would terminate—and the right and left vertical line segments mark the upper and lower adjacent values of the horizontal axis (Becketti and Gould, 1987).

The construction method for a rangefinder boxplot is shown in Figure 5.3. The data are correlated X and Y points that have been sampled randomly from a bi-variate normal distribution. The individual boxplots for the X and Y data are shown above and to the right of the figure respectively and illustrate the construction of the rangefinder line segments. In this example, the whiskers are drawn between the 5^{th} and 95^{th} percentile and a circular marker for the cross-median values has been added.

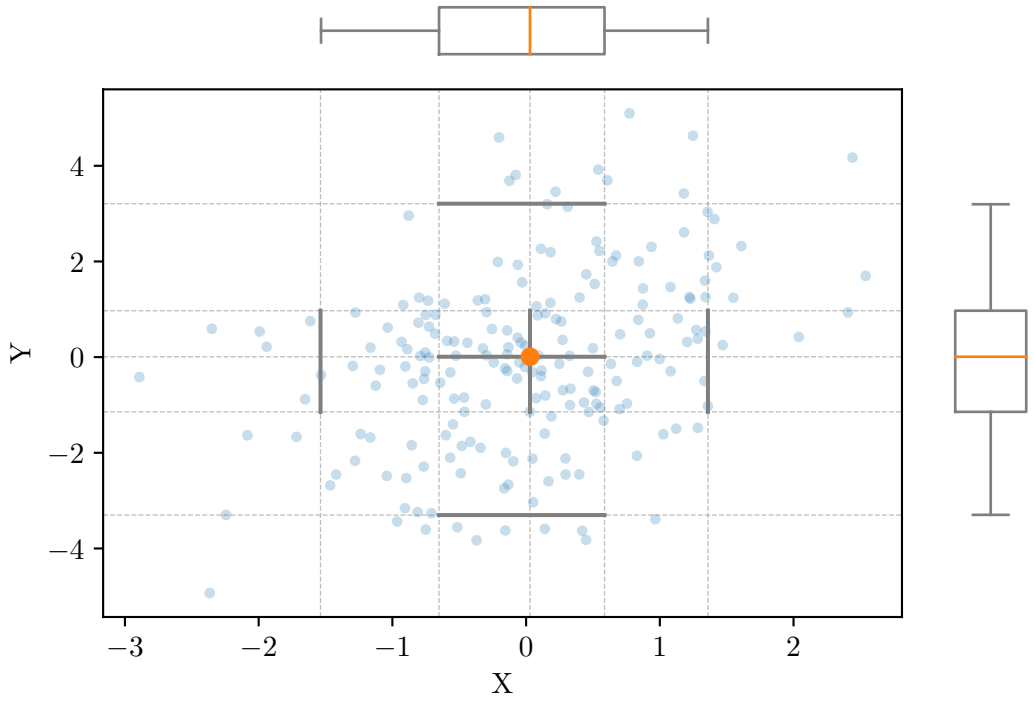

Figure 5.3: The rangefinder boxplot and its construction. Box-and-whiskers to the right and above show the equivalent single-variable boxplot for the Y and X variables respectively.

5.3 Methodology

5.3.1 Project Description

The industrial project used to demonstrate the data analysis methods and typical TDS outputs concerns the construction phase of a Round 3 offshore wind farm (OWF). As detailed in Section 2.4, the installation of an OWF can be broken down into the sequential steps of mobilisation, loadout, outward transit, installation, return transit and de-mobilisation. It is common for construction to be further divided into a *foundation phase*, when the foundations and transition pieces (TPs)—that connect the foundation to the wind turbine tower—are installed, and a *WTG phase*, when the wind turbines themselves are assembled on the previously-installed foundations. Each of these two phases will consist of the same six steps mentioned above. ForeCoast® Marine was used to assist both phases of the offshore wind farm in question, but the present analysis focuses on the WTG phase.

One turbine installation vessel (TIV), henceforth referred to as the *baseline vessel*, had already been chartered for a duration of 245 days (relative to the commencement of the WTG phase). The objective of the analysis was to assess various strategies for chartering an additional TIV. Delays in the foundation phase had resulted in greater uncertainty in the possibility of finishing the construction of the OWF within the agreed charter duration of the baseline vessel. Thus, the aims of the work were to assess whether a second vessel was required and if so, help inform the selection of the second vessel and the appropriate charter length. The charter start date for each of the additional WTG installation vessels was 92 days after the start of the WTG phase. The objective was to finish the installation of the entire OWF within a duration of 245 days at a minimal project cost.

Note that the 245 day charter period for the *baseline* vessel, that would have led to additional fees if exceeded, represents a constraint in this analysis. There may have been more optimal solutions available if this constraint had been relaxed. For example, three installation vessels may have comlpeted the project in a much shorter time and have resulted in a lower total project cost. However the 245 day charter period was a key assumption in this analysis and ignoring it was outside the scope of the work.

5.3.2 Scenario Details

Six scenarios were simulated in addition to the *baseline scenario* in which no additional installation vessel was chartered—the *business-as-usual* scenario. Charter durations of 90 and 120 days were considered for three separate TIVs (Vessels A, B and C). The resulting six scenarios are shown in Table 5.1.

Table 5.1: Summary of simulation scenarios.

	Second vessel	
Scenario name	*Name*	*Charter duration (days)*
Baseline	-	-
A90	Vessel A	90
A120	Vessel A	120
B90	Vessel B	90
B120	Vessel B	120
C90	Vessel C	90
C120	Vessel C	120

The characteristics of each TIV are summarised in Table 5.2. *WTG capacity* refers to the number of WTGs that can be loaded onto the vessel at one time and is thus inversely proportional to the number of *cycles* required to complete the installation programme. Transit durations have been normalised with respect to that of the *baseline vessel*. The variations in the significant wave height (H_s) and tidal current (v_{tc}) thresholds are listed for the appropriate operations.

Table 5.2: Summary of key vessel characteristics. H_s = Significant wave height. v_{tc} = tidal current. Note that costs are indicative only.

	Vessel			
	Baseline	*Vessel A*	*Vessel B*	*Vessel C*
WTG capacity	8	11	8	9
Outward transit (normalised duration)	1	1	1	1.3
Return transit (normalised duration)	1	1	1	1.25
Jacking operations H_s limit (m)	1.5	1.75	1.5	1.4
Jacking operations v_{tc} limit (m/s)	0.82	1	0.82	1
Reposition operation H_s limit (m)	1.5	2.5	1.5	1.5
Outward transit H_s limit (m)	2.65	3.5	2.75	2.5
Enter harbour H_s limit (m)	3	-	3	3
Indicative cost (GBP/day)	140,000	190,000	140,000	160,000

Charter rates for the vessels were not provided by the client—the industrial analysis focused on the durations of operations, activities and the project as a whole (see

Section 5.3.4). However, to reflect the true cost-benefit nature of the analysis, and help demonstrate the full capabilities of the software, *indicative costs* were assumed for each vessel. Lacal-Arántegui *et al.* (2018) state that the daily rate of a turbine installation vessel is between 150,000 and 250,000 USD. Assuming a conversion rate of 0.76 GBP/USD, this range corresponds to 114,000–190,000 GBP/day. Because it is a state-of-the-art TIV—as evidenced by its higher metocean thresholds and WTG capacity—the upper limit of this range was assumed to represent the cost of Vessel A. As noted by Lacal-Arántegui *et al.* (2018), the charter cost of an installation vessel is proportional to its capacity—a vessel that can carry two full turbine sets should be cheaper than a vessel capable of transporting ten turbine sets each trip. Consequently, estimates for the charter cost of the other three vessels were obtained by multiplying the assumed charter cost of Vessel A by the ratio of WTG capacities of each vessel.

It is noted that the vessel charter rate assumptions are quite simplistic and that actual rates are subject to large and frequent variations. However, the constant charter rate assumptions made here are necessarily simplistic for this analysis and a detailed vessel cost analysis would be outside the scope of the research.

Vessel A is clearly the superior vessel in terms of performance. However, this straightforward example highlights the difficulty that can arise in developing appropriate operational strategies. It is unclear whether the increased charter cost of Vessel A will be compensated by its superior performance and expected reduction in project duration. An intuitive assessment of Vessel C's performance is even more difficult because it has both favourable and unfavourable performance characteristics in comparison to the baseline vessel. Specifically, Vessel C has an additional capacity for one extra WTG and a higher tidal current threshold of 1 m/s but is slower and has more stringent significant wave height and wind speed thresholds.

5.3.3 Simulation Configuration

Job Sequence and Assumptions

Job sequence data was provided by the client in the form of Excel files and were converted to the appropriate flow-chart and .CSV format required as input to the TDS software. Figure 5.4 shows the model representation of the *activities* that comprise the WTG installation phase, which follows the typical sequence for wind farm installation campaigns discussed in Section 2.4. In the flowchart, n_v is a *resource parameter*—it is associated with a single vessel—corresponding to the number of turbines currently onboard that vessel; the related variable N_v is the WTG capacity of the vessel mentioned previously; n_t is a global *simulation parameter* corresponding to the total number of WTGs installed and N_t is the total number of WTGs that need to be installed.

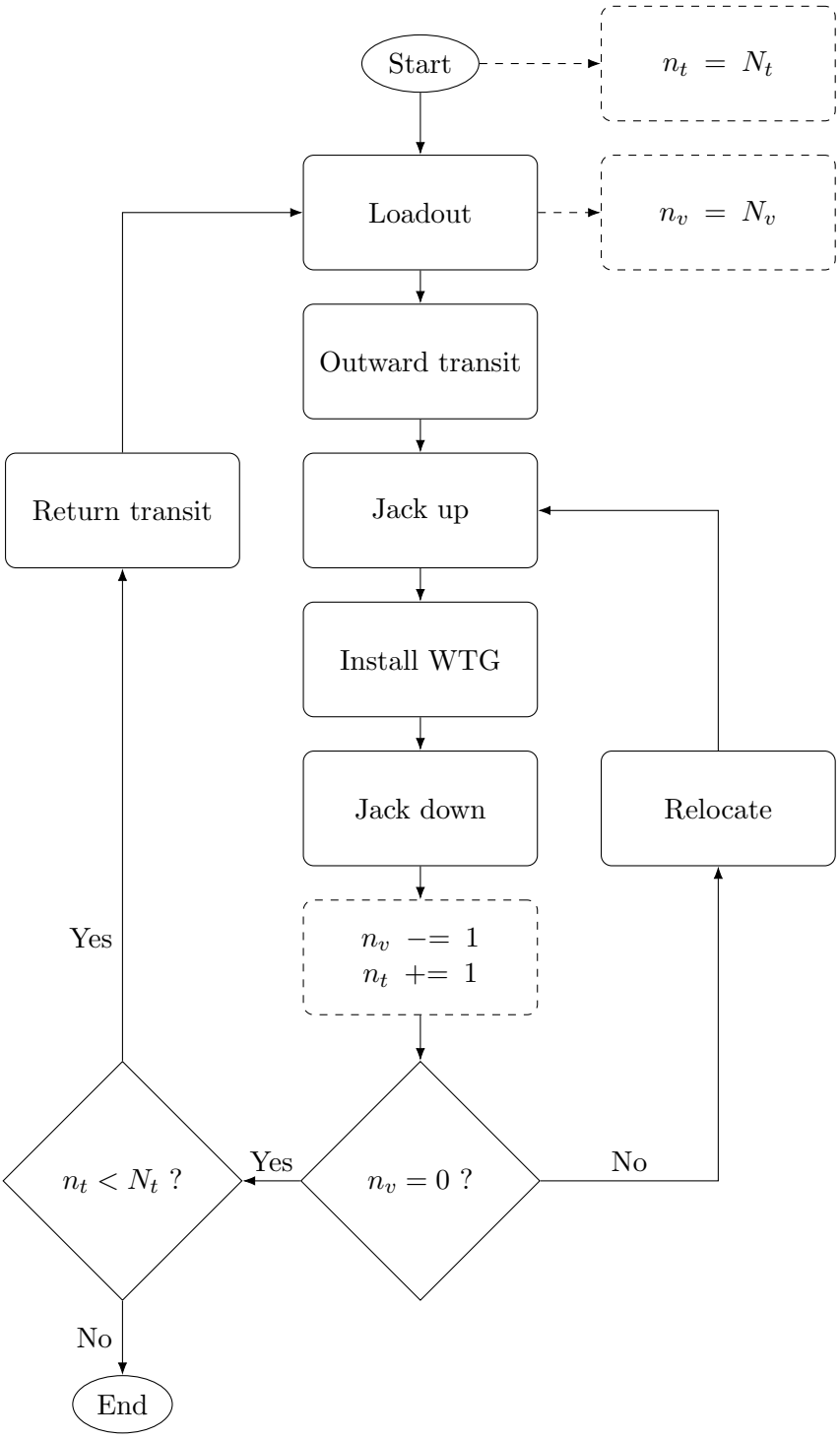

Figure 5.4: Representation of simulation model for WTG installation phase of demonstration project. n_v = number of turbines currently onboard vessel. N_v = WTG capacity of the vessel. n_t = total number of WTGs installed. N_t = total number of WTGs that need to be installed.

Each of the seven activities in the flow-chart in Figure 5.4 is comprised of a set of operations defined by their durations and thresholds. Single values—the best estimates—of operation durations were provided by the client. To enable a Monte Carlo analysis, a triangular distribution was assumed for each operation with the most likely duration set equal to the specified single value. The minimum and maximum parameters of the triangular distribution were set equal to 80% and 120% of this most-likely value. These percentage variations were chosen arbitrarily but it should be noted that this critical modelling assumption will be addressed in subsequent chapters. Specifically, the primary objective of Chapter 7 is to quantify this variability in operation durations.

Each vessel performs a job sequence identical to the one summarised by the activity flow-chart shown in Figure 5.4. The only differences for each vessel are the metocean thresholds for the operations specified in Table 5.2, along with the number of WTGs installed per cycle and the vessel transit speeds. The simulation logic does not allow simultaneous loadout operations at the port, reflecting the spatial limitations at the harbour in question.

For each year of metocean data and each Monte Carlo iteration, the simulation proceeds as follows;

1. The baseline vessel commences operations at the given start date (corresponding to the relative WTG phase duration of 0 days).
2. After a duration of 92 days, the second vessel begins its installation campaign.
3. The second vessel continues to work until its charter end date is reached (either 182 or 212 days after the beginning of the WTG installation phase, depending on the scenario). It was assumed that a new loadout and installation cycle would commence no later than 20 days before the charter end date of the second vessel, corresponding to the estimated time it would take for the baseline vessel to loadout, install 8 turbines and return to port.
4. The baseline vessel will continue to work after this date until all the WTGs have been installed (this may exceed the agreed 245 day charter date for the baseline vessel).

Metocean Data

Metocean data were provided by the client for six locations; one for the OWF site and five that divided the transit route into approximately equal sections. The time-series data were 18 years in length and had a temporal resolution of 1 hour. Time-series of significant wave height, tidal current and wind speed (measured at a height of 82 m) were provided. The proximity of the first point on the transit route to the port location justified the representation of both locations by the same data.

5.3.4 Quantitative Data Analysis Methods

Quantitative Variables

Two quantitative variables are used predominantly in the analysis; project duration and total vessel duration, both measured in days. Project duration is calculated as the difference between the start and end dates of each simulation.

This variable describes the end date of the WTG installation phase, but it does not account for the individual working time of each TIV. Individual vessel durations are thus calculated as the difference between the start and end date of each resource. The *total vessel duration* is then found by summing the duration values for each vessel involved in construction.

It is important to remember that this is a cost-benefit analysis—the major project objective is to complete the installation within a duration of 245 days at minimal project cost. If the total project cost was unimportant, TDS would not be needed to inform the decision to charter Vessel A. *Indicative costs* can be obtained for each scenario based on the assumed charter rates and the charter durations of each vessel and each scenario. The *indicative* nature of this additional quantitative variable should be emphasised—it does not include any additional cost components. However, the variable is useful for comparative analyses because most of the other cost components are expected to be independent of the scenario being tested (e.g. the capital cost of the WTGs, electrical cables, sub-station infrastructure and ancillary equipment).

Convergence Testing

The number of simulations required to obtain satisfactory convergence of simulation results was analysed by performing 600 simulations of the *baseline* scenario for the appropriate start date of each year of metocean data, leading to a total number of 10,800 simulations. A qualitative, graphical convergence analysis (e.g. see Ballio and Guadagnini, 2004) was performed on the project duration variable described above. This consisted of plotting the cumulative mean and cumulative standard deviation of project duration against the number of simulations performed. Note that for the baseline scenario, which uses a single installation vessel, the project duration is equal to the total vessel duration. The convergence analysis is split into three sections; one focuses on the effect of metocean data-set length; the second examines the Monte Carlo variation of operation duration and the final section assesses the combined effect of both phenomena. Further details on each specific analysis method are given in Section 5.4.1.

Scenario Testing

For each scenario and key quantitative variable discussed above, a box-and-whisker plot was generated using the technical methods discussed in Section 5.2. The whiskers of each boxplot are drawn between the 0.05 and 0.95 quantiles. Outliers are omitted.

Progress Plots

This thesis proposes a graphical assessment method, referred to as a *progress plot*, that is related to the standard box-and-whisker plot. The construction of the progress plot is illustrated in Figure 5.5. This example uses fabricated data to aid the explanation of progress plot construction.

Firstly, the *milestone* activities that are being assessed must be selected. The selection of milestone activity or activities is entirely at the user's discretion. For example, the milestone activity list could include the loadout, transit and installation activities. Conversely, the completion of the return transit activity could be set as the sole milestone, in which case the progress variable equates to the *cycle time*. In this analysis, the *Install WTG* activity is chosen as the progress plot variable.

Once the milestone activity is selected, the completion time of successive instances of those activities are extracted from the raw TDS output data. The duration required to complete sequential milestone activities is then calculated for each simulation. Subsequently, the progress plot can be viewed as a *horizontal* box-and-whisker plot of the durations required to complete consecutive milestone activities. This is shown in the top panel of Figure 5.5.

Progress lines are then drawn through the appropriate points of the horizontal box-and-whiskers. The resulting progress plot is shown in the bottom panel of Figure 5.5. The area between the P5 and P95 progress lines is shaded to show the 90% range of milestone durations. Typically, the horizontal axis of a progress plot shows the expected date-time based on the proposed construction start date. The examples in the present analysis show the milestone duration in days.

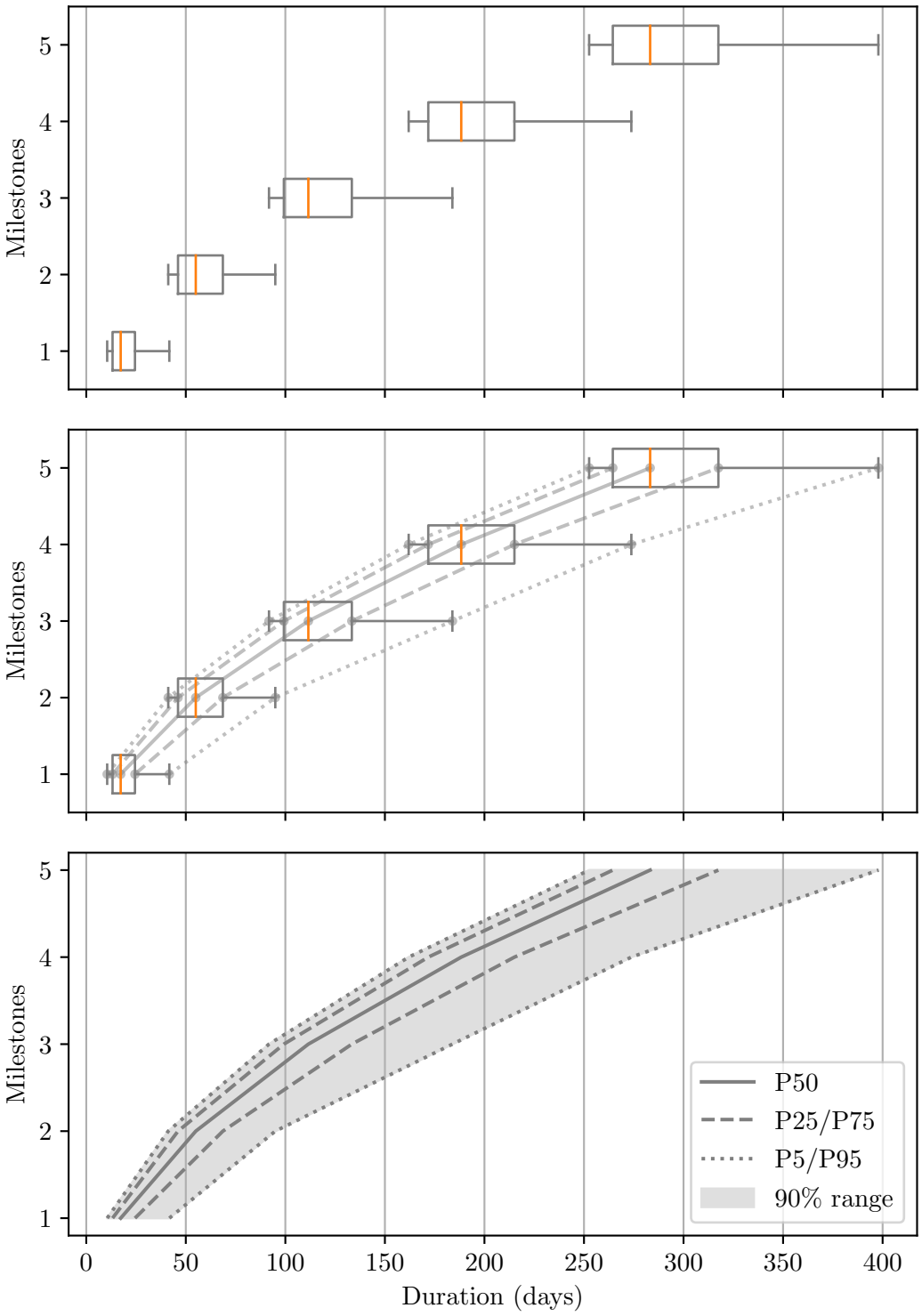

Figure 5.5: Stages in the construction of a progress plot.

In projects involving several vessels, the progress plots can be plotted individually or as a combined total. Individual progress plots for each vessel are complicated by the potential variation in the share of WTGs installed by each vessel—the quantity of WTGs required to be installed by the first vessel is directly related to the number installed by the second vessel during its charter period. To account for this two-dimensional variability, rangefinder boxplots can be added to the progress plot that simultaneously describe the number of WTGs installed and the corresponding milestone duration for each vessel.

In this bi-variate scenario, it is important to note that above a certain number of installations, the sample size will begin to diminish. For example, at least 43 WTGs may be installed by a single vessel in each of 1,000 simulations performed for a given scenario. Due to the observed metocean conditions and sampled operation durations, the number of simulations in which the same vessel completes 44 installations may fall to about 950, thus reducing the number of simulations in the sample set for milestones greater than 43. This can lead to anomalies in the progress lines when, continuing the previous example, the P95 duration for completing WTG number 44 is *lower* than the duration for WTG number 43, so that the P95 progress line appears to go backwards in time. To avoid this problem, a method that will be referred to as the *Delta-T* method is used to calculate the quantiles of milestone progression. Again using the example above, the quantile calculation is performed on the 950 simulations for installation numbers 44 and 43. The difference between these two durations is calculated and added to the previous point in the progress line. Note that this method requires a full ensemble for the first milestone to calculate the standard quantile values. If the number of simulations remains constant, the Delta-T method for calculating the progress lines is identical to the standard quantile calculation for each milestone number. The resulting progress lines are only drawn to the 0.05 quantile, which is the beginning of the rangefinder boxplot that describes the bi-variate end-point of each vessel.

Figure 5.6 shows the combined progress-rangefinder plot and a comparison of the Delta-T and standard quantile calculation methods. An example of the anomalies that can arise when using the standard methods is evident at milestone number 60. The predominant effect is on the upper-whisker progress line, where the Delta-T method has the effect of ignoring the anomaly but continuing the slope of the standard progress line. The figures also shows the minimal differences that arise in the remaining quantile progress lines.

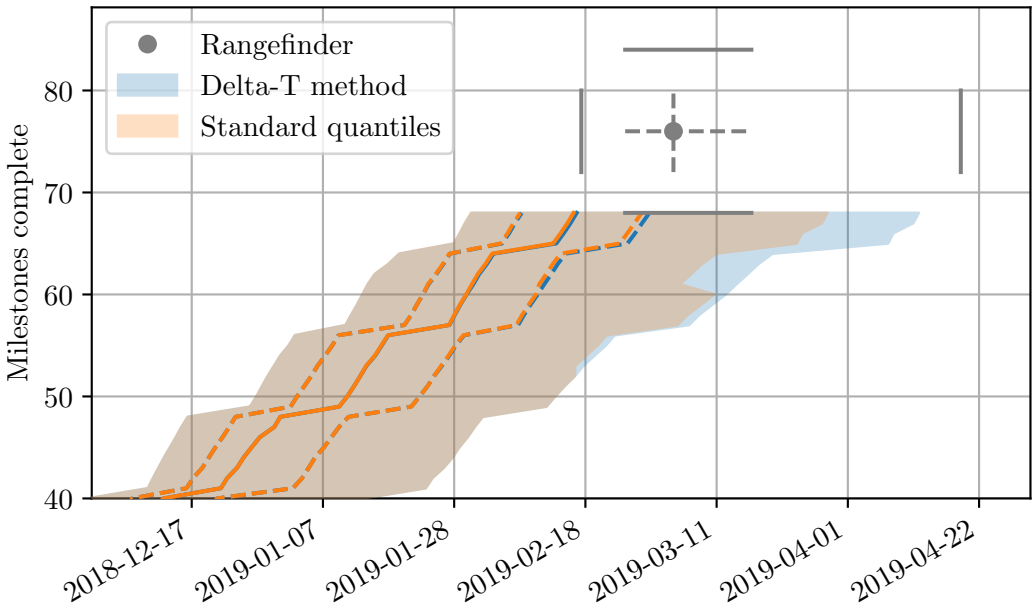

Figure 5.6: Progress plot with rangefinder boxplot for final installation.

Seasonal Variations

An alternative simulation procedure can be used to generate seasonal variation results. Up until now, the logic has been to simulate the entire construction phase, consisting of several repeated installation *cycles*, starting the simulation on a given start date of each year in the metocean data series. A different approach is to simulate a single cycle at a much higher frequency. Specifically, the time taken for the baseline vessel to loadout, transit to site, install 8 WTGs and return to the port was simulated, beginning at midnight on every date in the metocean time-series. As this type of analysis is more focused on metocean effects, a Monte Carlo approach was not used in this instance—a single simulation was run each day and the single values for operation durations were used. The resulting TDS outputs allowed the seasonal variations in expected activity duration to be assessed. Activity duration results were attributed to the month in which the activity began.

5.4 Results and Discussion

5.4.1 Convergence Testing

The *baseline* scenario was simulated 600 times for each of the 18 years of metocean data. Numerous simulations performed on the start date of the *final* year of metocean data were unable to complete the entire project within that year. This result gives an early indication that the baseline scenario of using a single TIV will not be sufficient for completing the project within the objective time-scale of 245 days. For the convergence analysis, every simulation that started in this final metocean year was removed from the data-set. Consistently selecting only the simulations that managed to complete the project in this final year—the "good" operational simulations—would have biased the results. Consequently, the total number of simulations performed was 10,200.

The results from the 600 simulation runs for each of the 17 years can be visualised as a table similar to that shown in Table 5.3, which shows the simulated project duration in days, categorised by year and simulation number. This table is useful for explaining the calculation methods of the next three sections.

Table 5.3: Template of simulated results for project duration (in days) categorised by simulation number and metocean year.

Simulation	Year 1	Year 2	...	Year 16	Year 17
1	418.6	301.1	...	293.5	389.7
2	418.4	301.1	...	336.5	389.8
⋮	⋮	⋮	⋱	⋮	⋮
599	421.1	301.1	...	335.5	389.8
600	418.3	301.2	...	335.5	389.9

Metocean Convergence

Firstly, the effect of metocean data-set length on simulation convergence was assessed by calculating the cumulative mean and cumulative standard deviation for each row of the simulated results as visualised in Table 5.3. Before calculating the mean and standard deviation of each row, the order of the years was randomised. The cumulative mean and standard deviation for each of these 600 subsets is plotted as a function of the number of years simulated in Figure 5.7. The figure also shows the mean and standard deviation of all 10,200 simulations.

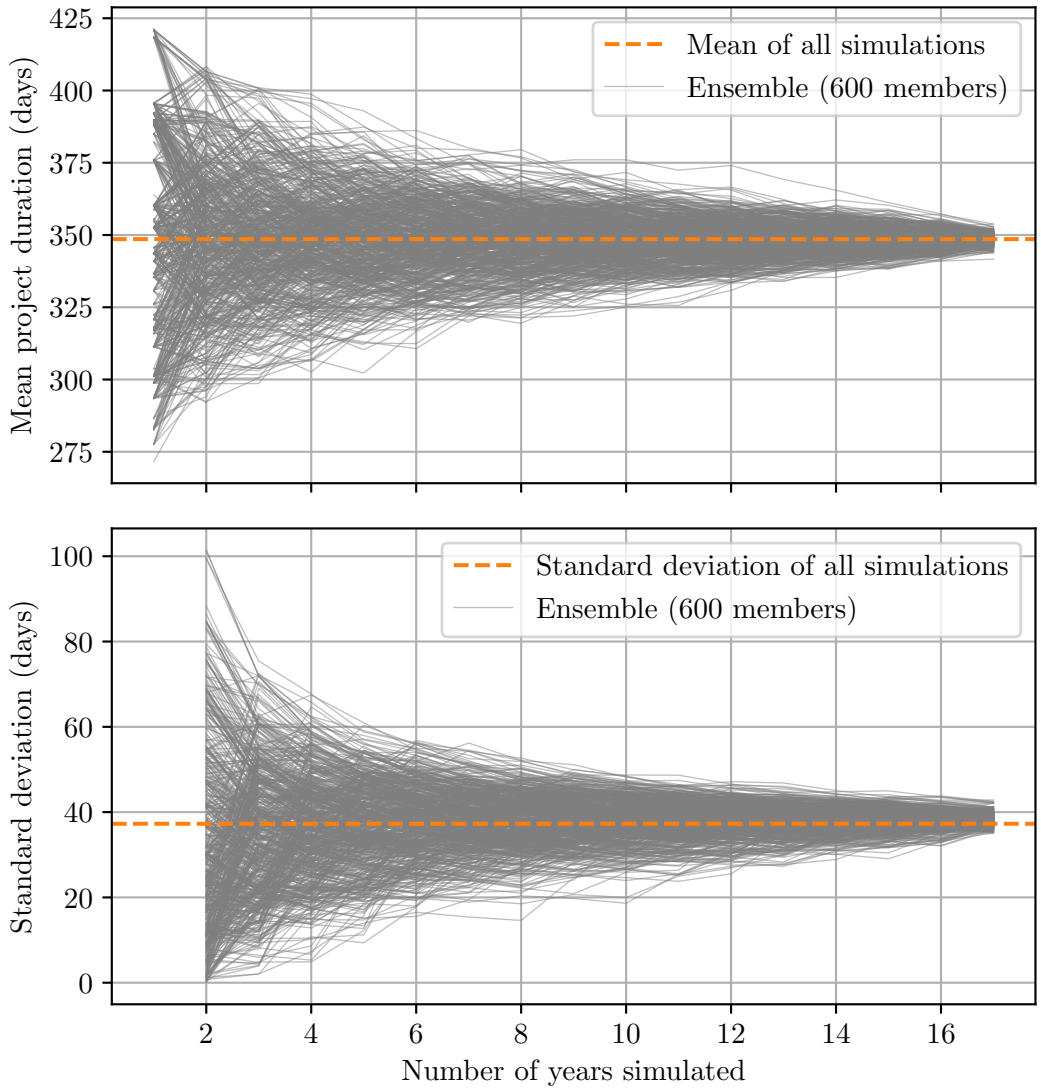

Figure 5.7: Convergence of simulation results categorised by number of metocean years.

The importance of maximising the number of distinct metocean years in the simulation model is highlighted in the results for both the mean and standard deviation. The range in mean project duration is approximately 275–425 days if only one metocean year is included. By including all 17 of the applicable years, the range in mean project duration reduces to 345-355 days. Similarly, the standard deviation, which varies between 0 and 100 days if only one year is considered, converges to a value of approximately 40 days. The metocean convergence results informed the scenario tests described in Section 5.4.2 which consequently performed simulations using the entire metocean data-set.

Operation Duration Convergence

The impact of Monte Carlo variation of operation duration on simulation convergence is assessed by calculating the cumulative mean for each column of the simulated results as represented by Table 5.3. The order does not need to be randomised because the Monte Carlo variation of operation duration is inherently random. Figure 5.8 shows the convergence of mean project duration for each of the 17 metocean years plotted against the number of simulations per year.

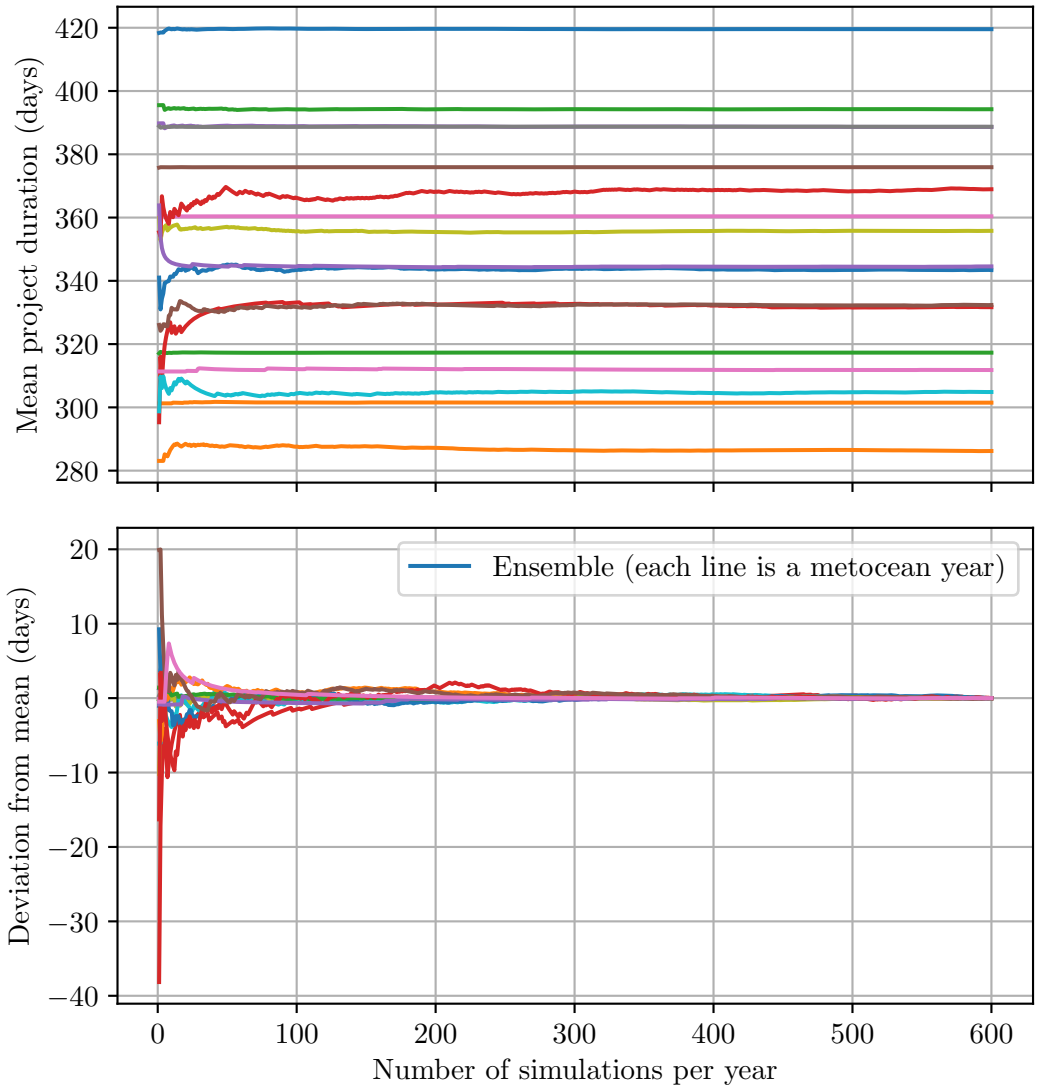

Figure 5.8: Convergence of simulation results categorised by number of simulations per metocean year.

The separation of the results into distinct metocean "bins" again highlights the importance of maximising the extent of the metocean data-set. There are some initial transients for about the first 50 simulations of each year but the results show that the mean project duration is far more sensitive to the specific metocean year being simulated than the number of Monte Carlo iterations performed.

For each metocean subset, the deviation of the cumulative mean from the mean of all simulations in that subset was calculated. This is also plotted against the number of simulations per year and shown in the bottom panel of Figure 5.8. The figure shows that the initial transients have converged after approximately 300 simulations per year. Crucially, the deviation from the mean is relatively small after the initial fluctuations; at a value of 100 simulations per year, the deviation from the mean varies between -1.5 and +1 days.

General Convergence

A general convergence test of the simulation results is obtained by plotting the cumulative mean and standard deviation against the number of simulations (on a log-scale) for all 10,200 results. This can be viewed as an assessment of the combined effect of the two phenomena discussed previously. The results, shown in Figure 5.9, suggest that convergence is achieved after approximately 1,000 simulations. This corresponds to running approximately 60 simulations per year. This parameter is used for the remainder of the analysis in this chapter.

The critical importance of a sufficiently extensive metocean data-set is again highlighted in Figure 5.9. The first 17 points of both plots correspond to the cumulative mean and standard deviation of the first row of values in Table 5.3. In other words, the first 17 points correspond to the convergence based on running a simulation for each year in the metocean data-set. Clearly, the results have already begun to converge after these 17 simulation results. The remaining fluctuations as the results continue to converge can be attributed to the Monte Carlo variations in operation duration.

The results of the convergence tests have highlighted the benefits of maximising the extent of metocean data used in TDS. Methods such as the Markov-chain model (e.g. see Hagen *et al.*, 2013) that can be used to generate synthetic metocean time-series from smaller, potentially insufficient metocean data-sets would thus be of significant interest. Future work should focus on appraising the application, suitability and accuracy of these types of methods within TDS models.

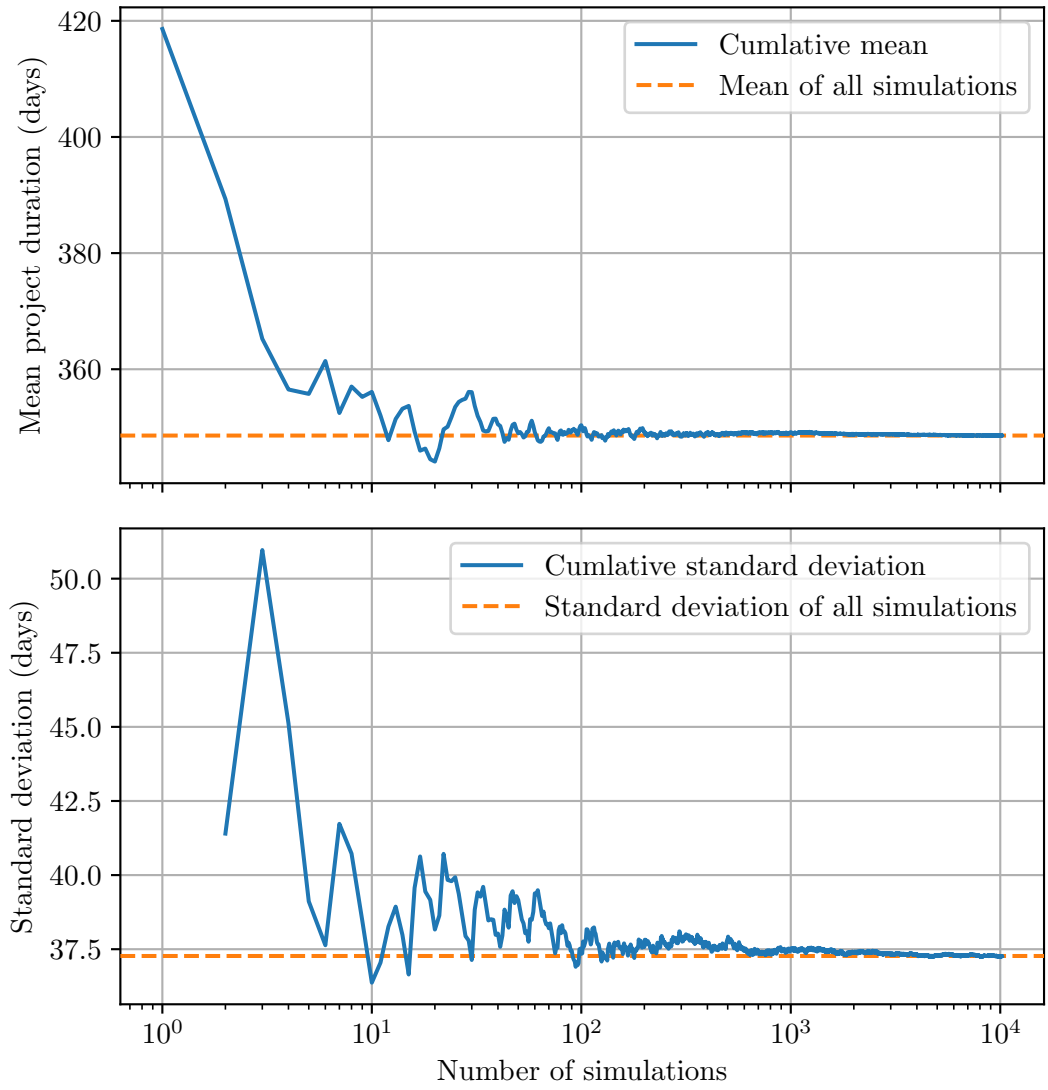

Figure 5.9: General convergence of simulation results.

5.4.2 Scenario Testing

Boxplots of the simulated results for project duration and total vessel duration for all seven scenarios are given in Figure 5.10. To ensure a fair comparison with the baseline scenario, which was unable to complete the installation project in the final year of metocean data, simulations commencing in the 18^{th} metocean year were also omitted for each of the six additional scenarios.

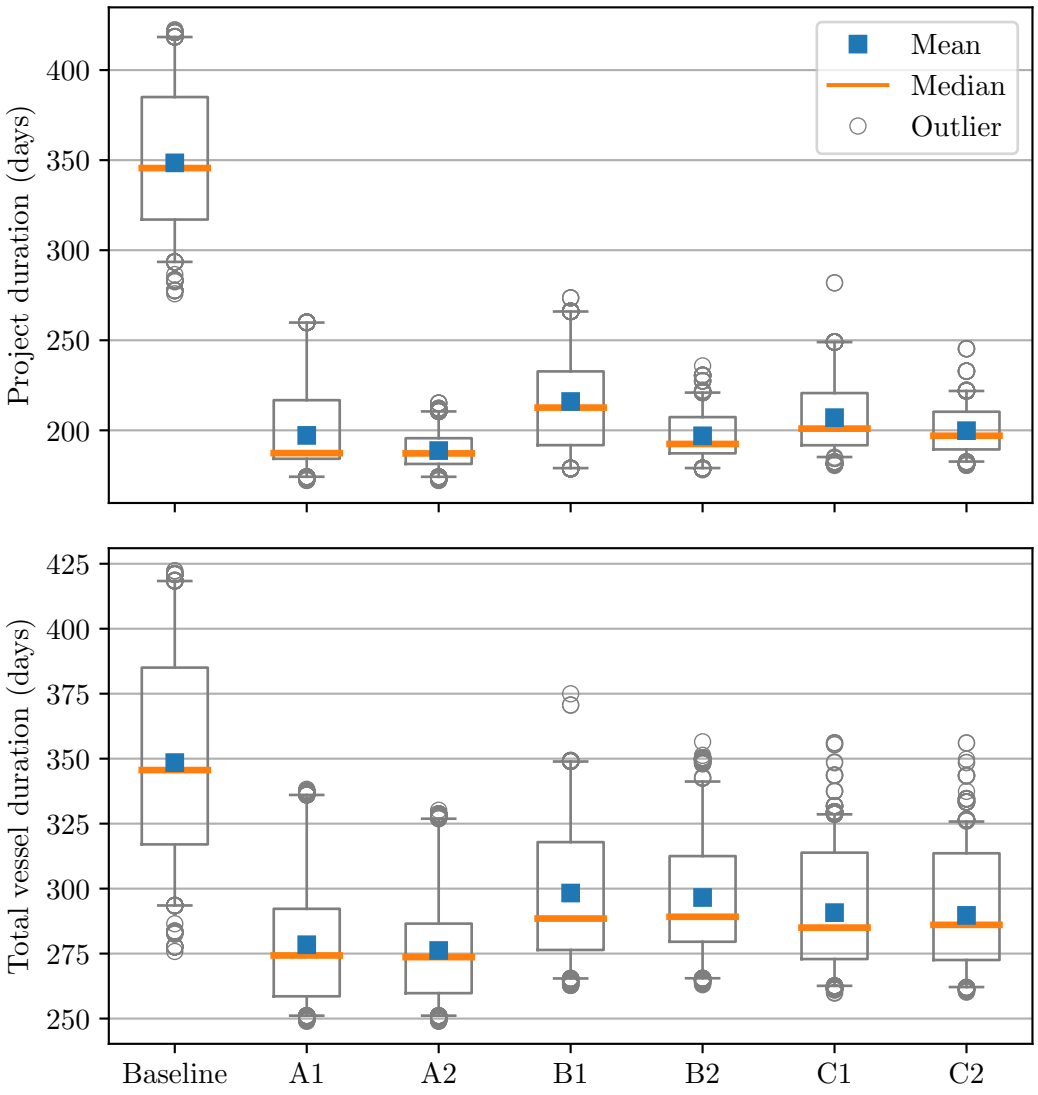

Figure 5.10: Boxplots of project duration and total vessel duration for all seven scenarios. Whiskers represent 5th and 95th percentiles.

Project Duration

For the baseline scenario, 95% of the simulations resulted in a project duration of greater than 294 days. The mean and median project durations were approximately 350 days and the upper limit was just under 420 days. Thus, it is clear that without an additional installation vessel, it is extremely unlikely that the construction project can be completed within the agreed charter date of the baseline vessel. Conversely, for every scenario that uses an additional vessel, the mean and median project duration values fall to a value of approximately 200 days. Additionally, the spread of possible results reduces dramatically upon procurement of an additional TIV, as shown by the reduction

in the IQR compared to the baseline. As expected, if the planning objective concerned only the minimisation of project duration, the results show that the procurement of Vessel A for a duration of 120 days is the most sensible option.

Interestingly, the TDS results imply that procuring an additional vessel for only 90 days may not be adequate. The P95 value of each of the 90-day scenarios are greater than the critical 245 days. Experience has shown that many firms make decisions based on a 90 or 95 percent chance of occurrence. Abiding by this rule, the results show that the secondary vessel, regardless of which vessel is selected, should be chartered for the longer duration of 120 days.

Unexpectedly, the P95 project duration of scenario A1 was larger than that of scenario C1, despite the superiority of Vessel A. Further investigation into the raw simulation output data revealed that the P25 value for the number of WTGs installed by the secondary vessel was 33 for scenario A1 and 36 for C1. This slightly counter-intuitive result can be attributed to the modelling assumption that a new cycle would commence no later than 20 days before the charter end date of the second vessel. For the "bad" years, this meant that fewer WTGs were installed by Vessel A in scenario A1, which completed 3 cycles of 11 turbines, than by Vessel C in scenario C1, which completed 4 cycles of 9 turbines. Subsequently, the *baseline* vessel had more installations to complete in these "bad" years and the corresponding project durations were larger for scenario A1 than for C1. It is expected that an improved modelling assumption that allowed vessels to load out a fraction of their capacity depending on its remaining charter duration would have improved the accuracy of the results and potentially led to a P95 duration of less than 245 days for scenario A1.

Total Vessel Duration

The scenario results depicted in the bottom panel of Figure 5.10 show that the total vessel duration for the baseline scenario is significantly greater than the total vessel durations for every other scenario that simulated the project with an additional vessel. Again, this result can seem counter-intuitive at first, but can be explained by the timing of the construction project. In the baseline scenario, the construction phase runs into the winter months and the associated adverse metocean conditions. The subsequent instances of weather downtime can be avoided by chartering an additional vessel. The results imply that it is better to charter two vessels during the calm summer months than it is to charter a single TIV for a longer duration. Seasonal aspects of planning marine operations are discussed further in Section 5.4.4.

A similar phenomenon is evident in the relationship between the 90- and 120-day scenarios of each vessel. The results for each quantile and mean duration for the 120-day scenarios are less than or approximately equal to the equivalent 90 day scenario. This is

because the reduction in duration of the baseline vessel in each scenario is greater than the increase in operation time of the secondary vessel. Subsequently, the total vessel duration is lower when using two vessels.

Indicative Costs

The previous sections outlined the necessity for procuring a secondary vessel and the reasoning for selecting a charter duration of 120 days. Because this is a cost-benefit analysis, the focus now turns to the financial implications of vessel selection and how this decision can be informed by the TDS results. Using the assumed charter rates and charter durations of each vessel discussed in Section 5.3.2, the indicative cost of each scenario can be calculated. The results are given in Table 5.4.

Table 5.4: Summary of charter durations and indicative costs for each scenario.

	Charter duration (days)		*Indicative cost (£m)*		
Scenario	*Vessel 1*	*Vessel 2*	*Vessel 1*	*Vessel 2*	*Total*
Baseline	245	-	34.30	-	34.30
A1	245	90	34.30	17.10	51.40
A2	245	120	34.30	22.80	57.10
B1	245	90	34.30	13.00	46.90
B2	245	120	34.30	17.00	51.10
C1	245	90	34.30	14.40	48.70
C2	245	120	34.30	19.20	53.50

The indicative cost of the baseline scenario is £34.3m, but the above results have shown that this will almost certainly result in exceeding the agreed charter length and incur a financial penalty on top of any additional charter cost. Following the convention of making operational decisions based on a minimum chance of occurrence of 95%, the question becomes a simple case of selecting the lowest cost scenario from A2, B2 and C2. Based on the assumed charter rates, the results show that scenario B2 is £2.4m less than the next cheapest alternative and plausible scenario, C2.

The P95 project duration values were 210 days for scenario A2 and approximately 220 days for scenarios B2 and C2. The indicative cost of scenario A2 is £6m greater than that of scenario B2. It is expected that this additional cost could not be justified for achieving only a 10 day reduction in the P95 project duration, especially considering the standard deviations for the simulation results of scenarios A2 and B2 are 10.3 and 13.5 days respectively.

Finally, the possibility of the P95 project duration for scenario A1 being reduced below the critical 245 days through improvements in the modelling assumptions was

previously discussed. The results suggest that Scenario B2 would still be preferential in this eventuality due to scenario A1 being £300,000 more expensive than scenario B2.

5.4.3 Progress Plots

Combined Progress

Progress plots for the total milestones completed by both installation vessels were generated for the Baseline, B1 and B2 scenarios and are shown in Figure 5.11. The rangefinder boxplot is not required when the combined progress is assessed because the total number of WTGs installed does not change. The figure follows the format described in Section 5.3.4 and summarised graphically in Figure 5.6—the P50 progress is plotted as a solid line, the P25 and P75 progress as dashed lines and the 90% range as a shaded region.

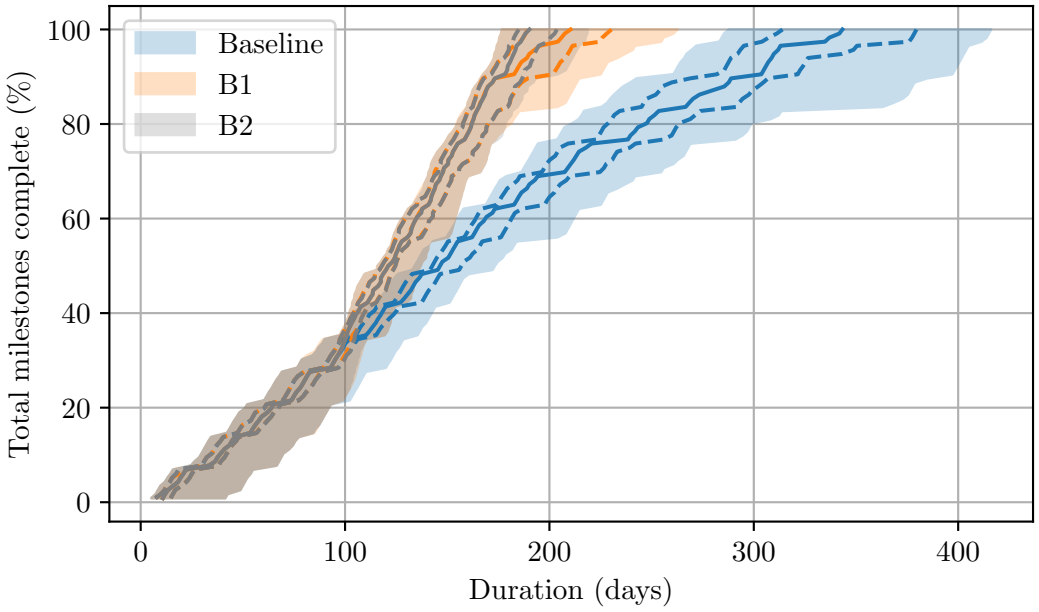

Figure 5.11: Progress plots for total milestones completed for Baseline, B1 and B2 scenarios.

Because the secondary vessel does not begin its charter until 90 days after the baseline vessel, the progress plots are identical for about the first 100 days of the project. After this time, the impact of chartering the second vessel can be seen in the sharp increase of the progress *gradient* for scenarios B1 and B2, in comparison to the uniform slope of the single vessel in the baseline scenario. Similarly, scenarios B1 and B2 are identical until just over 80% of the milestones have been completed. It is at this point that certain simulations in the B1 scenario begin to reach the end of their charter date.

Consequently, the difference between scenarios B1 and B2 is only evident in the last 20% of milestone completion progress.

Another benefit of acquiring a second TIV is the increased confidence achieved in the simulation results, as highlighted by the reduced spread of progress projections. Focusing on the baseline scenario, the spread of results remains relatively constant up until approximately 200 days. After this time which coincides with the beginning of winter and the associated adverse metocean conditions, the spread of simulation results grows continuously. In the end, the range for the project completion date is over 100 days. Conversely, the effect of the second vessel beginning its charter at the start of the calmer summer months leads to a high confidence in the simulation results between approximately 40 and 80% of milestone completion for scenarios B1 and B2. As discussed above, the spread increases for the final 20% of milestones in scenario B1 as Vessel B reaches the end of its charter date. Nevertheless, the differences between the P5 and P95 project duration values for the Baseline, B1 and B2 scenarios are 125, 87 and 42 days respectively. In fact the 90% confidence ranges for B1 and B2 are comparable to the 50% confidence range—the difference between the P25 and P75 durations—of the baseline scenario (68 days). It is clear then that the additional vessel leads to a significant reduction in the uncertainty of expected project duration.

Interestingly, the progress plots highlight the fact that in the "good" years—for P25 durations and below—the B1 and B2 scenarios are identical. In fact, there is a 75% chance that the short charter duration scenario of B1 will complete the project within a period of 233 days. These types of statistical insights are invaluable in the planning stages of large marine construction projects. As stated previously, this probability level is expected to be too low for most clients in the offshore renewable energy sector.

Individual Vessel Progress

Progress plots for the percentage of milestones completed by each vessel are shown in Figure 5.12. The top panel summarises the results for scenario B1 and the bottom panel refers to scenario B2.

Due to the assumption that vessels will begin a new cycle no later than 20 days before their charter end date, the counts of WTGs installed by each vessel fall into discrete *bins*. This is the reason for the slightly peculiar appearance of the rangefinder boxplots. For example in scenario B1; the P5, P25, P50 and P75 values for the percentage of installations completed by Vessel B are all equal to 27.6%. These values align with the P25, P50, P75 and P95 values for the baseline vessel of 72.4%. Similarly, the P95 value for Vessel B of 34.5% corresponds to the P5 value for the baseline vessel of 65.5%. These results imply there is a 95% chance that the share of WTG installations between the

vessels in scenario B1 will be approximately 72/28%. There is a 5% chance that Vessel B will outperform and increase its percentage share to 34.5%.

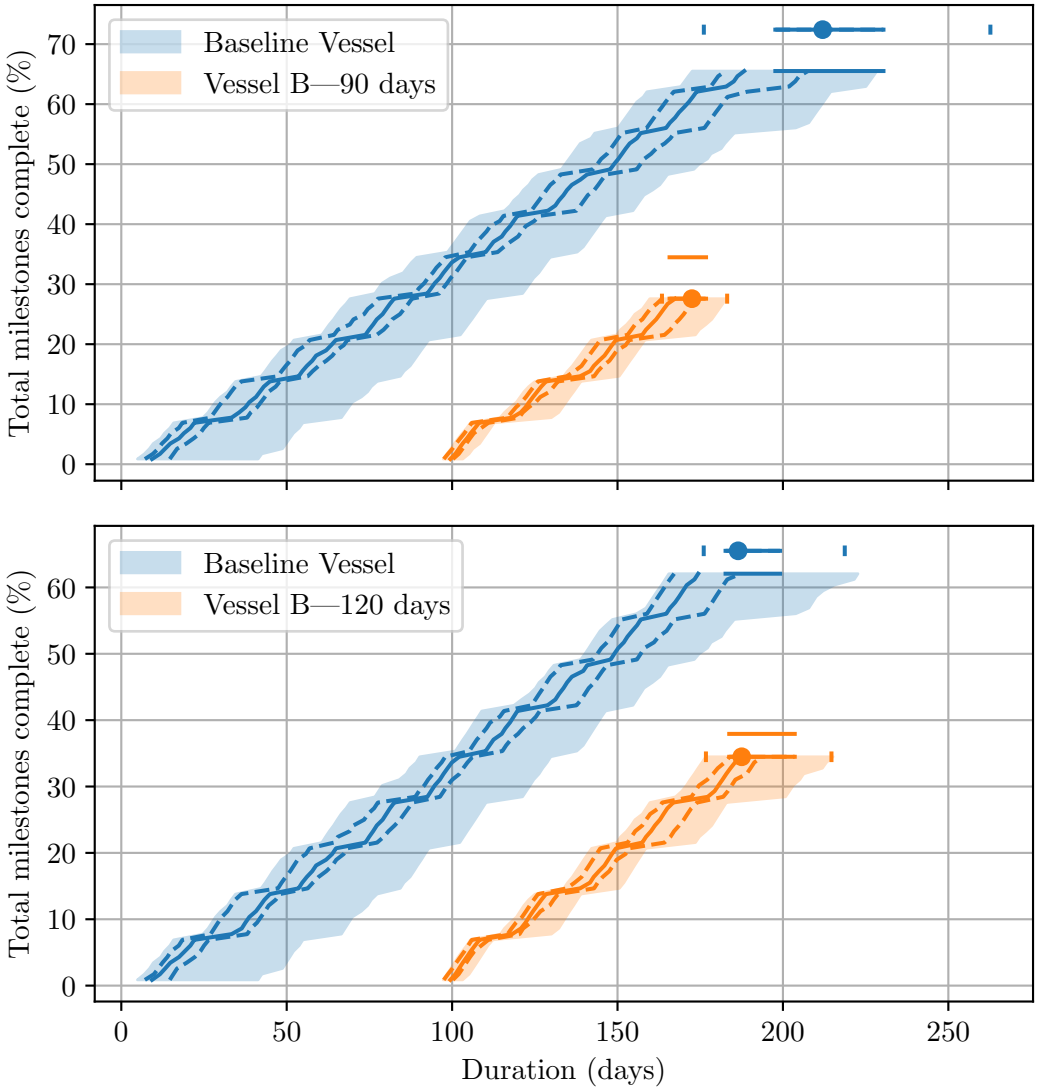

Figure 5.12: Individual progress plots for total milestones completed by each vessel for scenarios B1 (top panel) and B2 (bottom panel).

The main purpose of this figure is to compare the two B scenarios and to illustrate the effect that the increased charter duration of the additional vessel has on the operational duration of the baseline vessel. By increasing the charter length of Vessel B by 30 days, the expected number of installations completed by this vessel increases by about 6.9%. This means that the baseline vessel has to install about 7% fewer turbines and is thus expected to finish its installation programme earlier. Consequently, the expected value and uncertainty in the overall project end date is reduced significantly.

5.4.4 Seasonal Variation

Figure 5.13 shows the results of the alternative analysis that assesses the seasonal variations of the time to complete a single cycle of the installation process. In this case, the whiskers are drawn between the minimum and the maximum values of simulated cycle duration. As expected, and has already been shown in the preceding results, the cycle duration is much lower in the calm summer months than in the winter. The ideal month for performing an installation cycle is July, with a mean and median duration of under 20 days. For October through January, the mean cycle duration rises to approximately 35 days. Crucially, the maximum value for all four of these months show that a single cycle can take over 60 days.

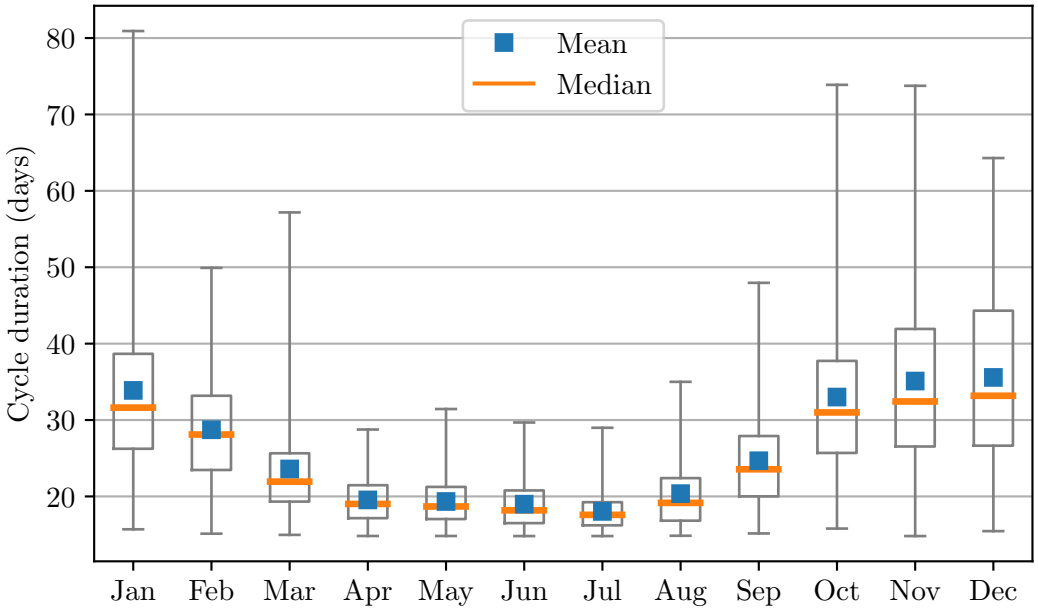

Figure 5.13: Monthly variation of duration to complete a single cycle of the WTG installation process. Whiskers drawn to minimum and maximum values.

This type of analysis can be repeated for entire construction projects and sometimes leads to more unexpected and surprising results than the example shown above. For instance, a large offshore construction project expected to take over two years to complete was analysed in the same manner and the results showed a similar trend to that shown in Figure 5.13, but shifted horizontally—the optimal start date of the project was in November. The reason for this counter-intuitive result was that this start date ensured a critical phase of the installation project, with particularly stringent metocean thresholds, coincided with the calmest metocean month. Identifying the start date that ensures the correct alignment of this activity with the most favourable metocean conditions would have been difficult without the use of TDS.

5.5 Further Analysis

The scenarios and example outputs discussed previously represent a small fraction of the analysis that can and has been performed using the developed TDS model. Section 5.5.1 briefly describes some alternative scenarios that were tested for the same OWF installation project and Section 5.5.2 outlines additional outputs that have not been described.

5.5.1 Alternative Scenarios

As stated previously, the *foundation phase* of the OWF construction project was also supported. The piling operations in this phase were of particular importance to the overall success of the offshore project. Previous geological surveys had identified several foundation locations susceptible to a *pile-refusal*. The turbine mono-piles are usually driven into the sea-bed. In the case where this *hammering* operation is impossible due to the sea-bed conditions, a more expensive and specialised procedure is required that *drills* the mono-piles into the ground. Crucially, this operation necessitates additional equipment to be fitted onto the installation vessels. The TDS software enabled a sensitivity analysis on the number of pile-refusal occurrences and the subsequent effect on project duration.

Additionally, an environmental ban prohibited piling operations during the spawning seasons of several fish species. This constraint became a crucial factor in the project strategy and execution. The baseline vessel was also involved in the foundation phase but required a complete *refit* of equipment before commencing its WTG installations. The simulations showed that the project was hugely sensitive to the baseline vessel completing its portion of mono-pile and transition piece installations before the beginning of one of these environmental bans. The risk of missing this window and the knock-on effect for the remaining *WTG phase* was significant. The TDS model was able to highlight this crucial project target. Another model scenario quantified the amount of time that would be saved if a ban that prohibited coincident piling by more than one TIV was removed.

Finally, a *safe-haven* analysis assessed the cost-benefit of obtaining an additional berth at a port location located approximately halfway between the loadout port and the OWF site. The increase in operational time attributed to this second port berth—in the order of a few days—and the subsequent reduction in project cost did not justify the cost of the additional berth.

5.5.2 Additional Outputs

The Monte Carlo approach of the simulation software is well-suited for sensitivity analyses of the model input parameters. The scenario mentioned previously that varied the number of pile-refusal occurrences is one particular example of this. Equally, the main analysis assessing vessel and charter duration options can be viewed as a sensitivity analysis of the operational thresholds, the WTG capacity and the cost of the installation vessels. However, a more typical and comprehensive sensitivity analysis can also be performed by varying the numerous input parameters to the model and analysing the sensitivity of the three quantitative variables to these inputs. This method can identify the operations and metocean thresholds that have the most significant effect on project duration.

Two methods have been used to produce Gantt charts—a useful organisational tool common in project management—from the raw TDS output results. The first is to produce the Gantt chart itself; a graph similar to a horizontal barplot or a horizontal box-and-whisker plot showing the duration of key activities. Alternatively, the time-series output data can be formatted so that it can be imported easily into a specific project management software. This requires a template that maps the formatted output .CSV to the appropriate columns in the software data-frame structure. This process has been completed for Microsoft Project and Primavera project management software. Crucially, the TDS Gantt charts consist of probabilistic, metocean-dependent estimates of task durations.

The animations discussed in Chapter 4 are used primarily for internal and external quality assurance reviews. However, the animations can also be used as an additional TDS output. These animated outputs are less appropriate for the type of scenario comparison discussed in this chapter and more suited to the identification of bottlenecks or previously-unknown project constraints.

The wide range of potential outputs discussed in this chapter highlights one of the biggest strengths of TDS for the planning and optimisation of offshore operation strategies. There is an extensive list of outputs that can be created and scenarios that can be tested. Moreover, the presentation of results—and indeed the simulation models themselves—can be tailored specifically to user requirements, with very little difficulty. Time-domain Monte Carlo simulations are capable of answering general questions about an entire offshore project, as well as *zooming-in* on the smallest details in a particular strategy. This flexibility is one of the major benefits of using TDS.

5.6 Conclusions

This chapter has shown that the use of TDS enables the marginal benefits of various offshore operation scenarios to be compared and helps identify and assess the most appropriate strategy for a specific marine project. Consequently, these simulation tools can help minimise the cost and mitigate the inherent risks of offshore operations.

The developed metocean planning tool has been used to support several marine projects, predominantly in the offshore renewable energy sector. The analysis has focused on the application of the simulation theory in the development of optimal installation strategies for a Round 3 offshore wind farm. Specifically, results from a bespoke model were used in the planning stages of the project to assess whether an additional installation vessel was required to complete construction within a period of 245 days. The results suggested that a secondary vessel was essential and that a charter duration of 120 days was required to achieve this objective. Based on the financial implications of the resulting indicative costs—calculated using assumed charter rates—and project durations, the analysis showed that the selection of the turbine installation vessel that resulted in the lowest indicative cost would lead to a saving of £6m in comparison to the most expensive scenario.

Convergence testing of the simulation outputs has revealed that obtaining a sufficiently extensive metocean data-set is critical for ensuring consistency and confidence in the results. For the specific project outlined in this chapter, it has been shown that the mean and standard deviation of project duration results are significantly more sensitive to the number of metocean years used as an input to the model than the number of Monte Carlo iterations that are performed for each year. Furthermore, for this particular simulation model, a minimum of 1,000 simulations is recommended to achieve an acceptable convergence in the mean and standard deviation of output results.

A graphical output referred to as a *progress plot* has been proposed. These graphs combine an alternative representation of a horizontal boxplot for consecutive milestone completion times with a rangefinder boxplot that describes the variation in both expected completion time and the number of milestones completed. The plots are beneficial for scenario testing and for assessing project progress when multiple vessels are assigned to the same task. One of the main benefits of these proposed graphical summaries—and one of the reasons for why they became known as progress plots—is their application in the continuous monitoring of project progress that will be discussed in the next chapter.

The results described in this chapter represent only a small percentage of the possible scenarios that can be assessed. Selected additional outputs and scenario tests for this specific project were discussed qualitatively in Section 5.5. This versatility is one of

the greatest strengths of using time-domain simulations in the planning of offshore operations; the models, analysis methods and presentation of results can be adapted and configured, readily and easily, to meet the particular requirements of the project.

PART II

During

Chapter 6

Continuous Project Monitoring and Progress Updates

6.1 Introduction

The previous chapter discussed the application of TDS in the planning stages of a marine project. It is also possible to apply these methods throughout the operational phase of these campaigns. This chapter describes how the developed simulation methods and in particular, the previously proposed *progress plots* can be used to provide continuous updates on project performance and make projections using the most up-to-date observed installation data available. An example application of how TDS were used in this manner is described for the WTG installation phase of the offshore wind farm described in Chapter 5. The development and application of a continuous project monitoring methodology and associated summary report known as a *weekly update* are discussed. Indicative values for the charter rates of turbine installation vessels (TIVs) are used to quantify the financial impacts of deviations between original and updated simulation projections. The benefit of iterative updates of model inputs based on the analysis of observed operation duration data is assessed.

This chapter is divided into two parts. Sections 6.2 and 6.3 discuss the continuous monitoring of project progress using TDS theory. The methodology for the generation of these *weekly updates* is discussed in Section 6.2. Two example weekly update results are then described in Section 6.3. The second part of the chapter (Sections 6.4 and 6.5) concerns the analysis of observed operation durations and the potential of using the results of this analysis to update continuously the simulation model inputs. The methods for analysing the operation durations at an approximate half-way stage of the wind farm construction project are outlined in Section 6.4. Section 6.5 discusses the results of the analysis and appraises their impact on the project outlook.

6.2 Weekly Update Methodology

Chapter 5 discussed how the developed TDS models were used to assess various operation strategies *before* the commencement of an offshore wind farm installation project. Vessel B was selected as the secondary WTG installation vessel and chartered for a duration of approximately 120 days. JBA Consulting were subsequently contracted to monitor the performance of this vessel and the baseline vessel for the entirety of the WTG installation campaign. To facilitate this, a recurrent simulation procedure and a summary report of results that became known as the *weekly updates* were developed.

Every Friday throughout the WTG installation phase the procedure consisted of the following steps, which will be expanded in Sections 6.2.1–6.2.4;

1. The observed installation data from the previous week were collated.
2. The model inputs were updated and the new simulations were performed.
3. The TDS output data were analysed.
4. The weekly progress report and associated output files were created and distributed to the relevant personnel.

6.2.1 Collating Observed Data

Observed installation data was provided by the client on a daily basis in the form of daily progress reports (DPRs) that describe the operations completed on a given day by a specific vessel. The first step in the creation of the weekly progress and projection reports was to collate this data. This involved extracting the cumulative number of WTGs installed by each TIV over the course of the week and identifying the most recent operation completed by each vessel. Incoming data were also examined to identify any exceptional events and unplanned decisions or movements that deviated significantly from the original strategies and modelling assumptions.

6.2.2 Updating and Running the Simulation Model

Each week, the simulation model was updated to reflect the cumulative number of WTGs installed by each vessel and the most recently completed operations. The updated scenario was then simulated assuming a model start date equal to the date on which the simulation was being performed—ensuring the projections were based on the prevailing status of the installation operations.

6.2.3 Analysing the Updated Simulation Results

Project Summary and Deviations

In addition to the summary of the cumulative installations completed by the two TIVs, the progress *deviations* between the baseline simulations and the actual installation data were computed. The baseline simulation refers to the original simulation performed before the beginning of the WTG phase. Deviations in the number of installations and in the *schedule*—the time-difference between the end-date of the most recently completed activity and the corresponding completion time of that activity in the baseline simulation—were calculated. These deviations were calculated for the P5, P25, P50, P75 and P95 percentile values of the baseline simulation results. For the schedule deviations, linear interpolation was used to find the exact percentile value. For the completed number of WTGs, which can only be an integer number, the value closest to the exact percentile value was selected. In the present analysis, the number of WTGs installed are expressed as a percentage of the total number of turbines to be constructed.

Progress Plots and Projection Ranges

A specialised version of the *progress plots* described in Chapter 5 were developed for the weekly updates—in fact their use in the weekly updates is one of the primary reasons for why they are referred to as *progress plots*. Progress plots for the baseline projection are drawn in light shade. Observed installation data are plotted as individual markers over these baseline projections. Finally, the progress plot of the prevailing projections is added, showing the most recent simulation results starting from the current date. The projection ranges corresponding to the rangefinder boxplots for each vessel (see Sections 5.2.3 and 5.3.4) are also calculated and tabulated.

The deviations in vessel charter duration between the original and updated projections are used to calculate indicative values for the deviations in projected cost. The charter rate of 140,000 GBP/day discussed previously in Section 5.3.2 is used to obtain values for this deviation in indicative cost parameter. Values for each TIV and the combined total are calculated.

Gantt Charts

The TDS output data were manipulated to match the format required for inputs to the *Primavera* project management software. These charts were used for short-term project planning of the upcoming week of operations. Gantt charts were requested for representative P50 and P90 model scenarios for each vessel.

6.2.4 Creating and Dispatching the Weekly Progress Report

A two-page weekly progress report was created in LaTeX that summarised all of the above-mentioned output results. In addition to the summary project information, deviations, progress plots and projection ranges discussed above, a *headline messages* section was added that described any major discussion points or anomalies in the data. An automated procedure was developed that generated the progress plots, weekly update report and .CSV files for the Gantt charts. The results were distributed to the client every Friday of the installation campaign.

6.2.5 Example Weekly Update Scenarios

Two examples are given that describe representative results obtained from these weekly update analyses. Example A relates to simulations performed after a period of 70 days from the beginning of the WTG installation phase. This corresponded to the Baseline Vessel commencing its *third* loadout activity, after having successfully completed its first two cycles.

Example B describes the weekly update performed 98 days after the commencement of WTG construction. This corresponds to the Baseline Vessel commencing its *fifth* loadout activity. Note that in this example, Vessel B will have been operational for 6 days and is expected to be close to completing its first WTG installation. For both of these scenarios, the resulting deviations, progress plots and updated projections are calculated as described above.

6.3 Example Weekly Update Results

Before presenting the two weekly update examples, it is useful to revisit the results for project duration and the percentage of WTGs allocated to each vessel for the original simulation performed before the installation phase began. The rangefinder boxplot results of scenario B2, first shown in Figure 5.12, are thus tabulated in Table 6.1. The data illustrate the initially counter-intuitive result that the P5 of baseline vessel installs (62.1%) corresponds to the P95 number installed by Vessel B (37.9%). For 95% of the simulations, the percentage installed by Vessel B is lower than 37.9%. The 5% of simulations greater than this value correspond to the 5% of simulations where the baseline vessel share of installations is lower than 62.1%.

Note that these baseline values for vessel duration are used to calculate the deviations in indicative cost. The difference between these baseline durations and the updated projection durations are multiplied by the assumed indicative charter rate of 140,000 GBP/day to calculate the change in project cost.

Table 6.1: Percentage share of installations and vessel duration for baseline scenario.

	Baseline Vessel		*Vessel B*	
Percentile	*Installs (%)*	*Duration (days)*	*Installs (%)*	*Duration (days)*
P5	62.1	176.1	34.5	176.7
P25	65.5	182.7	34.5	183.8
P50	65.5	186.4	34.5	187.5
P75	65.5	199.1	34.5	203.6
P95	65.5	218.7	37.9	214.7

6.3.1 Example A—70 days

The resulting progress plot for the weekly update example computed after 70 days of installation progress is shown in Figure 6.1. As mentioned previously, the progress plot and rangefinder boxplot for the original simulation are plotted in light shade. The observed installations and results of the latest projection are then added to the plot.

It can be seen that the observed progress tracked the P25–P75 projections for the first three installations accurately but is offset by a large delay after this third installation. This delay corresponds to an unexpected stoppage and failure of equipment in the observation records of the baseline vessel. Although instances of *technical downtime* (see Chapter 9) were analysed in certain scenarios in the planning stage of this project, this particular instance was far greater than expected and accounted for in any prior analysis. The knock-on effect of this small delay of approximately 15 days is evident in the end dates of both installation vessels and in the allocation of the installations between the two vessels. These updated projections are summarised in Table 6.2, alongside the deviations between the observed data and the original simulations. Positive deviations imply that actual progress is ahead of the original projections.

The delay after the third milestone has resulted in actual progress falling behind the original simulation projections. Specifically, when compared to the median simulation results, the baseline vessel has installed approximately 7% fewer turbines and has fallen about 18 days behind schedule. Compared to the worst case simulation scenario (P5 for installs and P95 for schedule), the vessel has installed 3.4% more and is 14.3 days ahead. Progress has fallen behind in the remaining 95% of simulation results.

The effect of this delay on the updated projections is clear. The P50 end dates have increased from 186.4 and 187.5 days to 202.5 and 202.8 days for the baseline vessel and Vessel B respectively. Furthermore, while the original simulations showed that there was a 95% chance that the baseline vessel would complete 65.5% of the total WTG installations, there is now only a 25% chance that the vessel will complete more than this percentage. There is a 5% chance that the percentage completed will drop to 58.6%.

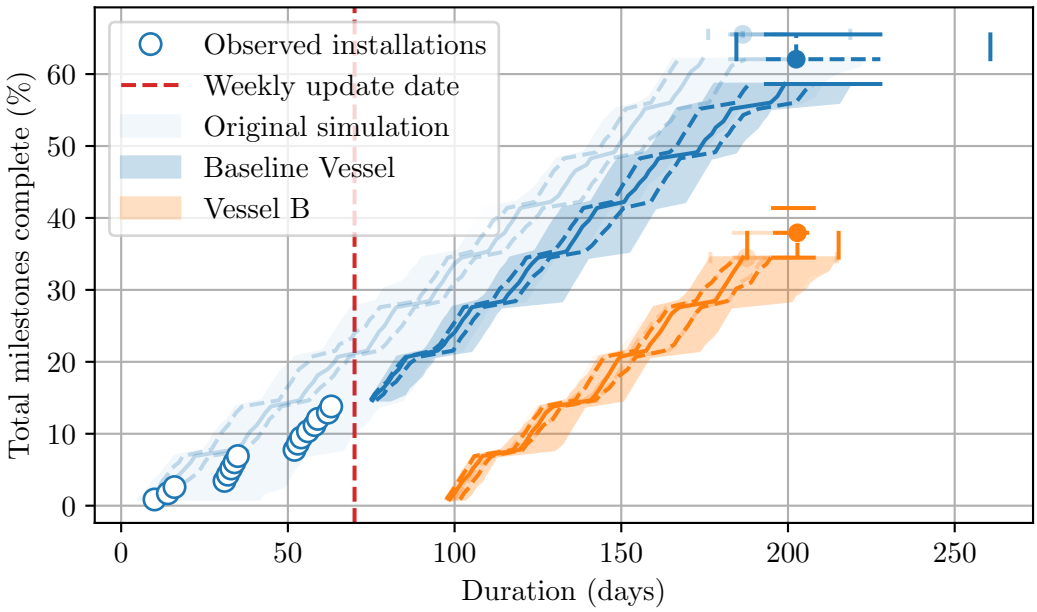

Figure 6.1: Example weekly update progress plot after 70 days.

Table 6.2: Summary of deviations and updated projections for weekly update after 70 days. Positive values for the deviation between observed data and original simulations indicates that actual progress is ahead of projections. Positive deviations in projected indicative cost suggest that the updated indicative cost estimates are greater than the original projections.

	P5	*P25*	*P50*	*P75*	*P95*
Deviation from original simulations					
Baseline Vessel					
Installs (%)	3.4	-6.9	-6.9	-9.5	-13.7
Schedule (days)	-28.5	-26.7	-18.1	-15.1	14.3
Updated projections					
Baseline Vessel					
Installs (%)	58.6	62.1	62.1	65.5	65.5
Duration (days)	184.5	193.4	202.5	227.7	260.7
Vessel B					
Installs (%)	34.5	34.5	37.9	37.9	41.4
Duration (days)	187.8	195.5	202.8	207.7	215.2
Deviations in projected indicative cost (£m)					
Baseline Vessel	1.18	1.50	2.25	4.00	5.88
Vessel B	1.55	1.64	2.14	0.57	0.07
Total	2.73	3.14	4.40	4.58	5.95

The corresponding increase in the proportion to be installed by Vessel B is evident in

the rangefinder boxplot and in Table 6.2. Crucially, the P95 project end date—the latter of the two vessel end dates—has increased from 218.7 days in the original simulations to 260.7 days following the poor initial performance. The weekly update results after 70 days thus imply that there is a risk of the baseline vessel exceeding its previously-agreed charter duration.

The effect of the delay after the third installation has a significant effect on projected indicative cost. There is a 90% chance that there will be an increase in total vessel charter cost of between £2.73m and £5.95m. The median estimate for this increase in cost is £4.4m. This example highlights the effect that random stoppages and equipment failures can have on project duration and cost estimates.

The P75 and P95 values for the deviation in indicative cost for Vessel B are lower than the P50 value because of the limited charter duration of this vessel. For the baseline results in these worst case scenarios, the second vessel has to work for the majority of this charter duration. In other words, there is a limit to the possible increases in duration (and thus indicative cost) for Vessel B.

Of critical importance is the discrepancy between the duration of the unexpected delay and the change in the estimated total vessel duration and indicative project cost. The delay was approximately 15 days in length. However, the knock-on effect of this delay increased the P50 duration of the Baseline vessel by 16.1 days and Vessel B by 15.3 days, leading to a total increase of 31.4 days and an increase in indicative cost of £4.4m. If the unexpected delay was simply added to the original total vessel duration, then the increase in indicative project cost should have been approximately £2m. The actual increase is twice this amount. The results show that an unexpected stoppage or delay cannot simply be added to the total project duration. This is because of the temporal variability of metocean conditions. For example, a significant delay in the calm summer months is exacerbated by having to complete these operations during the harsher weather typical in the winter months. This example shows how TDS models can be used to assess the impacts of these complexities and non-linearities.

6.3.2 Example B—98 days

The progress plots, deviations and updated projections for Example B are shown in Figure 6.2 and Table 6.3. The weekly update after 98 days shows that the baseline vessel has improved its performance relative to its progress after its first 70 days of operation and that the observed results show greater adherence to the original simulations results than was the case for Example A.

The median deviations now show that the actual progress is only 4.3% behind in terms of installations and 12.5 days behind in terms of schedule—an improvement from the

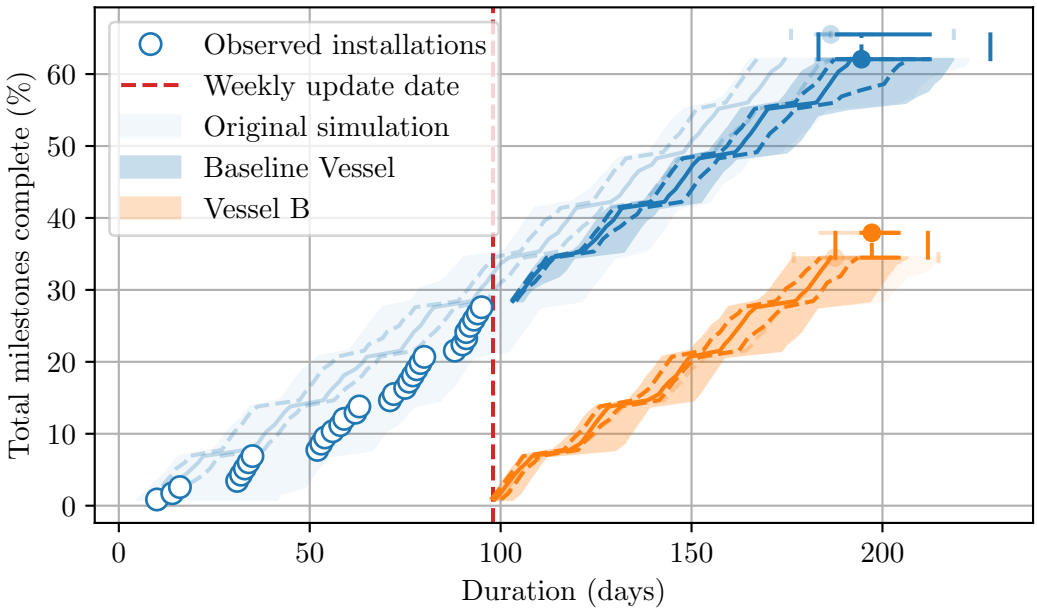

Figure 6.2: Example weekly update progress plot after 98 days.

situation after 70 days. Furthermore, 6.9% more installations have been completed than in the worst case simulation scenario and progress is about 15 days ahead in this case. The improvement in progress has not been enough to offset the large delay observed between the third and fourth installations; the median vessel end dates are still later than the original predictions and the P50 allocation of WTGs to the baseline vessel is still 62.1%. However, the P95 project end date has now reduced from 260.7 days in the weekly update of Example A to 228.3 days—within the critical charter duration of 245 days for the baseline vessel. Sections 6.4 and 6.5 investigate the causes behind the improved operational performance of the two TIVs.

The effect of the observed improvement in installation rate can also be seen in the updated indicative cost projections. For the best case scenario (P5), the increase in cost has dropped from £2.73m to £2.53m. Furthermore, the results suggest a dramatic reduction in the P95 results from approximately £6m to £1m. The median deviation in projected indicative cost is now £2.5m, falling by about £2m in comparison to Example A projections. Additionally, the change in indicative cost for Vessel B in the P95 scenario is negative, indicating that the upper range of projected duration and cost of the second vessel has fallen. However, despite the significant improvement in construction performance of the TIVs between examples A and B, the effect of the large delay after the third installation still has a notable effect on the total indicative cost of the project.

Table 6.3: Summary of deviations and updated projections for weekly update after 98 days. Positive values for the deviation between observed data and original simulations indicates that actual progress is ahead of projections. Positive deviations in projected indicative cost suggest that the updated indicative cost estimates are greater than the original projections.

	P5	*P25*	*P50*	*P75*	*P95*
Deviation from original simulation					
Baseline Vessel					
Installs (%)	6.9	-1.7	-4.3	-6.9	-6.9
Schedule (days)	-25.8	-17.4	-12.5	-7.1	15.3
Updated projections					
Baseline Vessel					
Installs (%)	62.1	62.1	62.1	65.5	65.5
Duration (days)	183.2	188.0	194.5	212.4	228.3
Vessel B					
Installs (%)	34.5	34.5	37.9	37.9	37.9
Duration (days)	187.7	194.5	197.2	204.2	211.9
Deviations in projected indicative cost (£m)					
Baseline Vessel	0.99	0.74	1.13	1.86	1.34
Vessel B	1.54	1.50	1.36	0.08	-0.39
Total	2.53	2.24	2.49	1.95	0.95

6.3.3 Weekly Update Discussion

The early identification of significant discrepancies between estimated and observed results can inform planning decisions and strategies. For example, the significant random delay observed after the installation of the third WTG introduced the risk of the project end date exceeding the previously-agreed charter duration. Without the improvement in installation rate evident after this delay, it may have been necessary to charter a *third* TIV to ensure that construction was completed within the allocated time period. Conversely, if observed progress had been better than expected, it may have been possible to reduce the charter duration of one or both of the TIVs. The weekly update results show that the continuous use of TDS models throughout the operational phase of an offshore project can support these key strategic decisions.

A significant advantage of TDS and the weekly update progress reports documented here is the speed with which the simulations and subsequent analysis could be performed. In the case of this particular project, the DPRs arrived between approximately approximately 08:00 and 09:00 each morning. Every Friday, it was possible to collate the data, update the models, run the simulations, analyse the simulation results, generate the weekly report and provide it to the client in time for their weekly progress meeting at midday each Friday. This enabled key decision makers and project managers to

use the latest projections—typically made 1–2 hours previously—to inform operational decisions for the days and week ahead.

One of the major benefits of using TDS for continuous project monitoring is the ability to identify significant deviations from baseline projections. For instance, Example A suggests that the occurrence of a large random stoppage in installation progress could have increased indicative cost estimates by up to £6m. Subsequent weekly update simulations account for the effect of this random stoppage. However, the results also highlight the need for incorporating an accurate model of the probability of occurrence and duration of these instances of random downtime. The incorporation of these random stoppages in the TDS model is discussed in Chapter 9.

In a similar manner, the performance of the baseline vessel highlighted in the weekly updates between 70 and 98 days was greater than expected and necessitated a detailed analysis of the recorded operation durations to date. The updated projection of Figure 6.1 showed that there was only a 5% chance that 27.6% of the total number of milestones could be completed by a duration of 100 days. The observed installation data 28 days later in Example B show that this percentage of total milestones was completed within approximately 95 days. Actual installation progress has outperformed the best-case simulation scenario. The weekly updates helped to identify this discrepancy. Sections 6.4 and 6.5 describe the analysis of the available operation duration recorded up to this point in an attempt to diagnose this issue.

6.4 Operation Duration Analysis Methodology

Operation duration data for the 98 days were extracted from all the DPRs obtained during this period. The mean of each operation was calculated and compared with the operation durations used in the original simulation model. Mean values for the *Loadout* and *Install WTG* activities were also obtained, by summing the mean durations of the individual operations that comprise each activity.

The input operation data to the simulation was then updated to reflect any discrepancies between the observed durations and those assumed originally in the model. Two simulations were performed to assess the effect of the updated operation duration input data; one for the entire installation campaign, starting at a duration of 0 days, and a second using the start-date and installation status of Example B, 98 days after the commencement of the construction campaign. These simulation results were then compared to the equivalent simulations performed with the original operation durations.

6.5 Example Operation Duration Analysis Results

6.5.1 Operation Duration Comparisons

The results of the operation duration analysis are summarised in Table 6.4, which shows the ratio of the updated operation durations to the original operation durations. Results for the transit operations are not shown because these differences were negligible and these operation durations were not updated. Although there is significant variation in the individual operations that comprise the loadout activity, the ratio for the total activity duration is nearly 1, highlighting the accuracy of the initial estimates for the time to loadout a set of WTGs. Conversely, the observed time to install a single WTG, based on the first 98 days of operation, was just under 70% of the duration specified in the original model. Considering that this activity is repeated on numerous occasions throughout the construction campaign, this over-estimate of activity duration is expected to have a significant effect on the simulation results. This discrepancy explains how the observed installation progress between days 70 and 98 was able to surpass the best case simulation projection made in Example A.

Table 6.4: Ratios of observed operation durations after 98 days to the original operation durations used in the simulation.

Loadout		*Install WTG*	
Operation	*Ratio*	*Operation*	*Ratio*
Positioning	0.415	Between locations	0.690
Backloading	1.823	Jack-up	0.445
Loading blades	1.165	Preparing to install	0.800
Loading towers	0.552	Installing tower	0.776
Loading nacelles	1.679	Installing nacelle	1.295
Seafastening	0.822	Installing blade 1	0.858
		Installing blade 2	0.629
		Installing blade 3	0.665
		Finishing installation	10.92
		Jack-down	0.205
Activity total	1.014	Activity total	0.687

The results show that the duration of the *finishing installation* operation—which includes tasks such as the seafastening of equipment—is approximately 11 times greater than originally specified. In this case, the original estimate of operation duration was 15 minutes. As such, the large ratio of 10.92 only corresponds to an observed operation duration of approximately 2.7 hours. The results for the jack-up and jack-down operations of 0.445 and 0.205 are the lowest ratios obtained for the install WTG activity and are expected to have a much greater impact on the simulation results, due to the strict

metocean thresholds associated with these two tasks—they are two of the operations most affected by the tidal current.

6.5.2 Updated Simulation Results

The observed mean operation durations were incorporated within an updated simulation model. Figure 6.3 shows a comparison of the resulting progress plots of the original and updated operation durations for the two starting points described previously.

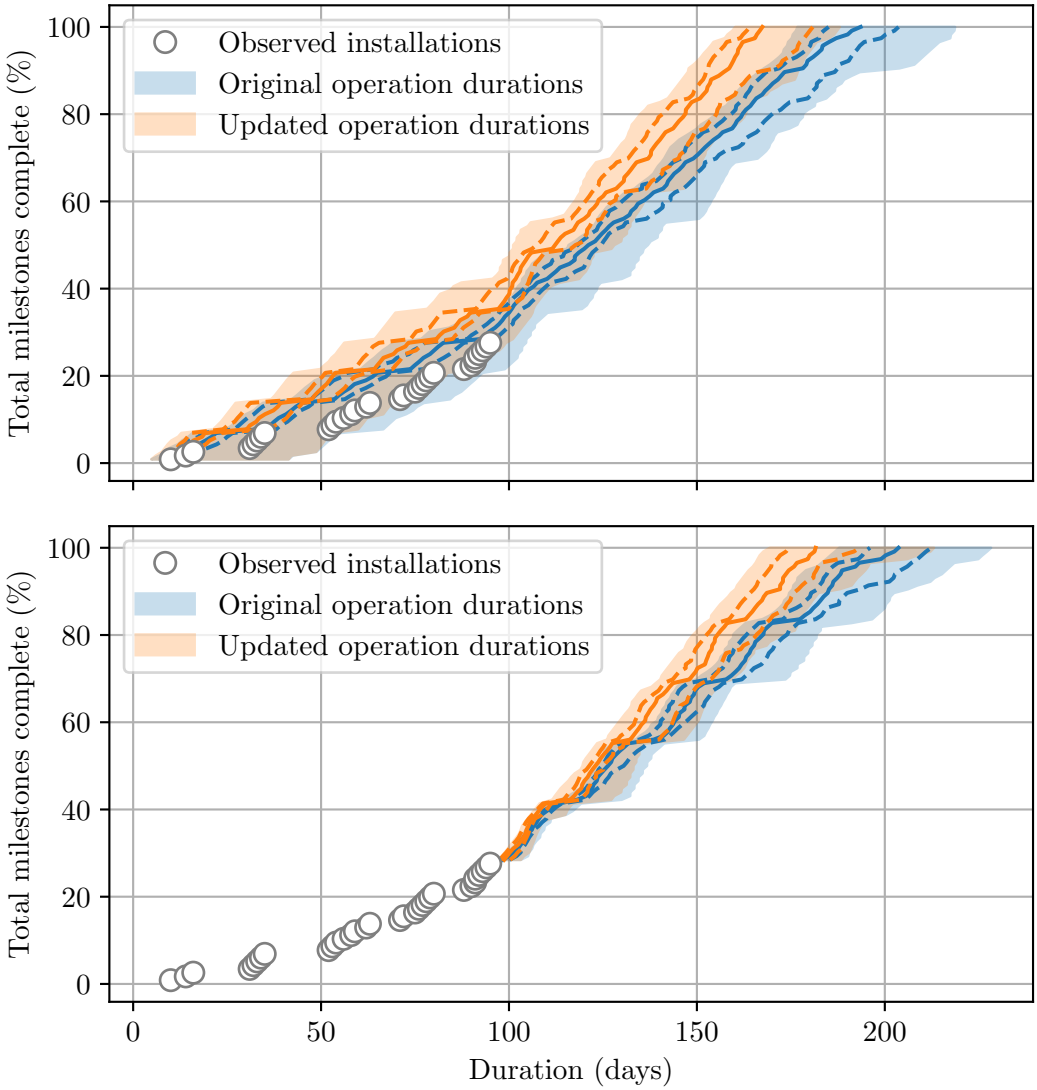

Figure 6.3: Comparison of projections with original and updated input operation durations. Top panel shows simulations at a starting point of 0 days. Bottom panel shows simulations at a starting point of 98 days.

The top panel shows the results of the two simulation models performed on the start

date of the construction phase. The bottom panel shows the results starting on day 98 and with 27.6% of the WTG installations complete. Note that the top panel is entirely academic. The orange progress plot showing the results when the updated operation duration are used as an input could not have been obtained without the observed installation data that are also shown on the plot. This figure is included to show an additional comparison of the two input data-sets that were used and to highlight how well the actual progress fits within the two sets of model predictions.

The updated operation durations are seen to have a significant impact on projected progress in both panels of Figure 6.3. Both comparisons show a much steeper progress gradient and a subsequent reduction in expected end date for the simulations with the updated input operation data. For the simulations with a starting point based on Example B, the median project duration has fallen from 204 days to 182 days—a reduction of 10.8%. For both simulation starting points, the P50 project end date calculated using the new operation data is earlier than the P5 simulation result for the original operation durations.

6.5.3 Updated Simulation Discussion

The example described above shows the impact that slight discrepancies in model inputs can have on the simulation results. This in turn highlights the advantage of continually monitoring project progress and the improvements in progress projections that can be achieved through iterative updating of simulation input data. The analysis presented here showed that the mean time for installing a single wind turbine was approximately 30% lower than initially specified. Updating the input operation data to reflect these changes resulted in the median project duration decreasing by 10.8%. If operational data similar to the DPRs described previously are available during the operational phase of a project, the task duration input data can be continuously updated based on the analysis of the incoming performance data. As the project progresses, more operational data will be obtained and analysed, leading to more precise estimates of mean operation duration values. This will in turn lead to more accurate and reliable simulation models and predictions of future progress.

This thesis is divided into three main parts; *Before*, *During* and *After*. The next chapter of this thesis, Chapter 7, is the first "after" chapter and discusses the operation duration analysis completed after the entire wind farm installation project had been completed. This analysis is an extension of the operation duration analysis discussed above that was performed approximately half-way through the installation process. The accuracy of representative operation durations that can be obtained is dependent on the length of the available data-set. Logically, the best representation will be obtained after the completion of the entire project. However, while the narrative of this thesis focuses on

the application of TDS before, during and after an entire offshore project, it is equally plausible to apply the theory before, during and after a specific date or key project milestone. The example in this chapter has described how TDS can be applied in this cyclical manner, throughout the entire offshore project.

The updated operational data have emphasised the importance of the accurate incorporation of random failures and stoppages in the simulation model. Despite the use of an extensive metocean data-set and representative operation duration input data, the top panel of Figure 6.3 shows that some of the observed installation data points are quite close to the P95 simulation results for the updated operation duration progress plot. This implies that the occurrence of large instances of random stoppages are not adequately represented in the simulations. Chapter 9 investigates the occurrence of these instances of *technical downtime* and discusses their implementation in the TDS model.

The present analysis has only compared the *mean* durations of operations and activities. The relationship between operation duration and the number of times that operation is repeated has not been assessed in this chapter. However, this relationship and specifically the concept of *learning curves* is assessed in Chapter 7. As will be shown, learning is an important factor that affects the duration of successive offshore operations. This learning effect will have contributed somewhat to the discrepancy between the observed mean operation durations and those specified for the original simulations. It also provides an additional explanation as to how the observed installation progress between days 70 and 98 was able to surpass the best case simulation projection made in Example A. The reader is referred to Chapter 7 for the detailed investigation of this learning phenomenon.

6.6 Conclusions

Time-domain simulations performed during the operational phase of a marine renewable energy project enable the continuous monitoring of project performance and the early identification of significant deviations from baseline projections and planned schedules of work. These deviations can be random or systematic in nature and examples of both errors are evident in the application to the offshore wind farm construction project discussed above. The early identification of similar discrepancies between estimated and observed results can be used to inform planning decisions and strategies throughout an offshore project.

The large instance of random downtime that occurred in the case study is an example of the stochastic deviations that can arise. This particular discrepancy delayed the

median charter end dates of both vessels by approximately 16 days and increased the median indicative cost of the project by £4.4m. In the worst case scenario, the increase in indicative cost was approximately £6m. The analysis identified that there can be a discrepancies between unexpected stoppages or delays and the knock-on effect on total project duration and cost, due to the temporal variability of metocean conditions. In this case, a delay of about 15 days increased the total vessel duration of the project by 31.4 days. TDS models can be used to assess the sensitivity of the project to random failures or delays. Such unexpected stoppages and their effect on estimates of project duration are accounted for through the continuous updating of the starting point of recurrent simulations. However, the analysis has identified that the quantification of these random interruptions and their implementation within the TDS models need to be addressed.

The inadequate representation of operation durations in the simulation model is an example of the systematic errors that continuous project monitoring can help to identify. In this case, realised installation progress outperforming the best-case simulation projections led to the detailed analysis of recorded operation durations. The subsequent results showed significant discrepancies between the initial estimates and the mean values of operation duration observed in the first half of the offshore project. Most significantly, the mean duration required to complete a single WTG installation was 30% lower than initially specified. Implementing the updated operation input data in the model had a significant impact on the simulation results—there was a 10.8% reduction in the remaining project duration—and ensured a more accurate representation of the activities being simulated. This highlights the potential improvements in progress projections that can be achieved through iterative updating of simulation input data. If a source of operational data is available, applying TDS in this cyclical manner will yield continual improvements in the accuracy and reliability of simulation models and subsequent predictions of future progress.

The speed with which the simulations and subsequent analysis can be performed is one of the major advantages of TDS methods. In the industrial application discussed in this chapter, the entire process—from receipt of the most recent observations to the distribution of the weekly update results—took between 3–4 hours. This meant that critical planning and operational decisions were informed by simulation results modelled on the immediate status of operations. The newly-proposed *progress plots* proved well-suited for summarising progress to date, deviations from planned schedules and the results of the latest simulations each week.

PART III

After

Chapter 7

Operation Duration Analysis

7.1 Introduction

The three main input data requirements for time-domain Monte Carlo simulations of offshore projects are (*i*) an appropriate metocean time-series data-set, (*ii*) representative estimates of operation durations and (*iii*) the metocean thresholds for each operation. Input specifications for the rate of occurrence and duration of random, technical failures and unplanned events are also important but these are addressed separately in Chapter 9. Accurately incorporating the variability of operation durations is an essential requirement for producing realistic predictions of the range of likely project duration. This chapter aims to quantify the stochastic nature of task durations through the analysis of recorded operation data that have been obtained for a Round 3 offshore wind farm installation project. Specifically, the presence of a *learning curve* is assessed for each operation in the observed data-set and the effect of this learning phenomenon on the representation of operation durations within TDS is investigated. It should be noted that this chapter focuses on the analysis and quantification of the learning factor using observed operation data. Chapter 8 describes the implementation of a subsequent learning module within the time-domain simulation software and Chapter 10 assesses the impacts of incorporating this module.

Section 7.2 describes the theoretical background to the methods used throughout the analysis. Firstly, standard methods for fitting parametric probability distributions to sample data are described. Subsequently, the fundamental learning curve theory is introduced. Non-linear curve fitting methods are also discussed, before an applicable stochastic learning curve model is explained. A description of the raw data is given in Section 7.3, touching on the data extraction methods that were developed and some of the issues with this process. A preliminary assessment of the presence of learning is presented in Section 7.4 before the methodology for the full analysis is outlined in Section 7.5. Finally, the results of the full operation duration analysis are presented and discussed in Section 7.6, before the main conclusions are summarised in Section 7.7.

7.2 Theoretical Background

7.2.1 Distribution Fitting

Fitting parametric probability distributions to sample data is a common task in statistics that involves the selection of a specific probability distribution to model the random variable in question, as well as the identification of the parameter estimates for the chosen distribution. Model selection typically requires an iterative process of distribution choice, parameter estimation and quality of fit assessment. There are several common procedures for performing this iterative analysis, such as those outlined by Delignette-Muller *et al.* (2015) and Wilks (2011). The distribution fitting methodology in this chapter closely follows that recommended by Delignette-Muller *et al.* (2015).

Candidate Distributions

Typically, it is necessary to select a pre-defined list of appropriate candidate distributions before performing the parametric fitting procedure. If possible, the choice of candidate distributions should be guided by the knowledge of the stochastic process governing the modelled variable (Delignette-Muller *et al.*, 2015). Here, the modelled variable is the duration required to complete an offshore operation. As such, probability distributions must be left-bounded at a minimum value of 0 to be considered viable. In other words, the probability of negative instances of operation duration must be 0 for any appropriate candidate distribution.

Furthermore, the physical limits of the personnel performing the offshore operations, as well as the machinery and equipment employed, suggest that a minimum duration (> 0) exists for each operation. To account for this, the selected distributions are expressed in both their *variable location* and *fixed location* forms. The location parameter, a, of a distribution has the effect of translating, or shifting, the probability distribution function on the horizontal axis (Natrella, 2010; Forbes *et al.*, 2011). The *fixed location* form of the distribution fixes this location parameter to be equal to 0. The *variable location* form allows this parameter to vary (Jones *et al.*, 2001–).

It is common for a skewed, or asymmetric, distribution to have one tail of the distribution considerably longer or drawn out relative to the other tail (Natrella, 2010). A *right-skewed* distribution is one in which the tail is on the right side. Skewed data often occur due to lower or upper bounds on the data. Specifically, data that have a lower bound, such as the operation duration variable in this analysis, are typically skewed right (Natrella, 2010). It makes sense that a theoretical distribution chosen to model the amount of time taken to complete an offshore operation, typically requiring the use of some form of machinery, would have a minimum possible value (i.e. be *left-bounded*)

and a non-negligible probability of durations greater than the most common value (i.e. be a *right-skewed* distribution).

As such, appropriate candidate distributions for modelling the duration of offshore operations had to be left-bounded at a minimum value; eliminate the possibility of returning negative operation durations and have a skewed right-hand tail. Seven of the most common distributions that satisfied these assumptions were chosen and are shown in Table 7.1. For each of the selected distributions, there is a *variable location* form and a corresponding *fixed location* specified with the suffix -a_0. Consequently, a total of 14 probability distributions are tested throughout this analysis.

Table 7.1: Selected candidate distributions for the analysis of operation durations.

Variable location	*Fixed location*	*Reference(s)*
Burr	Burr-a_0	Burr (1942)
Exponential	Exponential-a_0	See statistics text e.g. Forbes *et al.* (2011)
Gamma	Gamma-a_0	See statistics text e.g. Forbes *et al.* (2011)
Loglogistic	Loglogistic-a_0	Jones *et al.* (2001–); Burr (1942)
Lognormal	Lognormal-a_0	See statistics text e.g. Forbes *et al.* (2011)
Pareto	Pareto-a_0	See statistics text e.g. Forbes *et al.* (2011)
Weibull	Weibull-a_0	See statistics text e.g. Forbes *et al.* (2011)

The Burr distribution refers to the Burr Type XII distribution, which is the twelfth cumulative distribution function (CDF) given by Burr (1942). The Loglogistic distribution is referred to as the Fisk distribution in economics and is a special case of the Burr Type XII distribution where the second shape parameter, k, is equal to 1 (Jones *et al.*, 2001–). The majority of distributions listed in Table 7.1 are explained in more detail in Chapter 8.

Maximum Likelihood Estimation

Maximum likelihood estimation (MLE) is a versatile method that is used to fit a parametric distribution to sample data. Wilks (2011) defines the likelihood as a measure of "the degree to which the data support particular values of the parameter(s)". A Bayesian interpretation defines the likelihood of a parameter value, given a data sample, as the probability of the data given the parameter value. The likelihood function is notationally similar to the probability density function (PDF) and the two are easily confused. For clarity, the PDF describes a function of the data for fixed values of the parameters, while the likelihood is a function of the unknown parameters for fixed values of the data (Wilks, 2011).

The likelihood function, $\mathcal{L}(\theta)$, is defined by Delignette-Muller *et al.* (2015) as:

$$\mathcal{L}(\theta) = \prod_{j=1}^{N} f(x_j|\theta)\,, \tag{7.1}$$

where x_j are the N observations of variable X, θ refers to the distribution parameters and $f(.|\theta)$ is the density function of the parametric distribution.

MLE seeks to identify the values of the distribution parameters that maximise the likelihood function. As such, the maximum likelihood estimators are the most probable values for the parameters, given the observed data (Wilks, 2011). It is generally more convenient to work with the logarithm of the likelihood function (termed the log-likelihood function) because this simplifies the mathematical differentiation procedures. Because the logarithm is a strictly increasing function, the same parameters will maximise both the likelihood and the log-likelihood functions (Wilks, 2011). The analysis in this chapter follows the convention of maximising the log-likelihood function.

There are many methods for maximising the log-likelihood function for a given data sample and probability distribution. The Nelder-Mead method (Nelder and Mead, 1965), also referred to as the downhill simplex method, is used throughout the analysis. The method is described in detail by Nelder and Mead (1965) and Wright (1996).

Graphical Assessment of Goodness-of-fit

Goodness-of-fit refers to the closeness of fitted distributions to underlying data. Graphical assessments of goodness-of-fit are important, even if formal goodness-of-fit tests are to be conducted, for verifying that the theoretical probability model provides an adequate description of the sample data. As opposed to a formal test, graphical comparisons of the fitted distribution and the data can help identify the specific nature of the problem and diagnose where and how the theoretical representation may be inadequate (Wilks, 2011).

Throughout this chapter, four classical goodness-of-fit plots are used (see, e.g. Cullen and Frey, 1999; Delignette-Muller *et al.*, 2015):

- a density plot comparing the histogram of the empirical distribution and the density function of the fitted distribution,
- a cumulative distribution function (CDF) of both the empirical distribution and the fitted distribution,
- a Q-Q plot of empirical quantiles against the theoretical quantiles and
- a P-P plot of the empirical distribution function at each data point against the fitted distribution function.

The density plot and the CDF plot are considered the classical goodness-of-fit plots. The Q-Q and P-P plots are complementary and can be very important in some cases; the Q-Q plot emphasises the lack-of-fit at the distribution tails, while the P-P plot emphasises the lack-of-fit at the centre of the distribution (Delignette-Muller *et al.*, 2015). The units of the x-axes of the density and CDF plots and both axes of the Q-Q plot are the same as the units of the data, which in this case is hours. All other axes are probabilities. The units of the axes for all the Q-Q plots presented in this thesis are the same. An example of the four goodness-of-fit plots is given in Figure 7.1.

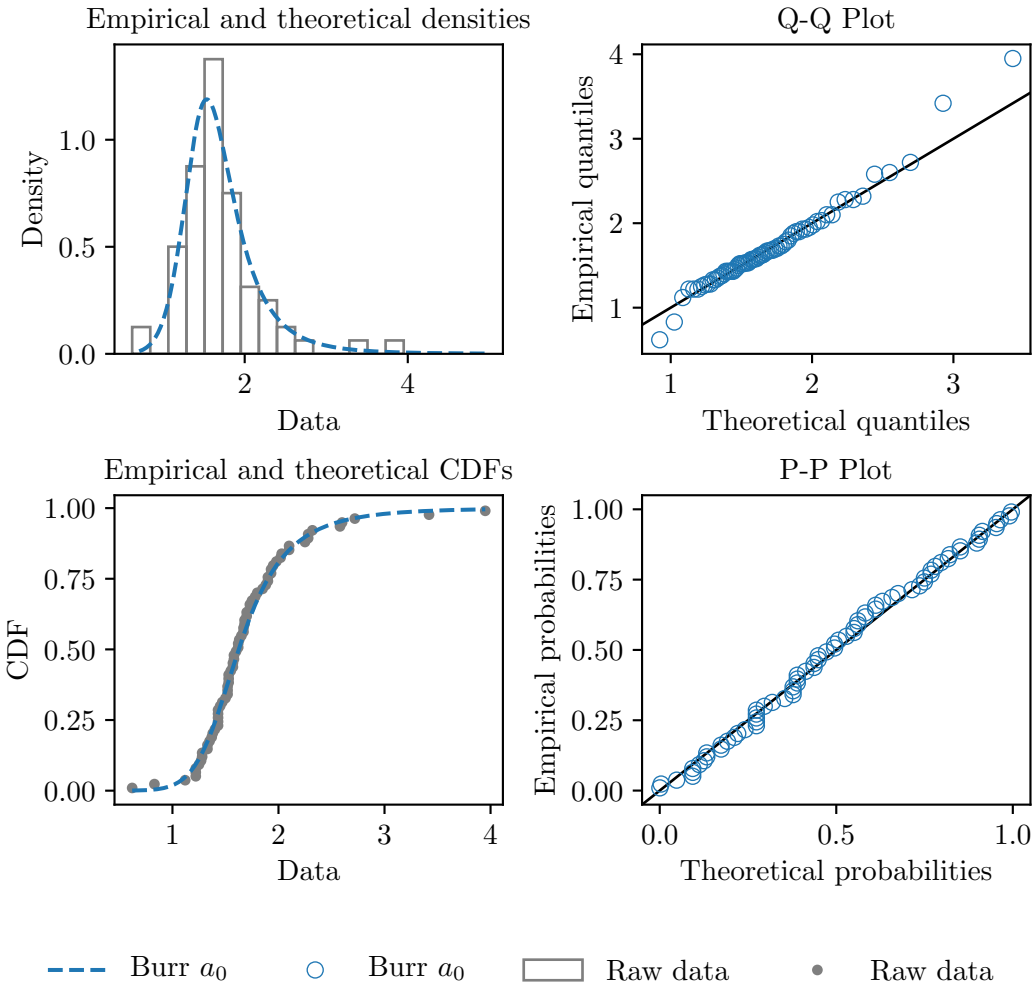

Figure 7.1: Fitted Burr-a_0 distribution for an example operation. The units of the x-axes of the density and CDF plots and both axes of the Q-Q plot are hours.

This figure shows a Burr-a_0 distribution fitted to the recorded duration data (in hours) for one of the operations in the installation campaign of the wind farm that is being analysed. The goodness-of-fit plot indicates an adequate fit for this operation. The density plot and the CDF plot show good agreement and the data follow the lines of

unit slope in the Q-Q and P-P plots. The example also shows the tendency of the Q-Q plot to accentuate the tails of the distribution.

For the CDF, Q-Q and P-P plots, the probability plotting position has been defined using Filliben's estimate (Filliben, 1975). For the histograms in the density plots, the bin width (or number of bins) is calculated as the maximum of the Sturges (Sturges, 1926; Scott, 2009) and Freedman-Diaconis (Freedman and Diaconis, 1981) estimators. This compromise avoids the conservative behaviour of Freedman-Diaconis and Sturges for small and large data-sets respectively. Both the probability plotting position and histogram bin width selection methods have been chosen as they are the recommended methods within the *SciPy* Python package (Jones *et al.*, 2001–), which has been used throughout the data analysis.

Goodness-of-fit Statistics

Formal, quantitative tests of goodness-of-fit statistics are proposed, in addition to the graphical methods described previously, to compare fitted distributions (Wilks, 2011; Delignette-Muller *et al.*, 2015). These goodness-of-fit statistics measure the distance between the fitted parametric distribution and the empirical distribution. Typically, three goodness-of-fit statistics are considered; Cramer-von Mises, Kolmogorov-Smirnov and Anderson-Darling (Delignette-Muller *et al.*, 2015).

The Anderson-Darling statistic is particularly suited for risk assessment as it equally emphasises the centre and tails of a distribution (Delignette-Muller *et al.*, 2015). For this reason, and as it is commonly used to select the best distribution among selected candidates (Delignette-Muller *et al.*, 2015), the Anderson-Darling statistic is used throughout the analysis. The computational formula for the Anderson-Darling statistic, as defined by D'Agostino and Stephens (1986) and Delignette-Muller *et al.* (2015), is

$$\text{A.D.} = -N - \frac{1}{N}\sum_{j=1}^{N}(2j-1)\log\left(F_j\left(1-F_{N+1-j}\right)\right), \tag{7.2}$$

where A.D. is the Anderson-Darling statistic, x_j are the N observations of the continuous variable X arranged in ascending order and $F_j \triangleq F(x_j)$ is the fitted cumulative distribution function evaluated at x_j.

The Anderson-Darling statistic, as well as the other two statistics mentioned above, do not consider the number of parameters of the distribution—termed the *complexity* of a model. Thus, these statistics can systematically promote the selection of more complex distributions (Delignette-Muller *et al.*, 2015). Two classical penalty-based criteria based on the log-likelihood are recommended to account for these issues; the Akaike information criterion (AIC) (Akaike, 1974) and the Bayesian information criterion (BIC)

(Schwarz, 1978). These two criteria are not considered in the main methodology due to the importance of the *location* parameter mentioned previously. The AIC and BIC could continually promote the *fixed location* form of a distribution over the *variable location* form. This would contradict the previously-stated hypothesis regarding the nature of the random variable being analysed—that there is a minimum duration (> 0) associated with each operation.

However, the penalty-based criteria are useful when comparing two *distinct* distributions. For one of the example results discussed in Section 7.6.1, the BIC was used as an additional comparative measure. The formula for the BIC given by Schwarz (1978) is

$$\mathrm{BIC} = \log(N)K - 2\log(\hat{\mathcal{L}})\,, \tag{7.3}$$

where $\hat{\mathcal{L}}$ is the maximised value of the likelihood function, K is the number of parameters estimated by the model and N is the number of observations in the sample.

7.2.2 Learning Curves

Background

A learning curve (LC) is a mathematical description of workers' performance in repetitive tasks. As repetitions take place, workers tend to demand less time to perform tasks due to familiarity with the operation and tools, and because shortcuts to task execution are found (see, e.g. Anzanello and Fogliatto, 2011). Alternatively, the LC can be defined as a model of the continual reduction in unit cost or labour that occurs with increasing cumulative production (Vigil and Sarper, 1994). Crucially, the theory assumes that the task is identical for each repetition that takes place.

The theory of the LC was first proposed by Wright (1936) who observed how the assembly cost of aeroplanes decreased as repetitions were performed. Wright (1936) noted that as the quantity of units manufactured doubles, the number of labour hours required to produce a single unit decreases at a constant rate (Yelle, 1979). Wright's model, also referred to as the "Log-linear Model", the related Crawford model (Crawford, 1944) and their modifications are still the most tested and validated models available today (see, e.g. Yelle, 1979; Tilindis and Kleiza, 2017).

Classical Learning Curve Models

There is a subtle but significant difference between the two classical LC models. Wright's model describes the reduction in cumulative average duration, while Crawford's model describes the reduction in unit duration. As such, both models have the common mathematical form (see Anzanello and Fogliatto, 2011);

$$y = C_1 s^m \,, \tag{7.4}$$

where C_1 is the time to produce the first unit and m is the slope of the LC on a log-scale ($-1 < m < 0$), referred to as the learning slope. In Wright's model, y is the average time of all units produced up to the s^{th} unit. In Crawford's model, y is the processing time of the s^{th} unit (see Tilindis and Kleiza, 2017).

As outlined by Anzanello and Fogliatto (2011), Wright's model can be modified to obtain an equation for the total time to produce s units, y_t, as follows:

$$\begin{aligned} & y_t = ys \,, \\ \implies & y_t = C_1 s^{m+1} \,. \end{aligned} \tag{7.5}$$

Subsequently, a transformation equation for the unit duration based on Wright's cumulative model, y_u, can be obtained:

$$\begin{aligned} & y_u = y_t - y_{t-1} \,, \\ \implies & y_u = C_1 s^{m+1} - C_1 (s-1)^{m+1} \,, \\ \implies & y_u = C_1 [s^{m+1} - (s-1)^{m+1}] \,. \end{aligned} \tag{7.6}$$

In log-linear form, Equation 7.4 can be written as

$$\ln y = \ln C_1 + m \ln s \,. \tag{7.7}$$

The learning rate, ϕ, is the percentage of y labour hours required to produce unit $2s$. Thus, letting

$$\begin{aligned} y_{s_1} &= C_1 {s_1}^m \,, \\ y_{s_2} &= C_1 {s_2}^m \end{aligned}$$

and

$$s_2 = 2s_1 \,,$$

the learning rate, ϕ, becomes

$$\begin{aligned}\phi &= \frac{y_{s_2}}{y_{s_1}}\,,\\ \phi &= \left(\frac{s_2}{s_1}\right)^m\,,\\ \phi &= 2^m\,. \end{aligned} \tag{7.8}$$

Subsequently,

$$m = \frac{\ln \phi}{\ln 2}\,. \tag{7.9}$$

As cumulative production doubles, the time required to produce a unit is reduced by a constant percentage, known as the progress ratio, L, defined as

$$L = 1 - \phi\,. \tag{7.10}$$

Modified Models

Several modifications to the basic mathematical form exist. A thorough description of the most important of these modifications is given by Anzanello and Fogliatto (2011). The most common log-linear model modifications are summarised here.

The Stanford-B model incorporates workers' prior experience, represented by the parameter B:

$$y = C_1(s + B)^m\,. \tag{7.11}$$

DeJong's model incorporates an 'incompressibility factor', M, that describes the fraction of the task executed by machinery ($0 \leq M \leq 1$):

$$y = C_1[M + (1 - M)s^m]\,. \tag{7.12}$$

The S-curve model resulted from merging DeJong's and Stanford-B's models:

$$y = C_1[M + (1 - M)(s + B)^m]\,. \tag{7.13}$$

Finally, the Plateau model introduces an additive constant C that describes the steady-state performance:

$$y = C + C_1 s^m\,. \tag{7.14}$$

Figure 7.2 gives a comparison of the LC profiles generated by the models described above. This figure has been generated using the following parameters;

$$C_1 = 200\,,$$
$$m = -0.5\,,$$
$$B = 5\,,$$
$$M = 0.1$$

and

$$C = 50\,.$$

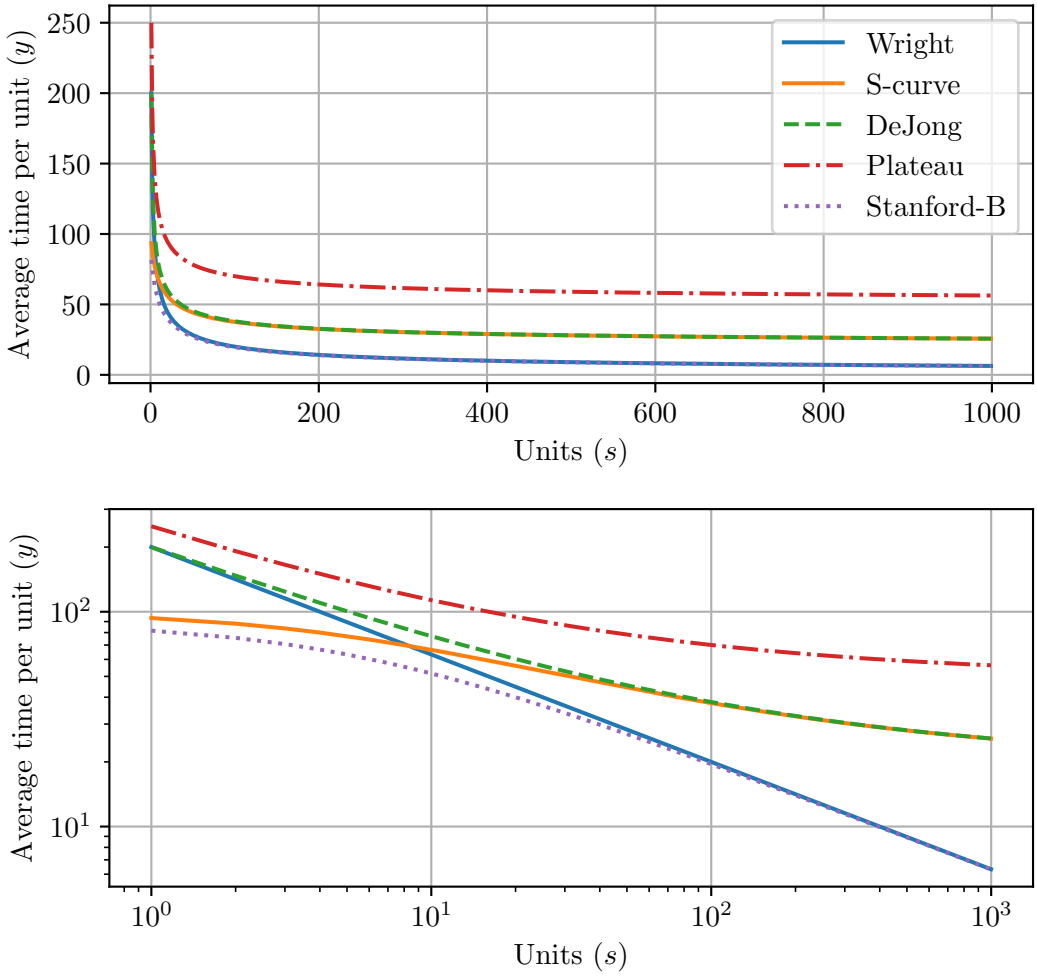

Figure 7.2: Example comparison of log-linear learning curve models.

The linear relationship of Wright's model is evident when plotted on a log-scale as

in the bottom panel of Figure 7.2. The effect of prior experience can be seen in the early stages of learning for the Stanford-B model. The benefits of previous experience diminish as more units are produced and the Stanford-B model approximates Wright's model.

The important concept of steady-state performance can be seen in the Plateau model. For offshore operations, it is clear that there will be some minimum time to complete each operation. In the DeJong model, it is assumed that no learning will take place for the portion of the task that is executed by machinery. As such, the DeJong model, as well as the related S-Curve model, also 'plateau' at a level corresponding to the fraction of work performed by machinery.

7.2.3 Learning Curve Model Fitting

Non-linear Least Squares

When fitting a LC to observed data, the LC parameters can be estimated through a non-linear optimization routine aimed at minimising the sum of squares error (see, e.g. Anzanello and Fogliatto, 2011). Linear regression is a method for analysing data described by models which are linear in the parameters, whereas non-linear regression refers to models that are non-linear in the parameters (see, e.g. Bates and Watts, 1988).

The standard non-linear regression model, as defined by Ruckstuhl (2010); Bates and Watts (1988); Baty *et al.* (2015), is of the form

$$y_i = f(x_i; \theta_v) + \epsilon\,, \quad \epsilon \sim \mathcal{N}(0, \sigma^2)\,, \tag{7.15}$$

with y_i as the response (dependent variable), x_i as the independent variable, θ_v as the vector of model parameters characterising the relationship between x and y through the expectation function f and ϵ as the residual error term that is assumed to be normally distributed, centred around 0 and with unknown variance (σ^2). Non-linear models are defined as those where at least one of the derivatives of the expectation function, with respect to the *parameters*, depends on at least one of the parameters (Bates and Watts, 1988).

As is the case for linear regression calculations, the principle of least squares is applied to get estimates for the parameters θ_v. The sum of the squared deviations

$$S(\theta_v) := \sum_{i=1}^{N} (y_i - \eta_i(\theta_v))^2\,, \quad \text{with } \eta_i(\theta_v) := f(x_i; \theta_v)\,, \tag{7.16}$$

should thus be minimised (Ruckstuhl, 2010; Bates and Watts, 1988; Baty *et al.*, 2015). Replacing $f(x_i; \theta_v)$ with $\eta_i(\theta_v)$ is reasonable as $[x_i, y_i]$ is given by the measurement

or observation of the data and only the parameters (θ_v) remain to be determined (Ruckstuhl, 2010).

For non-linear regression, the minimum of the squared sum $S(\theta_v)$, and thus the estimation, cannot be given explicitly as in linear regression; iterative numeric procedures are required (Ruckstuhl, 2010). The Gauss-Newton Algorithm (see Ruckstuhl, 2010; Bates and Watts, 1988) is used throughout this analysis when performing the non-linear optimisation. This iterative algorithm uses a linear approximation to the expectation function to improve continually an initial guess for the parameters (Bates and Watts, 1988).

The initial parameter estimates are crucial for non-linear regression and need to be relatively close to the unknown parameters to avoid convergence problems (Anzanello and Fogliatto, 2011; Baty *et al.*, 2015). For the basic LC model, as defined in Equation 7.4, a sensible estimate for C_1 is the recorded operation duration of the first unit. Furthermore, the slope of the LC is defined on $-1 < m < 0$ and thus an initial parameter of -0.5 is reasonable. By selecting the initial parameter estimates as above, convergence issues should be avoided.

Assessment of LC Model Fit

Several authors have made use of the coefficient of determination (R^2) as an assessment of a non-linear model's goodness-of-fit (see Anzanello and Fogliatto, 2011). However, it has long been known within the mathematical literature that the coefficient of determination is an inadequate measure for the goodness-of-fit in non-linear models (Spiess and Neumeyer, 2010).

Instead, the goodness-of-fit is assessed as recommended by Baty *et al.* (2015). Firstly, the fit is inspected graphically by comparing the fitted curve to the raw data and ensuring the results are sensible. As well as the best-fit curve, *confidence bands* and *prediction bands* are calculated and shown on the plot. Confidence bands indicate the location of the ideal function values and thus the expected learning curve parameters. Prediction bands indicate the regions where future observations will lie. In other words, prediction bands take into account not only the uncertainty of the true position of the LC, as for the confidence bands, but also the random error, or scatter, around the curve (Ruckstuhl, 2010). The methods for approximating the confidence and prediction bands outlined by Bates and Watts (1988) and Ruckstuhl (2010) are used in this analysis. Examples of confidence and prediction bands can be found throughout the results section of this chapter (e.g. see Figure 7.8).

In addition to the graphical methods above, 95% t-based confidence intervals (CIs) are calculated for the parameters. The related t-test statistics for evaluating the null

hypothesis that the model parameters are equal to 0, along with the corresponding p values calculated using a t-distribution as a reference, are also used to assess the LC model fit. More information on these methods is provided by, for example, Baty *et al.* (2015). For the basic LC model defined in Equation 7.4, the slope of the LC, m, is of primary concern. If the hypothesis test fails to reject the null hypothesis that $m = 0$, this shows that at the assumed significance level, α, the test fails to show that there is learning present.

7.2.4 Stochastic Learning Curve Model

Contrary to the majority of LC models, in which learning is treated as a deterministic phenomenon, Globerson and Gold (1997) address the stochastic nature of learning and treat it as a random process. It is argued that ignoring the randomness of the process will introduce significant errors to the model. This section summarises the methods proposed by Globerson and Gold (1997), who developed analytic expressions for the expected value, variance, coefficient of variation and probability density function (PDF) of the process as a function of the task repetition number.

Statistical Analysis of the LC Model

The analysis starts with the following equation:

$$y_s = y_1 s^m \,, \tag{7.17}$$

which is identical in form to Equation 7.4, but is stochastic in nature. The factor y_1 is defined as the *performance time* of the first iteration. *Performance time* is equivalent to the previously mentioned unit duration, y, in Crawford's LC model. Here, it is a random variable with:

$$\begin{aligned} \mathrm{E}[y_1] &= \text{the expected value of } y_1 \,, \\ {\sigma_{y_1}}^2 = \mathrm{Var}[y_1] &= \text{the variance of } y_1 \,, \\ \mathrm{CV}_{y_1} = \frac{\sigma_{y_1}}{\mathrm{E}[y_1]} &= \text{the coefficient of variation of } y_1 \text{ and} \\ f_{y_1}(y_1) &= \text{the PDF of } y_1 \,. \end{aligned}$$

The parameter y_s is defined as the *performance time* of the s^{th} iteration and is a random variable with:

$$\begin{aligned} \mathrm{E}[y_s] &= \text{the expected value of } y_s\,, \\ {\sigma_{y_s}}^2 = \mathrm{Var}[y_s] &= \text{the variance of } y_s\,, \\ \mathrm{CV}_{y_s} = \frac{\sigma_{y_s}}{\mathrm{E}[y_s]} &= \text{the coefficient of variation of } y_s \text{ and} \\ f_{y_s}(y_s) &= \text{the PDF of } y_s\,. \end{aligned}$$

As before, s refers to the unit number and the parameter m is the slope of the LC, also referred to as the *parameter of reduction*. Although the parameter of reduction is a random variable, Globerson and Gold (1997) assume that it is deterministic. This does not eliminate the deviation of the parameter, but merely adds it to the deviation of y_s.

Using Equation 7.17 together with standard rules for the expected value and variance of a random variable, it follows that:

$$\mathrm{E}[y_s] = \mathrm{E}[y_1 s^m] = \mathrm{E}[y_1] s^m \tag{7.18}$$

and

$$\mathrm{Var}[y_s] = \mathrm{Var}[y_1 s^m] = \mathrm{Var}[y_1](s^m)^2 \tag{7.19}$$

or

$${\sigma_{y_s}}^2 = {\sigma_{y_1}}^2 (s^{2m})\,. \tag{7.20}$$

Consequently,

$$\sigma_{y_s} = \sigma_{y_1} s^m\,. \tag{7.21}$$

The coefficient of variation of y_s, CV_{y_s}, is found by substituting Equation 7.18 and Equation 7.21 into the definition for the coefficient of variation:

$$\mathrm{CV}_{y_s} = \frac{\sigma_{y_s}}{\mathrm{E}[y_s]} = \frac{\sigma_{y_1} s^m}{\mathrm{E}[y_1] s^m} = \frac{\sigma_{y_1}}{\mathrm{E}[y_1]} = \mathrm{CV}_{y_1}\,. \tag{7.22}$$

This means that the coefficient of variation around the learning curve is constant and equal to the coefficient of variation around the first cycle (Globerson and Gold, 1997).

Probability Density Function Expression

The derivation of an exact expression for the PDF as a function of the number of repetitions of a task requires the use of a fundamental theorem proposed by Papoulis (1965). When a function $g(x)$ is performed on a random variable x, the random variable $y = g(x)$ is created. The random variable y is defined indirectly by the random variable x and the function $g(x)$. In this case, the aim is to find the probability density function of y, given the probability density function of x and the function $g(x)$.

The fundamental theorem given by Papoulis (1965) states that if the n_r real roots of $y = g(x)$ are denoted by x_i,

$$y = g(x_i)\,, \quad i = 1\,, 2\,, \ldots\,, n_r\,, \tag{7.23}$$

it follows that

$$f_y(y) = \sum_{i=1}^{n} \frac{f_x(x_i)}{|g'(x_i)|}\,, \tag{7.24}$$

where $g'(x)$ is the derivative of $g(x)$.

Relating the above theorem to Equation 7.17,

$$y_s = g(y_1) = y_1 s^m\,, \tag{7.25}$$

$$f_{y_s}(y_s) \equiv f_y(y) \text{ and} \tag{7.26}$$

$$f_{y_1}(.) \equiv f_x(.)\,. \tag{7.27}$$

As Equation 7.17 has a single solution for every y_s, it can be re-written as

$$y_1 = y_s s^{-m}\,. \tag{7.28}$$

The derivative of $g(y_1)$ is

$$g'(y_1) = s^m\,. \tag{7.29}$$

Using the fundamental theorem from Equation 7.24:

$$f_{y_s}(y_s) = \frac{f_{y_1}(y_s s^{-m})}{s^m} = s^{-m} f_{y_1}(y_s s^{-m})\,. \tag{7.30}$$

As described by Globerson and Gold (1997), Equation 7.30 implies that as the factor s^{-m} increases (as more repetitions are completed), the probability density function "shrinks" on the duration axis and its peak reaches a higher value on the probability axis.

Validation for Normal Distribution

A useful validation of the theory applied to data that follow a normal distribution, as summarised by Globerson and Gold (1997), is described in full here. Assuming that y_1 is normally distributed with $y_1 \sim \mathcal{N}(\mu_1, {\sigma_1}^2)$, then the PDF of y_1, as defined by Wilks (2011), is

$$f_{y_1}(y_1) = \frac{1}{\sqrt{2\pi{\sigma_1}^2}}\, e^{-\dfrac{(y_1-\mu_1)^2}{2{\sigma_1}^2}} . \tag{7.31}$$

Equation 7.30 can be used to obtain an expression for the PDF of y_s:

$$f_{y_s}(y_s) = s^{-m}\frac{1}{\sqrt{2\pi{\sigma_1}^2}}\, e^{-\dfrac{(y_s s^{-m}-\mu_1)^2}{2{\sigma_1}^2}} , \tag{7.32}$$

$$= \frac{1}{\sqrt{2\pi{\sigma_1}^2 s^{2m}}}\, e^{-\dfrac{({y_s}^2 s^{-2m} - 2y_s s^{-m}\mu_1 + {\mu_1}^2)}{2{\sigma_1}^2}} . \tag{7.33}$$

Focusing on the exponent of the exponential:

$$\begin{aligned}\frac{({y_s}^2 s^{-2m} - 2y_s s^{-m}\mu_1 + {\mu_1}^2)}{2{\sigma_1}^2} &\equiv \frac{({y_s}^2 s^{-2m} - 2y_s s^{-m}\mu_1 + {\mu_1}^2)}{2{\sigma_1}^2}\,\frac{s^{2m}}{s^{2m}} ,\\ &= \frac{{y_s}^2 - 2y_s s^m\mu_1 + {\mu_1}^2 s^{2m}}{2{\sigma_1}^2 s^{2m}} ,\\ &= \frac{(y_s - s^m\mu_1)^2}{2{\sigma_1}^2 s^{2m}} .\end{aligned}$$

Returning to Equation 7.33,

$$f_{y_s}(y_s) = \frac{1}{\sqrt{2\pi{\sigma_1}^2 s^{2m}}}\, e^{-\dfrac{(y_s - s^m\mu_1)^2}{2{\sigma_1}^2 s^{2m}}} . \tag{7.34}$$

Comparing Equation 7.34 to the PDF of y_s with $y_s \sim \mathcal{N}(\mu_s, {\sigma_s}^2)$,

$$f_{y_s}(y_s) = \frac{1}{\sqrt{2\pi{\sigma_s}^2}}\, e^{-\dfrac{(y_s-\mu_s)^2}{2{\sigma_s}^2}} , \tag{7.35}$$

it is clear that

$${\sigma_s}^2 = {\sigma_1}^2 s^{2m} , \tag{7.36}$$

$$\sigma_s = \sigma_1 s^m \tag{7.37}$$

and

$$\mu_s = \mu_1 s^m \,. \tag{7.38}$$

Therefore, the "nature" of the PDF remains the same over the entire learning curve. Figure 7.3 shows an example of the stochastic LC model for a normal distribution with $\mu_1 = 3.5$, $\sigma_1 = 1$ and $m = -0.5$, for the first four iterations of a task ($s = [1, 2, 3, 4]$). These figures show that as the number of repetitions of the task increase, both the mean and variance of the distribution decrease. In other words, the average task duration decreases and the probability of that duration occurring increases—the PDF becomes 'peakier'.

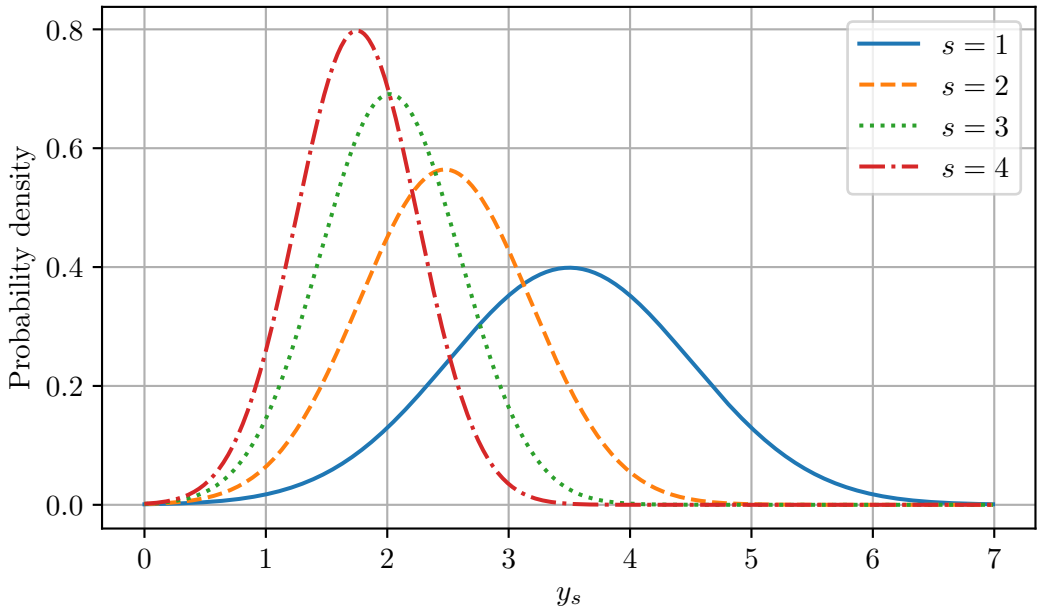

Figure 7.3: Stochastic LC example for normal distribution.

Estimating Statistical Characteristics

To use the method described in the previous section, the statistical characteristics (the PDF, expected value, variance and coefficient of variation) need to be estimated. Globerson and Gold (1997) outline two methods to do this; one for the *multiple data-set* model and one for the *single data-set* model.

Multiple data-sets are generated when several organisational systems, or individuals, work independently on identical products. These means there are multiple data-points

available for each repetition of the task. In this case, standard probability distribution fitting methods can be used to obtain the distribution for each repetition.

However, organisations and individuals often work on just a single item at a time, meaning that there is only one data point for each repetition (Globerson and Gold, 1997). As this is the case for the analysis of offshore operation durations, the transformation methods outlined by Globerson and Gold (1997) are required.

To derive the transformation equation used by Globerson and Gold (1997), first assume that a LC has been fitted to sample data and the parameter m has been determined. Then consider the recorded data point at operation iteration n that has a duration of y_n. Assuming that the learning slope m remains constant, it follows that

$$y_n = C_{n\to 1} n^m \,,$$

where $C_{n\to 1}$ is the duration of the n^{th} unit transformed to $s = 1$.

Subsequently, the operation duration transformed to an arbitrary cycle number κ is

$$\begin{aligned} y_{n\to\kappa} &= C_{n\to 1}\kappa^m = \frac{y_n}{n^m}\kappa^m \,, \\ \implies y_{n\to\kappa} &= y_n \left(\frac{\kappa}{n}\right)^m \,, \quad n = 1\,, 2\,, \ldots\,, N\,, \end{aligned} \tag{7.39}$$

where N is the number of recorded data points.

The transformation method is illustrated in Figure 7.4. The mathematical manipulations generate a distribution around the κ^{th} cycle, which enables the calculation of the required statistical parameters.

There are four steps required to estimate the statistical characteristics for the single data-set model:

1. Determine the learning slope parameter m using standard curve fitting techniques on the recorded data points. (Note that Globerson and Gold (1997) propose the use of linear regression applied to the logarithm of the data for this step. Ruckstuhl (2010) warns that a linearisation of the regression function can introduce significant errors to the model. Consequently, the analysis in this chapter applies the non-linear least square methods described previously.)
2. Transform the data to an arbitrary cycle number, κ, using Equation 7.39.
3. Determine the expected value, variance and coefficient of variation of the transformed data-set.
4. Fit a suitable probability density function to the transformed data-set. This step is performed using the methods described in Section 7.2.1.

Once these statistical characteristics have been estimated for the chosen κ, the charac-

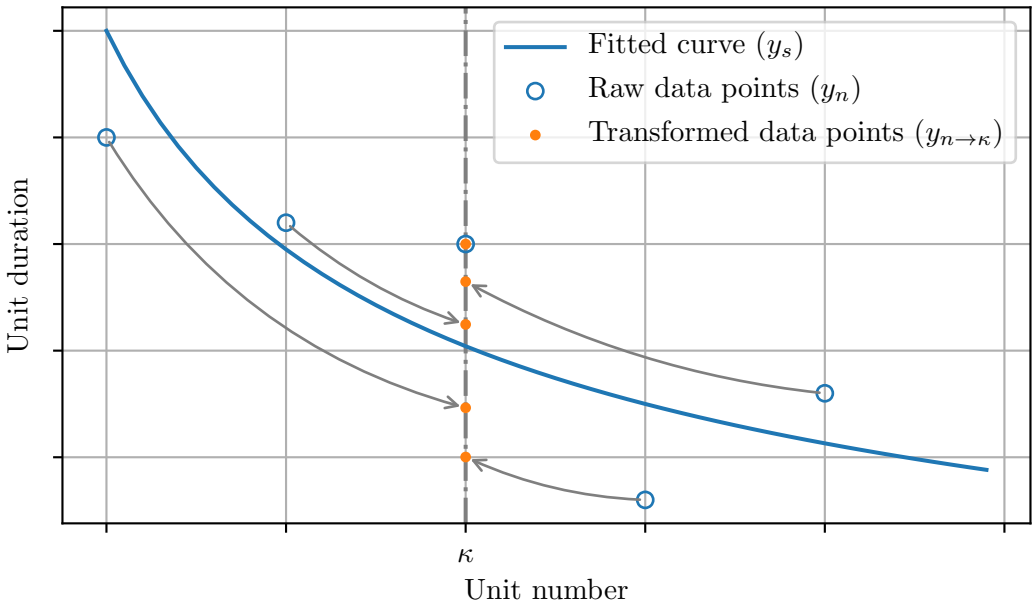

Figure 7.4: Transformation method for operation durations.

teristics for any arbitrary unit number, s, can be calculated.

7.3 Description of Raw Data

7.3.1 Data Extraction

Raw operation duration data was provided in the form of daily progress reports (DPRs) that detail the exact durations of the offshore operations completed on a given day by a specific vessel. Each DPR was provided in Extensible Markup Language (XML) file format. A Python script was created that extracted the operation duration data from each XML file and saved the data from all the reports to a single Comma Separated Variable (CSV) file. This process of retrieving data from unstructured data sources for further data processing is known as *data extraction*.

7.3.2 Miscellaneous Operations

Ambiguity in the categorisation of certain operations in the recorded data-set complicated the data collation process. These *miscellaneous* operations were either categorised under alternative headings or excluded entirely in particular DPRs. For example, there is evidence for four operations that were completed at the end of the loadout activity and before departing port for the wind farm; “Preparing to leave”, “Sea-fastening”,

"Fix cranes" and "Recover gangway". Sometimes all four of these operation durations were recorded, on other occasions the "Preparing to leave" operation was omitted and frequently "Preparing to leave" was the only operation that was recorded. To ensure consistency in the analysis, these four operations were combined into a single "Prepare to leave" operation by summing any of the four operations that were recorded in the DPRs. The summation of these operations introduces an averaging effect and ignores the variation within the individual operations that would ideally be categorised independently. However, this categorisation was considered the most appropriate for analysing the incomplete data-sets of the individual operations.

Several groups of operations had to be combined in this manner but each of these operations was similar to the example described above, with durations in the order of 1–2 hours. All of the critical operations, such as the installation of blades, towers and nacelles, were appropriately documented. As such, any errors introduced by combining groups of operations in this manner are expected to be insignificant.

To avoid this problem in the future, a systematic procedure for recording operation duration data is recommended. Enforcing a strict electronic template, for example a simple spreadsheet in which the operations are selected from a drop-down menu rather than manually typed, removes the possibility of ambiguity in the documentation of operation duration data and ensures accurate measurements. These changes would significantly improve the efficiency, ease and accuracy of the analysis methods discussed in this chapter, thus enhancing the representation of operation durations in time-domain simulations and the ensuing results.

Presumably, such a system already exists in industry—a similar procedure may even have been configured for the construction project in question—and the problem is with the implementation and enforcement of the recording processes. In this case, the recommendation is to focus on the adoption of these systems by the relevant personnel, through a combination of improved training, communication and regulation.

7.3.3 Categorising Data

The data in the DPRs included weather downtime and technical downtime. Weather downtime refers to any periods where operations had to be paused as a result of the limiting metocean conditions. Technical downtime, which is discussed in detail in Chapter 9, refers to any unexpected downtime that arises independently of the metocean conditions. For example, this includes downtime due to the mechanical failure of a critical piece of installation equipment or machinery. The *operational* components of the data were extracted by omitting instances of weather downtime and technical downtime.

Two vessels were used in the installation campaign. Although these vessels were identical in terms of their performance characteristics, it was important to categorise the data by vessel because the LC theory pertains to the personnel carrying out the task and assumes that there is no learning phenomenon associated with machinery.

To reflect the representation of the project in the simulation software, the tasks in the DPRs were categorised into major *activities*, each comprising several *operations*. Namely, the installation campaign was categorised into loadout, transit and WTG installation activities.

The sample size for each operation in the data-set can vary. The first reason for this is due to the uneven split of the total number of WTGs between the two vessels; the *Baseline vessel* (see Chapter 5) installed 62.1% of the total number of turbines and *Vessel B* installed the remainder. Secondly, the DPRs recorded the majority of loadout operations as the time to load all of the turbine components for that particular cycle. For example, the time taken to load the nacelles on to the vessel was categorised as the total time to load all 8 nacelles as opposed to the individual loading time for each nacelle. Thirdly, the cyclical nature of the installation procedure naturally affects the number of repetitions of certain operations. For example, the vessels only have to perform several loadout operations but numerous WTG installations. It was possible to group each data-set into one of two categories based on its sample size; none of the operations had sample sizes between 9 and 38. Thus, a *small sample* was defined that includes all data-sets with less than 9 observed durations and a *large sample* was defined that includes data-sets with 38 or more samples.

7.4 Preliminary Analysis

Initial investigations analysed the duration data of the WTG installation *activity* to assess the presence of learning. The total time to complete each WTG was obtained by summing the durations of the individual operations that comprise this activity. Best-fit LCs for both the unit duration (Crawford's model) and the cumulative average duration (Wright's model) of this activity were obtained using the Gauss-Newton Algorithm discussed in Section 7.2.3 to perform the non-linear curve fitting.

The results are shown in Figure 7.5 for the Baseline vessel and in Figure 7.6 for Vessel B. Data have been normalised with respect to the maximum installation time recorded for each vessel. Both figures clearly show that learning is an observable phenomenon for the WTG installation activity. The stochastic nature of the learning phenomenon is evident in both figures, particularly the scatter of the unit duration data around the Crawford model fits, but the general trend is clear.

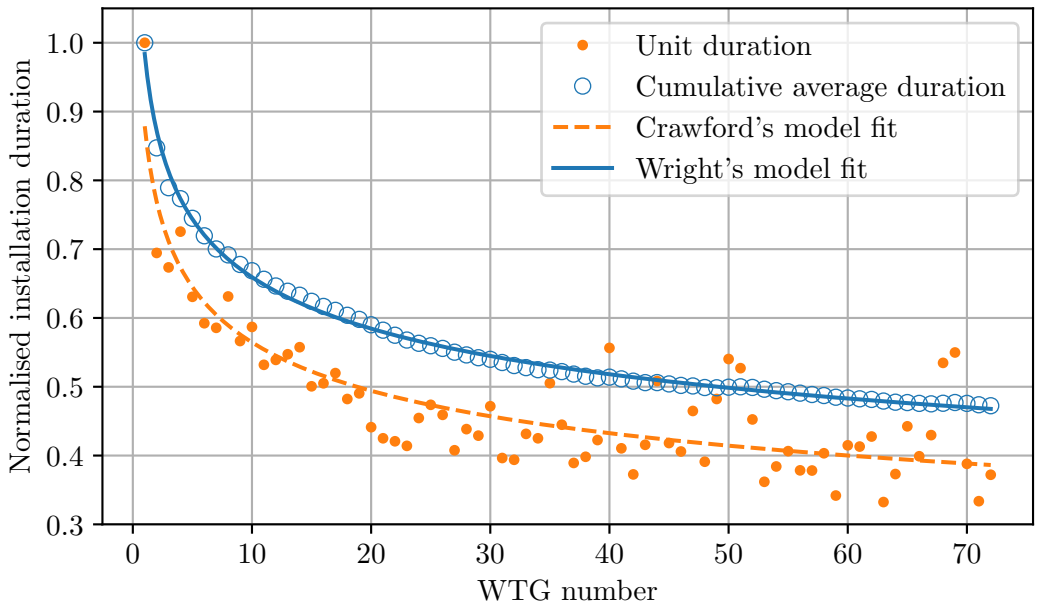

Figure 7.5: Learning curves for WTG installation activity comparing the raw data to both Crawford's and Wright's best-fit models—Baseline vessel.

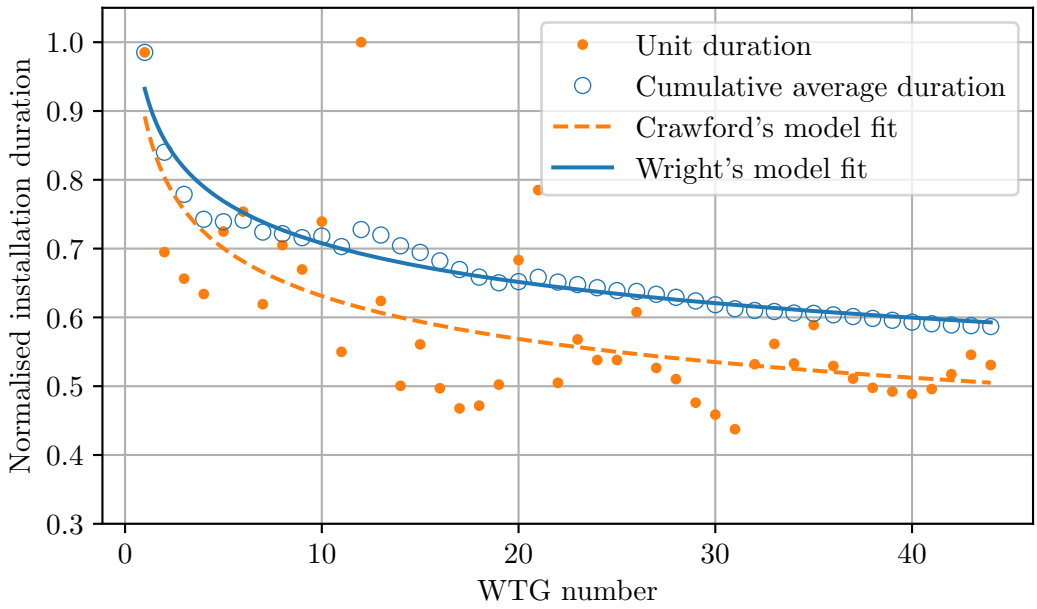

Figure 7.6: Learning curves for WTG installation activity comparing the raw data to both Crawford's and Wright's best-fit models—Vessel B.

For Vessel B, the normalised installation duration for WTG number 12 is significantly removed from the LC model fit. Further investigation of the raw data identified that the durations required to jack-up and jack-down at this specific turbine were far greater than the average time to complete these operations. This may have been because the sea floor conditions at this particular turbine made it more difficult to achieve a secure connection during jacking operations. The prevailing tidal current conditions when performing these operations may have also affected the activity durations.

Grouping the individual operations that comprise an activity introduces an averaging effect to the analysis. The extremely good fit between the cumulative average duration data and the best-fit Wright LC for both vessels, particularly the baseline vessel, is explained by the fact that it is the cumulative average of data that has essentially already been averaged through this grouping process. Nonetheless, the preliminary results demonstrate clear evidence of learning and encourage further investigation.

7.5 Methodology

The main objective of this chapter is to determine the presence of learning and identify the most appropriate probability distribution for each operation in the observed dataset. The flowchart in Figure 7.7 summarises the key components of the methodology.

7.5.1 Non-linear Curve Fitting and Determination of Learning

The Crawford model, relating to the unit duration of the raw data, is used in the analysis because this is the method recommended in the stochastic LC model proposed by Globerson and Gold (1997). As per the analysis of the WTG installation activities in Section 7.4, the Gauss-Newton Algorithm was used to perform the non-linear curve fitting. The assessment of the LC model fits follows the methods described in Section 7.2.3 and is summarised again here.

The fit is assessed graphically by comparing the fitted curve to the raw data, as well as showing the 95% confidence and prediction bands. The t-based 95% confidence intervals for the LC parameters are also calculated. Crucially, the t-test statistics for evaluating the null hypothesis that the learning slope m is equal to 0 and the corresponding p value are calculated. The presence of learning is assessed at a standard significance level of $\alpha = 0.05$, although this selection is addressed in more detail in Section 7.6.1.

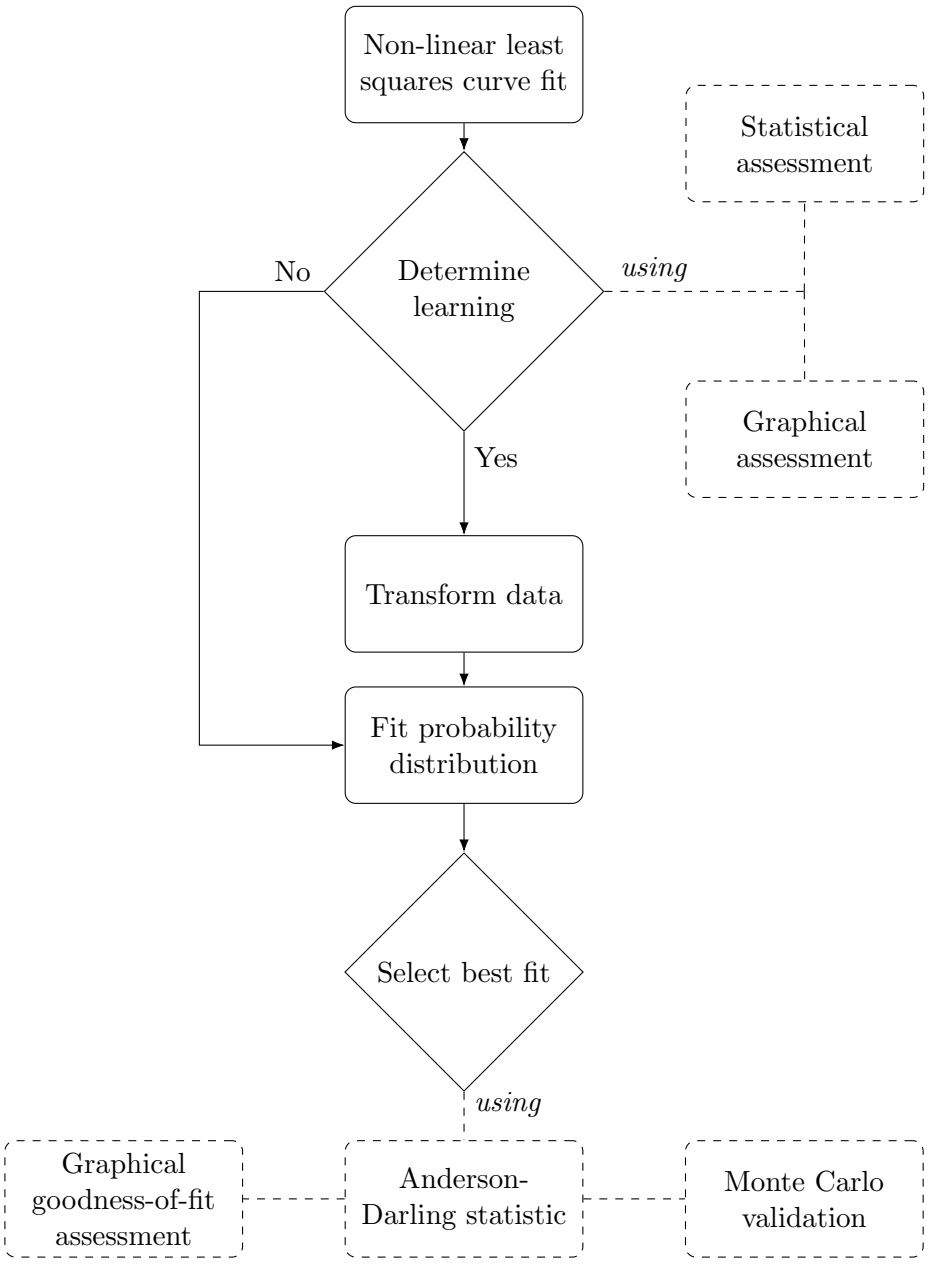

Figure 7.7: Methodology for the analysis of operation durations and determination of learning. The dashed components of the flow chart represent the individual methods contained within the 'determine learning' and 'select best fit' decision blocks, as discussed in Sections 7.5.1 and 7.5.2 respectively.

7.5.2 Probability Distribution Fitting and Best-fit Selection

The probability distribution fitting procedure is only performed for the large sample ($N > 38$) because the small sample size ($N < 9$) was inadequate for the application of the distribution fitting methods. The method of maximum likelihood estimation (MLE), as described in Section 7.2.1, was used to fit the probability distributions to the sample data for each of the 14 candidate distributions.

The first step required in selecting the most appropriate probability distribution was to remove any of the fitted distributions that resulted in a negative location parameter. As discussed previously, any distribution that can produce negative operation durations should be omitted. For each of the fitted distributions in this new subset of results, the Anderson-Darling statistic was calculated using Equation 7.2. The three distributions that resulted in the lowest values for the Anderson-Darling statistic were selected for further investigation. A graphical assessment of these three fitted distributions was performed, using the classical goodness-of-fit plots described in Section 7.2.1, to verify that the theoretical distribution was adequate.

7.5.3 Monte Carlo Validation

The final method for determining the best-fit distribution consisted of a Monte Carlo validation procedure. The purpose of this procedure was to ensure that both the centre and spread of the results obtained using the sampling methods were appropriate. Monte Carlo simulations were performed that replicated the manner in which the probability distributions and learning curves for operation durations are implemented within the time-domain simulation software. These implementation methods are discussed in detail in Chapter 8.

For each operation, a single Monte Carlo run consisted of sampling from the appropriate distribution N times, where N is the sample size of *recorded* observations for that particular operation. The *minimum*, *median*, *mean* and *maximum* duration of the simulated values were recorded for each Monte Carlo run, as well as the *sum* of all the durations in the sample. 10,000 Monte Carlo simulations were performed for each operation. The 2.5^{th} percentile (P2.5), median (P50), mean and 97.5^{th} percentile (P97.5) values of the 10,000 samples were then calculated for each of the five statistical categories. Finally, the ratios between the Monte Carlo results and the minimum, median, mean, maximum and total values of the observed data were calculated. The ratios of Monte Carlo results to observed data should be roughly equal to 1 for the mean and P50 categories, the P2.5 ratios should be less than 1 and the P97.5 ratios should be greater than 1.

When there is no significant evidence for learning, the probability distribution remains

stationary throughout the analysis. When learning is present and the analysis is being performed on the transformed operation duration data, the probability distribution varies with each successive sample—see Section 7.2.4 for further details. Consequently, for data-sets with no evidence of learning, the Monte Carlo validation simulations assess the accuracy and suitability of the fitted distributions. For the case when there is evidence for learning, the Monte Carlo validation simulations assess both the stochastic LC model and the chosen theoretical probability distribution. The methods for sampling from the varying probability distribution governed by Equation 7.30 are described in Chapter 8.

As shown in Figure 7.7, the Anderson-Darling statistic is the most critical test for assessing the distribution fit. The graphical assessment and the Monte Carlo simulations are used to identify significant anomalies. If any discrepancies arise from these two secondary methods, the distribution with the next lowest Anderson-Darling score is assessed. This process continues until all three assessment methods are passed.

7.6 Results and Discussion

The results section is divided into three parts. Section 7.6.1 describes three example operations from the WTG installation activity; one operation for which the presence of learning was most evident, one which clearly showed a lack of learning and a third example where the results were inconclusive. This section also describes several interesting anomalies highlighted by the analysis. Section 7.6.2 provides a more general overview and summary of the results. Section 7.6.3 describes two further applications of the proposed operation duration analysis methods.

7.6.1 Selected Results

Summaries of the numerical results for both the non-linear curve fitting and the probability distribution fitting are shown in Tables 7.2 and 7.3 respectively for the three selected examples. These are referenced throughout Section 7.6.1.

Example 1—Installing Blade 1

The first example describes the operation, completed by the baseline vessel, in which the first blade of each WTG is lifted from the jack-up vessel and connected to the previously installed nacelle. This operation was selected to demonstrate the presence of learning because it resulted in the lowest p value (3.68E-20) for the learning slope of all the operations in the WTG installation activity data-set. Figure 7.8 shows the graphical comparison of the raw unit duration data and the best-fit LC for this operation.

Table 7.2: Summary of curve fitting results for the learning slope parameter m.

	Example 1 Installing Blade 1	*Example 2 Between Locations*	*Example 3 Installing Blade 2*
Estimate	-0.356	-0.096	-0.081
Standard Error	0.028	0.137	0.0398
t-statistic	-12.892	-0.703	-2.036
p value	3.68E-20	0.486	0.048
Lower CI (2.5%)	-0.411	-0.374	-0.162
Upper CI (97.5%)	-0.301	0.181	-0.0007

Table 7.3: Calculated values for the Anderson-Darling statistic (AD) for the three most suitable fitted distributions for each example operation.

Example 1 Installing Blade 1		*Example 2 Between Locations*		*Example 3 Installing Blade 2*	
Distribution	*AD*	*Distribution*	*AD*	*Distribution*	*AD*
Burr-a_0	0.189	Burr	0.267	Burr-a_0	0.657
Loglogistic-a_0	0.245	Burr-a_0	0.286	Weibull-a_0	0.658
Gamma-a_0	0.280	Loglogistic	0.413	Loglogistic-a_0	1.278

Despite the scatter of the raw data around the best-fit LC, there is clear evidence of learning for this particular operation. The estimate for the learning slope of -0.356, corresponding to a learning rate of approximately 78%, is the second steepest result in the WTG installation activity data-set[1]. This means that every time the cumulative number of installed WTGs doubles, the time required to install the first blade of each turbine reduces by about 22%. The first WTG installation duration of 10.7 hours is approximately four times greater than the mean of the entire sample (2.64 hours). The figure also shows that the learning has plateaued at some stage between WTG numbers 30 and 40.

There is an indication of heteroscedasticity in the data shown in Figure 7.8. For the first 20 WTG installations, the data-points tend to fall below the best-fit LC. For WTG numbers greater than about 55, there is a tendency for the data to fall above the trend line. There are many potential reasons for these differences in variability around the Crawford model fit. The effect of prevailing metocean conditions is of particular interest. Although recorded instances of weather downtime have been omitted from the observed operation durations, the metocean conditions experienced at the time of operating can still impact the duration. The present analysis does not take account of the metocean conditions experienced and this may explain some of the variations

1. The steepest result in the data-set, for the jacking-down operation for Vessel B, corresponded to a learning slope of -0.37288 and a learning rate of 77%.

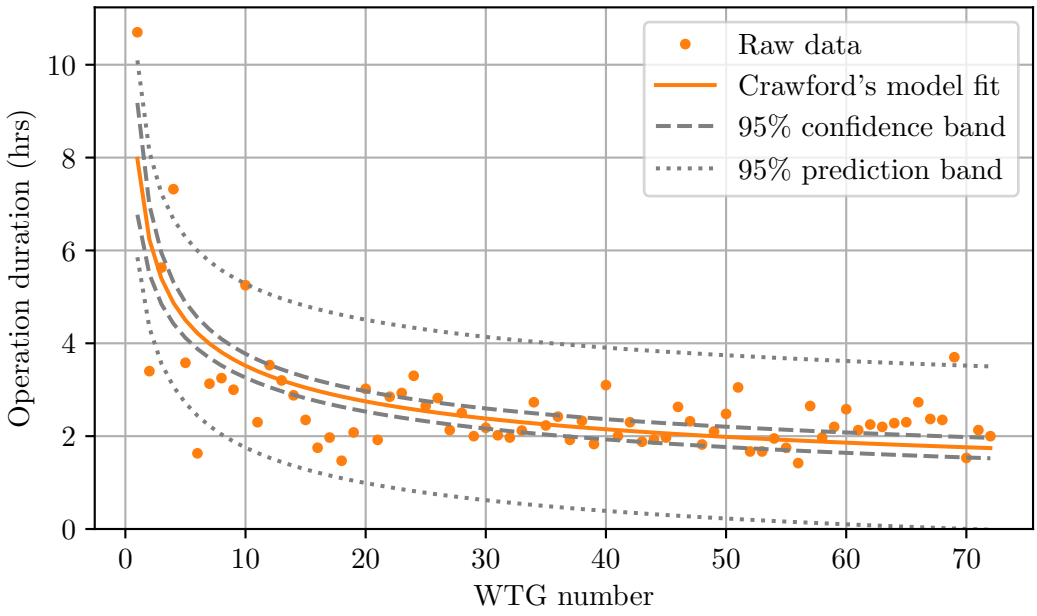

Figure 7.8: Graphical assessment of LC fit for Example 1.

evident in Figure 7.8. Future work should normalise the observed operation durations with respect to the prevailing wind, wave and tidal current conditions. This might explain some of the larger variations around the underlying learning trend in the data.

Several of the outliers in Figure 7.8 can also be explained by the prevailing weather conditions, reinforcing the need to perform the normalisation process mentioned above. For instance, the two outliers below the 95% prediction band for installation numbers 2 and 6 correspond to operations that were performed in very low wind speeds; 0 m/s and 4 m/s respectively. Conversely, two of the installations that lie above the prediction band, for WTG numbers 4 and 69, experienced weather conditions that were very close to the limiting threshold for crane operations. The additional remarks section of the DPR for installation number 69 stated that the prevailing wind speeds were "right on the limit".

Unlike the other outliers, the reason for the particularly large duration of the first installation was unrelated to the prevailing weather conditions. In this case, there was a prolonged spell of technical downtime (see Chapter 9) immediately prior to the operation which neccessitated additional tasks to be completed for the installation of this first blade. These additional tasks were not required for any other iterations of this task and were perhaps categorised incorrectly as being components of this operation.

As shown in Table 7.2, the statistical fitting results for the learning slope corroborate the graphical assessment. The narrow confidence interval (CI) shows a 95% chance that

m is between -0.411 and -0.301. Most importantly, the p value is essentially equal to 0, implying the null hypothesis that the learning slope is equal to zero can be rejected. In other words, the null hypothesis that there is no learning is rejected.

As there is significant evidence for learning, the raw data were transformed to the 1st cycle using the fitted value for m and Equation 7.39. Table 7.3 shows that the three distributions that resulted in the lowest calculated values for the Anderson-Darling statistic were the Burr-a_0, Loglogistic-a_0 and Gamma-a_0 distributions. The comparison of the fitted distributions to the transformed data-set is shown in Figure 7.9.

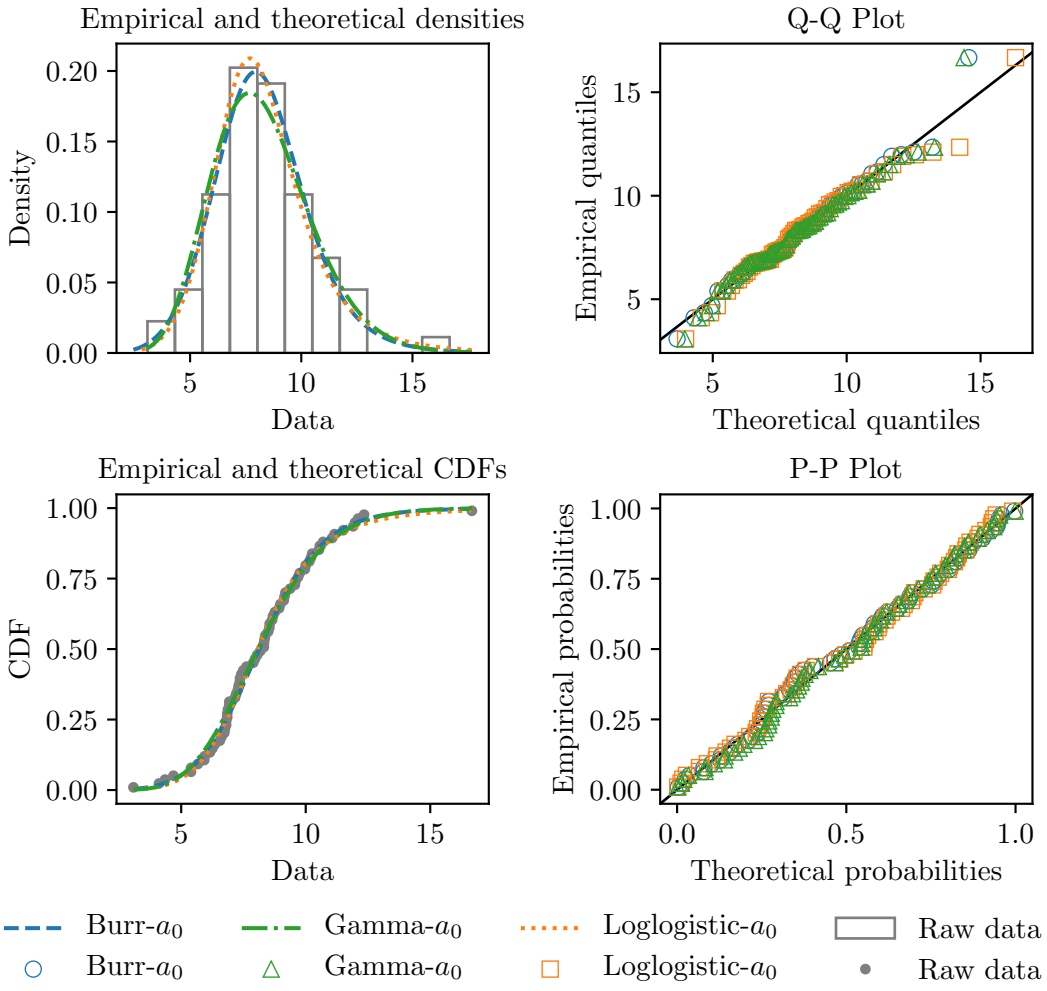

Figure 7.9: Goodness-of-fit plot for transformed data and fitted distributions for Example 1—data in hours.

Figure 7.9 shows that all three of the distributions are an excellent fit for the transformed values of operation duration. It is difficult to compare the distributions graphically, such is their proximity to the raw data and each other. However the main purpose of these goodness-of-fit plots is to compare potential candidate distributions. This makes

it easier to identify the most suitable distribution. In this case, the fitted Burr-a_0 distribution is marginally more accurate for the tails of the distribution, as emphasised by the Q-Q plot.

The results of the Monte Carlo validation procedure for the Burr-a_0 distribution are shown in Table 7.4. The samples from the fitted distribution accurately capture the centre of the observed data, as shown by ratios approximately equal to 1 for the P50 and mean Monte Carlo categories. Further, the Monte Carlo results for the maximum and sum of operation durations for installing the first blade are appropriately distributed around the recorded values. However, the results show that the minimum recorded duration for the operation is larger than the envelope of minimum values predicted by the Monte Carlo simulations. This implies that the fitted distribution, together with the stochastic learning curve algorithms, do not quite capture the left-hand tail of the data. Despite this small inconsistency, the fitted Burr-a_0 distribution is considered an appropriate fit for the installation of the first blade for the baseline vessel. The absolute differences for this minimum category of less than 1 hour are deemed acceptable on the basis that this represents less than approximately 6% of the total time taken to complete a single WTG installation.

Table 7.4: Monte Carlo validation results for the fitted Burr-a_0 distribution in Example 1—data in hours.

	Minimum	*Median*	*Mean*	*Maximum*	*Sum*
Observed data					
	1.42	2.3	2.635	10.7	189.7
Monte Carlo simulation results—Burr-a_0					
P2.5	0.537	2.162	2.525	6.126	181.807
P50	0.973	2.351	2.700	8.635	194.428
Mean	0.960	2.353	2.702	8.910	194.576
P97.5	1.313	2.561	2.891	13.461	208.146
Ratio of Monte Carlo: Observed data—Burr-a_0					
P2.5	0.378	0.940	0.958	0.573	0.958
P50	0.685	1.022	1.025	0.807	1.025
Mean	0.676	1.023	1.026	0.833	1.026
P97.5	0.925	1.114	1.097	1.258	1.097

Example 2—Between Locations

The second example concerns the operation where Vessel B transits between WTGs after completing an installation. This operation was chosen as the clearest example of a lack of learning because it resulted in the largest p value (0.486) for the learning slope of all the operations in the WTG installation activity data-set. The graphical comparison of the raw unit duration data and the best-fit LC for this operation is shown in Figure 7.10. The figure shows that even the best-fit curve is quite flat, $m = -0.096$, reflecting the lack of learning evident in the raw data. Furthermore for early WTG installations, the lower curve of the 95% confidence band is positively sloping and the 95% prediction band is predicting negative operation durations.

As with Example 1, it would be beneficial to assess the impact of normalising the data in Example 2 with respect to the prevailing metocean conditions to see if this reduced the variation around the mean duration for this operation.

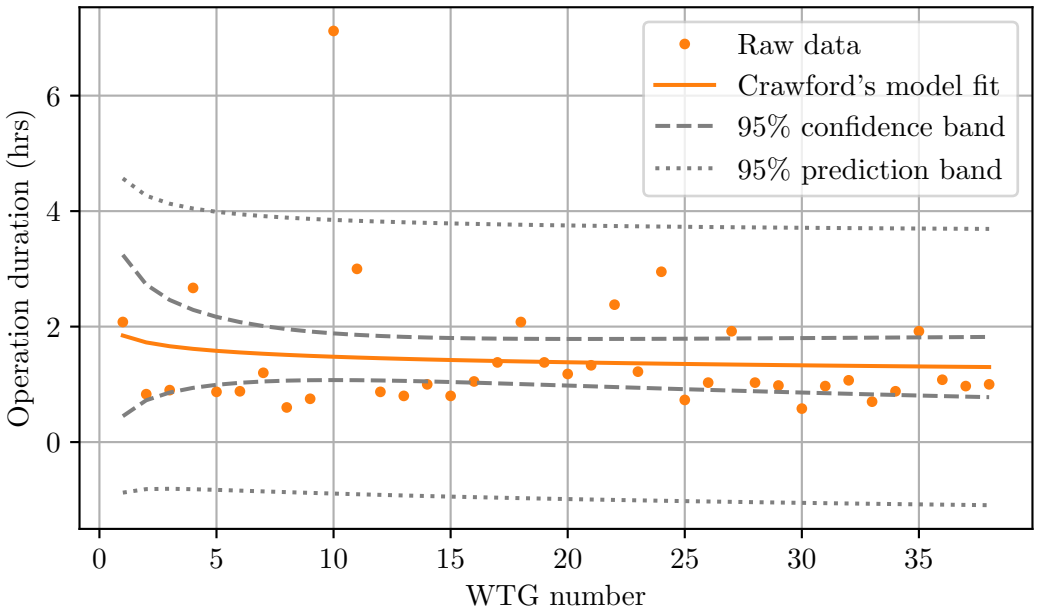

Figure 7.10: Graphical assessment of LC fit for Example 2.

The graphical evidence for a lack of learning is reflected in the statistical results shown in Table 7.2. The upper value of the 95% confidence interval (CI) for the learning slope m is positive (+0.181). As discussed in Section 7.2.2, this parameter is restricted to $-1 < m < 0$ in the LC model. As such the upper 97.5% confidence interval for this parameter indicates that the operation durations increase with unit number. Crucially, the p value for the hypothesis test is 0.486, meaning the null hypothesis that the learning slope is equal to zero cannot be rejected.

The fact that this transiting operation shows no evidence for learning can be seen as a validation of the analysis. For short transits between WTG locations, it is plausible that not much learning is possible. This task is constrained by the physical limits of the vessel and by the required transiting distance. In fact, there is a legitimate argument that this particular operation should not have been included in the learning analysis because there are minor variations in the transit distances between each turbine. This means that the tasks being analysed are not identical, invalidating one of the major assumptions of the LC theory. Future work could investigate if normalising the transit duration with respect to the distance travelled affects the LC analysis. The varying distances between turbine locations might also explain the outlier evident for the 10^{th} iteration of this operation.

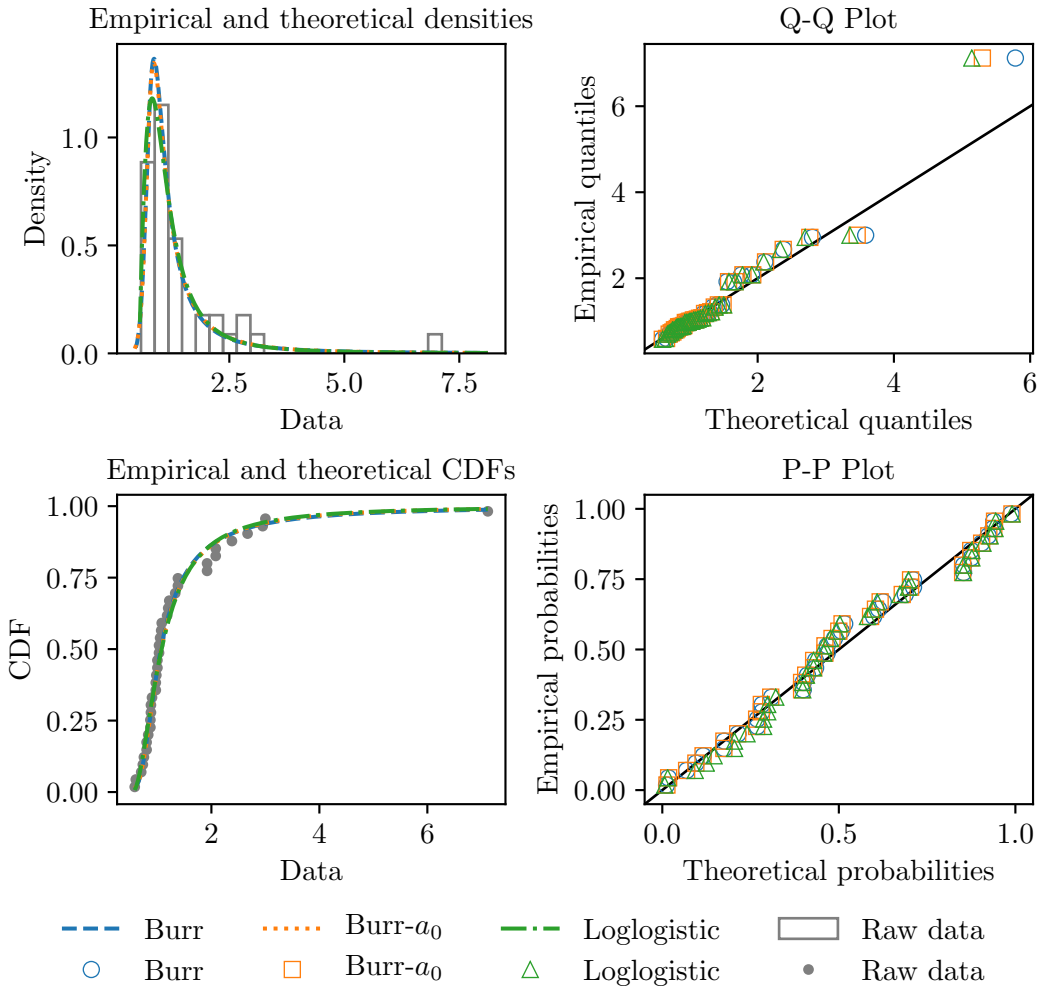

Figure 7.11: Goodness-of-fit plot for raw data and fitted distributions for Example 2—data in hours.

As there is no learning for this operation, the candidate probability distributions are

fitted to the raw data. Table 7.3 shows that the Burr, Burr-a_0 and Loglogistic distributions resulted in the lowest calculated values for the Anderson-Darling statistic.

The comparison of the fitted distributions to the raw data-set is shown in Figure 7.11. Each of the four plots suggest that the Burr, Burr-a_0 and Loglogistic distributions are adequate fits for this operation, despite the slight discrepancy at durations of approximately 2 hours. There is also quite a significant discrepancy at the uppermost quantile, as shown in the Q-Q plot. This discrepancy is lowest for the Burr distribution.

The results of the Monte Carlo validation procedure for the Burr distribution are shown in Table 7.5. Once again, the results show that the samples from the fitted distribution capture accurately the centre of the observed data, as shown by ratios approximately equal to 1 for the P50 and mean Monte Carlo results. In contrast to the results for Example 1, the Monte Carlo simulations show that the fitted Burr distribution accurately captures the spread around the recorded minimum value for this operation. The only area of concern is the fact that the P97.5 value for the maximum duration from the Monte Carlo simulations is nearly 5 times greater than the observed maximum. However, the fact that the P97.5 ratio for the sum of all durations is only 1.715 suggests that this large maximum value does not have too significant an impact on the total time spent on this operation over the entire project.

Table 7.5: Monte Carlo validation results for the fitted Burr distribution in Example 2—data in hours.

	Minimum	*Median*	*Mean*	*Maximum*	*Sum*
Observed data					
	0.58	1.03	1.426	7.12	54.18
Monte Carlo simulation results—Burr					
P2.5	0.450	0.933	1.113	2.404	42.285
P50	0.603	1.064	1.413	5.854	53.692
Mean	0.600	1.073	1.516	9.554	57.616
P97.5	0.730	1.267	2.445	35.097	92.903
Ratio of Monte Carlo: Observed data—Burr					
P2.5	0.775	0.906	0.780	0.338	0.780
P50	1.040	1.033	0.991	0.822	0.991
Mean	1.034	1.041	1.063	1.342	1.063
P97.5	1.259	1.230	1.715	4.929	1.715

Example 3—Installing Blade 2

The third and final example concerns the installation of the second blade of each WTG by Vessel B. This operation was chosen as a less conclusive example because the calculated p value for the learning slope was 0.048, the closest to the chosen significance level of 0.05 in the data-set. The graphical comparison of the raw data and the fitted LC is shown in Figure 7.12. This figure highlights the fact that the estimated learning slope is quite small; the curve is quite flat.

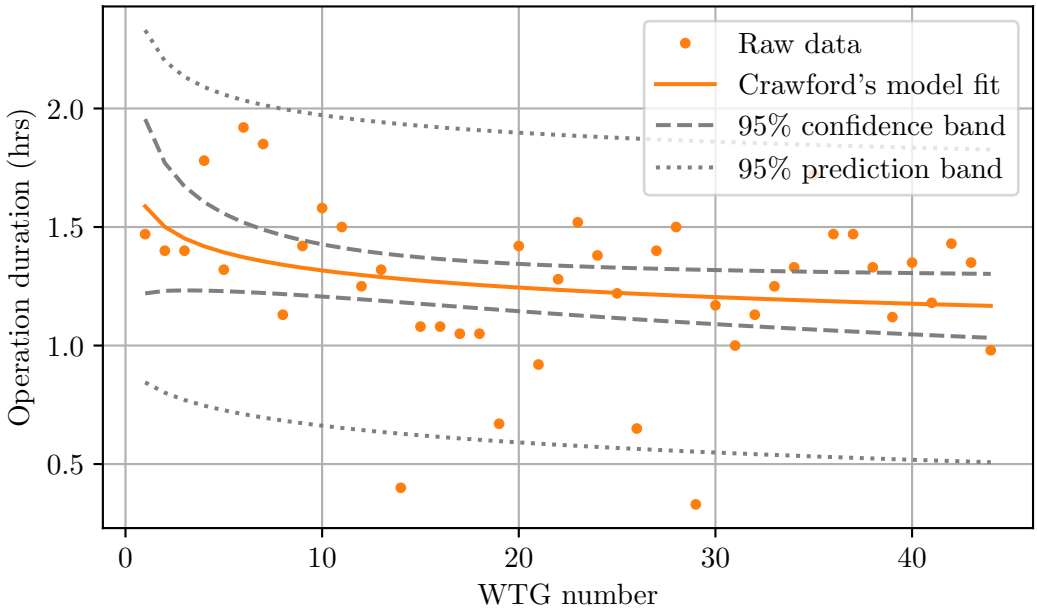

Figure 7.12: Graphical assessment of LC fit for Example 3.

There are two points below the 95% prediction band that are significantly smaller than the mean operation duration. The second of these outliers, for WTG number 29, may be explained by the fact that that this operation was interrupted by an instance of technical downtime. The durations that were logged for this particular operation were categorised as 10 minutes of performing the task, followed by 50 minutes of technical downtime and a final 10 minutes of operation time. The random stoppage may have led to errors in the recording of this operation. There is no obvious explanation for the first outlier for installation number 14. The prevailing weather conditions were not particularly benign—the wind speeds were recorded as 10 m/s. The only abnormal characteristic of this particular data-point is that the operation took place around midnight. This meant that the operation duration data were split across two separate DPRs which, in a similar manner to the outlier for WTG number 29, may have led to an incorrect record of this particular operation. Though neither of these outliers can be explained by the impact of the prevailing weather, it would still be beneficial to assess

the effect of metocean conditions on the other operation duration data-points.

The p value for the learning slope of 0.048 implies the null hypothesis that the learning slope is equal to 0 can be rejected, but a selection of the other graphical and numerical results can be interpreted differently. For example, the lower curve of the 95% confidence band is slightly upward sloping for the first few WTG installations. Furthermore, the upper value of the 95% confidence interval of -0.0007, as shown in Table 7.2, indicates negligible learning—this learning slope corresponds to a learning rate of 99.95%.

In the WTG installation activity data-set, there were 4 operations that resulted in p values of between 0.01 and 0.05. Each of these operations were completed by Vessel B, indicating that the smaller sample size for the second vessel may affect the determination of learning. More importantly, the lower curves of the 95% confidence bands were positively sloping at early WTG installations for 3 of these 4 operations. Additionally, the upper values of the 95% confidence intervals for the learning slope were all greater than -0.008 for the same 3 operations, indicating negligible learning. These results suggest that a significance level of 0.01 may have been appropriate for the determination of learning.

Nevertheless, the hypothesis test at a significance level of 0.05 was selected as the critical test of determining the presence of learning. Consequently, the raw data were transformed to the first cycle using Equation 7.39 and the candidate probability distributions were fitted to this transformed data-set. The calculated Anderson-Darling results show that the most appropriate distributions are the Burr-a_0, Weibull-a_0 and Loglogistic-a_0 distributions.

The goodness-of-fit plots comparing the three selected distributions to the transformed data for Example 3 are shown in Figure 7.13. The figure, corroborating the statistical goodness-of-fit results, shows that the third choice Loglogistic-a_0 distribution should be disregarded. The CDF and Q-Q plots show a significant discrepancy at the right-hand tail of this distribution that is not evident for the other two distributions.

Interestingly, the fitted Burr-a_0 and Weibull-a_0 distributions look identical in Figure 7.13. The Burr distribution approaches the Weibull distribution as the second shape parameter $k \to \infty$ (Tadikamalla, 1980; Rodriguez, 1977). The fitted distribution parameters for the two models in Table 7.6 show that $k \approx 1,000$ for the Burr-a_0 distribution, explaining why these fitted distributions are so similar. The BIC scores for the two fitted distributions were calculated and these are also shown in Table 7.6. As expected, the BIC score for the Weibull-a_0 is lower, due to the fact that it has one less model parameter than the Burr-a_0 distribution and they both produce similar maximum log-likelihood values.

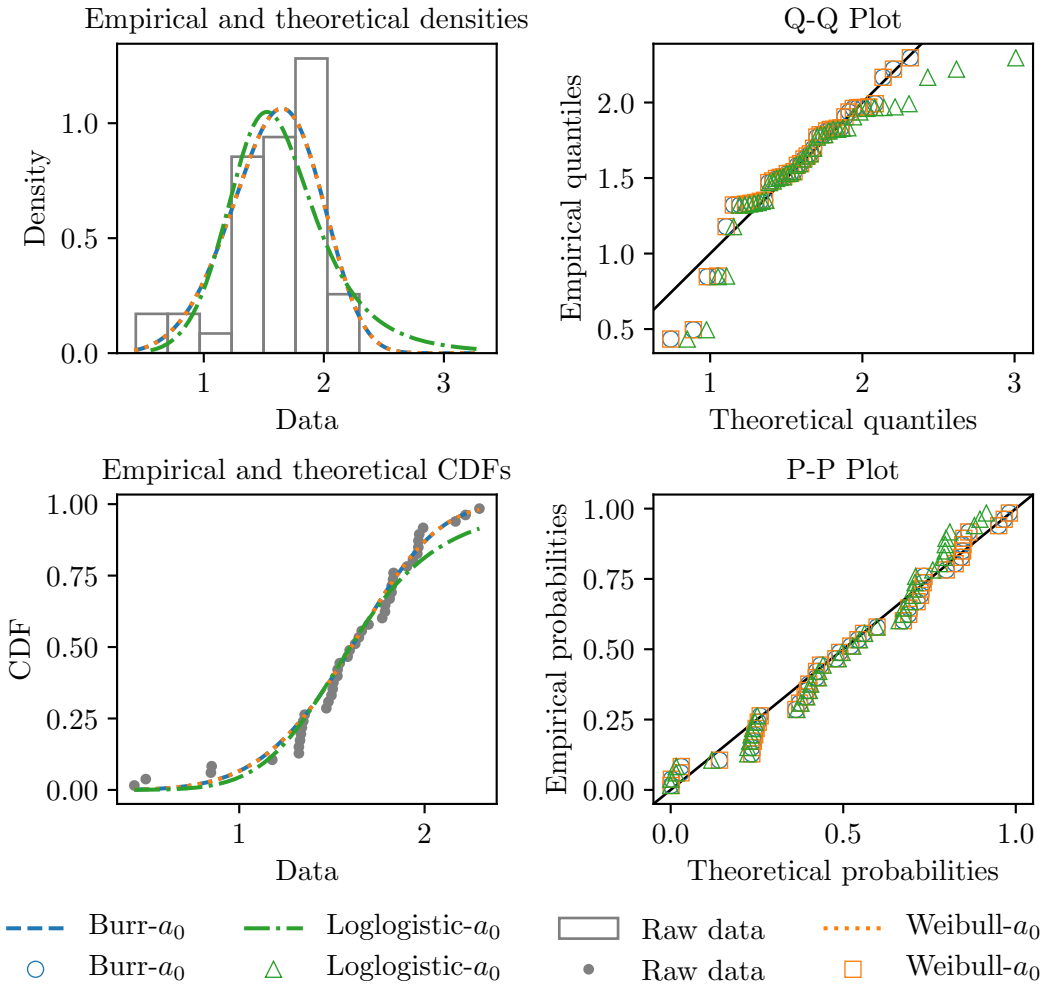

Figure 7.13: Goodness-of-fit plot for transformed data and fitted distributions for Example 3—data in hours.

Table 7.6: Fitted distribution parameters and goodness-of-fit statistics for the Monte Carlo validation results for the Burr-a_0 and Weibull-a_0 distributions in Example 3.

	Burr-a_0	*Weibull-a_0*
Location parameter (a)	0	0
Scale parameter (b)	7.090	1.730
Shape parameter 1 (c)	4.897	4.892
Shape parameter 2 (k)	999.464	-
Anderson-Darling statistic	0.657	0.658
Bayesian information criterion (BIC)	52.475	48.682

Table 7.7: Monte Carlo validation results for the fitted Burr-a_0 and Weibull-a_0 distributions in Example 3—data in hours.

	Minimum	*Median*	*Mean*	*Maximum*	*Sum*
Observed data					
	0.33	1.325	1.263	1.92	55.57
Monte Carlo simulation results—Burr-a_0					
P2.5	0.299	1.157	1.175	1.699	51.701
P50	0.582	1.268	1.263	1.932	55.557
Mean	0.575	1.268	1.263	1.950	55.556
P97.5	0.816	1.378	1.350	2.302	59.379
Ratio of Monte Carlo: Observed data—Burr-a_0					
P2.5	0.906	0.874	0.930	0.885	0.930
P50	1.763	0.957	1.000	1.006	1.000
Mean	1.743	0.957	1.000	1.016	1.000
P97.5	2.472	1.040	1.069	1.199	1.069
Monte Carlo simulation results—Weibull-a_0					
P2.5	0.296	1.158	1.173	1.696	51.622
P50	0.580	1.268	1.262	1.929	55.522
Mean	0.574	1.267	1.262	1.949	55.516
P97.5	0.818	1.375	1.349	2.315	59.346
Ratio of Monte Carlo: Observed data—Weibull-a_0					
P2.5	0.897	0.874	0.929	0.883	0.929
P50	1.758	0.957	0.999	1.005	0.999
Mean	1.740	0.956	0.999	1.015	0.999
P97.5	2.479	1.038	1.068	1.206	1.068

The Monte Carlo validation results for both distributions are shown in Table 7.7. As expected, the results for both distributions are very similar. The only remarkable results, common to both distributions, are the ratios for the mean and P50 values for the minimum duration category, which are all approximately 1.75. These slightly high values imply that the fitted distributions routinely predict marginally larger minimum duration values for this operation. This phenomenon is somewhat understandable, as Figure 7.13 shows that none of the fitted distributions model adequately the left-hand tail of the transformed data. Still, both distributions are considered adequate because the deviation in the absolute values are minimal. Each of the three distribution fitting assessment methods show that the Burr-a_0 and Weibull-a_0 distributions are viable candidates for this operation. Based on the additional scores from the BIC calculations, the Weibull-a_0 is selected as the most representative parametric model.

Further Investigation of Blade Installation Operations

Surprisingly, the results from Examples 1 and 3 show significant evidence of learning for the installation of the *first* turbine blade for the baseline vessel, but the determination of learning for the installation of the *second* blade by Vessel B was inconclusive. Further investigation of this unusual phenomenon revealed that at a significance level of 0.05, there was evidence of learning for the installation of the *first* and *third* blades for both vessels but no evidence of learning for the installation of the *second* blade for the baseline vessel. Crucially, for this second vessel with a larger sample size, the hypothesis test clearly indicated no learning with a p value of 0.178.

As mentioned previously, the DPRs categorise the tasks completed on a given day into *activities* comprised of several *operations*. There is an additional column in the DPRs that can record short comments that provide further details on the components of each operation. The curious discrepancy between the installation duration for the wind turbine blades was investigated by assessing these additional comments.

The analysis showed that the operations corresponding to the installation of blades 1 and 3 included additional tasks relating to the rigging and de-rigging of the installation equipment on the vessel—different tools are required for installing the tower, nacelle and blades. Understandably, these rigging and de-rigging operations were unnecessary for the second turbine blade. The analysis suggests that these rigging operations are more susceptible to learning than the actual lifting and installation of the turbine blades. In other words, the discrepancies in the results are attributed to the classification of the constituent tasks of each operation, rather than any operational differences between the installation of each blade.

Ideally, the analysis of the operation durations could have been analysed at a finer resolution, taking into account the constituent tasks of each operation. However, the unstructured and variable nature of the additional comments in the DPRs necessitated this task to be completed manually for the entire data-set. Future work could focus on this higher resolution analysis.

Reiterating the recommendation made in Section 7.3.2 for the improved structuring of these recorded observation data, an alternative solution is to increase the resolution, or granularity, of the recorded offshore tasks. For example, the discrepancy in blade installation operations may have been avoided by the introduction of additional rigging and de-rigging operations as part of the WTG installation activity.

Stochastic LC Model Visualisation

It is useful to visualise the results using the fitted distribution parameters and learning slope parameter. Figure 7.14 shows the variation of probability density function with unit number for Example 1, calculated using Equation 7.30. The figure shows similar trends to that of the theoretical plot in Figure 7.3. As more units are completed, both the expected value and the variance decrease—the PDF becomes 'peakier'. As expected, the change in shape of the PDF is much more significant between units 1 and 35 than between units 35 and 70—the mode for units 1, 35 and 70 are 7.95, 2.25 and 1.75 hours respectively.

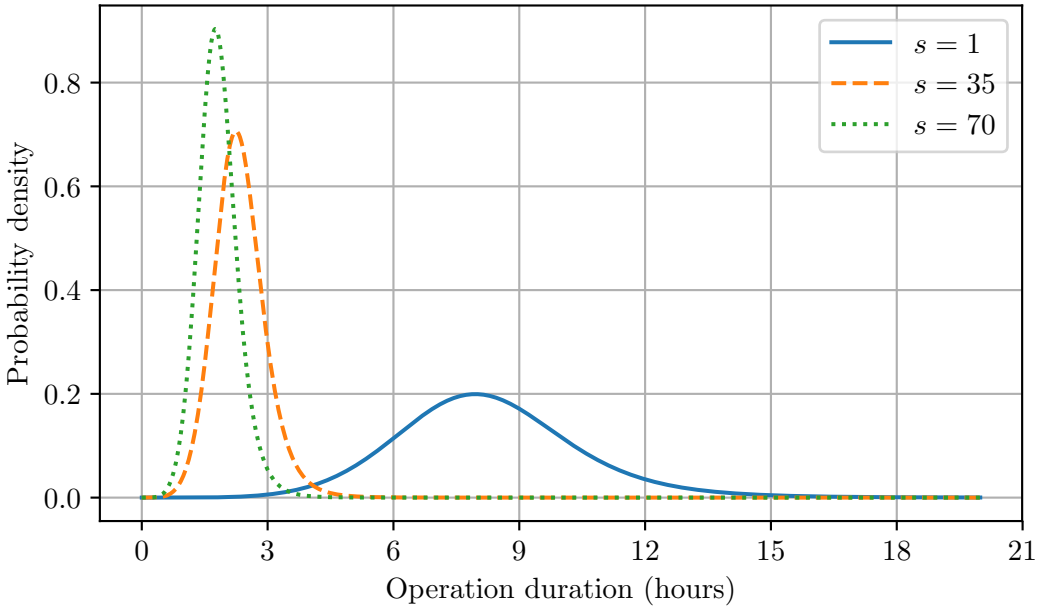

Figure 7.14: PDFs as a function of unit number for fitted Burr-a_0 distribution for Example 1—2d.

The same data and trends are shown in three dimensions (3D) in Figure 7.15, which includes a PDF for each of the WTG installations completed by the baseline vessel. This figure is particularly useful for visualising how the stochastic LC model can be implemented within the time-domain simulation software. Assuming that each operation in the simulation model is associated with a similar plot and noting that the software has continuous access to the current operation and WTG number, the operation duration sampling procedure can be viewed as a simple case of cycling through the appropriate 3D plot for the given operation, selecting the appropriate PDF based on the WTG number and randomly sampling from that distribution.

Figure 7.15 demonstrates how the stochastic learning curve method is well-suited for representing the operation duration inputs to time-domain Monte Carlo simulations.

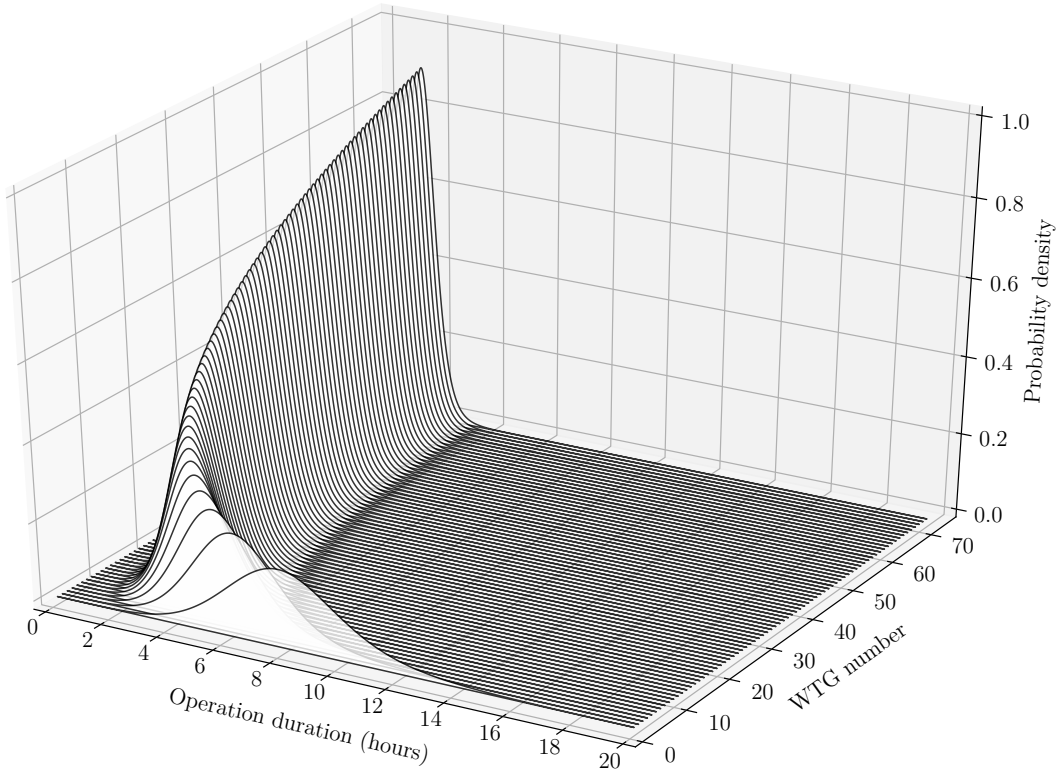

Figure 7.15: PDFs as a function of unit number for fitted Burr-a_0 distribution for Example 1—3d.

The method allows a probability density function to be specified for each consecutive repetition of an operation, accounting for the presence of learning. Specifying the input data for an operation with no learning is achieved by simply defining a single probability distribution.

Another benefit of the described LC method is that it can be implemented regardless of the prior knowledge of the user. If no prior data exist for related projects or if the user only has an intuitive knowledge of the expected learning rates, then the progress ratio L, as defined in Equation 7.10, can be specified. This intuitive parameter corresponds to the percentage reduction in duration that can be expected when the number of units completed doubles.

Alternatively, an experienced user with confident estimates of the statistical characteristics can choose the learning rate explicitly. Thus, regardless of the accuracy and confidence of input data, the stochastic LC model ensures a constant, statistically sound method for the random sampling of operation durations that incorporates the crucial learning phenomenon. Chapter 8 focusses on the implementation and evaluation of the stochastic LC model within the ForeCoast® Marine Gamer Mode.

Further Anomalies

Two further operations showed the same phenomenon observed in Example 3 where the Burr and Weibull fits resulted in near-identical distributions. These two operations were the installation of the third blade for Vessel B and the finishing installation operation for the baseline vessel. In contrast to Example 3, the Anderson-Darling statistics favoured the less complex Weibull model for both of these operations.

For four of the analysed operations, the ratios of Monte Carlo simulated values to observed data for the *minimum* durations were greater than 1 for all four of the Monte Carlo statistical measures, implying that the fitted distributions never sampled values as low as the minimum observed duration. For two of these four operations—installing the second blade for the baseline vessel and preparing to install for Vessel B—the issues did not arise in the Monte Carlo validation for the second ranked distributions according to the Anderson-Darling statistics, which were subsequently chosen as the most appropriate distributions. For the other two operations—installing the third blade for vessels 1 and 2 respectively—the same issue arose for all three of the distributions with the lowest Anderson-Darling statistic scores. In these two cases, as in Example 3, the absolute deviations between the minimum simulated and observed data were insignificant. Consequently, the distributions with the lowest Anderson-Darling score were used as normal. The chosen distributions for every operation are summarised in Section 7.6.2.

Finally, for the best-fit Loglogistic distribution for the jack-down operation for the baseline vessel, the P97.5 ratio for the maximum durations was 11.121. The observed maximum duration was 3.83 hours but the 97.5^{th} percentile of the maximum durations from the Monte Carlo simulations was 147.439 hours. This ratio was considered too high and a duration of nearly 150 hours, considering the mean observed duration was 1.363 hours, was considered inappropriate. The problem did not arise for the distribution with the second lowest Anderson-Darling statistic, the Lognormal distribution. The P97.5 ratio for the maximum duration of this distribution of 3.601 was deemed more appropriate and the Lognormal fit was subsequently chosen.

7.6.2 Results Summary

Determination of Learning

A summary of the results for the determination of learning is given in Table 7.8. For the large sample, the majority of operations in the data-set show significant evidence for learning, regardless of the inclusion or exclusion of transit operations. For the small sample, the percentage of operations that showed learning is much smaller and varies between 14.3% and 28.6%. For the combined data-set, exactly half of the operations

showed signs of learning when the transit operations are included and this rises to between 56.3% and 62.5% when transit operations are removed.

Table 7.8: Summary of results for the determination of learning.

	Small Sample	*Large Sample*	*Total*
Including Transit Operations			
Baseline vessel			
Count of Learning Operations	2	8	10
Total Number of Operations	10	10	20
Percentage Learning Operations (%)	20.0	80.0	50.0
Vessel B			
Count of Learning Operations	2	8	10
Total Number of Operations	10	10	20
Percentage Learning Operations (%)	20.0	80.0	50.0
Total			
Count of Learning Operations	4	16	20
Total Number of Operations	20	20	40
Percentage Learning Operations (%)	20.0	80.0	50.0
Excluding Transit Operations			
Baseline vessel			
Count of Learning Operations	1	8	9
Total Number of Operations	7	9	16
Percentage Learning Operations (%)	14.3	88.9	56.3
Vessel B			
Count of Learning Operations	2	8	10
Total Number of Operations	7	9	16
Percentage Learning Operations (%)	28.6	88.9	62.5
Total			
Count of Learning Operations	3	16	19
Total Number of Operations	14	18	32
Percentage Learning Operations (%)	21.4	88.9	59.4

The minimum number of data-points in the large sample is 38, while the sample size of the small data-set varies between 4 and 9. It is possible that the small sample data-sets are not sufficiently large for the accurate quantification of learning. For example in Figure 7.12, it is hard to detect learning based on the first 9 units. It is only with the consideration of the 40+ data samples that the weak evidence for learning becomes clearer.

Conversely, if clear learning is evident for an operation, the trends should be most evident for the earliest unit numbers, as in Figure 7.8, where it is clear, even after 9 units, that the installation durations are decreasing. Consequently, it is difficult to say whether the lack of learning for the small sample is attributed to the smaller sample size

or that the operations in this data-set tend not to be affected by learning. Regardless, there is more confidence in the results for the large sample.

The argument was put forward in Section 7.6.1 that it may not be appropriate to include transit operations in the learning analysis. This is because the operations are not identical for each repetition—the distances that need to be travelled are constantly varying. This theory is corroborated by the fact that of the 8 transit operations in the data-set, only 1 of these operations showed evidence for learning.

Considering the above discussion, the greatest confidence is in the results for the large sample excluding transit operations. Of these operations, 88.9% showed significant evidence for learning. Even if the small sample is included, the percentage of total operations for which learning is a factor remains high at 59.4%.

Table 7.9: Comparison of learning results between vessels. The learning rate (ϕ) is shown for the operations for which there is strong evidence of learning.

	Baseline vessel		*Vessel B*	
	p value	*ϕ (%)*	*p value*	*ϕ (%)*
Small Sample				
Positioning	0.686	No learning	0.734	No learning
Backloading	0.070	No learning	0.804	No learning
Loading blades	0.398	No learning	0.759	No learning
Loading towers	0.071	No learning	0.008	79
Loading nacelles	0.033	86	0.025	90
Seafastening	0.465	No learning	0.861	No learning
Departing port	0.466	No learning	0.128	No learning
Outward transit	0.007	93	0.945	No learning
Return transit	0.720	No learning	0.681	No learning
Dynamic positioning trial	0.297	No learning	0.765	No learning
Large Sample				
Between locations	0.132	No learning	0.486	No learning
Jack-up	0.0006	92	0.0006	90
Preparing to install	0.0002	89	0.454	No learning
Installing tower	1.31E-06	90	8.48E-06	87
Installing nacelle	2.26E-10	87	0.034	93
Installing blade 1	3.68E-20	78	0.0002	89
Installing blade 2	0.178	No learning	0.048	95
Installing blade 3	3.29E-11	88	0.018	94
Finishing installation	3.53E-06	87	0.043	92
Jack-down	0.0003	85	0.0004	77

Because both vessels involved in the wind farm installation project were essentially identical and completed exactly the same tasks, it is possible to compare the learning

results of both vessels for each operation in the data-set. The results in Table 7.9 show that in each of the large and small samples, there are only two operations with discrepancies in the determination of learning. This means that of the 20 operations analysed, only 20% of them produced alternative results for the two vessels. Additionally, one of these four operations that shows a discrepancy is the installation of blade 2, which could easily be classified as an operation with no learning, as described for Example 3 above. The agreement between the two vessels is particularly interesting in relation to one of the main assumptions of the learning curve theory; that learning is a *human factor* and it arises as workers become more familiar with the task they are repeating. That only 20% of the analysed operations showed discrepancies in the determination of learning suggest that the nature of the operation being performed also has an impact on the presence of learning.

Probability Distribution Fitting

A summary of the selected probability distributions for the large sample, categorised by whether the data has been transformed due to the presence of learning, is given in Table 7.10. The results show that the Burr-a_0 distribution is the most commonly selected probability distribution for modelling both the raw data and the transformed data. The proportions of operations represented by the Burr-a_0 distribution are 56.25%, 50% and 55% for the learning, no learning and total categories respectively.

Table 7.10: Summary of the selected probability distributions for raw and transformed data—separated *fixed location* and *variable location* forms.

	Transformed Data		*Raw Data*		*Total*	
	Count	*Percent (%)*	*Count*	*Percent (%)*	*Count*	*Percent (%)*
Burr-a_0	9	56.25	2	50	11	55
Lognormal	2	12.5	0	0	2	10
Weibull-a_0	2	12.5	0	0	2	10
Burr	1	6.25	1	25	2	10
Loglogistic	1	6.25	1	25	2	10
Weibull	1	6.25	0	0	1	5

Table 7.11 shows the same results but combines the *fixed location* and *variable location* versions of each distribution, rather than keeping them separate as in Table 7.10. The proportions of operations represented by either the Burr or Burr-a_0 distributions are thus 62.5%, 75% and 65% for the learning, no learning and total categories respectively. The Weibull, Lognormal and Loglogistic distributions are the next most viable distributions for modelling the operation duration data.

Table 7.11: Summary of the selected probability distributions for raw and transformed data—combined *fixed location* and *variable location* forms.

	Transformed Data		*Raw Data*		*Total*	
	Count	*Percent (%)*	*Count*	*Percent (%)*	*Count*	*Percent (%)*
Burr	10	62.5	3	75	13	65
Weibull	3	18.75	0	0	3	15
Lognormal	2	12.5	0	0	2	10
Loglogistic	1	6.25	1	25	2	10

Table 7.12 shows the three distributions that resulted in the lowest Anderson-Darling statistics for both vessels and for each operation. The empty cells in the table correspond to the discrepancies in the determination of learning discussed previously. The distribution that was selected in each case, which was not always the first-ranked distribution for reasons mentioned previously, is highlighted in italics.

While the presence of learning for identical operations completed by each vessel was shown to be comparable in the previous section, there are more discrepancies with regard to the selection of probability distribution. There are 8 instances where comparative operations exist between the two vessels. Of these 8, only 1 operation resulted in the exact same distribution—the installation of the nacelle. If the *fixed location* and *variable location* versions of each distribution are considered equivalent, the number of operations with the same distribution increases to 3. Further, the best-fit Weibull-a_0 distribution for the installation of the third blade for Vessel B has been shown to be identical to the fitted Burr-a_0 distribution for this operation, adding another operation that resulted in the same distribution for each vessel. Consequently, at most there is a 50% agreement for the selected probability distribution between vessels for the analysed operations. These results are more consistent with the underlying theory that learning is a *human factor*. While the previous section showed that certain operations might be more susceptible to learning than others, the discrepancy in model selection for identical operations suggests that the exact shape of the learning curve is dependent on the people who perform the tasks.

The results offer a different perspective when looking at the top three distributions for each operation. The Burr or Burr-a_0 distributions are ranked first or second for 19 of the 20 operations and ranked third in the remaining operation. This implies that the Burr distribution can be used to represent accurately every operation in the data-set. Furthermore, the Loglogistic or Loglogistic-a_0 distributions are viable candidate models for 16 of the 20 operations and are consistent for identical operations completed by each vessel.

Table 7.12: Comparison of selected probability distributions for operations completed by each vessel. Selected distributions in italics.

	Anderson-Darling rank		
	First	*Second*	*Third*
Baseline vessel			
Raw data			
Between locations	*Burr-a_0*	Loglogistic	Loglogistic-a_0
Preparing to install	-	-	-
Installing blade 2	Burr-a_0	*Loglogistic*	Loglogistic-a_0
Transformed data			
Jacking up	*Lognormal*	Burr-a_0	Weibull
Preparing to install	*Burr-a_0*	Burr	Weibull
Installing tower	*Burr-a_0*	Burr	Weibull
Installing nacelle	*Burr-a_0*	Loglogistic	Loglogistic-a_0
Installing blade 1	*Burr-a_0*	Loglogistic-a_0	Gamma-a_0
Installing blade 2	-	-	-
Installing blade 3	*Burr-a_0*	Loglogistic-a_0	Weibull-a_0
Finishing installation	*Weibull*	Burr-a_0	Burr
Jacking down	Loglogistic	*Lognormal*	Burr-a_0
Vessel B			
Raw data			
Between locations	*Burr*	Burr-a_0	Loglogistic
Preparing to install	Loglogistic-a_0	*Burr-a_0*	Gamma-a_0
Installing blade 2	-	-	-
Transformed data			
Jacking up	*Burr-a_0*	Loglogistic	Loglogistic-a_0
Preparing to install	-	-	-
Installing tower	*Loglogistic*	Burr-a_0	Lognormal
Installing nacelle	*Burr-a_0*	Loglogistic	Loglogistic-a_0
Installing blade 1	*Burr*	Loglogistic	Loglogistic-a_0
Installing blade 2	Burr-a_0	*Weibull-a_0*	Loglogistic-a_0
Installing blade 3	*Weibull-a_0*	Burr-a_0	Loglogistic-a_0
Finishing installation	*Burr-a_0*	Loglogistic	Loglogistic-a_0
Jacking down	*Burr-a_0*	Loglogistic	Loglogistic-a_0

Interestingly, 13 of the 20 selected distributions relate to the *fixed location* versions, rejecting the proposition of a minimum duration greater than 0 for each operation. The sample size for each operation may be insufficient for capturing this hypothetical minimum value. However, the analysis also shows that there are only 5 instances where the top 3 distributions are all *fixed location* versions of the distribution. In other words, 75% of the operations can be appropriately modelled by parametric distributions with a minimum value.

7.6.3 Further Applications

Iterative Updating of Input Data

A major benefit of the presented operation duration analysis method is the possibility of iteratively updating the input data for ongoing projects. If progress updates, similar to the DPRs described previously, are available during the operational phase of a project, the task duration input data can be continuously updated based on the analysis of the incoming performance data.

In an identical manner to the *progress plots* and *weekly updates* discussed in Chapter 6, the operation duration analysis then becomes a cyclical simulation process. As the project progresses, more operational data will be obtained and analysed, leading to more accurate estimates of the operation duration probability distributions and learning parameters. This will in turn lead to more accurate and reliable simulations and predictions of future progress.

This iterative procedure of updating the input data has been implemented successfully for several ForeCoast® Marine projects. The example described in detail in Chapter 6 is perhaps the best demonstration of the benefits of this type of analysis. Significant deviations between the simulations and actual performance were identified approximately halfway through the campaign. A detailed analysis of the operational data received up to that point revealed that the original estimates of project duration slightly overestimated the time it was taking to complete specific tasks. Specifically, the mean duration required to complete a single WTG installation was 30% lower than initially specified. Updating the input data for the constituent operations reduced the project duration estimates by 10.8% and ensure a more accurate representation of the activities being simulated for the remainder of the campaign.

Building an Operations Database

Jablonowski *et al.* (2011) have stated that it is possible to estimate the LC for prospective marine operations with some certainty in the cases where comparable operations exist. Similarly, prior knowledge of the expected value and variance of the duration of historic operations can be used to estimate the durations of similar tasks in the future. At present it is impossible, due to the lack of adequate operational data from comparable projects, to assess the validity of these phenomena. Future work should focus on determining the viability of using duration and learning statistics from one project for similar operations in a completely distinct project.

Thus, it is worthwhile to develop a database of operational characteristics using available performance data. Correctly categorising this data is of extreme importance. For example, an offshore WTG can be installed in myriad ways, so it is essential to categorise

the data based on criteria such as the size and type of turbine; the size and type of installation vessel and the site conditions that include water depth, wave climate and tidal regime.

The benefits of continually expanding this database of carefully categorised observed operation data are twofold. Firstly, it will enable the comparison of operation duration and learning statistics between projects. On the other hand, regardless of these comparative analysis results, the expertise obtained from developing this operational database will undoubtedly improve the general representation of input operation data in time-domain Monte Carlo simulations.

7.7 Conclusions

A stochastic learning curve model that treats the phenomenon of a *learning curve* as a random process has been described. The model allows a probability density function for operation duration to be defined for consecutive repetitions of an offshore operation, assuming that there is a reduction in these durations due to this learning curve effect. Thus, this stochastic model is well-suited for representing the operation duration inputs to time-domain Monte Carlo simulations for offshore operations.

The stochastic learning curve theory and standard probability distribution fitting techniques have been used to analyse recorded operation duration data for the construction of a Round 3 offshore wind farm. The results show that learning is an observable phenomenon for the majority of operations in the data-set. Specifically, of the 18 WTG installation operations that were analysed, 16 showed evidence of learning. In other words, learning was observed for just under 90% of recorded operations.

The effect of learning on operation duration can be significant. For the installation of the first blade by the Baseline vessel (the operation with the second largest result for learning slope), the learning rate was approximately 78%. This means that the time required to complete this operation reduced by about 22% every time there was a doubling of the cumulative number of WTGs installed.

The Burr Type XII distribution has been identified as the distribution that most suitably models the operation duration data, regardless of the presence of learning. The Burr distribution resulted in the best-fit distribution for 65% of the analysed operations. Furthermore, the Burr family of distributions were ranked in the top 2 most suitable distributions for 19 of the 20 operations that were analysed and in the top 3 for every operation in the data-set. The Loglogistic, Weibull and Lognormal distributions were also identified as applicable theoretical representations for modelling operation duration data.

It is recommended to extend the analysis discussed in this chapter by normalising the observed operation durations with respect to the prevailing wind, wave and tidal current conditions. This may help explain some of the larger variations around the underlying learning trends. It might also account for some of the heteroscedasticity that can be seen in certain results. Future work should investigate these possibilities.

The method of analysing performance data throughout the operation phase of a project is recommended. Estimates for the expected value, variance and learning slope of the operation data can be iteratively updated as the campaign progresses, leading to a continual improvement of project progress predictions.

The possibility of using previously determined duration and learning statistics for comparable operations in a prospective marine operation has been discussed. To help evaluate the validity of this statement, the continued development of a knowledge database of operational data using available performance data is recommended.

Finally, enforcing a systematic procedure for recording operation duration data, that categorises the tasks comprising an offshore activity at a sufficient resolution, is recommended and will help expand this operational knowledge database.

Chapter 8

Incorporating Learning in Time-domain Simulations

8.1 Introduction

This chapter describes the implementation of the stochastic learning curve model discussed in the previous chapter within the developed time-domain simulation software. Specifically, the analysis attempts to expand the validation of the established learning curve theory—which was only validated and applied explicitly to the Normal distribution—to seven additional probability distributions. The objective is to develop and incorporate computationally efficient, intuitive and comprehensive procedures for the generation of random samples of operation duration that account for the learning phenomenon. There is a focus on the performance and processing speed of the sampling methods due to the importance of these aspects in Monte Carlo simulations.

The theoretical background is given in Section 8.2, which summarises the important definitions for statistical distributions, describes the two proposed sampling methods for implementing the learning curve model and introduces the additional distributions that will be investigated. The methodology applied to each of the additional distributions is briefly explained in Section 8.3, along with the details of the performance tests used to analyse each new sampling method. Section 8.4 describes the validation and derivation of the sampling methods for each of the seven distributions and summarises the results of the performance tests. Finally, the implementation of the developed methods within the simulation software is outlined in Section 8.5 and the conclusions are summarised in Section 8.6.

8.2 Theoretical Background

8.2.1 Statistical Distributions and Parameters

Most standard statistical distribution can be defined by a set of *parameters*. Although the detailed choice of parameters that appear in a distribution function is somewhat arbitrary, three *basic* parameters are typically defined (Forbes *et al.*, 2011);

1. The *location* parameter, a, is the horizontal distance to the location point (usually the lower or mid-point) of the range of the random variable.
2. The *scale* parameter, b, determines the scale of measurement of the probability distribution.
3. The *shape* parameter, c, determines the shape of the distribution function.

Generally, the symbols a, b, and c will be used to denote the location, scale and shape of the distribution throughout this chapter. Other symbols may be used where alternative conventions have been established. Furthermore, statistical distributions can have more than one shape parameter. For example, the Burr Type XII distribution (see Section 8.4.6) is defined by a location parameter a, a scale parameter b and *two* shape parameters; c and k.

8.2.2 Implementing the Stochastic Learning Curve Model

The stochastic learning curve (LC) model, proposed by Globerson and Gold (1997) and described in Chapter 7, defines formulae for the expected value, variance and probability density function (PDF) of a statistical distribution as a function of the task repetition number s. To implement this model within the time-domain Monte Carlo simulation software, additional methods are required that enable values to be sampled randomly, and efficiently, from these varying probability distributions. This chapter investigates two approaches; (i) a method that will be referred to as *parametric sampling* and (ii) the well-known *inverse transform sampling* method.

Parametric Sampling

Numerous statistical software packages are available that enable random samples to be drawn from a statistical distribution if the parameters of that distribution are known. Thus, a straightforward implementation of the LC model is possible if equations for the distribution parameters as a function of the task repetition number are obtained. Globerson and Gold (1997) described the implementation for the *Normal* distribution, which is defined by its location parameter μ, and its scale parameter σ, equal to the standard deviation of the distribution (Forbes *et al.*, 2011). The expected value of the Normal distribution is equal to the location parameter μ and its variance is equal to

the square of the scale parameter (σ^2). Consequently, the parameters of the Normal distribution are defined at each task repetition number by the mean and variance (see Equation 7.37 and Equation 7.38). Globerson and Gold (1997) state that their method is applicable for any probability distribution and outline a theoretical validation for the Normal distribution (see Section 7.2.4).

The *standardised* form of a distribution has a location parameter equal to 0 and a scale parameter equal to 1 (Natrella, 2010). Several formulae exist for converting from the *standardised* form to the *generalised* form where alternate location and scale parameters are specified. The formula for converting between the standardised and generalised form of the PDF, as described by Natrella (2010); Jones *et al.* (2001–); Forbes *et al.* (2011); Oliphant (2006), is

$$f(x;\, a\,,\, b) = \frac{1}{b}\, f\left(\frac{x-a}{b};\, 0\,,\, 1\right)\,, \tag{8.1}$$

where a and b are the location and scale as defined previously and $f(x)$ is the PDF.

Crucially, the location and scale parameters affect the distribution in a known way. As outlined by Oliphant (2006); Jones *et al.* (2001–), if y is a number drawn from a distribution with PDF $f_y(y)$, then

$$x = by + a \tag{8.2}$$

is a number drawn from a distribution with

$$f_x(x) = \frac{1}{b} f_y(y)\left(\frac{x-a}{b}\right)\,. \tag{8.3}$$

Equation 7.30, describing the PDF as a function of the task repetition number in the stochastic LC model, can be re-written as

$$f_s(x;\, a_s\,,\, b_s) = s^{-m}\, f_1\left(xs^{-m};\, a_1\,,\, b_1\right)\,, \tag{8.4}$$

where f_s and f_1 are the PDFs of the s^{th} and 1^{st} iterations respectively; s is the task repetition number; m is the learning slope; a_s and b_s are the location and scale parameters of the s^{th} unit and a_1 and b_1 are the location and scale parameters for the 1^{st} unit. The shape parameter(s) are not included in the formula but are represented within the PDFs.

Combining Equation 8.1 and Equation 8.4 demonstrates that the learning factor s^m

alters the location and scale parameters of the distribution;

$$f_s(x;\, a_s\,,\, b_s) = \frac{s^{-m}}{b_1}\, f_1\left(\frac{xs^{-m} - a_1}{b_1};\, 0\,,\, 1\right)\,,$$
$$f_s(x;\, a_s\,,\, b_s) = \frac{1}{b_1 s^m}\, f_1\left(\frac{x - a_1 s^m}{b_1 s^m};\, 0\,,\, 1\right)\,. \tag{8.5}$$

Furthermore, comparing Equation 8.5 and the normal expression for f_s;

$$f_s(x;\, a_s\,,\, b_1) = \frac{1}{b_s}\, f_s\left(\frac{x - a_s}{b_s};\, 0\,,\, 1\right)\,, \tag{8.6}$$

shows that

$$b_s = b_1\, s^m \tag{8.7}$$

and

$$a_s = a_1\, s^m\,. \tag{8.8}$$

The stochastic LC model thus implies that the 'nature' of the distribution, corresponding to the *shape* parameter(s), remains constant as the task repetition number varies, but the *location* and *scale* parameters are multiplied by a factor of s^m. Consequently, the parameters of the distribution are known for each iteration and the optimised sampling methods within standard statistical software packages can be employed.

It is common for statistical software packages to only compute the standardised form of probability distributions (Natrella, 2010). For example, the *NumPy* Python package (Oliphant, 2006) only implements optimal sampling methods, predominantly based on the algorithms described by Devroye (1986), for distributions in their standardised form. Conversely, packages such as *SciPy* (Jones *et al.*, 2001–) allow the full, generalised distribution to be defined. Often, as is the case with the SciPy package, the distributions first need to be *initialised*—a step when the parameters are explicitly defined—before random samples can be generated. The methods in NumPy (Oliphant, 2006) avoid these initialisation stages and act as simple functions that accept the distribution shape parameters as input arguments and return the random variable directly.

Inverse Transform Sampling

Inverse transform sampling is a method for generating non-uniform, pseudo-random numbers (Devroye, 1986). Most statistical software packages use this method—or accurate approximations to the underlying theory—to implement random sampling functionality for a large proportion of distributions (Lemieux, 2009; Devroye, 1986). The inversion principle states that if Y is a random variable with a standard uniform distribution, $Y \sim \mathcal{U}(0,1)$, and if X is a continuous random variable with cumulative distribution function F_X, then the random variable ${F_X}^{-1}(Y)$ has the same distribution as X (Devroye, 1986). As such, the inverse transform sampling method can be broken down into two steps:

1. Generate a random number u from the standard uniform distribution, $u \sim \mathcal{U}(0,1)$.
2. Compute the value x such that $F_X(x) = u$ or $x = {F_X}^{-1}(u)$.

The value x is thus a random number drawn from the distribution F_X. Inverse transform sampling is only applicable for distributions that have closed-form expressions for their cumulative distribution functions (CDFs). The CDFs of certain distributions, such as the Normal and Gamma distributions are not invertible and thus the inversion principle cannot be applied directly (Lemieux, 2009).

As an example, consider the exponential distribution with CDF

$$y = F(x) = 1 - e^{-\lambda x} \quad \text{for } x \geq 0\,. \tag{8.9}$$

The inverse function can be obtained by solving $y = F(x)$:

$$x = F^{-1}(y) = -\frac{1}{\lambda}\ln(1-y)\,. \tag{8.10}$$

Figure 8.1 shows the transformation method for $\lambda = 0.5$. A sample of 10 evenly-spaced points on [0, 1] are substituted into Equation 8.10, to obtain the corresponding x-values. The figure shows that many of the points are transformed to a point close to 0, while only a few are transformed to high values of x. This is the expected result for an exponential distribution.

8.2.3 Cumulative Distribution Function

It is possible to derive a relationship for the variation of the cumulative distribution function (CDF) with the task repetition number using the equation derived by Globerson and Gold (1997) for the PDF. Equation 8.4 can be simplified as

$$f_s(x) = s^{-m} f_1(s^{-m}x)\,. \tag{8.11}$$

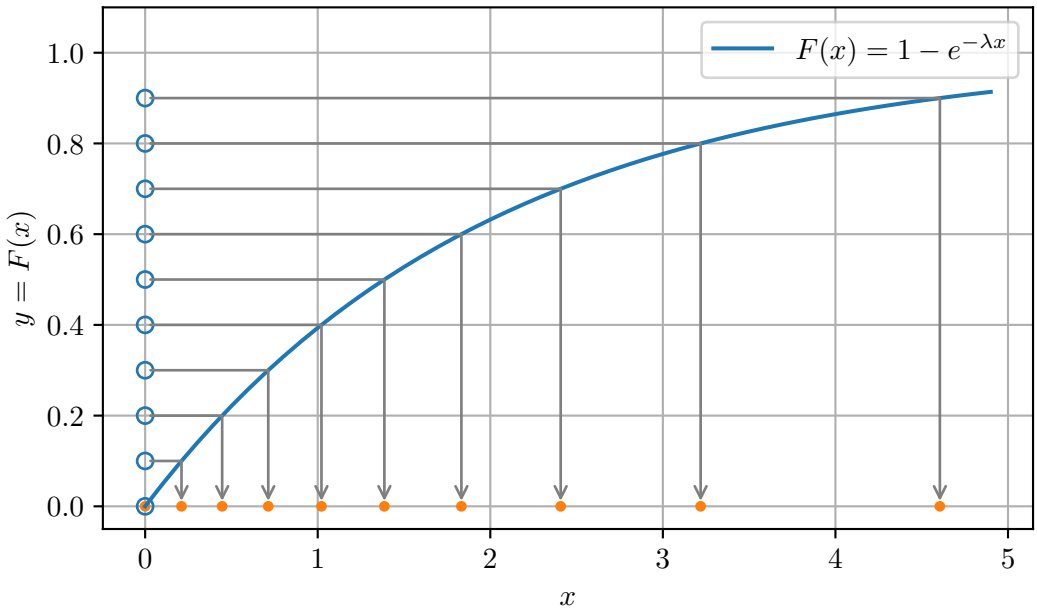

Figure 8.1: Inverse transform sampling method.

Using the standard rule for integration that

$$\int f(qx)\,dx = \frac{1}{q}\,F(qx) + Q \tag{8.12}$$

where $f(x)$ is the PDF, $F(x)$ is the CDF and q and Q are constants, the equation for the CDF can be derived:

$$\begin{aligned} F_s(x) &= \int_{-\infty}^{x} f_s(x)\,dx\,, \\ F_s(x) &= \int_{-\infty}^{x} s^{-m} f_1(s^{-m}x)\,dx\,, \\ F_s(x) &= s^{-m}\int_{-\infty}^{x} f_1(s^{-m}x)\,dx\,, \\ \implies F_s(x) &= F_1(s^{-m}x) \end{aligned} \tag{8.13}$$

Applying the theory of inverse transform sampling:

$$\begin{aligned} x &= {F_s}^{-1}(y)\,, \\ s^{-m}x &= {F_1}^{-1}(y)\,, \\ \implies x &= {F_s}^{-1}(y) = s^m {F_1}^{-1}(y)\,. \end{aligned} \tag{8.14}$$

8.2.4 Selected Distributions

The five candidate distributions that were ranked in the top three distributions according to the Anderson-Darling statistic, as summarised in Table 7.12, are included for analysis, along with the Beta-PERT and Triangular distributions. The Beta-PERT (Program Evaluation and Review Technique) distribution has received significant attention since it was first proposed by Malcolm *et al.* (1959). The distribution is a transformation of the four-parameter Beta distribution (Forbes *et al.*, 2011) and is particularly suitable for simulation methods that model variable activity times—especially when there is no data available to which a distribution can be fitted and when subjective knowledge of the process under study is required (Farnum and Stanton, 1987). Similarly, the Triangular distribution (Kotz and Van Dorp, 2004; Forbes *et al.*, 2011) is defined by the minimum, maximum and most common values and is often used in simulation models and risk assessment.

Consequently, this chapter focuses on the following statistical distributions;

1. Gamma,
2. Lognormal,
3. Beta-PERT,
4. Triangular
5. Weibull,
6. Burr and
7. Loglogistic.

8.3 Methodology

The analysis of each of the statistical distributions listed above is divided into five categories; (*i*) distribution definitions, (*ii*) theoretical validation, (*iii*) derivation of the inverse transform sampling formula, (*iv*) empirical validation and (*v*) performance testing. The derivation of the inverse transform sampling formula is only possible for those distributions that have closed-form expressions for their CDFs. Specifically, these derivations are not included for the Gamma, Lognormal and Beta-PERT distributions.

8.3.1 Distribution Definitions

The parameters and PDF of each distribution are defined. If applicable, the definition for the CDF is also given. As far as possible, the statistical distribution definitions follow the conventions of Forbes *et al.* (2011).

8.3.2 Theoretical Validation

In a similar manner to the validation of the theory for the Normal distribution described by Globerson and Gold (1997), a theoretical validation of the stochastic LC model is outlined for each distribution. The purpose of these mathematical descriptions is to confirm that the *shape* of the distribution remains constant as the task repetition number varies, but the *location* and *scale* parameters are multiplied by a factor of s^m.

8.3.3 Derivation of Inverse Transform Sampling Formula

The inverse transform sampling method is used to derive an equation that enables random sampling from the specified distribution. Crucially, the derived equations incorporate the learning curve phenomenon and require the task repetition number s and the learning slope m as arguments.

8.3.4 Empirical Validation

The derived sampling methods are validated empirically for a hypothetical set of distribution and learning parameters. 10,000 random samples are generated using the developed sampling methods and normalised histograms of these data are plotted against the theoretical PDFs calculated using Equation 7.30. As in Chapter 7, the histogram bin widths are calculated as the maximum of the Sturges (Sturges, 1926; Scott, 2009) and Freedman-Diaconis (Freedman and Diaconis, 1981) estimators.

For the parametric sampling method, the *NumPy* package is used to generate a random sample from the standardised form of the appropriate distribution. The value is then transformed to the appropriate task repetition number using Equation 8.2 where $b = b_s = b_1 s^m$ and $a = a_s = a_1 s^m$. For the inverse transform sampling method, the derived equations developed as per Section 8.3.3 are used directly. For the Gamma, Lognormal and Beta-PERT distributions, only the parametric sampling methods are used because the inversion principle is not applicable. The Burr and Loglogistic distributions are not available in the NumPy package so only the inverse transform sampling method is applied in these cases. The impact of their availability is appraised in the results section (8.4.8). Both sampling methods are used for the Triangular and Weibull distributions.

8.3.5 Performance Testing

Finally, the computational performance of the sampling methods are assessed, assuming the same hypothetical set of distribution and learning parameters used for the empirical validation. The performance tests emulate the implementation of the sampling procedures within the time-domain simulations that is discussed in Section 8.5. A single *simulation* consists of generating 100 samples corresponding to successive iterations of a hypothetical operation. 10,000 of these simulations are performed. Following conventions for profiling code and measuring average run-times (see notes on the `timeit` module in McKinney, 2012; Lutz, 2013), this entire procedure is repeated three times for each sampling method and the fastest of these is recorded.

Three sampling methods are assessed in the performance tests. The *standardised parametric* sampling method follows the procedure described in Section 8.3.4 where the *NumPy* package (Oliphant, 2006) is used to sample from the standardised form of the distribution and Equation 8.2 is used to transform the data according to the task repetition number. Similarly, the *inverse transform* sampling method uses the formulae derived in Section 8.3.3. The third method, referred to as the *generalised parametric* sampling method, uses the *SciPy* package (Jones *et al.*, 2001–) and specifies the generalised distribution for each iteration of the operation. As mentioned previously, these generalised distribution methods require the distributions to be initialised for each task repetition. For the performance tests, this initialisation stage is not included in the function being analysed. The Python script that implements these performance tests is documented in Appendix A.

8.4 Validations, Derivations and Results

8.4.1 Gamma Distribution

Distribution Definitions

The Gamma distribution is defined by its location parameter a, its scale parameter $b > 0$ and its shape parameter $c > 0$ (see, e.g. Forbes *et al.*, 2011). The PDF of the Gamma distribution is given by

$$f(x) = \frac{1}{\Gamma(c)\, b^c}\ (x-a)^{c-1}\ e^{-\dfrac{(x-a)}{b}}\ , \tag{8.15}$$

where Γ is the gamma function.

Theoretical Validation

An equation for the PDF of the s^{th} unit can be obtained using Equation 8.4:

$$\begin{aligned} f_s(x) &= s^{-m} f_1(s^{-m}x)\,, \\ &= \frac{s^{-m}}{\Gamma(c_1)\, {b_1}^{c_1}}\ \left(s^{-m}x - a_1\right)^{c_1-1}\ e^{-\dfrac{(s^{-m}x - a_1)}{b_1}}\,, \\ &= \frac{1}{\Gamma(c_1)\, {b_1}^{c_1}\, s^m}\ \left(\frac{x - a_1 s^m}{s^m}\right)^{c_1-1}\ e^{-\dfrac{(x - a_1 s^m)}{b_1 s^m}}\,, \\ &= \frac{1}{\Gamma(c_1)\ (b_1 s^m)^{c_1}}\ (x - a_1 s^m)^{c_1-1}\ e^{-\dfrac{(x - a_1 s^m)}{b_1 s^m}}\,. \end{aligned} \tag{8.16}$$

Comparing Equation 8.16 to Equation 8.15 evaluated at $f_s(x; a_s, b_s, c_s)$, shows that

$$\begin{aligned} a_s &= a_1 s^m\,, \\ b_s &= b_1 s^m \end{aligned}$$

and

$$c_s = c_1\,.$$

Empirical Validation

The empirical validation for the Gamma distribution shown in Figure 8.2 was generated assuming that $a_1 = 2$, $b_1 = 0.5$, $c_1 = 6.3$, $s = 10$ and $m = -0.15$. The figure shows an adequate validation of the parametric sampling method for the Gamma distribution.

8.4.2 Lognormal Distribution

Distribution Definitions

A Lognormal distribution is the continuous probability distribution of a random variable whose logarithm is normally distributed (see Forbes *et al.*, 2011). It is defined by its location parameter a, its scale parameter $\omega > 0$ and its shape parameter $\sigma > 0$. An alternative parameter μ_L is defined that is the mean of the logarithm of the random variable X and is related to the scale parameter by $\omega = e^{\mu_L}$ and $\mu_L = \ln \omega$. The shape parameter σ is the standard deviation of the logarithm of the random variable X. The scale parameter ω is usually given the symbol m (see Forbes *et al.*, 2011), but this has been changed to avoid confusion with the learning slope m.

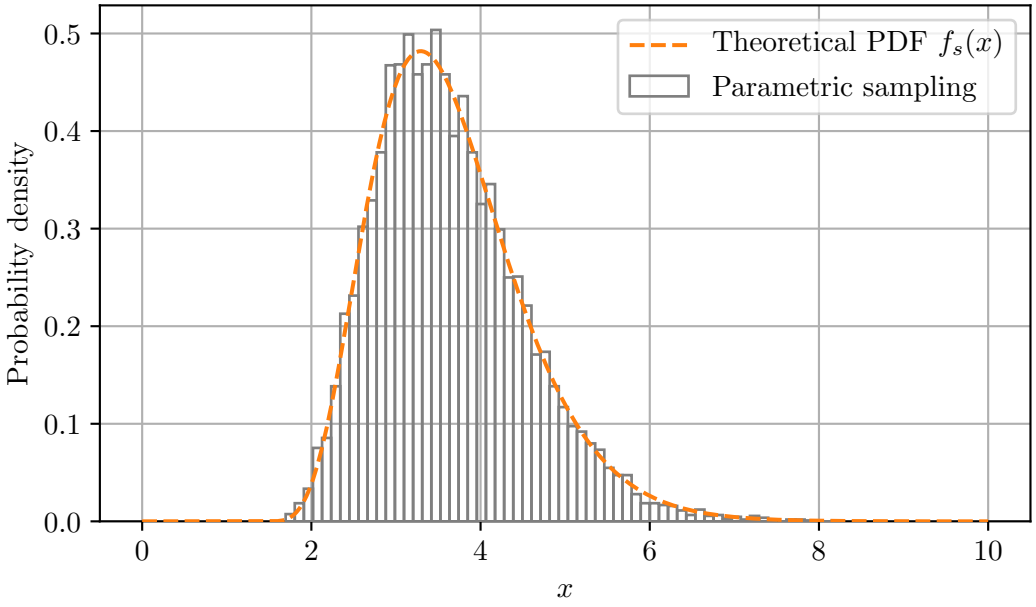

Figure 8.2: Empirical validation of parametric sampling method for the Gamma distribution.

The PDF of the lognormal distribution, as defined by Forbes *et al.* (2011), is

$$f(x) = \frac{1}{(x-a)\sigma\sqrt{2\pi}}\, e^{-\frac{\left(\ln\frac{x-a}{\omega}\right)^2}{2\sigma^2}}. \tag{8.17}$$

Theoretical Validation

An equation for the PDF of the s^{th} unit can be obtained using Equation 8.4:

$$\begin{aligned} f_s(x) &= s^{-m} f_1(s^{-m}x)\,, \\ &= \frac{s^{-m}}{(s^{-m}x - a_1)\sigma_1\sqrt{2\pi}}\, e^{-\frac{\left(\ln\frac{s^{-m}x - a_1}{\omega_1}\right)^2}{2{\sigma_1}^2}}\,, \\ &= \frac{1}{(x - a_1 s^m)\sigma_1\sqrt{2\pi}}\, e^{-\frac{\left(\ln\frac{x - a_1 s^m}{\omega_1 s^m}\right)^2}{2{\sigma_1}^2}}. \end{aligned} \tag{8.18}$$

Comparing Equation 8.18 to Equation 8.17 evaluated at $f_s(x; a_s, \sigma_s, \omega_s)$, shows that

$$a_s = a_1 s^m \,,$$
$$\omega_s = \omega_1 s^m$$

and

$$\sigma_s = \sigma_1 \,.$$

Empirical Validation

The empirical validation for the Lognormal distribution shown in Figure 8.3 was generated assuming that $a_1 = 2$, $\sigma_1 = 0.4$, $\mu_1 = 1.1$, $s = 10$ and $m = -0.15$. The figure shows an adequate validation of the parametric sampling method for the Lognormal distribution.

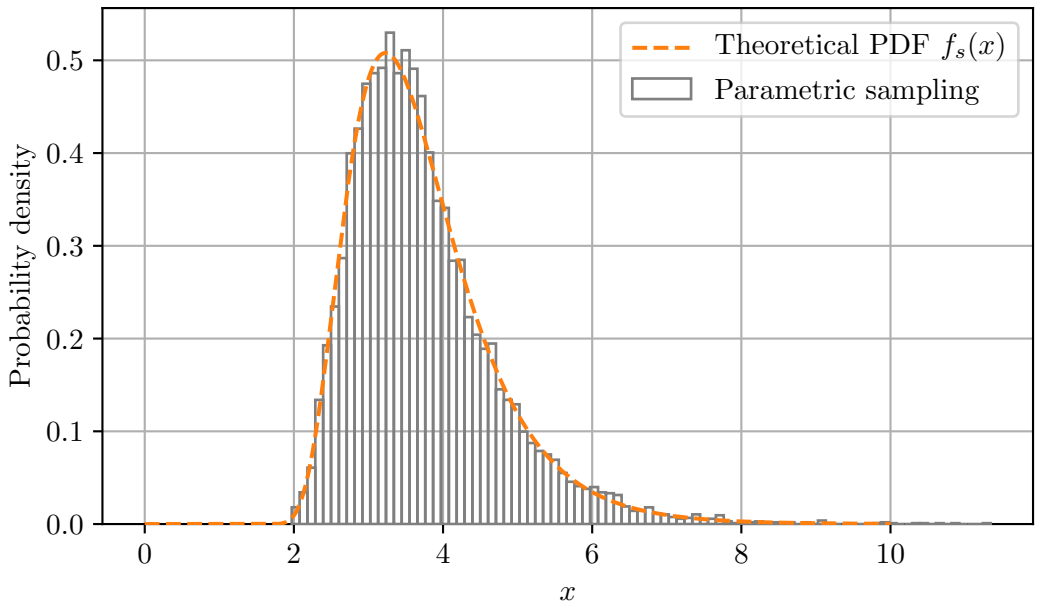

Figure 8.3: Empirical validation of parametric sampling method for the Lognormal distribution.

8.4.3 Beta-PERT Distribution

Distribution Definitions

The Beta-PERT distribution (for example, as discussed by Forbes *et al.* (2011); Malcolm *et al.* (1959); Farnum and Stanton (1987); Littlefield Jr and Randolph (1987) and Davis (2008)) has three parameters; a is the location parameter, equal to the minimum possible value; b is the maximum possible value and ν is the most likely or modal value. The scale parameter is equal to $b - a$. The distribution has two shape parameters, α and β, which are defined below. The PDF of the Beta-PERT distribution is given by

$$f(x) = \frac{(x-a)^{\alpha-1}(b-x)^{\beta-1}}{\mathrm{B}(\alpha,\beta)(b-a)^{\alpha+\beta-1}}\,, \tag{8.19}$$

where $\mathrm{B}(\alpha,\beta)$ is the beta function,

$$\alpha = \frac{4\nu + b - 5a}{b-a} \tag{8.20}$$

and

$$\beta = \frac{5b - a - 4\nu}{b-a}\,. \tag{8.21}$$

As part of the definition and derivation of the Beta-PERT distribution (see, e.g. Malcolm *et al.*, 1959; Farnum and Stanton, 1987; Littlefield Jr and Randolph, 1987; Davis, 2008), the formula for the expected value is

$$\mathrm{E}[X] = \frac{a + 4\nu + b}{6} = \mu\,. \tag{8.22}$$

Theoretical Validation

An equation for the PDF of the s^{th} unit can be obtained using Equation 8.4:

$$\begin{aligned}
f_s(x) &= s^{-m} f_1(s^{-m}x)\,,\\
&= s^{-m}\frac{(s^{-m}x - a_1)^{\alpha_1-1}(b_1 - s^{-m}x)^{\beta_1-1}}{\mathrm{B}(\alpha_1,\beta_1)(b_1-a_1)^{\alpha_1+\beta_1-1}}\,,\\
&= \frac{(x - a_1 s^m)^{\alpha_1-1}(b_1 s^m - x)^{\beta_1-1}}{s^m\,\mathrm{B}(\alpha_1,\beta_1)(b_1-a_1)^{\alpha_1+\beta_1-1}\,s^{m(\alpha_1-1)}\,s^{m(\beta_1-1)}}\,,\\
&= \frac{(x - a_1 s^m)^{\alpha_1-1}(b_1 s^m - x)^{\beta_1-1}}{\mathrm{B}(\alpha_1,\beta_1)(b_1-a_1)^{\alpha_1+\beta_1-1}\,(s^m)^{\alpha_1+\beta_1-1}}\,,\\
&= \frac{(x - a_1 s^m)^{\alpha_1-1}(b_1 s^m - x)^{\beta_1-1}}{\mathrm{B}(\alpha_1,\beta_1)(b_1 s^m - a_1 s^m)^{\alpha_1+\beta_1-1}}\,.
\end{aligned} \tag{8.23}$$

Comparing Equation 8.23 to Equation 8.19 evaluated at $f_s(x; \alpha_s, \beta_s, a_s, b_s)$, shows that

$$\begin{aligned} a_s &= a_1 s^m \,, \\ b_s &= b_1 s^m \,, \\ \alpha_s &= \alpha_1 \end{aligned}$$

and

$$\beta_s = \beta_1 \,.$$

Equation 8.22 can be used to derive an expression for the modal parameter ν. Starting with the relationship given in Equation 7.18;

$$\begin{aligned} \mu_s = \mathrm{E}[X_s] = \mathrm{E}[X_1] s^m = \mu_1 s^m \\ \implies \frac{a_s + 4\nu_s + b_s}{6} = \frac{a_1 + 4\nu_1 + b_1}{6} s^m \,, \\ \implies a_1 s^m + 4c_s + b_1 s^m = a_1 s^m + 4\nu_1 s^m + b_1 s^m \,, \\ \implies \nu_s = \nu_1 s^m \,. \end{aligned}$$

The relationship for the scale parameter also follows from the above validation;

$$\begin{aligned} b_s - a_s &= b_1 s^m - a_1 s^m \,, \\ b_s - a_a &= (b_1 - a_1) s^m \,. \end{aligned}$$

Empirical Validation

The empirical validation for the Beta-PERT distribution shown in Figure 8.4 was generated assuming that $a_1 = 1$, $b_1 = 9$, $\nu_1 = 5$, $s = 10$ and $m = -0.15$. The figure shows an adequate validation of the parametric sampling method for the Beta-PERT distribution.

8.4.4 Triangular Distribution

Distribution Definitions

Similar to the Beta-PERT distribution, the Triangular distribution has three parameters; a is the location parameter, equal to the minimum possible value; b is the maximum possible value and ν is the most likely or modal value. The scale parameter is equal to

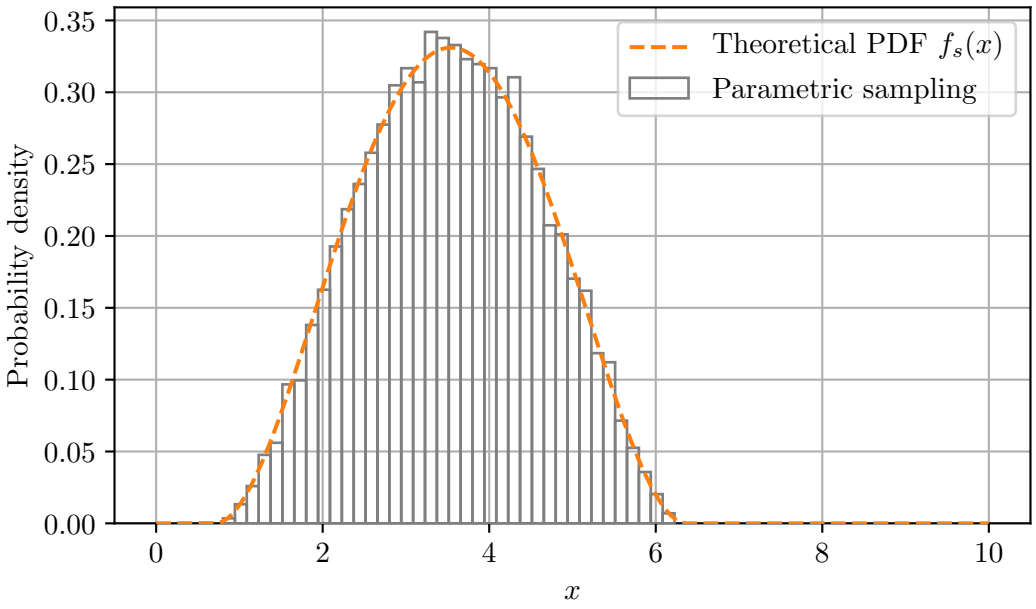

Figure 8.4: Empirical validation of parametric sampling method for the Beta-PERT distribution.

$b - a$. The PDF of the Triangular distribution is given by

$$f(x) = \begin{cases} \dfrac{2(x-a)}{(b-a)(\nu-a)}, & \text{if } a \leq x \leq \nu \\ \dfrac{2(b-x)}{(b-a)(b-\nu)}, & \text{if } \nu \leq x \leq b\,. \end{cases} \tag{8.24}$$

Theoretical Validation

If $a_s \leq x \leq \nu_s$;

$$\begin{aligned} f_s &= s^{-m} f_1(s^{-m}x)\,, \\ &= \frac{2s^{-m}(s^{-m}x - a_1)}{(b_1 - a_1)(\nu_1 - a_1)}\,, \\ &= \frac{2(x - a_1 s^m)}{s^m s^m (b_1 - a_1)(\nu_1 - a_1)}\,, \\ &= \frac{2(x - a_1 s^m)}{(b_1 s^m - a_1 s^m)(\nu_1 s^m - a_1 s^m)}\,. \end{aligned} \tag{8.25}$$

If $\nu_s \leq x \leq b_s$;

$$\begin{aligned} f_s &= s^{-m} f_1(s^{-m}x)\,, \\ &= \frac{2s^{-m}(b_1 - xs^{-m})}{(b_1 - a_1)(b_1 - \nu_1)}\,, \\ &= \frac{2(b_1 s^m - x}{s^m s^m (b_1 - a_1)(b_1 - \nu_1)}\,, \\ &= \frac{2(b_1 s^m - x)}{(b_1 s^m - a_1 s^m)(\nu_1 s^m - a_1 s^m)}\,, \end{aligned} \tag{8.26}$$

Comparing Equations 8.25 and 8.26 to Equation 8.24 evaluated at $f_s(x; a_s, b_s, \nu_s)$, shows that

$$\begin{aligned} a_s &= a_1 s^m\,, \\ b_s &= b_1 s^m \end{aligned}$$

and

$$\nu_s = \nu_1 s^m\,.$$

Similar to the Beta-PERT distribution, the scale parameter of the Triangular distribution is

$$\begin{aligned} b_s - a_s &= b_1 s^m - a_1 s^m\,, \\ b_s - a_a &= (b_1 - a_1)s^m\,. \end{aligned}$$

The shape parameter is defined by Jones *et al.* (2001–) as the distance between the minimum a and the mode ν divided by the scale $b - a$;

$$c = \frac{\nu - a}{b - a}\,. \tag{8.27}$$

Consequently,

$$\begin{aligned} c_s &= \frac{\nu_s - a_s}{b_s - a_s}\,, \\ &= \frac{\nu_1 s^m - a_1 s^m}{b_1 s^m - a_1 s^m}\,, \\ &= \frac{\nu_1 - a_1}{b_1 - a_1}\,, \\ \implies c_s &= c_1\,. \end{aligned}$$

Inverse Transform Sampling Function

Kotz and Van Dorp (2004) have already derived the inverse CDF for the Triangular distribution;

$$x = F^{-1}(y) = \begin{cases} a + \sqrt{y(\nu - a)(b - a)}, & \text{if } 0 \leq y \leq c \\ b - \sqrt{(1 - y)(b - \nu)(b - a)}, & \text{if } c \leq y \leq 1\,. \end{cases} \tag{8.28}$$

Applying Equation 8.14, the sampling function for the Triangular distribution for any task repetition number is given by

$$x = s^m {F_1}^{-1}(y)\,, \tag{8.29}$$

where

$${F_1}^{-1}(y) = \begin{cases} a_1 + \sqrt{y(\nu_1 - a_1)(b_1 - a_1)}, & \text{if } 0 \leq y \leq c_1 \\ b_1 - \sqrt{(1 - y)(b_1 - \nu_1)(b_1 - a_1)}, & \text{if } c_1 \leq y \leq 1\,. \end{cases} \tag{8.30}$$

Empirical Validation

The empirical validation for the Triangular distribution shown in Figure 8.5 was generated assuming that $a_1 = 1$, $b_1 = 9$, $\nu_1 = 5$, $s = 10$ and $m = -0.15$. The figure shows an adequate validation for both the parametric and inverse transform sampling methods for the Triangular distribution.

8.4.5 Weibull Distribution

Distribution Definitions

The Weibull distribution is defined by its location parameter a, its scale parameter η and its shape parameter γ (Forbes *et al.*, 2011). The PDF of the Weibull distribution is

$$f(x) = \frac{\gamma\,(x - a)^{\gamma - 1}}{\eta^{\gamma}}\, e^{-\left(\frac{x - a}{\eta}\right)^{\gamma}}\,. \tag{8.31}$$

The Weibull distribution CDF is given by

$$F(x) = 1 - e^{-\left(\frac{x - a}{\eta}\right)^{\gamma}}\,. \tag{8.32}$$

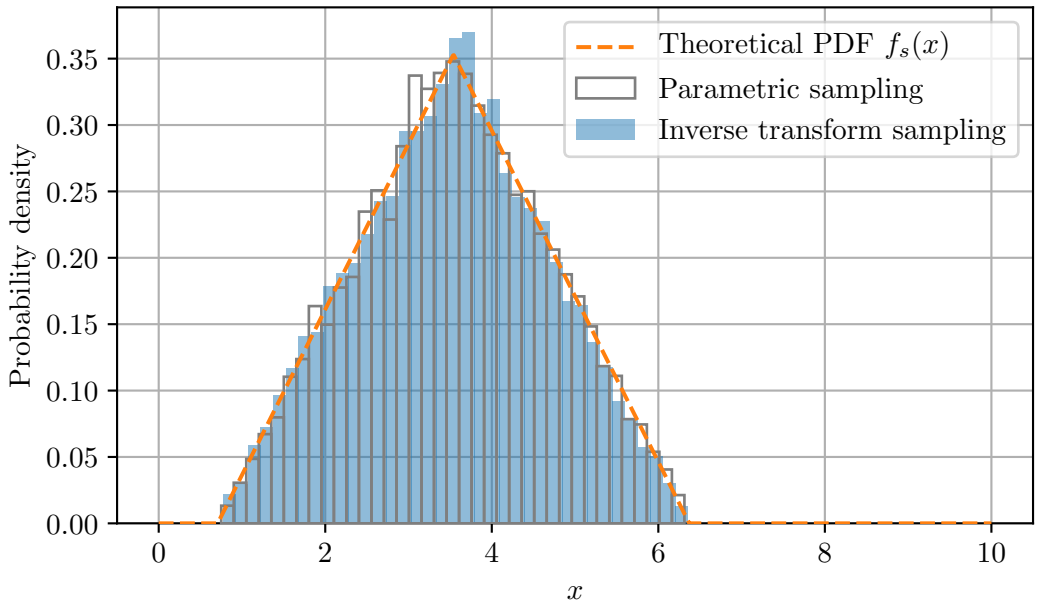

Figure 8.5: Empirical validation of parametric and inverse transform sampling methods for the Triangular distribution.

Theoretical Validation

An equation for the PDF of the s^{th} unit can be obtained using Equation 8.4:

$$
\begin{aligned}
f_s(x) &= s^{-m} f_1(s^{-m}x)\,, \\
&= \frac{s^{-m}\,\gamma_1\,(s^{-m}x - a_1)^{\gamma_1 - 1}}{{\eta_1}^{\gamma_1}}\, e^{-\left(\frac{s^{-m}x - a_1}{\eta_1}\right)^{\gamma_1}}\,, \\
&= \frac{\gamma_1\,(x - a_1 s^m)^{\gamma_1 - 1}}{{\eta_1}^{\gamma_1}\, s^m\, s^{m(\gamma_1 - 1)}}\, e^{-\left(\frac{x - a_1 s^m}{\eta_1 s^m}\right)^{\gamma_1}}\,, \\
&= \frac{\gamma_1\,(x - a_1 s^m)^{\gamma_1 - 1}}{(\eta_1 s^m)^{\gamma_1}}\, e^{-\left(\frac{x - a_1 s^m}{\eta_1 s^m}\right)^{\gamma_1}}\,.
\end{aligned}
\tag{8.33}
$$

Comparing Equation 8.33 to Equation 8.31 evaluated at $f_s(x; a_s, \eta_s, \gamma_s)$, shows that

$$
\begin{aligned}
a_s &= a_1 s^m\,, \\
\eta_s &= \eta_1 s^m
\end{aligned}
$$

and

$$\gamma_s = \gamma_1 \,.$$

Inverse Transform Sampling Function

Using Equation 8.13,

$$\begin{aligned} y &= F_s(x)\,, \\ &= F_1(s^{-m}x)\,, \\ &= 1 - e^{-\left(\frac{s^{-m}x - a_1}{\eta_1}\right)^{\gamma_1}} \,. \end{aligned} \tag{8.34}$$

Following the inversion principle and solving for x;

$$\begin{aligned} 1 - y &= e^{-\left(\frac{s^{-m}x - a_1}{\eta_1}\right)^{\gamma_1}}\,, \\ \ln(1-y) &= -\left(\frac{s^{-m}x - a_1}{\eta_1}\right)^{\gamma_1}\,, \\ (-\ln(1-y))^{\frac{1}{\gamma_1}} &= \frac{s^{-m}x - a_1}{\eta_1}\,, \\ \implies x &= s^m\left(\eta_1\left(-\ln(1-y)\right)^{\frac{1}{\gamma_1}} + a_1\right)\,. \end{aligned} \tag{8.35}$$

Empirical Validation

The empirical validation for the Weibull distribution shown in Figure 8.6 was generated assuming that $a_1 = 0.5$, $\eta_1 = 1$, $\gamma_1 = 2$, $s = 10$ and $m = -0.15$. The figure shows an adequate validation for both the parametric and inverse transform sampling methods for the Weibull distribution.

8.4.6 Burr Type XII Distribution

Distribution Definitions

The Burr Type XII distribution is defined by its location parameter a, its scale parameter b and two shape parameters; c and k (Burr, 1942). The PDF of the Burr distribution is

$$f(x) = \frac{ck}{b}\left(\frac{x-a}{b}\right)^{c-1}\left(1 + \left(\frac{x-a}{b}\right)^{c}\right)^{-k-1} \,. \tag{8.36}$$

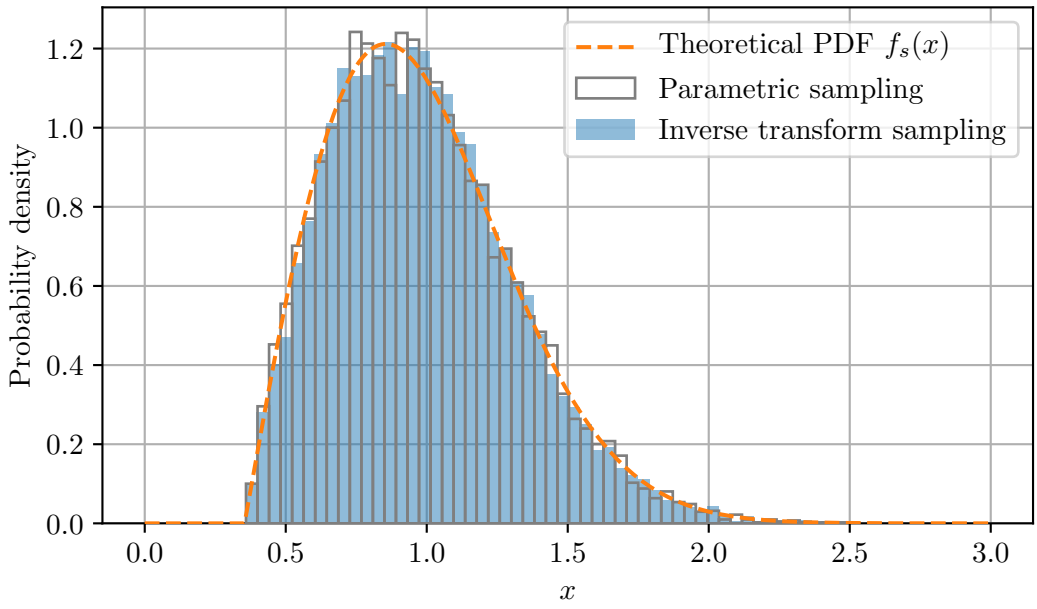

Figure 8.6: Empirical validation of parametric and inverse transform sampling methods for the Weibull distribution.

The CDF of the Burr distribution is

$$F(x) = 1 - \left(1 + \left(\frac{x-a}{b}\right)^{c}\right)^{-k} . \tag{8.37}$$

Theoretical Validation

An equation for the PDF of the s^{th} unit can be obtained using Equation 8.4:

$$\begin{aligned} f_s(x) &= s^{-m} f_1(s^{-m}x)\,, \\ &= \frac{s^{-m}c_1k_1}{b_1}\left(\frac{s^{-m}x - a_1}{b_1}\right)^{c_1-1}\left(1 + \left(\frac{s^{-m}x - a_1}{b_1}\right)^{c_1}\right)^{-k_1-1}\,, \\ &= \frac{c_1k_1}{b_1s^m}\left(\frac{x - a_1s^m}{b_1s^m}\right)^{c_1-1}\left(1 + \left(\frac{x - a_1s^m}{b_1s^m}\right)^{c_1}\right)^{-k_1-1} . \end{aligned} \tag{8.38}$$

Comparing Equation 8.38 to Equation 8.36 evaluated at $f_s(x; a_s, b_s, c_s, k_s)$, shows that

$$\begin{aligned} a_s &= a_1s^m\,, \\ b_s &= b_1s^m\,, \\ c_s &= c_1 \end{aligned}$$

and

$$k_s = k_1 \,.$$

Inverse Transform Sampling Function

Using Equation 8.13,

$$\begin{aligned} y &= F_s(x)\,, \\ &= F_1(s^{-m}x)\,, \\ &= 1 - \left(1 + \left(\frac{s^{-m}x - a_1}{b_1}\right)^{c_1}\right)^{-k_1} . \end{aligned} \tag{8.39}$$

Following the inversion principle and solving for x;

$$\begin{aligned} 1 - y &= \left(1 + \left(\frac{s^{-m}x - a_1}{b_1}\right)^{c_1}\right)^{-k_1} , \\ (1-y)^{-\frac{1}{k_1}} &= \left(1 + \left(\frac{s^{-m}x - a_1}{b_1}\right)^{c_1}\right) , \\ \left((1-y)^{-\frac{1}{k_1}} - 1\right)^{\frac{1}{c_1}} &= \frac{s^{-m}x - a_1}{b_1}\,, \\ \implies x &= s^m \left(b_1 \left((1-y)^{-\frac{1}{k_1}} - 1\right)^{\frac{1}{c_1}} + a_1\right) . \end{aligned} \tag{8.40}$$

Empirical Validation

The empirical validation for the Burr distribution shown in Figure 8.7 was generated assuming that $a_1 = 0.5$, $b_1 = 1.5$, $c_1 = 8$, $k_1 = 0.5$, $s = 10$ and $m = -0.15$. The figure shows an adequate validation for the inverse transform sampling method for the Burr distribution.

8.4.7 Loglogistic Distribution

Distribution Definitions

The Loglogistic distribution, also known as the Fisk distribution, is defined by its location parameter a, its scale parameter b and shape parameter c. The Loglogistic distribution is a equal to the Burr Type XII distribution when the second shape parameter of the Burr distribution $k = 1$ (Jones *et al.*, 2001–; Burr, 1942). As such, the

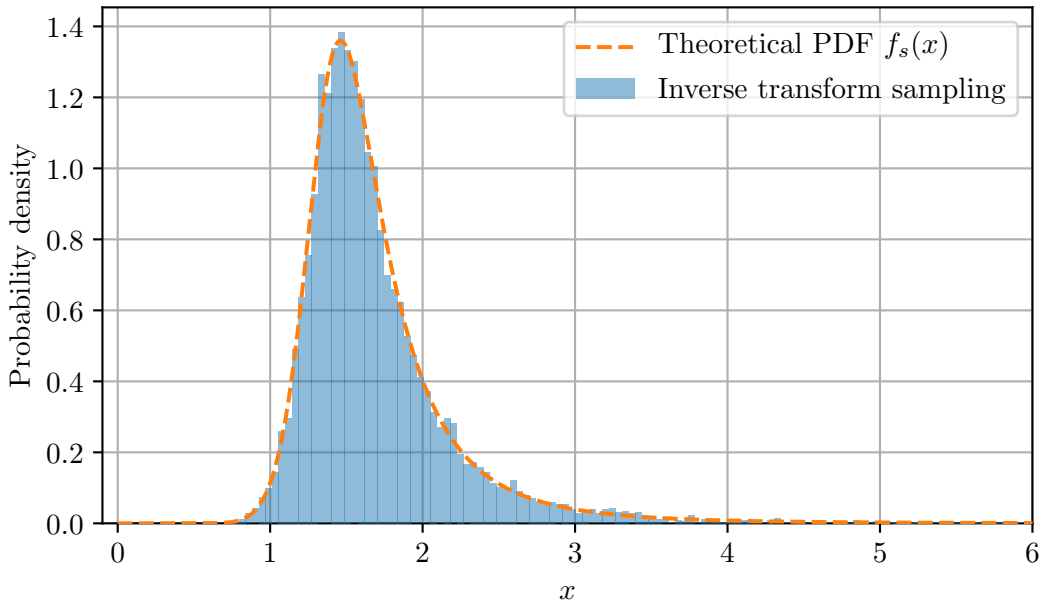

Figure 8.7: Empirical validation of inverse transform sampling method for the Burr distribution.

PDF and CDF follow directly from Equations 8.36 and 8.37;

$$\begin{aligned} f(x) &= \frac{c}{b}\left(\frac{x-a}{b}\right)^{c-1}\left(1+\left(\frac{x-a}{b}\right)^{c}\right)^{-2}. \\ &= \frac{\frac{c}{b}\left(\frac{x-a}{b}\right)^{c-1}}{\left(1+\left(\frac{x-a}{b}\right)^{c}\right)^{2}}. \end{aligned} \tag{8.41}$$

$$\begin{aligned} F(x) &= 1-\left(1+\left(\frac{x-a}{b}\right)^{c}\right)^{-1}, \\ &= \frac{1+\left(\frac{x-a}{b}\right)^{c}-1}{1+\left(\frac{x-a}{b}\right)^{c}}, \\ &= \frac{1}{1+\left(\frac{x-a}{b}\right)^{-c}}. \end{aligned} \tag{8.42}$$

The theoretical validation is identical to that previously described for the Burr distri-

bution with $k = k_s = k_1 = 1$ and thus is not presented.

Inverse Transform Sampling Function

Using Equation 8.13,

$$\begin{aligned} y &= F_s(x)\,, \\ &= F_1(s^{-m}x)\,, \\ &= \frac{1}{1 + \left(\dfrac{s^{-m}x - a_1}{b_1}\right)^{-c_1}}\,. \end{aligned} \tag{8.43}$$

Using the inverse transform sampling method and solving for x;

$$\begin{aligned} \left(\frac{s^{-m}x - a_1}{b_1}\right)^{-c_1} &= \frac{1}{y} - 1\,, \\ \frac{s^{-m}x - a_1}{b_1} &= \left(\frac{1-y}{y}\right)^{-\frac{1}{c_1}}\,, \\ s^{-m}x - a_1 &= b_1 \left(\frac{y}{1-y}\right)^{\frac{1}{c_1}}\,, \\ \implies x &= s^m \left(b_1 \left(\frac{y}{1-y}\right)^{\frac{1}{c_1}} + a_1\right)\,. \end{aligned} \tag{8.44}$$

Empirical Validation

The empirical validation for the Loglogistic distribution shown in Figure 8.8 was generated assuming that $a_1 = 0.5$, $b_1 = 1.5$, $c_1 = 8$, $s = 10$ and $m = -0.15$. The figure shows an adequate validation for the inverse transform sampling method for the Loglogistic distribution.

8.4.8 Performance Testing

The performance test results for the three sampling methods are summarised in Table 8.1. The standardised parametric and inverse transform sampling methods are far superior to the generalised parametric methods. The range in simulation time for the standardised parametric and inverse transform sampling methods is 0.721–1.94 seconds while the range for the generalised parametric results is 24.5–35.1 seconds. Considering the tests measure the simulation time of a single operation, this discrepancy in results is significant. On average, the run-times for the generalised parametric sampling methods

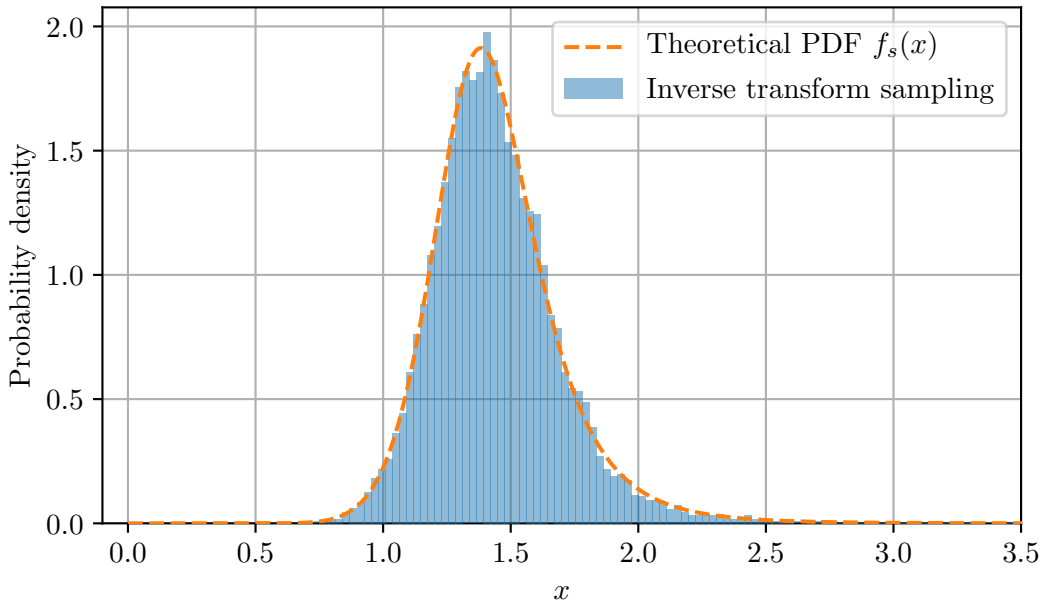

Figure 8.8: Empirical validation of inverse transform sampling method for the Loglogistic distribution.

are 23 times slower than the equivalent inverse transform and standardised parametric sampling implementations. Noting the importance of computational efficiency and speed in Monte Carlo simulation procedures, the standardised parametric and inverse transform sampling methods are strongly recommended. Additionally, the results shown in Table 8.1 do not take into account the *initialisation* stage that is required for the generalised case but not for the other two methods.

Table 8.1: Performance test results—simulation time measured in seconds.

	Sampling method		
	Standardised Parametric	*Inverse Transform*	*Generalised Parametric*
Gamma	1.94	-	27.2
Lognormal	1.41	-	27.8
Beta-PERT	0.985	-	31.0
Triangular	0.924	1.45	24.5
Weibull	1.38	1.8	29.3
Burr	-	0.856	35.1
Loglogistic	-	0.721	30.0

Interestingly, the *SciPy* package used to implement the generalised parametric methods is essentially a "wrapper" around the *NumPy* methods used to perform the standardised parametric sampling. The longer simulation times are thought to be related to the

additional error checks and function calls that are required for each random sample in the generalised case. As such, slightly poorer performance was expected for the generalised parametric methods, but not to the extent shown in the performance test results. Consequently, while it may be more convenient in terms of explicitly defining the distribution for each task repetition, the direct methods are preferable when optimising computational speed is the main objective.

For the Triangular and Weibull distributions, the performance test results reveal that the standardised parametric methods outperform the inverse transform sampling methods. This is believed to be due to the presence of the *if* decision block in the inverse CDF formula for the Triangular distribution (see Equation 8.30) and the natural logarithm in the equation for the Weibull distribution (see Equation 8.35). The *NumPy* package uses optimal sampling methods described by Devroye (1986) and Oliphant (2006) that avoid these marginally more computationally expensive calculations. For example, Devroye (1986) describes a method for sampling from a Weibull distribution by inverting an exponential random variate. For the Triangular distribution there are methods such as the 'One Line method' (Devroye, 1996) and the 'MINMAX' method (Stein and Keblis, 2009). Despite the standardised parametric methods outperforming the inverse transform methods in the two cases that can be compared, the inverse transform sampling method is still recommended alongside the standardised parametric procedures. The results for both methods are comparable and the two fastest simulation times correspond to the inverse transform sampling method for the Burr and Loglogistic distributions.

8.5 Implementation

8.5.1 User Inputs

The input data required for each of the statistical distributions incorporated within the time-domain simulation software are summarised in Table 8.2. The tick-marks represent mandatory fields. Optional inputs are marked with a star. m is the learning slope defined previously in Chapter 7. Alternatively, the learning rate ϕ (see Equation 7.8) can be specified by the user. S is the task repetition number corresponding to the distribution parameters defined for each operation. It is crucially important to specify the iteration at which the distribution parameters are defined. The location and scale parameters of the 1^{st} unit are required for the implementation of the stochastic LC model. Thus, if a value of $S > 1$ is selected, then the distribution parameters for the 1^{st} iteration need to be calculated using Equations 8.7 and 8.8.

Two additional options are included alongside the seven statistical distributions described previously; Single Value and Uniform. The ability to specify a single value for

Table 8.2: Required input data for implemented distributions. ✓= required, ⋆ = optional, m = learning slope, S = task repetition number corresponding to the defined distribution parameters.

Distribution	*Shape 1*	*Shape 2*	*Loc*	*Scale*	*Min*	*Mode*	*Max*	m	S
Gamma	✓		✓	✓				⋆	⋆
Lognormal	✓		✓	✓				⋆	⋆
Beta-PERT					✓	✓	✓	⋆	⋆
Triangular					✓	✓	✓	⋆	⋆
Weibull	✓		✓	✓				⋆	⋆
Burr	✓	✓	✓	✓				⋆	⋆
Loglogistic	✓		✓	✓				⋆	⋆
Single Value						✓		⋆	⋆
Uniform					✓		✓		

operation durations is important when users are confident in their single point estimates and do not wish to represent task length as a stochastic phenomenon. Furthermore, the Single Value option is beneficial when conducting quality assurance (QA) checks on model results or developing a new simulation feature. Additionally, a Uniform distribution can be specified when every value in the range between the minimum and maximum parameters is equally likely to occur. The Single Value option—although not a theoretical statistical distribution in its own right—is a particular case of the Uniform distribution with its minimum parameter equal to its maximum parameter.

It is assumed that there is no observable learning phenomenon for any operation that does not specify a value for the learning slope or learning rate. Equally, specifying $m = 0$ or $\phi = 1$ implies that there is no learning present. In these situations, the simulation software samples from the same distribution irrespective of the task repetition number.

8.5.2 Sampling Procedure

The sampling procedures for each statistical distribution within the time-domain simulation software are summarised in Table 8.3. The sampling methods are defined alongside the *NumPy* functions used to generate the corresponding random numbers and the equations used to transform the data to the appropriate operation iteration. The sampling methods have been selected according to the performance test results summarised in Table 8.1. The methods within the *NumPy* random number generator functions are explained in detail by Oliphant (2006) and Jones *et al.* (2001–).

The transformation equations for the Beta-PERT and Triangular distributions require slight modifications to Equation 8.2. The scale parameter of these distributions is the distance between the maximum and minimum values of the distribution; $b - a$.

Table 8.3: Input parameters and sampling procedure for implemented distributions.

Distribution	*Sampling Method*	*Random Number Generator*	*Equation*
Gamma	Standardised parametric	numpy.random.gamma	8.2
Lognormal	Standardised parametric	numpy.random.lognormal	8.2
Beta-PERT	Standardised parametric	numpy.random.beta	8.2
Triangular	Standardised parametric	numpy.random.triangular	8.2
Weibull	Standardised parametric	numpy.random.weibull	8.2
Burr	Inverse transform	numpy.random.random	8.40
Loglogistic	Inverse transform	numpy.random.random	8.44
Single Value	-	-	7.4
Uniform	-	numpy.random.uniform	-

Consequently, Equation 8.2 becomes

$$x = (b - a)y + a \tag{8.45}$$

where $b = b_s = b_1 s^m$ and $a = a_s = a_1 s^m$. Similarly, for generating random samples from the Lognormal distribution using *NumPy* it is slightly more efficient to specify the mean of the logarithm of the random variable and consequently transform the equation using Equation 8.2 with the scale parameter $b_1 = 1$. These subtle difference can be seen in the Python script that implements the performance tests in Appendix A.

Learning can be still be incorporated for operations defined by a Single Value and in this case, the simulation model becomes a direct implementation of the deterministic learning curve model discussed in Section 7.2.2. It is not appropriate to implement the learning phenomenon for an operation that is uniformly distributed.

A three-dimensional visualisation of the stochastic LC model within the time-domain simulation software was provided in Section 7.6.1 (see Figure 7.15). The methods summarised in Table 8.3 describe the actual implementation of these methods. The probability distribution for each repetition of an operation, corresponding to the individual PDFs in the 3D plot, are fully defined by the random number generator functions and associated transformation equations listed in Table 8.3.

8.6 Conclusions

The stochastic learning curve theory has been expanded through the application of the proposed methods to seven additional probability distributions. The established theory stated that the 'nature' of the distributions remains constant as successive iterations of an operation are completed. This analysis has shown that the shape parameters of the statistical distribution remain constant as the task repetition number increases, while the location and scale parameters are scaled by the learning factor s^m. This hypothesis has been validated both theoretically and empirically for all seven of the additional distributions.

Three methods for the generation of random samples of operation duration that account for the learning phenomenon have been described. On average, sampling from distributions in their standardised form, where the location and scale parameters are 0 and 1 respectively, and subsequently transforming the data using the learning factor and distribution parameters, is approximately 20–25 times faster than the equivalent generalised sampling methods which define each distribution parameter for every task repetition number. The third method of inverse transform sampling has been applied to the four applicable distributions and shows comparable performance to the standardised parametric sampling procedure. These two methods are strongly recommended for use within Monte Carlo simulations because of their superior computational performance, which is such a critical requirement for TDS.

Finally, the incorporation of the derived methods within the developed TDS software has been outlined. The stochastic learning curve model is well-suited to Monte Carlo simulations of offshore operations as it implements well-known, statistically sound techniques, while remaining intuitive and comprehensive to users of the software. The methods described in this chapter enable the stochastic learning curve methodology to be implemented within a TDS model. Chapter 7 provided evidence of this phenomenon for the majority of operations required to construct an offshore wind farm. The methods facilitate computationally-efficient sampling of random values from a theoretical probability distribution. These methods are also applicable for the representation of technical downtime within TDS models, which is the subject of the next chapter.

Chapter 9

Technical Downtime

9.1 Introduction

Technical downtime is the term given to unplanned and random interruptions to the operation schedule of an offshore project that are independent of the metocean conditions. Accounting for these unexpected stoppages, delays and failures is essential if accurate and reliable estimates of project duration are to be made using TDS. The aim of this chapter is to assess the viability of representing technical downtime as the joint probability of (*i*) downtime occurring and (*ii*) the downtime duration being equal to a certain value. This representation is assessed through the analysis of observed instances of technical downtime for an offshore wind farm construction project. Methods of implementing technical downtime within TDS models are also described and assessed. The impacts of incorporating technical downtime in the simulation algorithms are then assessed in detail in Chapter 10.

Firstly, the theoretical background to the analysis is described. Section 9.2.1 defines what is meant by technical downtime and suggests a method for its representation, while Section 9.2.2 describes the Poisson distribution and its applicability for modelling the probability of occurrence of technical downtime. The methodology is outlined in Section 9.3. The data extraction and categorisation procedures are briefly mentioned before the three main analysis methods are described that assess (*i*) the probability of occurrence of technical downtime; (*ii*) the fitted distributions for downtime duration and (*iii*) the combination of occurrence and duration probabilities. The results are summarised and discussed in Section 9.4, before the implementation of the proposed method is described and appraised in Section 9.5.

9.2 Theoretical Background

9.2.1 Technical Downtime

Technical downtime refers to any unexpected downtime that arises independently of metocean conditions. The term covers a broad range of unplanned stoppages and random delays that can include time lost due to breakdown of equipment, periods spent waiting for pilots and unplanned mechanical and electrical (M&E) works. Crucially, the representation of technical downtime within time-domain simulations differs significantly from the sampling methods for operation durations because the probability of *occurrence* of these random stoppages needs to be taken into account, in addition to the stochastic nature of the downtime duration.

Consequently, it was decided to assess the representation of technical downtime as the joint probability of (*i*) technical downtime occurring at a specific time and (*ii*) the distribution function of downtime duration, assuming that downtime has occurred. The Poisson distribution was proposed to represent the probability of occurrence of technical downtime.

9.2.2 Poisson Distribution

As outlined by Wilks (2011), the Poisson distribution describes the number of discrete events occurring in a series, or a sequence, and pertains to data that can take on only non-negative integer values. The sequence is typically understood to be in time. The individual events being counted are independent in the sense that they do not depend on whether or how many other events may have occurred elsewhere in the sequence.

Poisson events occur randomly, but at a constant rate. As such, the distribution has a single parameter, μ_p, that specifies the average occurrence rate. The probability mass function of the Poisson distribution, as defined by, for example, Wilks (2011) is

$$f(k_p;\mu_p) = \Pr(X = k_p) = \frac{{\mu_p}^{k_p} e^{-\mu_p}}{k_p!} \quad \text{for } k_p = 0, 1, 2, \dots , \tag{9.1}$$

where e is Euler's number ($e = 2.718...$) and $k_p!$ is the factorial of k_p.

The Poisson distribution can be fitted to a sample of data by finding a specific value for the single parameter μ that makes Equation 9.1 behave as similarly as possible to the data-set. As outlined in Wilks (2011), this is especially straightforward using the method of moments because the single parameter is the mean number of occurrences per unit time, which can be estimated directly as the sample average.

9.2.3 Distribution Fitting

The distribution fitting methods used to analyse technical downtime durations follow those described previously in Chapter 7. The candidate distributions, implementation of maximum likelihood estimation, graphical goodness-of-fit assessment and statistical goodness-of-fit tests used in this chapter are identical to those described in Section 7.2.1.

9.3 Methodology

9.3.1 Data Extraction

Instances of technical downtime were specifically categorised in the daily progress reports (DPRs) received for the offshore wind construction project described previously in Chapter 7. The occurrences and durations of these technical downtime instances were extracted in a similar manner to the data extraction procedures outlined in Section 7.3.

9.3.2 Categorising Data

The average occurrence rate can be defined in several ways; as the number of instances per activity, per vessel or even as the total number of occurrences over the entire project. As previously discussed, the project can be divided into four activities; loading out at port, transiting to site, installing a group of eight WTGs and transiting to port. Because significantly different types of random stoppages can occur for each of these activity types, this analysis quantifies the average rate as the number of occurrences per activity.

The probability of occurrence of technical downtime is assumed to be negligible for transit operations. Any technical faults in the tools or equipment will not be discovered until the vessel has safely jacked-up at site or at port because the majority of equipment is securely fastened before commencing any transit operations. This assumption is corroborated by the observed data—there were no recorded instances of technical downtime during any of the 30 transit operations.

It is still desirable to categorise the data in a manner that maximises the sample size. As the two vessels involved in this construction project were essentially identical, it was decided to combine the occurrence and duration data for both vessels into a single data-set for each of the applicable activities. Consequently, the analysis of technical downtime was performed on two data-sets; one for the *loadout* activity and one for the *WTG* activity. This categorisation impacted the implementation of technical downtime in the TDS software that will be discussed in Section 9.5.

9.3.3 Probability of Occurrence

The average occurrence rate is calculated for each data-set using the definition from the previous section—the total number of occurrences divided by the number of times that activity was performed. Furthermore, a comparative graph is plotted for each activity showing the theoretical and empirical probability mass functions (PMFs). The theoretical PMFs are calculated using Equation 9.1 with the calculated average occurrence rates. The empirical PMFs are calculated using

$$\Pr(X = k_p) = \frac{c_p}{A_p} \quad \text{for } k_p = 0, 1, 2, \dots , \tag{9.2}$$

where c_p is the number of times the occurrences are equal to k_p and A_p is the number of times the activity was performed, referred to as the activity count.

9.3.4 Duration Distribution Fitting

Fitted probability distributions for technical downtime duration, assuming that downtime has occurred, are obtained using the method of maximum likelihood estimation described in Section 7.2.1. Subsequently, the selection of the best-fit distribution for the technical downtime durations follows the methods described in Section 7.5 for the analysis of operation durations when there is no learning present. In summary, the procedure consists of three steps;

1. The three distributions that resulted in the lowest values for the calculated Anderson-Darling statistic are selected.
2. The classical goodness-of-fit plots are generated for these top three distributions.
3. A Monte Carlo validation is performed, that emulates the sampling methods within the time-domain simulation software, for each of the three distributions.

9.3.5 Combined Occurrence and Duration Validation

A second Monte Carlo validation procedure is performed that assesses both the fitted Poisson distribution and the chosen probability distribution for downtime duration. The procedure is similar to the first Monte Carlo validation and only differs in relation to the sample size in each of the Monte Carlo runs. In the first Monte Carlo assessment, the number of samples that are drawn is equal to the sample size of the raw data, thus ensuring a fair comparison between the statistics calculated using the raw data and those based on the simulation results. In the secondary Monte Carlo validation test, the fitted Poisson distribution is used to generate the total number of occurrences of downtime that occur in each Monte Carlo run. The number of samples drawn from the probability distribution for this particular run is then set equal to the Poisson-generated number of occurrences. As such, the combined Monte Carlo approach assesses

the representation of technical downtime as the joint probability of downtime occurring and the distribution function of downtime duration. For this second method, the number of occurrences of technical downtime is recorded in addition to the minimum, mean, median and maximum durations recorded for each Monte Carlo run as before.

9.4 Results and Discussion

9.4.1 Probability of Occurrence

The average occurrence rate was 0.638 for the *WTG* installation activity and 1.769 for the *Loadout* activity. The comparison of the theoretical and empirical PMFs are shown in Figures 9.1 and 9.2 for the *WTG* and *Loadout* activities respectively. The results show good agreement between the theory and raw data, particularly for the *WTG* activity. Significant discrepancies are evident for the *Loadout* activity at $k = 2$ and $k = 3$. The discrepancies may be attributed to the smaller sample size of the *Loadout* activity (less than 15 samples) in comparison to the *WTG* activity (over 100 samples). Nevertheless, both fitted distributions show appropriate representations for the probability of occurrence of technical downtime.

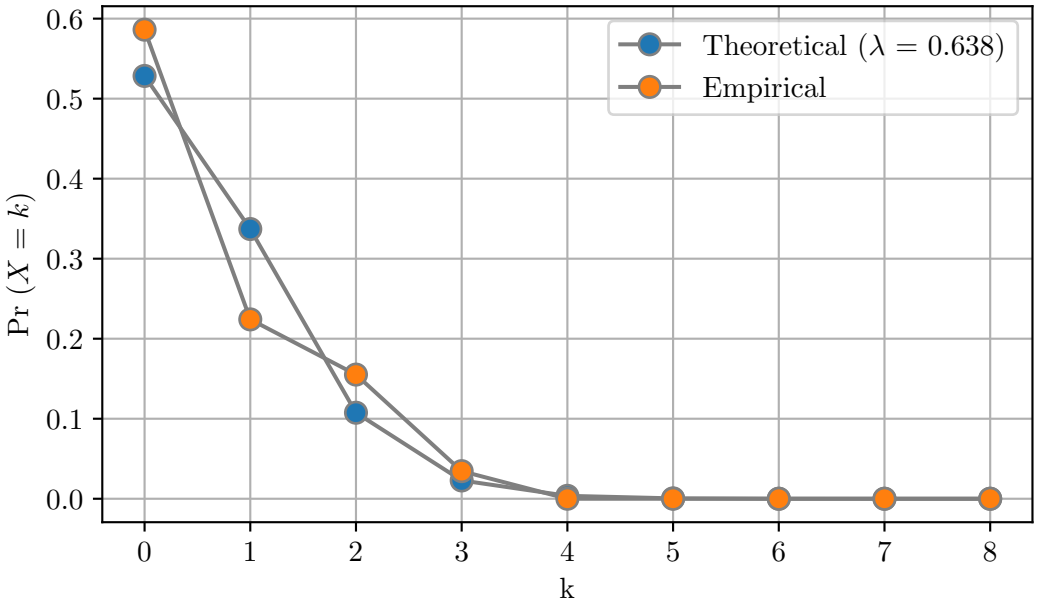

Figure 9.1: Theoretical and empirical probability mass functions (PMFs) for *WTG* activity.

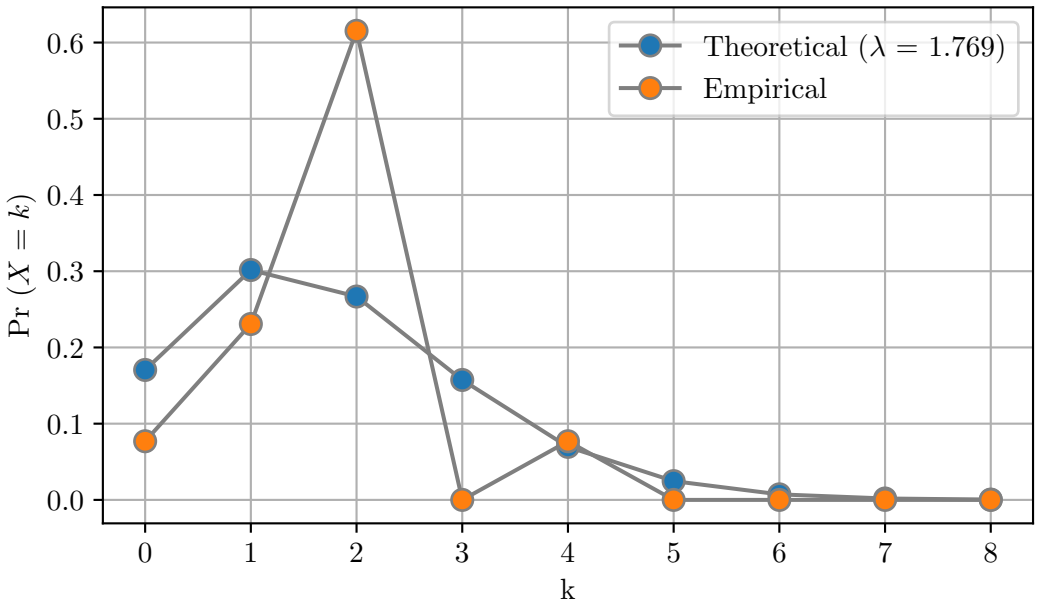

Figure 9.2: Theoretical and empirical probability mass functions (PMFs) for *Loadout* activity.

9.4.2 Duration Distribution Fitting

The mean duration of technical downtime was 9.2 hours for the WTG installation activity and 12.2 hours for the loadout activity. In both cases, the majority of occurrences were quite small; 95% of the occurrences were less than 30 hours. However, large instances of technical downtime were also observed, with three instances greater than 100 hours and the largest duration occurrence resulting in 236 hours of random downtime.

Table 9.1 shows the lowest three Anderson-Darling statistics calculated for the *WTG* and *Loadout* activities. The results show that the fitted Burr-a_0 distribution is the most appropriate distribution for both activities.

Table 9.1: Calculated values for the Anderson-Darling statistic for the *WTG* and *Loadout* activities.

WTG		*Loadout*	
Distribution	*Anderson-Darling*	*Distribution*	*Anderson-Darling*
Burr-a_0	0.145	Burr-a_0	0.304
Burr	0.152	Loglogistic-a_0	0.304
Loglogistic-a_0	0.465	Lognormal	0.344

The goodness-of-fit plots for the relevant distributions are shown in Figures 9.3 and 9.4.

The P-P plots for both activities show that there is excellent agreement for the centre of the distributions. The remaining plots show significant deviations at the right-hand tail of each of the fitted distributions, indicating that none of the distributions are accurately capturing the extreme values of downtime duration that have been observed. Most of the examples of the poorly-modelled instances of technical downtime with larger durations were related to the breakdown or malfunctioning of technical installation equipment on board the turbine-installation vessels.

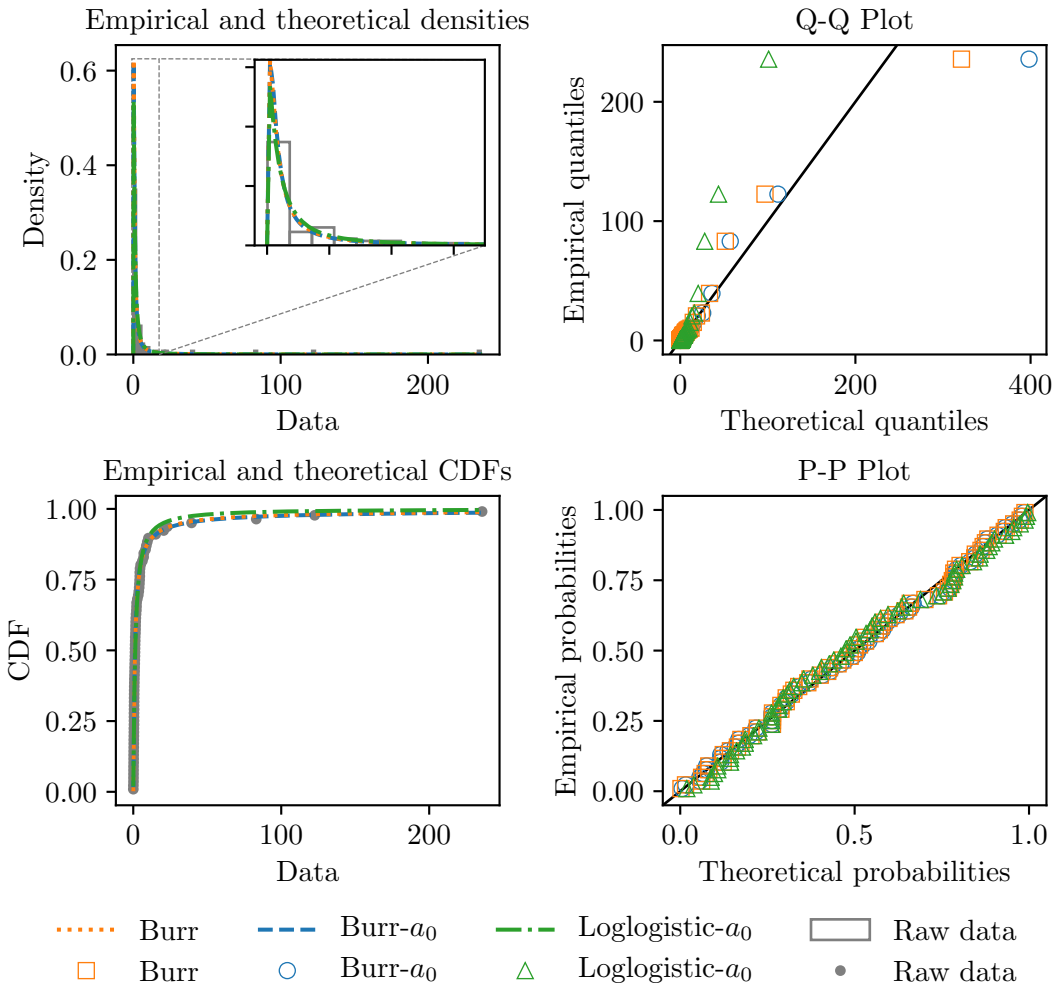

Figure 9.3: Goodness-of-fit plot for technical downtime durations of *WTG* activity—data in hours.

The results of the Monte Carlo validation of the fitted distributions for the *WTG* activity are summarised in Table 9.2. The table shows the ratio of the Monte Carlo results to the observed data for each of the analysed distributions. The objective of these tests is to assess the accuracy and spread of the chosen representations of technical downtime duration. As it is only the ratios that are shown in the table the *mean* sample

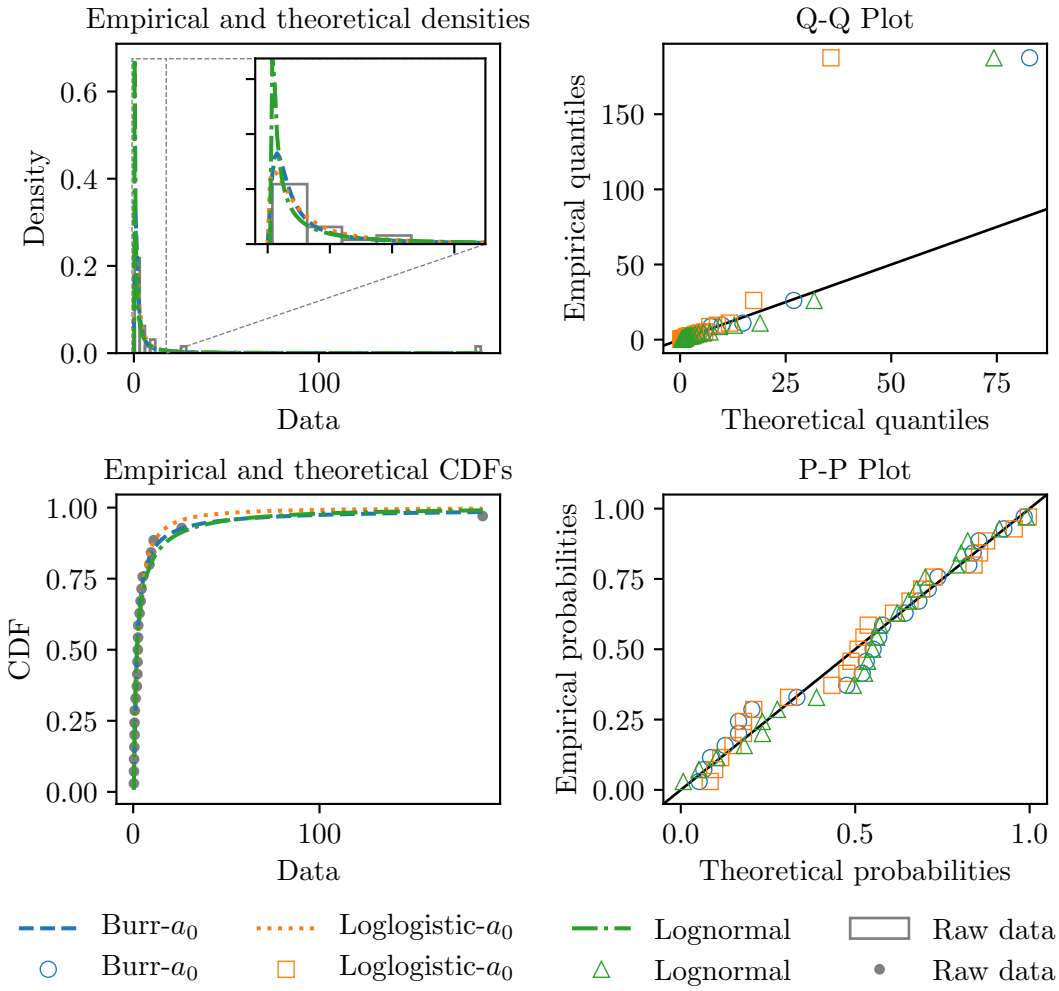

Figure 9.4: Goodness-of-fit plot for technical downtime durations of *Loadout* activity—data in hours.

category of each run is omitted, as it is equal to the ratio for the *sum* category.

The results indicate that the Loglogistic-a_0 is the only suitable distribution and that both the Burr-a_0 and Burr distributions are inappropriate because of their tendency to sample extremely large values of downtime duration. For the Burr-a_0 representation of the *WTG* activity, the P97.5 ratio for the maximum value sampled in each of the Monte Carlo runs was approximately 187. This corresponds to a duration of 44,000 hours or 5 years—for a single instance of technical downtime. Clearly, this is an unacceptably large duration, especially considering that approximately 250 of the 10,000 simulations that were performed in this case resulted in a greater value. The tendency to sample such enormous values of downtime duration distorts the results for both the mean downtime and the total downtime in each run. Furthermore, similar trends are evident for the generalised Burr distribution—the mean ratio for the maximum value sampled in this

Table 9.2: Monte Carlo validation results for fitted distributions of technical downtime durations for *WTG* activity—observed data in hours.

	Minimum	*Median*	*Maximum*	*Sum*
Observed data (hours)				
	0.033	1.192	235.750	677.850
Ratio of Monte Carlo: Observed data—Burr-a_0				
P2.5	0.191	0.661	0.164	0.355
P50	1.438	0.961	1.775	1.398
Mean	1.619	0.990	94.171	33.792
P97.5	4.152	1.470	186.843	69.033
Ratio of Monte Carlo: Observed data—Burr				
P2.5	0.772	0.670	0.147	0.337
P50	1.606	1.000	1.401	1.185
Mean	1.790	1.026	259.754	91.291
P97.5	3.848	1.542	123.713	45.635
Ratio of Monte Carlo: Observed data—Loglogistic-a_0				
P2.5	0.021	0.722	0.085	0.275
P50	0.517	1.099	0.427	0.587
Mean	0.704	1.126	1.803	1.084
P97.5	2.440	1.673	9.473	3.955

case is approximately 260.

The phenomenon is not evident for the fitted Loglogistic-a_0 distribution. For each of the minimum, median, maximum and sum categories, the Monte Carlo results show an acceptable variation around the statistics based on the observed data. Crucially, the P97.5 ratio for the maximum value sampled is approximately 9.5. This value is still quite high, corresponding to a duration of nearly 2,240 hours or approximately 3 months, but is a more plausible upper value to the potential range.

The Monte Carlo validation results for the *Loadout* activity, summarised in Table 9.3, show similar trends to the *WTG* activity. The Burr-a_0 distribution shows significantly large ratios for the maximum and total sample categories. The ratios, and corresponding durations, are not as large as for the *WTG* activity, but the Loglogistic-a_0 distribution results are more reasonable and capture a more appropriate range of sampled values about the observed durations. Additionally, the results show that the Lognormal distribution is another viable candidate model.

The Monte Carlo validation results, as well as the CDF and Q-Q goodness-of-fit plots, show that the Loglogistic is the most conservative of the probability distributions with respect to the sampling of large duration values. For both activities, the fitted

Table 9.3: Monte Carlo validation results for fitted distributions of technical downtime durations for *Loadout* activity—observed data in hours.

	Minimum	*Median*	*Maximum*	*Sum*
Observed data (hours)				
	0.383	2.483	187.533	279.983
Ratio of Monte Carlo: Observed data—Burr-a_0				
P2.5	0.146	0.485	0.059	0.221
P50	0.737	0.855	0.449	0.728
Mean	0.801	0.912	16.639	11.666
P97.5	1.823	1.684	29.687	20.897
Ratio of Monte Carlo: Observed data—Loglogistic-a_0				
P2.5	0.034	0.528	0.049	0.214
P50	0.436	0.977	0.190	0.464
Mean	0.545	1.030	0.506	0.685
P97.5	1.652	1.825	2.493	2.262
Ratio of Monte Carlo: Observed data—Lognormal				
P2.5	0.979	0.385	0.073	0.242
P50	1.066	0.813	0.402	0.733
Mean	1.110	0.903	0.863	1.080
P97.5	1.500	1.996	4.236	3.809

Loglogistic distribution is the model that yields the least accurate representation of the observed extreme data-points. However, the results also show that the Loglogistic distribution ensures that these large values are still being accurately represented, whilst avoiding the excessive quantity of unrealistically large samples that are obtained when using the Burr distributions.

9.4.3 Combined Occurrence and Duration Validation

The Monte Carlo results for the combined probability of occurrence and probability density function for downtime duration are shown in Table 9.4 and Table 9.5 for the *WTG* and *Loadout* activities respectively. Once again, the results show the ratios of the Monte Carlo results to the observed data for each of the analysed distributions. Since the number of samples drawn from the duration probability distribution in this case corresponds to the number sampled from the Poisson distribution, the mean ratio is not identical to the sum ratio and is thus included in the analysis.

The number of occurrences of technical downtime is adequately represented by the Poisson distribution. The range of ratios for the number of occurrences is 0.770–1.23 for the *WTG* activity and 0.609–1.435 for the *Loadout* activity. The same trends of

Table 9.4: Combined occurrence and duration Monte Carlo validation results for the *WTG* activity—observed data in hours.

	Occurrences	*Minimum*	*Median*	*Mean*	*Maximum*	*Sum*
Observed data (hours)						
	74	0.033	1.192	9.160	235.750	677.850
Ratio of Monte Carlo: Observed data—Burr-a_0						
P2.5	0.784	0.188	0.658	0.340	0.151	0.319
P50	1.000	1.440	0.967	1.345	1.680	1.356
Mean	1.001	1.627	0.991	30.501	89.537	32.157
P97.5	1.230	4.149	1.469	69.060	194.423	70.296
Ratio of Monte Carlo: Observed data—Burr						
P2.5	0.770	0.778	0.669	0.339	0.144	0.319
P50	1.000	1.625	0.998	1.200	1.393	1.199
Mean	0.998	1.818	1.025	67.032	197.819	69.708
P97.5	1.230	3.883	1.541	47.152	125.124	45.164
Ratio of Monte Carlo: Observed data—Loglogistic-a_0						
P2.5	0.784	0.024	0.723	0.280	0.086	0.261
P50	1.000	0.513	1.099	0.582	0.423	0.585
Mean	1.001	0.715	1.125	1.966	4.258	1.942
P97.5	1.230	2.492	1.673	4.331	9.657	4.192

Section 9.4.2 can be seen in the sampling results of technical downtime duration. The Burr distributions are inappropriate because of their tendency to sample extremely large values of downtime duration. The Loglogistic-a_0 is more appropriate in this regard and is thus recommended as the modelling distribution for both activities. The Lognormal distribution is a viable model for the *Loadout* activity but preference is given to the Loglogistic distribution because of the statistical goodness-of-fit results.

Crucially, the results show that the method of representing technical downtime as the joint probability of downtime occurring, using the Poisson distribution, and the distribution function of downtime duration assuming downtime has occurred, using the fitted Loglogistic-a_0 and Lognormal distributions, is appropriate, representative and suitable for implementation within time-domain simulations of offshore operations.

Table 9.5: Combined occurrence and duration Monte Carlo validation results for the *Loadout* activity—observed data in hours.

	Occurrences	*Minimum*	*Median*	*Mean*	*Maximum*	*Sum*
Observed data (hours)						
	23	0.383	2.483	12.173	187.533	279.983
Ratio of Monte Carlo: Observed data—Burr-a_0						
P2.5	0.609	0.149	0.482	0.210	0.051	0.173
P50	1.000	0.753	0.852	0.711	0.433	0.724
Mean	1.002	0.820	0.914	6.902	10.229	7.382
P97.5	1.435	1.933	1.695	22.106	31.238	22.088
Ratio of Monte Carlo: Observed data—Loglogistic-a_0						
P2.5	0.609	0.033	0.504	0.214	0.046	0.171
P50	1.000	0.431	0.978	0.458	0.184	0.462
Mean	0.998	0.554	1.027	0.721	0.566	0.727
P97.5	1.435	1.766	1.846	2.207	2.370	2.218
Ratio of Monte Carlo: Observed data—Lognormal						
P2.5	0.609	0.980	0.384	0.237	0.068	0.196
P50	1.000	1.066	0.812	0.735	0.393	0.738
Mean	1.000	1.115	0.920	1.082	0.863	1.087
P97.5	1.435	1.524	2.079	3.972	4.264	3.915

9.5 Implementation

In the time-domain simulation software, technical downtime is implemented on an *activity level*. This means that an optional average occurrence rate of technical downtime and the statistical distribution and parameters of downtime duration can be set for any activity in the simulation model.

In the software, a project is defined as a set of activities, each comprising several operations. In the most simplistic case, the simulation logic evaluates each activity in a specified order. The evaluation procedure for each operation involves the comparison of the metocean thresholds of that operation to the metocean time-series at the appropriate simulation time. As discussed in Chapter 8, each operation will have an associated statistical distribution. At each evaluation step, an operation duration will be sampled from this distribution—using the same computationally-efficient methods described in Chapter 8—and this value will be used, together with the operation thresholds and metocean time-series, to determine the end date of that particular operation. The simulation software moves on to the next operation in the activity and continues in this manner until all the activities are complete. An example of the simulation workflow for this simplistic case is shown in the left-hand column of Table 9.6.

Table 9.6: Implementation of technical downtime within time-domain simulations. The left-hand column shows the standard list of operations that must be completed in order. The right-hand side column shows the list of activities and operations after the instances of technical downtime have been sampled and inserted randomly into the list as *proxy operations*.

Activity A		*Activity A*
Operation A1		Operation A1
Operation A2		Technical Downtime A1
Operation A3	$\longrightarrow$	Operation A2
⋮		Operation A3
⋮		Technical Downtime A2
⋮		⋮
Operation A_x		Operation A_x
Activity B		*Activity B*
Operation B1		Operation B1
Operation B2		Operation B2
Operation B3	$\longrightarrow$	Operation B3
⋮		⋮
Operation B_x		Operation B_x
Activity C		*Activity C*
Operation C1		Technical Downtime C1
Operation C2		Operation C1
Operation C3	$\longrightarrow$	Operation C2
⋮		Technical Downtime C2
⋮		Technical Downtime C3
⋮		Operation C3
⋮		⋮
⋮		Operation C_x
Operation C_x		Technical Downtime C_x

An additional step in the simulation logic is required for activities specified with technical downtime. At the beginning of the evaluation procedure for these types of activities, a random sample is drawn from the Poisson distribution defined for that activity. This returns the number of occurrences of technical downtime for this particular iteration. Next, a list of *instances* of technical downtime is created with the same number of instances as the previously sampled number of occurrences. These *instances* of technical downtime are then randomly inserted into the list of operations for the activity in question. An example of this process is shown in Table 9.6.

Crucially, these *instances* of technical downtime are *proxy operations*. In the same way that each operation has a *sampling method* with an associated statistical distribution, so too does each technical downtime instance have an equivalent *sampling method*,

which uses the technical downtime distribution parameters specified as an input for that activity. As such, the simulation model processes each member of an activity in an identical fashion, regardless of whether it is an operation or an instance of technical downtime.

As shown in Table 9.6, it is possible, and often quite probable, that no instances of technical downtime are added to the operation list, as is the case for the example activity B. Equally, it is plausible that successive instances of technical downtime are added to the operation list as seen for Activity C.

A major shortcoming of this approach is that it does not enable technical downtime to occur during an operation. Incorporating technical downtime on an *operational level* would be more realistic—several observations of this phenomenon are evident in the DPR records. For example; a minor malfunction in the components of the on-board crane during a lifting operation. Implementing methods that can interrupt operations is considerably more complex than the implementation described above, particularly in relation to the simulation algorithms for operations that cannot be interrupted and need to be completed in a single weather window. Work is currently progressing on developing this functionality. Its implementation, although more realistic, is not expected to have a significant effect on simulation results. This is because several thousand simulations of the project are being performed and the precise position of instances of technical downtime within the project work flow is of minor importance. The critical functionality is that random stoppages can now be introduced.

9.6 Conclusions

This chapter has shown that the occurrence of random delays and stoppages—often referred to as *technical downtime*—is an observable phenomenon when conducting offshore operations and that these delays can have a significant impact on project duration and cost. For the offshore wind farm installation data that were analysed, the observed average occurrence rate of technical downtime was 0.638 per WTG installation activity and 1.769 per loadout activity. The mean duration of technical downtime was 9.2 hours for the WTG installation activity and 12.2 hours for the loadout activity. While the majority of observed occurrences of technical downtime were less than 30 hours, larger occurrences of downtime were also quite common. There were 3 observations of stoppages greater than 100 hours and the largest example of random failure resulted in 236 hours of downtime.

The hypothesis was put forward that instances of technical downtime could be modelled as the joint probability of downtime occurring—assuming a Poisson distribution—and

the downtime duration being equal to a certain value, assuming a standard statistical distribution. The analysis of the observed technical downtime data from the offshore wind farm construction project has shown that this method is realistic, representative and appropriate for implementation within time-domain simulations of offshore operations. For both of the analysed data-sets, corresponding to the installation of the WTGs and the loading of the installation vessels at port, the Loglogistic distribution has been shown to be the most suitable distribution for representing the durations of technical downtime.

The analysis has demonstrated the importance of additional validation tests for the assessment of fitted statistical distributions. The candidate distributions were assessed using a Monte Carlo validation procedure that emulated the implementation method within the time-domain simulation software. These tests showed that the fitted distribution with the best goodness-of-fit score showed a tendency to sample extreme values of downtime duration. The analysis has highlighted the benefit of assessing fitted distributions in a manner that reflects their implementation within the proposed model.

Finally, a method of incorporating the proposed representation of technical downtime within a time-domain simulation model has been described and appraised. When each activity is simulated, the occurrence of technical downtime is modelled by sampling from a Poisson distribution using the previously discussed average occurrence rates. For each simulation, the resulting number of technical downtime instances are inserted randomly into the list of operations that need to be completed. The computationally-efficient methods for sampling durations from probability distributions that were discussed in Chapter 8 are then used to sample the durations of technical downtime. Future work should focus on the ability of interrupting operations with technical downtime which is a shortcoming of the current implementation.

Epilogue

Chapter 10

Completing the Cycle

10.1 Introduction

This penultimate chapter assesses the impacts of using the results of the operation duration and technical downtime analyses as inputs to the time-domain simulation model. Obtaining such accurate and specific representations of operational data prior to the commencement of an offshore project is highly unlikely—perhaps the expansion of a large operational database discussed in Chapter 7 will make it more likely—but the analysis can be used to answer several important questions. The chapter assesses whether the inclusion of learning and technical downtime affect the rate of convergence of simulation results; investigates the impact of representative operation duration probability distributions, the learning curve phenomenon and technical downtime on the simulation results; and compares the simulation results obtained when using the *before*, *during* and *after* model configurations.

The methodology is outlined in Section 10.2 including sections on the scenario details and simulation configuration; the convergence testing methods; the impact of technical downtime and representative operation duration distributions and the comparison of the before, during and after scenarios. The corresponding results and discussion for each of these sections are given in Section 10.3. This subsection also includes additional results and discussion around failed missions—in which simulations are unable to complete the project due to the lack of metocean data (Section 10.3.1). Finally, the main conclusions of the chapter are given in Section 10.4.

10.2 Methodology

10.2.1 Scenarios and Simulation Configuration

To assess both the individual and combined effect of learning and technical downtime on simulation results, six simulations were performed. These simulations are summarised in Table 10.1 and the reasons for their selection are outlined in this subsection.

In the "no learning" scenario (NL), the operation durations are represented by a triangular distribution, with the minimum, modal and maximum values set equal to the sample minimum, mode and maximum durations from the observed data-set for the entire construction phase. The *NL S1* and *NL S100* scenarios use the shape of the best-fit distribution for each operation as detailed in Chapter 7. In these scenarios, S corresponds to the task repetition number for which the distribution parameters are defined but, as shown in Table 10.1, these two scenarios do not include the learning phenomenon. As such, the *shapes* of the operation distributions in these two cases are set equal to the results of the operation duration analysis but the *location* and *scale* parameters are set equal to the results for the 1^{st} operation iteration in the case of NL S1 and the 100^{th} operation iteration in the case of NL S100. In other words, NL S100 assumes the probability distribution of each iteration of an operation is equal to the *steady-state* distribution—assuming steady-state is reached after approximately 100 iterations of each operation. Note that approximately 100 repetitions were completed in the offshore wind farm construction project that has informed the analysis in previous chapters. Conversely, NL S1 assumes the probability distribution of each operation is equal to the distribution for the *first* iteration of that operation, as suggested by the results of Chapter 7. This scenario is included to enable a comparison with the NL S100 scenario—it is expected to over-estimate operation durations significantly. Finally, the implementation of learning and technical downtime in the appropriate scenarios is as outlined in Chapters 7 and 9 respectively.

Table 10.1: Scenario descriptions for the impact of learning and technical downtime on the simulation model. S refers to the task repetition number for which the operation distribution parameters are defined.

Scenario	*Description*	*Triangular distribution*	*Best-fit distribution*	*Learning*	*Technical downtime*
NL	No learning	✓			
TD	Technical downtime	✓			✓
NL S1	No learning $S = 1$		✓		
NL S100	No learning $S = 100$		✓		
L	Learning		✓	✓	
L&TD	Learning and technical downtime		✓	✓	✓

For each of the scenarios listed above, 600 simulations were performed for the project start date on each of the 18 years of metocean data. This led to a total of 10,800 simulations for each scenario. The number of simulations performed per year was increased in comparison to the majority of analysis in Chapter 5, to assess the impact

of learning and technical downtime on the simulation convergence rate.

10.2.2 Convergence Testing

To assess the impact of the learning and technical downtime modules on simulation results, the qualitative convergence methods proposed by Ballio and Guadagnini (2004) and applied in Chapter 5 were applied to the no learning (NL), technical downtime (TD), learning (L) and learning and technical downtime (L&TD) scenarios. The analysis consisted of calculating the cumulative mean and standard deviation for successive simulations and plotting this against the number of simulations performed.

10.2.3 The Impact of Learning and Technical Downtime

Box-and-whisker plots were used to compare the simulation results for each of the six scenarios described above. Additionally, progress plots were generated to assess further the results of selected scenarios. Progress plots were created for both the combined milestone completion parameter and for the progress of individual vessels.

10.2.4 Comparison of Before, During and After Scenarios

Finally, box-and-whisker plots and combined milestone progress plots were produced for the learning and technical downtime (L&TD) scenario—also referred to as the *after* scenario. These results were compared to those obtained when using the simulation models *before* and *during* the offshore wind farm construction. In this case, the *during* scenario refers to the simulation model that incorporated the results of the operation duration analysis completed approximately half-way through the installation campaign—see Chapter 6 for more details.

10.3 Results and Discussion

10.3.1 Failed Missions

There is a possibility that certain simulations will not be able to finish all of their operations and activities within the limited quantity of input metocean data These *failed missions* have already appeared in Chapter 5; for the baseline scenario which only used a single vessel, a significant proportion of simulations that started in the final year of metocean data were unable to complete the entire project. For that baseline scenario, any simulation that started in this final year was omitted from the analysis to avoid introducing bias to the simulation results.

With the inclusion of technical downtime and probability distributions of operation duration that can potentially result in extremely large durations, there is an increased probability that more simulations—even those that commence in the earliest years of the metocean dataset—will fail. Consequently, a counter of the number of failed missions was implemented in the simulation model. This failed mission counter was useful for assessing the extent to which large samples of technical downtime or operation duration were affecting simulation results.

Table 10.2 shows the number of failed missions for each of the tested scenarios and the percentage of total missions (10,8000) that this represents. The number of failed missions in each scenario is slightly different but this is not expected to have a significant effect on results due to the low percentage of total simulations in each case.

Table 10.2: Results for the total number of failed missions in each scenario.

Scenario	*Number of failed missions*	*Percent of total simulations (%)*
NL	0	0
TD	53	0.5
NL S1	2	0.02
NL S100	0	0
L	1	0.01
L&TD	44	0.4

10.3.2 Convergence Testing

The cumulative mean and standard deviation of project duration for the NL, TD, L and L&TD scenarios are shown in Figure 10.1. For the two cases *without* technical downtime—the learning and no learning scenarios—the mean project duration converges after about 1,000 simulations (for further details see the original convergence reults in Chapter 5 where the smaller range of the vertical axis shows the convergence after 1,000 simulations more clearly). Conversely, the addition of technical downtime has led to large spikes in the cumulative mean and standard deviation of project duration and has increased the number of simulations required for convergence to the total number of simulations performed—approximately 10,800. There are significant fluctuations in the cumulative standard deviation values right up to the last simulation that was performed. The results imply that if technical downtime is incorporated in the simulation model, the number of simulations that should be performed to ensure convergence should be increased by an order of magnitude—from 1,000 to 10,000. The incorporation of learning, although it clearly affects the final results, does not have an effect on the rate of convergence of the simulations.

The order of the simulations in the cumulative mean and standard deviation calculation is important. As explained in Section 5.3.4 for the general convergence tests, the first

18 simulations of Figure 10.1 correspond to the simulations performed in each of the 18 years of metocean data. The convergence over these points give an indication of the variation that can be expected due to the metocean data experienced. Comparing these fluctuations to the magnitude of the jumps when technical downtime is introduced, the relative influence of large instances of random failures and stoppages is clear. It should be noted that the duration of simulation number 9 of the L&TD scenario, that caused the cumulative mean project duration to increase from approximately 187.5 days to 350 days, is in the top 5% of all simulated project durations and is thus considered an outlier. The clear separation of results according to scenario shown in Figure 10.1 also provide early indications of the effect of learning and technical downtime on the simulation results.

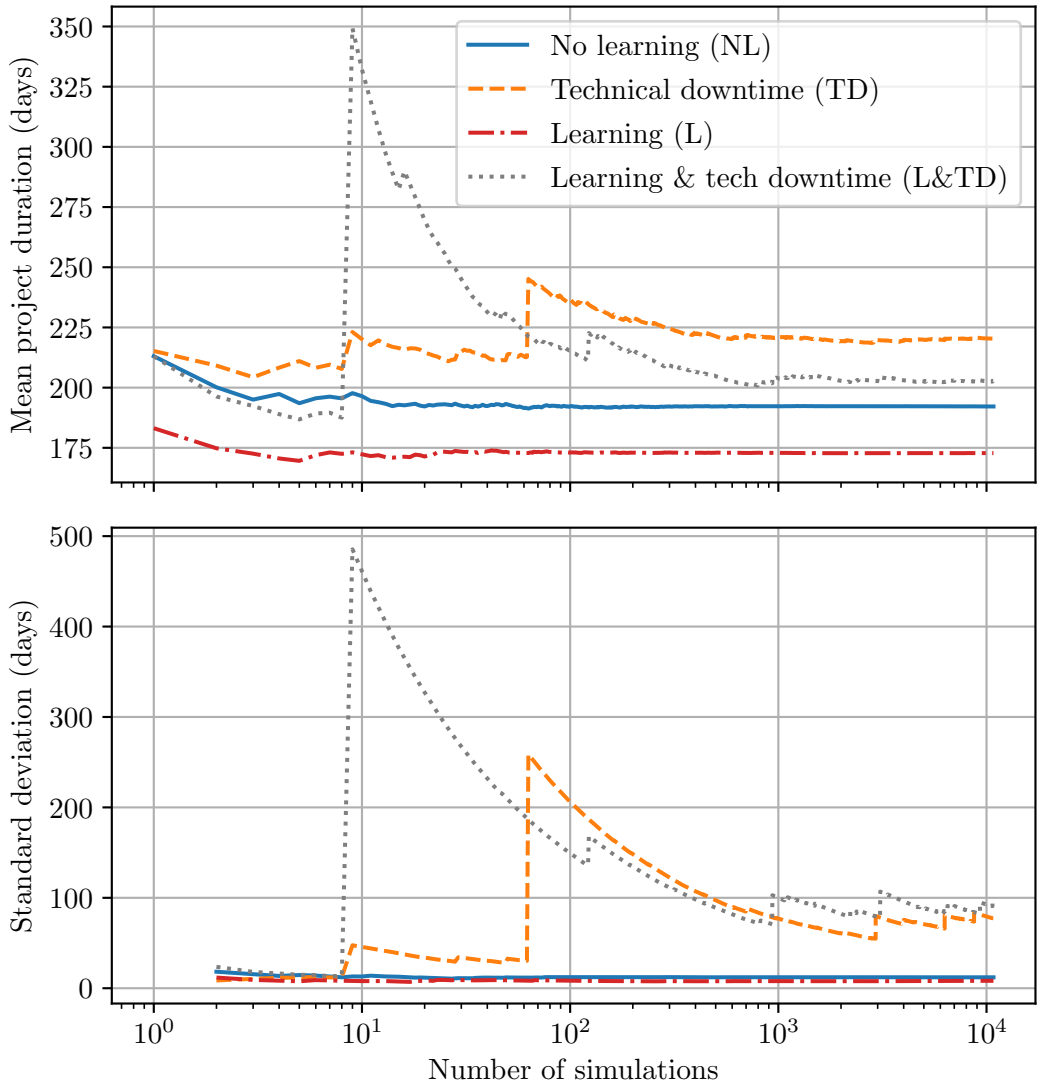

Figure 10.1: The effect of learning and technical downtime on simulation convergence.

10.3.3 The Impact of Learning and Technical Downtime

Figure 10.2 shows box-and-whisker plots for the six scenarios that were tested. Comparisons of simulated project duration and total vessel duration are shown, together with the corresponding recorded values. The whiskers extend to the 0.05 and 0.95 quantiles for all of the boxplots in this chapter. As alluded to previously, the potential for sampling extremely large instances of technical downtime and operation duration has led to several exceptionally large project duration estimates. The inclusion of these outliers distorts the figures, making it impossible to assess the P5–P95 range of results, and are thus omitted from subsequent box-and-whisker plots.

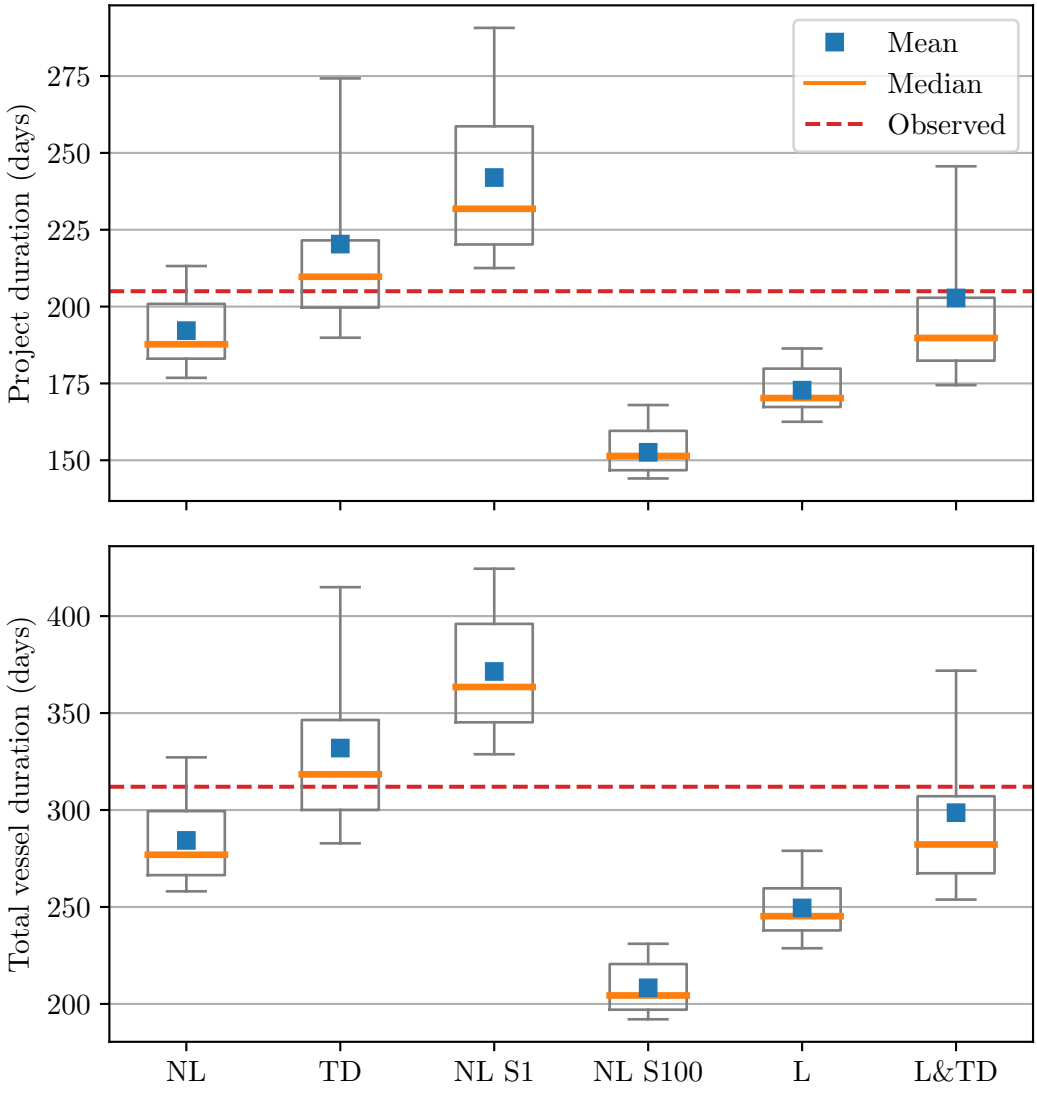

Figure 10.2: The effect of learning and technical downtime on project duration and total vessel duration. Whiskers extend to the 5th and 95th percentile values. Outliers are omitted.

Impacts of Learning

The effect of learning can be seen by comparing the learning and learning plus technical downtime scenarios to the equivalent scenarios *excluding* learning—scenarios NL and TD respectively. Understandably, the scenarios that exclude learning yield more pessimistic projections of campaign duration. In other words; if learning is assumed, the simulation model will result in lower estimates of project duration. Specifically, introducing the learning phenomenon reduces the mean project duration by 19.4 days when technical downtime is omitted—a reduction of 10%—and by 17.5 days when technical downtime is included—corresponding to a reduction of 8%. Using the previously discussed indicative charter rate for a turbine installation vessel of 140,000 GBP/day (see Section 5.3.2), the corresponding estimate for the reduction in project cost is £2.5–2.7m. Furthermore, the P5–P95 range for scenario NL is approximately 1.5 times greater than the range in the equivalent learning scenario. Again, this is an intuitive result; both the spread and mean value of operation durations decrease as more iterations are completed if learning is assumed, while the range and expected value of operation durations are defined by a constant triangular distribution in the case of scenario NL.

Scenarios NL S1 and NL S100 used the shape parameter(s) of the best-fit distributions suggested by the analysis in Chapter 7, but assume there was no learning. NL S1 assumed the location and scale parameters corresponding to the durations required for the first iteration of each operation. NL S100 assumed a "steady-state" value, in this case taken to be the parameters for the 100^{th} iteration. As expected, NL S1 over-estimates and NL S100 under-estimates both the project duration and total vessel duration. The ranges of results for these two scenarios are also the furthest from the observed values of both project duration and total vessel duration, suggesting that if learning is to be omitted, it is recommended to assume a simple triangular distribution based on the minimum, mode and maximum of the sample data. Future work could investigate the use of the beta-PERT distribution with the same parameters or the best-fit distribution obtained if learning is ignored.

Impacts of Technical Downtime

Comparing scenario TD to NL and scenario L&TD to L shows the increase in project duration that is likely to occur when technical downtime is added to the simulation model. Excluding learning, the mean project duration increases by 28.2 days, or 14.6%, when technical downtime is added. Including learning, the mean duration increases by 30.1 days, equivalent to an increase of 17.4%. These larger estimates of project duration correspond to an increase in indicative project cost of between £3.9m and £4.2m. The increase in P95 duration for both scenarios is even more significant; from 213 to 275 days

with no learning and from 186 to 246 days with learning—an increase of about 60 days in each case, translating to an increase in project cost of £8.4m. The more significant impact on larger percentile values is to be expected—in the worst simulations, the sampled values for random stoppages will tend to be largest. Interestingly, the inclusion of technical downtime leads to highly skewed distributions for project duration and total vessel duration results. For the two scenarios that include technical downtime, the mean project duration is approximately equal to the P75 value. The presence of extreme outliers, as discussed in the convergence test results and attributed to large instances of technical downtime, affects the skewness of the simulation results.

Combined Impacts

The results show that only three of the scenarios produce 90% probability ranges that contain the observed result; the no learning scenario, the technical downtime scenario and the learning and technical downtime scenario. The fact that the P95 learning *without* technical downtime scenario result is lower than the observed durations implies that—for this particular project—the incorporation of random failures and stoppages is more important than representing accurately the learning phenomenon. The remaining analysis in this section focuses on the comparison of the TD and L&TD scenarios as these are believed to be the most accurate simulation models; the mean project duration of the L&TD scenario is almost identical to the observed result—which is understandable considering the representative and specific model inputs used in the simulation—while the P50 value of the TD scenario is the closest to the recorded project duration and this scenario resulted in the only set of duration estimates with a 50% probability range that contained the observed value. The results show that the decision to include learning and technical downtime is critical; recalling that clients often make their operational decisions on P90/P95 probability levels, the inclusion or exclusion of learning in this case would have changed the decision on whether the chosen scenario was sufficient to complete the installation project within a duration of 245 days.

Figure 10.3 shows the combined vessel progress plots for both the TD and L&TD scenarios, along with the progression of observed installation durations. The progress plots for both scenarios capture the progress gradient of the observed installations accurately and the observed installations fall within the 90% range of both models. Once more, this accuracy should be noted with the caveat that both models incorporate the results from the analysis of observed installation durations. It is more interesting to assess the difference between the two scenarios. The actual installation durations that transpired fall more accurately within the centre of the range of the TD scenario, but is this the more accurate model? Is the model that excludes learning more accurate—the actual installation progress transpired as predicted by the median projections—or is the

full model including learning more representative and the actual construction process experienced a "P75" year?

The detailed investigation of Chapter 7 has shown with great certainty that learning is an observable phenomenon for many of the operations in the offshore project. Monte Carlo validation tests have shown that the implementation of the stochastic learning curve theory in the simulations has modelled this learning factor accurately. This suggests that the L&TD simulation model is the more representative and other factors contributed to the relatively larger installation durations that transpired.

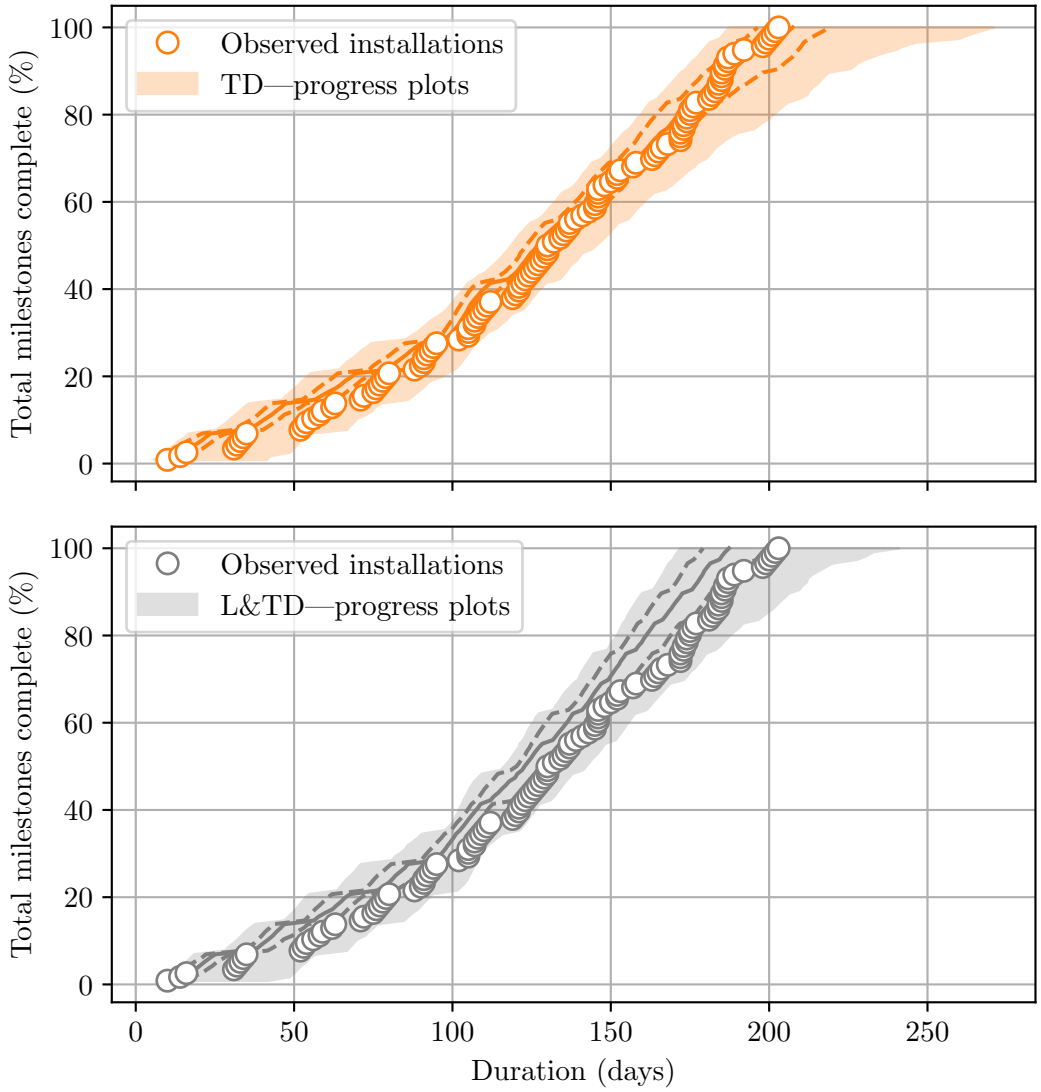

Figure 10.3: Combined vessel progress plots for the TD and L&TD scenarios.

There are several potential explanations for why the observed data closely follows

the P75 projection of the L&TD scenario. As discussed in Chapter 9, it is quite difficult to capture the distribution of technical downtime durations. For both *Loadout* and *Install WTG* activities, there is a peak in the distribution at low durations, but several extreme values in the right-hand tail have also been recorded. The implemented method captures specific instances of extreme durations—the presence of extremely large outliers discussed above proves this—but the sampling frequency of these large durations, in the order of 100–300 hours, may be too low. As such, the representation of technical downtime might under-estimate the durations of random stoppages and failures. Unfortunately, the most suitable method of investigating this further is to expand the database of observed operation data as discussed in Chapter 7. This would help assess whether the durations of technical downtime in this project were representative or exceptional, but additional data were unavailable for analysis.

Perhaps the most critical component of the time-domain simulations that has not yet been mentioned and a potential explanation of the discrepancy between the observed data and the simulation model is the actual metocean data that was experienced during construction. A very simple explanation for this discrepancy is that the operation durations and technical downtime were represented adequately, but the particular metocean conditions that were experienced during the installation campaign were approximately 25% worse than average. Future work could further investigate this hypothesis by obtaining accurate representations of the actual weather conditions experienced during construction and re-run the simulations with this single time-series of metocean data. Removing the variation attributable to the metocean conditions would enable a more definitive analysis of the representation of operation durations and technical downtime.

For future projects, it is extremely easy to run both the TD and L&TD scenarios as a type of sensitivity analysis. Subsequently, the scenario *excluding* learning can be viewed as a pessimistic projection while the scenario *including* learning becomes a more optimistic estimate. Regardless, both scenarios produce accurate estimates of installation progress. Further evidence of this is provided through the individual vessel progress plots shown in Figure 10.4.

Both scenarios predict the same P5–P95 range in allocation of WTG installations but the median number installed by the baseline when learning is excluded is slightly less than predicted by the simulation that includes learning—further confirmation that the TD scenario is more pessimistic than the the L&TD scenario.

Interestingly, the individual vessel progress plots highlight another large instance of technical downtime that is less obvious in the combined progress plots. For Vessel B, another prolonged random stoppage is evident between the third and fourth milestone completed by this vessel. This occurrence supports the theory discussed above that the sampling frequency of large instances of technical downtime may be too low.

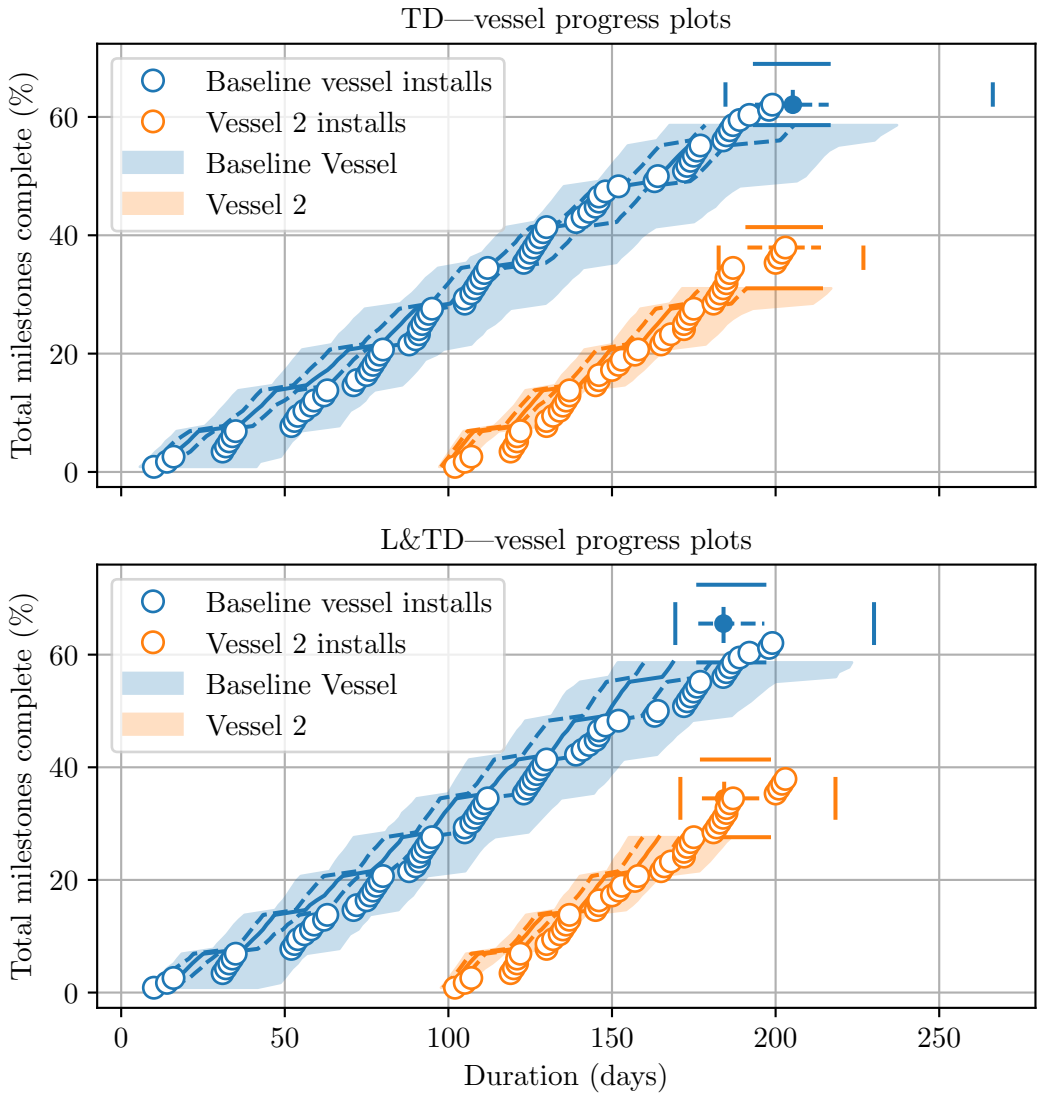

Figure 10.4: Individual vessel progress plots for the TD and L&TD scenarios.

10.3.4 Comparison of Before, During and After Scenarios

This section describes the comparison of results obtained from the simulation models used before, during and after the construction of the offshore wind farm. Figure 10.5 shows the combined progress plots for the three scenarios and Figure 10.6 shows box-and-whisker plots for the project duration and total vessel duration. The boxplots show a more detailed summary of the range of results for the final milestone completion durations shown in the progress plots. As with the previous section, outliers are not shown in the boxplots due to the presence of extreme values in the case of the *after* scenario.

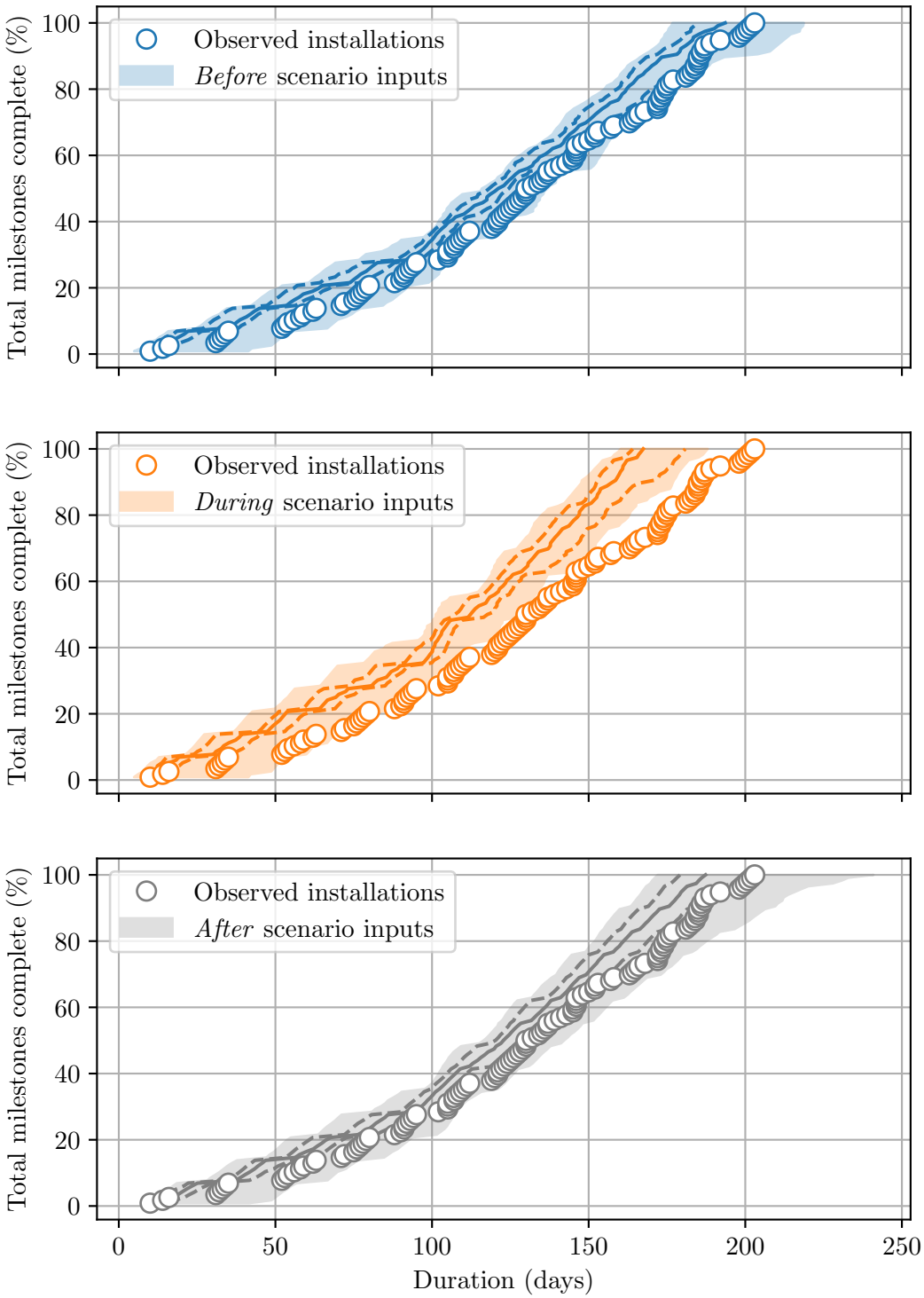

Figure 10.5: Combined progress plots for the before, during and after scenarios.

The three progress plot serves as a summary of the work completed throughout the wind

farm construction. The top panel shows the simulation results *before* the assembly of the WTG components on the pre-installed turbine foundations. These results suggest that these initial projections were quite accurate—the observed data follow approximately the P75 progress projection. However, the analysis of Chapter 6 highlighted significant discrepancies between the estimates of operation duration used as inputs and the mean values of the observed data at an approximate half-way stage of the project. Furthermore, this initial model did not include an accurate representation of technical downtime, which was shown in the early stages of construction to be a critical factor to the success of the project. As such, the over-estimates of operation duration and the omission of technical downtime effectively cancelled each other out. Thus, the perceived accuracy of the *before* simulations was achieved somewhat accidentally.

First impressions of the *during* scenario results would suggest that the representation is inferior to the *before* scenario. However, the representation of operation durations in the *during* scenario incorporates the differences between model inputs and observed operation data obtained for the first half of the project and is thus expected to be more accurate than the equivalent *before* representation. Crucially, the *during* scenario does not include an accurate representation of technical downtime and this is believed to be the biggest factor in the significant deviation between the observed results and projections. What isn't shown in the middle panel of the progress plots is the projection made at the half-way stage of the project that would have taken into account all the random stoppages and failures that had arisen up to that point. The estimate of progress that would have been produced if the *during* model inputs were used from the start of the project are shown here, primarily to emphasise the need for the technical downtime module as part of the simulations.

The effect of incorporating technical downtime, along with accurate models of the learning curve phenomenon for consecutive operation iterations, is shown in the *after* scenario results. As expected, the range of simulation results shown in the bottom panel of Figure 10.5 contain the observed milestone completion data and capture accurately the eventual progress gradient. Importantly, the P5–P95 range of results has increased in comparison to the *before* scenario, due to the added technical downtime module and the increased potential for large operation duration samples for those best-fit distributions that did not have an upper limit. The increased range is particularly evident for the final milestone duration which corresponds to the project duration and total vessel duration summarised in Figure 10.6. In the worst case P95 scenario, the project duration is just under 250 days. Conversely, the best case P5 scenario suggests that the construction project will be complete within approximately 170 days.

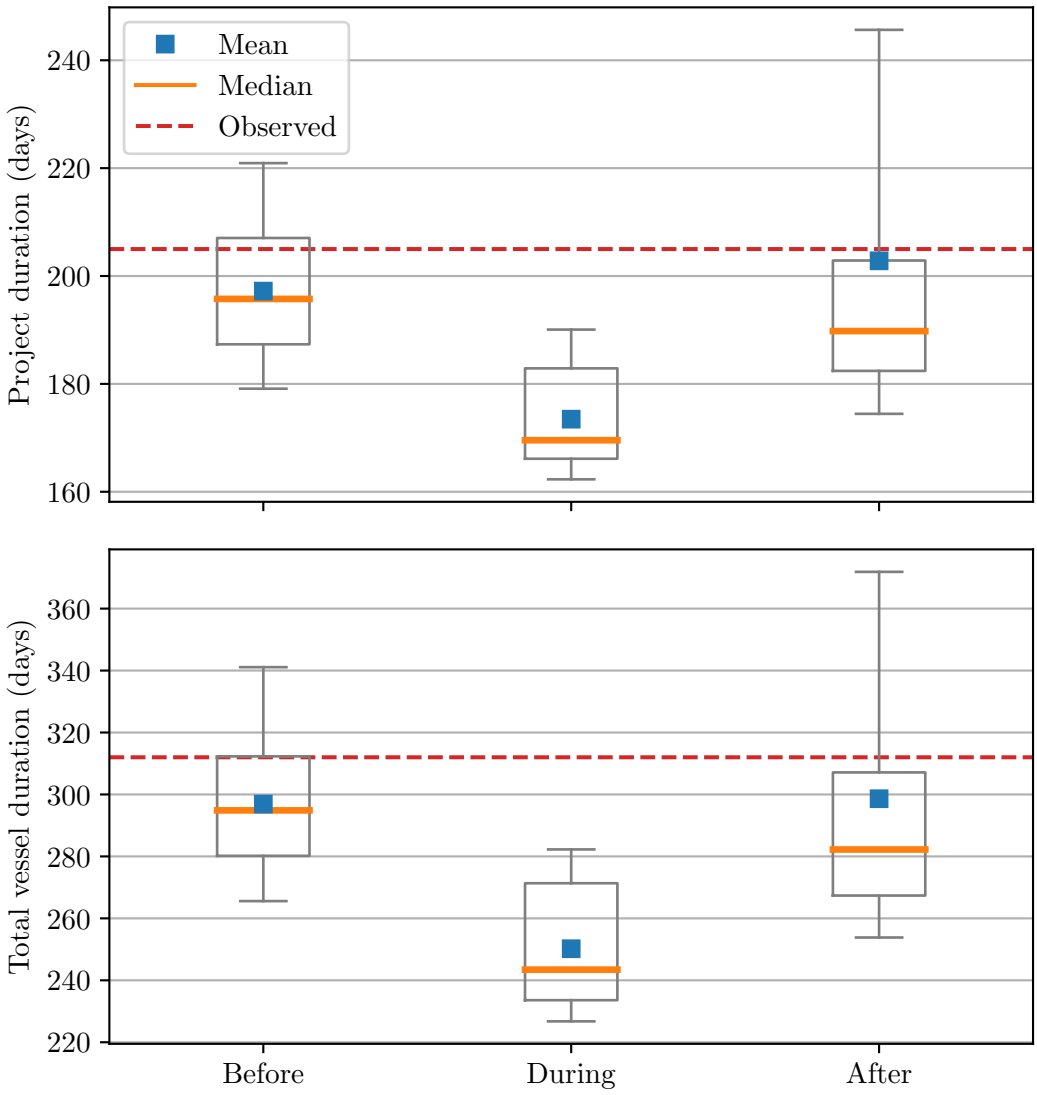

Figure 10.6: Comparison of project duration and total vessel duration for the before, during and after scenarios. Whiskers extend to the 5th and 95th percentile values. Outliers are omitted.

This thesis has shown that the addition of a technical downtime module and a stochastic learning curve model for operation durations have improved the representation of operations for this particular offshore wind farm construction project. Future work needs to assess the viability of using the developed models and analysis results obtained from this specific project in alternative offshore projects. The methods are expected to be transferable across projects but the same cannot be said for the model inputs. Are the learning rates, average occurrence rates of technical downtime and selected operation duration probability distributions valid for different vessels, technicians and projects?

Ignoring the obvious variation between installation and maintenance activities for wave, wind and tidal devices, there is enormous scope within the offshore wind sector alone. Varying WTG sizes and installation methods may have a significant impact on the application of the model inputs derived in this thesis. Applying the same methods to several distinct offshore wind farm construction projects would help provide the answer to these questions.

10.4 Conclusions

The analysis in this chapter has shown that if accurate representations of operation durations are used as inputs, time-domain simulation models can generate accurate stochastic predictions of project progress. Although it is improbable that such precise and specific representations of operational data will be available prior to the commencement of an offshore project, the analysis can be viewed as a validation of the underlying simulation theory. This is in line with comparable findings in Chapter 3.

Incorporating accurate and representative models of the random technical failures and stoppages that can arise during an offshore project is essential if accurate predictions of total project duration are to be made. In the example described in this chapter and based on the modelling methods described in Chapter 9, the inclusion of technical downtime increased the mean project duration by between 28–30 days, equating to 14.6–17.4% and potential increases in project cost of approximately £4m. Under the P95 worst-case scenario, the project duration increases by approximately 60 days and the indicative project cost by over £8m.

Similarly, implementing the learning curve phenomenon addressed in Chapter 7 can have a dramatic effect on simulation results. Based on the examples described above, the inclusion of learning reduced the mean project duration by an average of about 18.5 days, or between 8–10%. This corresponds to estimated increases in project cost of £2.5–2.7m. Accounting for the learning factor of certain operations has also been shown to reduce the total range of project duration and total vessel duration.

The benefits of implementing representative models of operation duration and technical downtime have been highlighted. However, there is a recommendation for further research to assess the viability of applying the derived results for this particular project to similar but separate offshore construction projects.

Chapter 11

Conclusions

11.1 Aim and Objectives

The aim of this thesis was to appraise the use of time-domain simulations of offshore operations to estimate the likely duration of offshore projects and inform planning decisions in the offshore renewable energy sector. The research intended to investigate the suitability of these simulation methods for estimating and minimising the cost of installation and maintenance activities for marine renewable energy devices, in an attempt to support the continued growth of these promising technologies.

While most of the analysis presented in this thesis was similar to work carried out for a client in the offshore wind energy sector, the results were different due to changes made in the exact scenarios modelled, specific modelling assumptions (e.g. vessel charter rates, which were not provided by the client) and other factors which have been changed to ensure client confidentiality.

11.2 Investigating and Validating Time-domain Simulations

One of the major shortcomings in the literature was the lack of research targeting the validation of time-domain simulation theory. This thesis has validated the use of TDS for modelling offshore operations by comparing the results of a bespoke TDS model to observed operation data from an offshore wind farm construction project. Validation results showed that if accurate metocean and operational data are provided, TDS models can produce precise estimates of project duration. The discrepancy between the simulated and observed completion date, for a project that took 8 weeks to complete, was 1.5 days. On average, the deviation between simulated and observed milestone completion dates was 1.7 days, with the simulation under-predicting observed durations.

A comparison of the results obtained from the time-domain simulation model and from using the classical probabilistic methods of occurrence and persistence supports the idea that the probabilistic methods ignore the sequential nature of marine operations and the effect that small cumulative delays can have on the overall progression of the project.

It has been shown that the conventional methods tend to underestimate metocean downtime and mean project duration. TDS models generate *probabilistic* estimates of the duration of offshore operations that are useful in the planning stages of a marine project and help assess the inherent risks of working in the harsh and complex marine environment. For a hypothetical test activity, occurrence and persistence methods predicted a mean duration of approximately 5 and 6.5 days respectively. The probabilistic TDS results implied that there was a 25% chance that the activity duration would be less than that estimated using the occurrence method. Conversely, the mean of the TDS simulations was nearly double the mean occurrence result and the maximum value simulated by the TDS model suggested an activity that would take 3 days to complete without weather downtime could potentially take up to 70 days.

11.3 Animating the Outputs of Time-domain Simulations

A method for animating the outputs of a TDS model has been developed. Selected results from a hypothetical offshore wind farm construction project have demonstrated how the animations provide clear and intuitive visualisations of simulation results. The animated outputs enable comparisons to be made between various offshore strategies and can support the project management of complex projects involving multiple vessels and contractors.

The incorporation of the animation functionality as a quality-assurance method within the model configuration process eliminates the need for time-consuming manual checks of tabular output data. Additionally, TDS animations enable easy identification of modelling and configuration errors and omissions. They also improve communication links between model developers and end-users. An indicative case study has highlighted the potential cost implications of failing to identify erroneous modelling assumptions or omissions. If restrictions on coincident piling and port operations were accidentally omitted, the median value for total project cost would have been underestimated by £400,000—£650,000. In the hypothetical worst-case scenario, the piling installation project was likely to have been about 5% longer and £1m more expensive than the simulation results suggested.

11.4 Simulation Outputs and Data Analysis Methods

Time-domain simulations can be used to generate probabilistic estimates of the duration of offshore operations. In turn, this enables the marginal benefits of various scenarios to be compared and helps identify and appraise the most appropriate and cost-effective strategy for a specific project. These *scenario testing* methods were described through an industrial case study that aimed to develop optimal installation strategies for a Round 3 offshore wind farm. Specifically, a bespoke TDS model was used to assess whether an additional installation vessel was required to complete construction within a period of 245 days. The results suggested that a secondary vessel was essential and that a charter duration of 120 days was required to achieve this objective. Simulations were also performed to compare three alternative turbine installation vessels and to identify the most appropriate and cost-effective secondary installation vessel. The total indicative project costs of selecting secondary vessel A, B or C were £57.1m, £51.1m and £53.5m respectively. The selection of Vessel B was thus expected to save between £2.4m and £6m.

Convergence testing of the simulation outputs revealed that obtaining a sufficiently extensive metocean data-set is critical for ensuring consistency and confidence in the results. The work has shown that the simulation results are significantly more sensitive to the number of metocean years used as an input to the model than the number of Monte Carlo iterations that are performed for each year. For this particular case study and TDS model, a minimum of 1,000 simulations is recommended to achieve an acceptable convergence in the mean and standard deviation of output results.

A graphical output referred to as a *progress plot* has been proposed. These graphs combine an alternative representation of a horizontal boxplot for consecutive milestone completion times with a rangefinder boxplot that describes the variation in both expected completion time and the number of milestones completed. The plots are beneficial for scenario testing and for assessing project progress when multiple vessels are assigned to the same task.

11.5 Progress Updates and Continuous Monitoring

Time-domain simulations can be performed during the operational phase of a marine renewable energy project. This enables the continuous monitoring of project performance and the early identification of significant deviations from baseline projections and planned schedules of work. In turn, these deviations can be used to inform planning decisions and strategies throughout an offshore project.

The delivery of *weekly updates* to the construction team throughout the installation phase of a Round 3 offshore wind farm was used to illustrate the continuous project monitoring process. This highlighted one of the major advantages of the TDS method; the speed with which the simulations and subsequent analysis can be performed. The entire process—from receipt of the most recent observations to the distribution of the weekly update results—took between 3–4 hours. This meant that critical planning and operational decisions were informed by simulation results modelled on the immediate status of operations. Additionally, the newly-proposed *progress plots* proved well-suited for summarising progress to date, deviations from planned schedules and the results of the latest simulations each week.

Continuous monitoring of project progress enabled the identification of one particular random delay in project progress that had a significant impact on expected results. This discrepancy delayed the median charter end dates of both vessels by approximately 16 days and increased the median indicative cost of the project by £4.4m. In the worst-case scenario, the increase in indicative cost was £6m. Although subsequent weekly updates accounted for the effects of this random stoppage, the analysis helped identify the major limitation of the software not being able to represent adequately these large instances of technical downtime. The analysis also highlighted the possibility of discrepancies between unexpected stoppages and the knock-on effect on total project duration and cost, due to the temporal variability of metocean conditions. For example, in the described case study a delay of 15 days during the relatively "calmer" summer weather led to an in increase in total vessel duration of 31.4 days—twice the original delay.

Continuous project monitoring also enables the identification of systematic errors in the simulation model. Realised installation progress outperforming the best-case simulation projections prompted the critical exploration of observed data. The resulting analysis showed that the mean duration required to complete a single WTG installation was 30% lower than initially specified. Subsequent implementation of the updated operation input data in the model led to a 10.8% reduction in the remaining duration of the project. This demonstrates how TDS can be applied in a cyclical manner, leading to continuous improvements in subsequent predictions of future progress.

11.6 Operation Duration Analysis

Observed operation data recorded throughout the installation phase of a Round 3 offshore wind farm were analysed. Preliminary investigations led to the hypothesis that the phenomenon of *learning* was a critical factor that affects the durations of consecutive offshore operations. Subsequent analyses confirmed this hypothesis and identified the stochastic learning curve theory as an appropriate model. The theory is well-suited for representing the operation duration inputs in time-domain simulations of offshore operations because it allows a probability density function for operation duration to be defined for consecutive task repetitions, assuming that there tends to be a reduction in consecutive durations due to the learning curve effect.

The analysis of observed operation durations has shown that learning is an observable phenomenon for the majority of operations in the data-set. Of the 18 turbine installation tasks that were analysed, 16 showed evidence of learning—90% of recorded operations. The effect of learning on the duration of operations can be significant. For the installation of the first blade of each wind turbine, the learning rate was 78%, meaning that the time required to complete this operation reduced by 22% every time there was a doubling of the cumulative number of turbines installed.

The Burr Type XII probability distribution has been identified as the distribution that most suitably models the durations of offshore wind farm installation operations, irrespective of the presence of learning. This distribution resulted in the best-fit for 65% of the analysed operations while the Burr family of distributions were ranked in the top 2 most suitable distributions for 19 of the 20 operations that were analysed and in the top 3 for every operation in the data-set.

Finally, the analysis of performance data throughout the operational phase of a project can yield continually improving estimates of expected value, variance and learning parameters. This procedure is recommended and, as with the weekly progress updates, is expected to lead to continuous improvements in project progress predictions.

11.7 Incorporating Learning within Time-domain Simulations

The expansion of the underlying stochastic learning curve theory—which was only validated and applied explicitly to the Normal distribution—has been expanded through the application of the proposed methods to seven additional probability distributions. The analysis has shown that the shape parameters of the statistical distribution remain constant as the task repetition number increases, while the location and scale parameters are multiplied by the learning factor. This hypothesis has been validated both theoretically and empirically for all seven of the additional distributions.

Three methods for generating random samples of operation duration, accounting for the learning phenomenon, and their implementation within the developed time-domain simulation software were compared. To achieve the requisite computational performance for the Monte Carlo methods, it is recommended to use either inverse transform sampling methods or to sample from standard probability distributions and subsequently transform the data using the appropriate learning and distribution factors. These methods are approximately 20–25 times faster than the equivalent generalised sampling methods that were tested. The incorporation of these methods and the recommended stochastic learning curve theory within a TDS model has also been outlined.

11.8 Technical Downtime

This work has shown that the occurrence of random delays and stoppages—often referred to as *technical downtime*—is an observable phenomenon when conducting offshore operations and that these delays can have a significant impact on project duration and cost. For the two analysed data-sets, corresponding to the installation of the WTGs and the loading of the installation vessels at port, the average technical downtime occurrence rates per activity were 0.6 and 1.8 respectively. The mean durations of the downtime experienced for each activity were approximately 9 and 12 hours. While the majority of observed technical downtime durations were less than 30 hours, several records of significant stoppages were also observed. For example, there were 3 observations of delays greater than 100 hours and the largest example of random failure resulted in 236 hours of downtime.

The hypothesis that technical downtime can be modelled as the joint probability of downtime occurring and the downtime duration being equal to a certain value as modelled by a standard statistical distribution has been proposed. Analysis has shown that this hypothesis is appropriate and that the proposed methodology is realistic, representative and appropriate for implementation within time-domain simulations of offshore operations. The thesis has described the implementation of the proposed representation of technical downtime within the time-domain simulation software, thus addressing one of the major limitations of the simulation software identified by the weekly progress updates discussed above. The Poisson distribution is recommended for modelling the probability of occurrence of technical downtime and the Loglogistic probability distribution has been identified as the most suitable for representing downtime durations.

11.9 Limitations and Future Work

11.9.1 Normalising the Observed Operation Data

The investigation of the learning phenomenon in Chapter 7 should be extended by normalising the observed operation durations with respect to the prevailing wind, wave and tidal current conditions. This may help explain some of the larger variations around the underlying learning trends. It might also account for some of the heteroscedasticity that can be seen in certain results. Investigating the effect of this normalisation process is recommended as future work.

11.9.2 Forecast Uncertainty

One of the major limitations of the current simulation model is that operational decisions are currently based on the input metocean data, which is also assumed to be the actual representation of the metocean conditions. In reality, operational decisions are made using imperfect metocean forecasts and there are occasions when the decision is made to suspend operations on account of the most recent weather forecast. On occasions, the actual metocean conditions that transpire are such that the planned operation could have been completed. This scenario cannot be represented by the simulation model in its current form, which can thus lead to under-estimates of project duration, or slightly optimistic projections.

To address this issue, future development should incorporate an additional representation of the weather forecast, on which the operational decisions should be based. This would ensure that key decisions are made using imperfect forecasts and account for the human element that arises when making important decisions in the marine environment.

11.9.3 Building an Operations Database

The analysis presented in this thesis has focused on one offshore renewable energy project in particular. At present, the results of the learning curve parameters, selected probability distributions and representation of technical downtime have only been verified and assessed using this single project. It is imperative that the viability of applying these derived results to similar but distinct projects is assessed. Several authors have suggested that transferring derived results between analogous projects in this manner is possible, but the lack of adequate operational data from comparable operations has prevented this assessment.

The development of an operational database would help obtain these comparable data. Subsequently, the validity of transferring learning curve parameters, probability distributions and technical downtime representations between similar offshore operations

could be investigated in detail. For this reason, the continued expansion of such a database is highly recommended.

11.9.4 Markov Chain Weather Models

The convergence testing of simulation model results highlighted the importance of metocean data in obtaining accurate and reliable simulation results. As far as possible, the extent of metocean data should be maximised. For instance, even the 18 years of weather data used for the majority of analysis in this thesis is sub-optimal. However, it is difficult to obtain the requisite quantity of data. A Markov-chain weather model that can generate synthetic metocean time-series from smaller, insufficient data-sets would be beneficial. Future work should focus on appraising the application, suitability and accuracy of these types of methods within TDS models.

11.10 Completing the Cycle—Impact and Applications

Using the operation duration, learning curve and technical downtime analysis results from the case study as inputs to the simulation model—duly noted as an unrealistically accurate and case-specific representation—demonstrated that time-domain simulation models can produce accurate stochastic predictions of the likely duration of offshore projects if representative operation durations and metocean data are used as inputs. This is in line with the comparable findings discussed in the targeted validation study.

Incorporating accurate and representative models of the random technical failures and stoppages that can arise during an offshore project is essential if accurate predictions of total project duration are to be made. The inclusion of technical downtime increased mean project duration by between 28–30 days, equating to 14.6–17.4% and an additional indicative cost of £3.9–4.2m. In the P95 scenario, project duration increased by 60 days and indicative cost by £8.4m. Implementing the learning curve phenomenon reduced the mean project duration by an average of about 18.5 days, or between 8–10%, corresponding to a decrease in indicative cost of £2.5–2.7m.

11.11 Final Summary

This work has shown that time-domain simulations of offshore operations can be used to estimate the likely duration, manage the inherent risks and inform planning strategies of offshore projects. Consequently, these methods can be used to reduce the costs of installation, operations and maintenance tasks. The incorporation of the TDS algorithms within JBA Consulting's metocean planning software has been described. The case

study describing the use of TDS to support the construction of a Round 3 offshore wind farm has shown that cost savings in the order of several million pounds are achievable. Scenario testing conducted before construction, continuous project monitoring during installation and detailed analysis of operational data after project completion have helped demonstrate the benefits and application of time-domain simulations. The use of TDS for modelling offshore operations is expected to help contribute to the growth of the promising offshore renewable energy sector.

References

Acero, W. G., Li, L., Gao, Z. and Moan, T. (2016), 'Methodology for assessment of the operational limits and operability of marine operations', *Ocean Engineering* **125**, 308 – 327. doi: 10.1016/j.oceaneng.2016.08.015.

Akaike, H. (1974), 'A new look at the statistical model identification', *IEEE Transactions on Automatic Control* **19**(6), 716–723. doi: 10.1109/TAC.1974.1100705.

Anastasiou, K. and Tsekos, C. (1996), 'Operability analysis of marine projects based on markov theory', *Applied Ocean Research* **18**(6), 329 – 352. doi: 10.1016/S0141-1187(96)00032-6.

Ang, A. H., Chaker, A. A. and Abdelnour, J. (1975), 'Analysis of activity networks under uncertainty', *Journal of the Engineering Mechanics Division* **101**(4), 373–387.

Anzanello, M. J. and Fogliatto, F. S. (2011), 'Learning curve models and applications: Literature review and research directions', *International Journal of Industrial Ergonomics* **41**(5), 573–583. doi: 10.1016/j.ergon.2011.05.001.

Ballard, E. and Evans, M. (2014), Use of sequential downtime analysis in planning offshore operations, *in* 'Offshore Technology Conference-Asia', Offshore Technology Conference. doi: 10.4043/24822-MS.

Ballio, F. and Guadagnini, A. (2004), 'Convergence assessment of numerical monte carlo simulations in groundwater hydrology', *Water Resources Research* **40**(4). doi: 10.1029/2003WR002876.

Barlow, E., Öztürk, D. T., Revie, M., Akartunalı, K., Day, A. H. and Boulougouris, E. (2017), On using simulation to model the installation process logistics for an offshore wind farm. **URL:** *https://strathprints.strath.ac.uk/60880/*

Barlow, E., Öztürk, D. T., Revie, M., Akartunalı, K., Day, A. H. and Boulougouris, E. (2018), 'A mixed-method optimisation and simulation framework for supporting logistical decisions during offshore wind farm installations', *European Journal of Operational Research* **264**(3), 894 – 906. doi: 10.1016/j.ejor.2017.05.043.

Barlow, E., Öztürk, D. T., Revie, M., Boulougouris, E., Day, A. H. and Akartunalı, K. (2015), 'Exploring the impact of innovative developments to the installation process for an offshore wind farm', *Ocean Engineering* **109**, 623 – 634. doi: 10.1016/j.oceaneng.2015.09.047.

Bates, D. M. and Watts, D. G. (1988), 'Nonlinear regression analysis and its applications', *Wiley Series in Probability and Mathematical Statistics*. .

Baty, F., Ritz, C., Charles, S., Brutsche, M., Flandrois, J.-P., Delignette-Muller, M.-L. *et al.* (2015), 'A toolbox for nonlinear regression in r: the package nlstools', *Journal of Statistical Software* **66**(5), 1–21. doi: 10.18637/jss.v066.i05.

Beamsley, B. J., McComb, P., Johnson, D. and Silk, J. (2007), Estimating weather downtime for ocean engineering using sequential downtime analysis (sda), *in* '18th Australasian Coastal and Ocean Engineering Conference 2007 and 11th Australasian Port and Harbour Conference 2007 (COASTS and PORTS 2007)', pp. 386–391.

Becketti, S. and Gould, W. (1987), 'Rangefinder box plots: A note', *The American Statistician* **41**(2), 149–149. doi: 10.2307/2684233.

Blanco, M. I. (2009), 'The economics of wind energy', *Renewable and Sustainable Energy Reviews* **13**(6), 1372 – 1382. doi: 10.1016/j.rser.2008.09.004.

Borthwick, A. G. (2016), 'Marine renewable energy seascape', *Engineering* **2**(1), 69 – 78. doi: 10.1016/J.ENG.2016.01.011.

Bosch, J., Staffell, I. and Hawkes, A. D. (2018), 'Temporally explicit and spatially resolved global offshore wind energy potentials', *Energy* **163**, 766 – 781. doi: 10.1016/j.energy.2018.08.153.

Boudière, E., Maisondieu, C., Ardhuin, F., Accensi, M., Pineau-Guillou, L. and Lepesqueur, J. (2013), 'A suitable metocean hindcast database for the design of marine energy converters', *International Journal of Marine Energy* **3-4**, e40 – e52. doi: 10.1016/j.ijome.2013.11.010, Special Issue - Selected Papers - EWTEC2013.

Boyle, G. (2012), *Renewable energy: power for a sustainable future*, 3 edn, Oxford University Press.

Burr, I. W. (1942), 'Cumulative frequency functions', *The Annals of Mathematical Statistics* **13**(2), 215–232. doi: 10.1214/aoms/1177731607.

CEC (1996), 'Wave energy project results: The exploitation of tidal marine currents', *DGXII – Report EUR16683EN, Commission of the European Communities* .

Charlier, R. H. and Justus, J. R. (1993), *Ocean energies: environmental, economic and technological aspects of alternative power sources*, Vol. 56, Elsevier.

Colmenar-Santos, A., Perera-Perez, J., Borge-Diez, D. and dePalacio Rodríguez, C. (2016), 'Offshore wind energy: A review of the current status, challenges and future development in spain', *Renewable and Sustainable Energy Reviews* **64**, 1 – 18. doi: 10.1016/j.rser.2016.05.087.

Copernicus Climate Change Service (C3S) (2017), 'ERA5: Fifth generation of ECMWF atmospheric reanalyses of the global climate'. **URL:** *https://cds.climate.copernicus.eu*

Cornett, A. M. (2008), A global wave energy resource assessment, *in* 'The Eighteenth International Offshore and Polar Engineering Conference', International Society of Offshore and Polar Engineers.

Crawford, J. (1944), 'Learning curve, ship curve, ratios, related data', *Lockheed Aircraft Corporation* **144**.

Cullen, A. C. and Frey, H. C. (1999), *Probabilistic techniques in exposure assessment: a handbook for dealing with variability and uncertainty in models and inputs*, Springer Science & Business Media.

D'Agostino, R. B. and Stephens, M. A. (1986), *Goodness-of-fit techniques*, Vol. 68 of *Statistics: Textbooks and Monographs*, Marcel Dekker, Inc., New York.

Dalgic, Y., Lazakis, I., Turan, O. and Judah, S. (2015*a*), 'Investigation of optimum jack-up vessel chartering strategy for offshore wind farm o&m activities', *Ocean Engineering* **95**, 106 – 115. doi: 10.1016/j.oceaneng.2014.12.011.

Dalgic, Y., Lazakis, I., Turan, O. and Judah, S. (2015*b*), 'Advanced logistics planning for offshore wind farm operation and maintenance activities', *Ocean Engineering* **101**, 211 – 226. doi: 10.1016/j.oceaneng.2015.04.040.

Davis, R. (2008), 'Teaching note—teaching project simulation in excel using pert-beta distributions', *INFORMS Transactions on Education* **8**(3), 139–148. doi: 10.1287/ited.1080.0013.

Dee, D. P., Uppala, S. M., Simmons, A. J., Berrisford, P., Poli, P., Kobayashi, S., Andrae, U., Balmaseda, M. A., Balsamo, G., Bauer, P., Bechtold, P., Beljaars, A. C. M., van de Berg, L., Bidlot, J., Bormann, N., Delsol, C., Dragani, R., Fuentes, M., Geer, A. J., Haimberger, L., Healy, S. B., Hersbach, H., Hólm, E. V., Isaksen, L., Kållberg, P., Köhler, M., Matricardi, M., McNally, A. P., Monge-Sanz, B. M., Morcrette, J.-J., Park, B.-K., Peubey, C., de Rosnay, P., Tavolato, C., Thépaut, J.-N. and Vitart, F. (2011), 'The ERA-Interim reanalysis: configuration and performance of the data assimilation system', *Quarterly Journal of the Royal Meteorological Society* **137**(656), 553–597. doi: 10.1002/qj.828.

Delignette-Muller, M. L., Dutang, C. *et al.* (2015), 'fitdistrplus: An r package for fitting distributions', *Journal of Statistical Software* **64**(4), 1–34. doi: 10.18637/jss.v064.i04.

Det Norske Veritas (2010), 'Modelling and analysis of marine operations', *Recommended practice DNV-RP-H103* .

Devroye, L. (1986), *Non-Uniform Random Variate Generation*, Springer-Verlag, New York, Berlin, Heidelberg, Tokyo.

Devroye, L. (1996), Random variate generation in one line of code, *in* 'Proceedings Winter Simulation Conference', pp. 265–272. doi: 10.1109/WSC.1996.873288.

Drew, B., Plummer, A. R. and Sahinkaya, M. N. (2009), 'A review of wave energy converter technology', *Proceedings of the Institution of Mechanical Engineers, Part A: Journal of Power and Energy* **223**(8), 887–902. doi: 10.1243/09576509JPE782.

Dupont, E., Koppelaar, R. and Jeanmart, H. (2018), 'Global available wind energy with physical and energy return on investment constraints', *Applied Energy* **209**, 322 – 338. doi: 10.1016/j.apenergy.2017.09.085.

Edenhofer, O., Pichs-Madruga, R., Sokona, Y., Seyboth, K., Kadner, S., Zwickel, T., Eickemeier, P., Hansen, G., Schlömer, S. and von Stechow, C., eds (2011), *Renewable energy sources and climate change mitigation: Special report of the intergovernmental panel on climate change*, Cambridge University Press.

Ellabban, O., Abu-Rub, H. and Blaabjerg, F. (2014), 'Renewable energy resources: Current status, future prospects and their enabling technology', *Renewable and Sustainable Energy Reviews* **39**, 748 – 764. doi: 10.1016/j.rser.2014.07.113.

Endrerud, O.-E. V. and Liyanage, J. P. (2015), Decision support for operations and maintenance of offshore wind parks, *in* P. W. Tse, J. Mathew, K. Wong, R. Lam and C. Ko, eds, 'Engineering Asset Management - Systems, Professional Practices and Certification', Springer International Publishing, pp. 1125–1139. doi: 10.1007/978-3-319-09507-3_95.

Endrerud, O. V., Liyanage, J. P. and Keseric, N. (2014), Marine logistics decision support for operation and maintenance of offshore wind parks with a multi method simulation model, *in* 'Proceedings of the Winter Simulation Conference 2014', pp. 1712–1722. doi: 10.1109/WSC.2014.7020021.

Entec (2007), 'Tidal power in the uk: Research report 2 - tidal technologies overview', *An evidence-based report by Entec for the Sustainable Development Commission* .

ETI and UKERC (2014), *Marine Energy Technology Roadmap 2014*, Loughborough, London, Energy Technology Institute (ETI) and the UK Energy Research Centre (UKERC).

Farnum, N. R. and Stanton, L. W. (1987), 'Some results concerning the estimation of beta distribution parameters in pert', *Journal of the Operational Research Society* **38**(3), 287–290. doi: 10.2307/2581949.

Filliben, J. J. (1975), 'The probability plot correlation coefficient test for normality', *Technometrics* **17**(1), 111–117. doi: 10.1080/00401706.1975.10489279.

Forbes, C., Evans, M., Hastings, N. and Peacock, B. (2011), *Statistical Distributions*, Probability and Statistics, 4 edn, Wiley, Hoboken, New Jersey.

Freedman, D. and Diaconis, P. (1981), 'On the histogram as a density estimator: L2 theory', *Zeitschrift für Wahrscheinlichkeitstheorie und Verwandte Gebiete* **57**(4), 453–476. doi: 10.1007/BF01025868.

Gintautas, T. and Sørensen, J. D. (2017), 'Improved methodology of weather window prediction for offshore operations based on probabilities of operation failure', *Journal of Marine Science and Engineering* **5**(2), 20. doi: 10.3390/jmse5020020.

Gintautas, T., Sørensen, J. D. and Vatne, S. R. (2016), 'Towards a risk-based decision support for offshore wind turbine installation and operation & maintenance', *Energy Procedia* **94**, 207–217. doi: 10.1016/j.egypro.2016.09.225.

Globerson, S. and Gold, D. (1997), 'Statistical attributes of the power learning curve model', *International Journal of Production Research* **35**(3), 699–711. doi: 10.1080/002075497195669.

Goldberg, K. M. and Iglewicz, B. (1992), 'Bivariate extensions of the boxplot', *Technometrics* **34**(3), 307–320. doi: 10.2307/1270037.

Graham, C. (1982), 'The parameterisation and prediction of wave height and wind speed persistence statistics for oil industry operational planning purposes', *Coastal Engineering* **6**(4), 303 – 329. doi: 10.1016/0378-3839(82)90005-9.

GWEC (2017), 'Global wind report: Annual market update 2017', *Global Wind Energy Council* .

Hagen, B., Simonsen, I., Hofmann, M. and Muskulus, M. (2013), 'A multivariate markov weather model for o&m simulation of offshore wind parks', *Energy Procedia* **35**, 137 – 147. doi: 10.1016/j.egypro.2013.07.167.

Hannon, M., Griffiths, J., Vantoch-Wood, A., Carcas, M., Bradley, S., Boud, R. and Wyatt, S. (2016), 'World energy resources marine energy 2016', *World Energy Council* .

Heffron, R. J., McCauley, D. and Sovacool, B. K. (2015), 'Resolving society's energy trilemma through the energy justice metric', *Energy Policy* **87**, 168 – 176. doi: 10.1016/j.enpol.2015.08.033.

Hess, R. (2010), *Blender Foundations: The Essential Guide to Learning Blender 2.6*, Focal Press.

Hudson, B., Kay, E., Lawless, M. and Bruce, T. (2017), Advanced metocean planning tools for the wave and tidal energy sectors, *in* 'Proc. 12th European Wave and Tidal Energy Conference', EWTEC.

Hudson, B., Kay, E., Lawless, M. and Bruce, T. (2018), Learning curves for marine operations in the offshore renewable energy sector, *in* 'Proc. 4th Asian Wave and Tidal Energy Conference', AWTEC.

Hunter, J. D. (2007), 'Matplotlib: A 2D graphics environment', *Computing in Science & Engineering* **9**(3), 90–95. doi: 10.1109/MCSE.2007.55.

Hussain, A., Arif, S. M. and Aslam, M. (2017), 'Emerging renewable and sustainable energy technologies: State of the art', *Renewable and Sustainable Energy Reviews* **71**, 12 – 28. doi: 10.1016/j.rser.2016.12.033.

Hyndman, R. J. (1996), 'Computing and graphing highest density regions', *The American Statistician* **50**(2), 120–126. doi: 10.2307/2684423.

International Energy Agency (2017), *Key World Energy Statistics 2017*. doi: 10.1787/key_energ_stat-2017-en.

International Energy Agency (2018), *Key World Energy Statistics 2018*. doi: 10.1787/key_energ_stat-2018-en.

IPCC (2014*a*), Summary for Policymakers, *in* 'Climate Change 2014: Mitigation of Climate Change. Contribution of Working Group III to the Fifth Assessment Report of the Intergovernmental Panel on Climate Change', Cambridge University Press, Cambridge, United Kingdom and New York, NY, USA.

IPCC (2014*b*), *Climate Change 2014: Synthesis Report: Contribution of Working Groups I, II and III to the Fifth Assessment Report of the Intergovernmental Panel on Climate Change*, IPCC Geneva, Switzerland.

IPCC (2018), *Global Warming of 1.5°C: an IPCC special report on the impacts of global warming of 1.5°C above pre-industrial levels and related global greenhouse gas emission pathways, in the context of strengthening the global response to the threat of climate change, sustainable development, and efforts to eradicate poverty*, IPCC Incheon, Republic of Korea.

Jablonowski, C., Ettehadtavakkol, A., Ogunyomi, B. and Srour, I. (2011), 'Integrating learning curves in probabilistic well-construction estimates', *SPE Drilling & Completion* **26**(01), 133–138. doi: 10.2118/125472-PA.

James, R. and Ros, M. C. (2015), 'Floating offshore wind: market and technology review', *Carbon Trust: UK* p. 168.

Jones, E., Oliphant, T. and Peterson, P. (2001–), 'SciPy: Open source scientific tools for Python'. [Online; accessed 18th January 2020]. **URL:** *http://www.scipy.org/*

Kent, B. R. (2013), 'Visualizing astronomical data with blender', *Publications of the Astronomical Society of the Pacific* **125**(928), 731. doi: 10.1086/671412.

Kotz, S. and Van Dorp, J. R. (2004), The triangular distribution, *in* 'Beyond beta: other continuous families of distributions with bounded support and applications', World Scientific.

Krewitt, W., Simon, S. and Pregger, T. (2008), 'Renewable energy deployment potentials in large economies', *DLR (German Aerospace Center), 37pp* .

Kuwashima, S. and Hogben, N. (1986), 'The estimation of wave height and wind speed persistence statistics from cumulative probability distributions', *Coastal Engineering* **9**(6), 563 – 590. doi: 10.1016/0378-3839(86)90004-9.

Lacal-Arántegui, R., Yusta, J. M. and Domínguez-Navarro, J. A. (2018), 'Offshore wind installation: Analysing the evidence behind improvements in installation time', *Renewable and Sustainable Energy Reviews* **92**, 133 – 145. doi: 10.1016/j.rser.2018.04.044.

Lemieux, C. (2009), Sampling from known distributions, *in* 'Monte Carlo and Quasi-Monte Carlo Sampling', Springer New York, New York, NY, pp. 1–16. doi: 10.1007/978-0-387-78165-5_2.

Littlefield Jr, T. K. and Randolph, P. H. (1987), 'Reply—an answer to sasieni's question on pert times', *Management Science* **33**(10), 1357–1359. doi: 10.1287/mnsc.33.10.1357.

Lu, X., McElroy, M. B. and Kiviluoma, J. (2009), 'Global potential for wind-generated electricity', *Proceedings of the National Academy of Sciences* **106**(27), 10933–10938. doi: 10.1073/pnas.0904101106.

Lutz, M. (2013), *Learning Python: Powerful Object-Oriented Programming*, O'Reilly Media, Inc.

Magagna, D., Monfardini, R. and Uihlein, A. (2016), 'Jrc ocean energy status report 2016 edition', *Technology, market and economic aspects of ocean energy in Europe* .

Magagna, D., Monfardini, R. and Uihlein, A. (2018), 'Ocean energy in europe: assessing support instruments and cost-reduction needs', *International Marine Energy Journal* **1**(1 (Aug)), 1–7.

Malcolm, D. G., Roseboom, J. H., Clark, C. E. and Fazar, W. (1959), 'Application of a technique for research and development program evaluation', *Operations research* **7**(5), 646–669. doi: 10.1287/opre.7.5.646.

Maples, B., Saur, G., Hand, M., Van de Pietermen, R. and Obdam, T. (2013), *Installation, operation, and maintenance strategies to reduce the cost of offshore wind energy*, National Renewable Energy Laboratory.

Martini, M., Guanche, R., Losada-Campa, I. and Losada, I. (2018), 'The impact of downtime over the long-term energy yield of a floating wind farm', *Renewable Energy* **117**, 1 – 11. doi: 10.1016/j.renene.2017.10.032.

Mathiesen, M. (1994), 'Estimation of wave height duration statistics', *Coastal Engineering* **23**(1), 167 – 181. doi: 10.1016/0378-3839(94)90021-3.

McKinney, W. (2010), Data structures for statistical computing in python, *in* 'Proceedings of the 9th Python in Science Conference', Vol. 45, pp. 51 – 56.

McKinney, W. (2012), *Python for Data Analysis: Data wrangling with Pandas, NumPy, and IPython*, O'Reilly Media, Inc.

Morandeau, M., Walker, R. T., Argall, R. and Nicholls-Lee, R. F. (2013), 'Optimisation of marine energy installation operations', *International Journal of Marine Energy* **3-4**, 14 – 26. doi: 10.1016/j.ijome.2013.11.002, Special Issue - Selected Papers - EWTEC2013.

Muhabie, Y. T., Rigo, P., Cepeda, M., de Almeida D'Agosto, M. and Caprace, J.-D. (2018), 'A discrete-event simulation approach to evaluate the effect of stochastic parameters on offshore wind farms assembly strategies', *Ocean Engineering* **149**, 279 – 290. doi: 10.1016/j.oceaneng.2017.12.018.

Natrella, M. (2010), 'NIST/SEMATECH e-Handbook of Statistical Methods'. **URL:** *http://www.itl.nist.gov/div898/handbook/*

Neill, S. P., Angeloudis, A., Robins, P. E., Walkington, I., Ward, S. L., Masters, I., Lewis, M. J., Piano, M., Avdis, A., Piggott, M. D., Aggidis, G., Evans, P., Adcock, T. A., Židonis, A., Ahmadian, R. and Falconer, R. (2018), 'Tidal range energy resource and optimization - past perspectives and future challenges', *Renewable Energy* **127**, 763 – 778. doi: 10.1016/j.renene.2018.05.007.

Nelder, J. A. and Mead, R. (1965), 'A simplex method for function minimization', *The Computer Journal* **7**(4), 308–313. doi: 10.1093/comjnl/7.4.308.

O'Connor, M., Lewis, T. and Dalton, G. (2013), 'Weather window analysis of irish west coast wave data with relevance to operations and maintenance of marine renewables', *Renewable Energy* **52**, 57 – 66. doi: 10.1016/j.renene.2012.10.021.

Olauson, J. (2018), 'Era5: The new champion of wind power modelling?', *Renewable Energy* **126**. doi: 10.1016/j.renene.2018.03.056.

Oliphant, T. E. (2006), *A guide to NumPy*, Vol. 1, Trelgol Publishing USA.

Oliphant, T. E. (2007), 'Python for scientific computing', *Computing in Science Engineering* **9**(3), 10–20. doi: 10.1109/MCSE.2007.58.

Papoulis, A. (1965), 'Probability, random variables, and stochastic processes'.

Paul, R. J. and Chanev, T. S. (1998), 'Simulation optimisation using a genetic algorithm', *Simulation Practice and Theory* **6**(6), 601 – 611. doi: 10.1016/S0928-4869(98)00007-X.

Pelc, R. and Fujita, R. M. (2002), 'Renewable energy from the ocean', *Marine Policy* **26**(6), 471 – 479. doi: 10.1016/S0308-597X(02)00045-3.

Petri, C. (1962), Kommunication mit Automaten (Communication with Automata), PhD thesis, University of Bonn.

Reisig, W. (2013), *Understanding petri nets: modeling techniques, analysis methods, case studies.*, Springer.

REN21 (2018), 'Renewables 2018 global status report', *An evidence-based report by Entec for the Sustainable Development Commission* (Paris: REN21 Secretariat).

Rodrigues, S., Restrepo, C., Kontos, E., Pinto, R. T. and Bauer, P. (2015), 'Trends of offshore wind projects', *Renewable and Sustainable Energy Reviews* **49**, 1114 – 1135. doi: 10.1016/j.rser.2015.04.092.

Rodriguez, R. N. (1977), 'A guide to the Burr type XII distributions', *Biometrika* **64**(1), 129–134. doi: 10.1093/biomet/64.1.129.

Rousseeuw, P. J., Ruts, I. and Tukey, J. W. (1999), 'The bagplot: a bivariate boxplot', *The American Statistician* **53**(4), 382–387. doi: 10.1080/00031305.1999.10474494.

Ruckstuhl, A. (2010), 'Introduction to nonlinear regression'. **URL:** *Introduction to Nonlinear Regression*

Sanchez, J. and Canton, M. P. (2007), *Software solutions for engineers and scientists*, CRC Press.

Sarker, B. R. and Faiz, T. I. (2017), 'Minimizing transportation and installation costs for turbines in offshore wind farms', *Renewable Energy* **101**, 667 – 679. doi: 10.1016/j.renene.2016.09.014.

Schwarz, G. (1978), 'Estimating the dimension of a model', *Ann. Statist.* **6**(2), 461–464. doi: 10.1214/aos/1176344136.

Scott, D. W. (2009), 'Sturges' rule', *Wiley Interdisciplinary Reviews: Computational Statistics* **1**(3), 303–306. doi: 10.1002/wics.35.

Shao, Z., Liang, B., Li, H. and Lee, D. (2018), 'Study of sampling methods for assessment of extreme significant wave heights in the south china sea', *Ocean Engineering* **168**, 173 – 184. doi: 10.1016/j.oceaneng.2018.09.015.

SI Ocean (2013), 'Ocean energy: cost of energy and cost reduction opportunities', *Strategic Initiative for Ocean Energy (SI OCEAN) May* .

Spiess, A.-N. and Neumeyer, N. (2010), 'An evaluation of r2 as an inadequate measure for nonlinear models in pharmacological and biochemical research: a monte carlo approach', *BMC Pharmacology* **10**(1), 6. doi: 10.1186/1471-2210-10-6.

Stallard, T., Dhedin, J., Saviot, S. and Noguera, C. (2010), 'Procedures for assessing site accessibility and appraisal of implications of site accessibility', *EQUIMAR D7* **4**.

Stein, W. E. and Keblis, M. F. (2009), 'A new method to simulate the triangular distribution', *Mathematical and Computer Modelling* **49**(5), 1143 – 1147. doi: 10.1016/j.mcm.2008.06.013.

Sturges, H. A. (1926), 'The choice of a class interval', *Journal of the American Statistical Association* **21**(153), 65–66. doi: 10.1080/01621459.1926.10502161.

Tadikamalla, P. R. (1980), 'A look at the burr and related distributions', *International Statistical Review / Revue Internationale de Statistique* **48**(3), 337–344. doi: 10.2307/1402945.

Thorpe, T. W. (1999), *A brief review of wave energy*, Harwell Laboratory, Energy Technology Support Unit London.

Tilindis, J. and Kleiza, V. (2017), 'Learning curve parameter estimation beyond traditional statistics', *Applied Mathematical Modelling* **45**, 768–783. doi: 10.1016/j.apm.2017.01.025.

Tukey, J. W. (1977), *Exploratory Data Analysis*, Addison-Wesley series in behavioral science, Addison-Wesley Publishing Company.

van der Wal, R. J. and de Boer, G. (2004), Downtime analysis techniques for complex offshore and dredging operations, *in* 'ASME 2004 23rd International Conference on Offshore Mechanics and Arctic Engineering', American Society of Mechanical Engineers, pp. 93–101. doi: 10.1115/OMAE2004-51113.

Van Os, J., Caires, S. and Gent, M. (2011), Guidelines for metocean data analysis, *in* 'Proc. 21st International Offshore and Polar Engineering Conference', pp. 290–297.

Verbruggen, A., Fischedick, M., Moomaw, W., Weir, T., Nadaï, A., Nilsson, L. J., Nyboer, J. and Sathaye, J. (2010), 'Renewable energy costs, potentials, barriers: Conceptual issues', *Energy Policy* **38**(2), 850 – 861. doi: 10.1016/j.enpol.2009.10.036.

Vigil, D. P. and Sarper, H. (1994), 'Estimating the effects of parameter variability on learning curve model predictions', *International Journal of Production Economics* **34**(2), 187 – 200. doi: 10.1016/0925-5273(94)90035-3.

Walker, R. T., van Nieuwkoop-McCall, J., Johanning, L. and Parkinson, R. J. (2013), 'Calculating weather windows: Application to transit, installation and the implications on deployment success', *Ocean Engineering* **68**, 88 – 101. doi: 10.1016/j.oceaneng.2013.04.015.

Waters, S. and Aggidis, G. (2016), 'Tidal range technologies and state of the art in review', *Renewable and Sustainable Energy Reviews* **59**, 514 – 529. doi: 10.1016/j.rser.2015.12.347.

Wilks, D. S. (2011), *Statistical methods in the atmospheric sciences*, Vol. 100, Academic press.

Williams, J. J. and Esteves, L. S. (2017), 'Guidance on setup, calibration, and validation of hydrodynamic, wave, and sediment models for shelf seas and estuaries', *Advances in Civil Engineering* **2017**. doi: 10.1155/2017/5251902.

Wind Europe (2017), 'The European offshore wind industry—Key trends and statistics 2016'.

Wind Europe (2018*a*), 'Offshore Wind in Europe—Key trends and statistics 2017'.

Wind Europe (2018*b*), 'Wind power in 2017—Annual combined onshore and offshore wind energy statistics'.

Wright, M. (1996), Direct search methods: Once scorned, now respectable, *in* D. Griffiths and G. Watson, eds, 'Numerical analysis: Proceedings of the 1995 Dundee Biennial Conference in Numerical Analysis', Addison-Wesley, pp. 191–208.

Wright, T. P. (1936), 'Factors affecting the cost of airplanes', *Journal of the Aeronautical Sciences* **3**(4), 122–128. doi: 10.2514/8.155.

Wyre Energy Ltd. (2013), 'Comparisons of tidal power stations around the World'.

Yelle, L. E. (1979), 'The learning curve: Historical review and comprehensive survey', *Decision sciences* **10**(2), 302–328. doi: 10.1111/j.1540-5915.1979.tb00026.x.

Appendix A

Performance Test Python Scripts

```
import numpy as np
from scipy import stats


"""
Example %timeit usage in Python Console

%timeit -n 1 gamma_parametric()
"""

A = 0.5
B = 1.5
C = 8.
D = 0.5
M = -0.15
S = range(1, 101)
MC = range(10000)
# Beta-PERT parameter calculations
Mu = (A + 4.0 * C + B) / 6.0
Alpha = 6.0 * (Mu - A) / (B - A)
Beta = 6.0 * (B - Mu) / (B - A)
# Triangular parameter calculations
C_strd = (C - A) / (B - A)
# Frozen distribution initialisation
GammaDists = \
    [stats.gamma(C, loc=A * (s_i ** M),
                 scale=B * (s_i ** M)) for s_i in S]
LognormDists = \
    [stats.lognorm(C, loc=A * (s_i ** M),
                   scale=np.exp(B) * (s_i ** M)) for s_i in S]
```

```
BetaPertDists = \
    [stats.beta(Alpha, Beta, loc=A * (s_i ** M),
                scale=(B - A) * (s_i ** M)) for s_i in S]
TriangDists = \
    [stats.triang(C_strd * (s_i ** M), loc=A * (s_i ** M),
                  scale=(B - A) * (s_i ** M)) for s_i in S]
WeibullDists = \
    [stats.weibull_min(C, loc=A * (s_i ** M),
                       scale=B * (s_i ** M)) for s_i in S]
BurrDists = \
    [stats.burr12(C, D, loc=A * (s_i ** M),
                  scale=B * (s_i ** M)) for s_i in S]
LoglogisticDists = \
    [stats.fisk(C, loc=A * (s_i ** M),
                scale=B * (s_i ** M)) for s_i in S]


""" Gamma distribution """


def gamma_parametric():

    for mc in MC:
        for s_i in S:
            u = np.random.gamma(C, 1)
            x = (s_i ** M) * ((u * B) + A)


def gamma_parametric_generalised():

    for mc in MC:
        for d in GammaDists:
            x = d.rvs()


""" Lognormal distribution """


def lognorm_parametric():
```

```
70
71      for mc in MC:
72          for s_i in S:
73              u = np.random.lognormal(B, C)
74              x = (s_i ** M) * (u + A)
75
76
77  def lognorm_parametric_generalised():
78
79      for mc in MC:
80          for d in LognormDists:
81              x = d.rvs()
82
83
84  """ Beta-PERT distribution """
85
86
87  def beta_pert_parametric():
88
89      for mc in MC:
90          for s_i in S:
91              u = np.random.beta(Alpha, Beta)
92              x = (s_i ** M) * ((u * (B - A)) + A)
93
94
95  def beta_pert_parametric_generalised():
96
97      for mc in MC:
98          for d in BetaPertDists:
99              x = d.rvs()
100
101
102 """ Triangular distribution """
103
104
105 def triangular_parametric():
106
107     for mc in MC:
108         for s_i in S:
```

```
109             u = np.random.triangular(0, C_strd, 1)
110             x = (s_i ** M) * ((u * (B - A)) + A)
111
112
113 def triangular_inverse_transform():
114
115     for mc in MC:
116         for s_i in S:
117             u = np.random.random()
118             if u < C_strd:
119                 f = A + np.sqrt(u * (C - A) * (B - A))
120             else:
121                 f = B - np.sqrt((1 - u) * (B - C) * (B - A))
122             x = (s_i ** M) * f
123
124
125 def triangular_parametric_generalised():
126
127     for mc in MC:
128         for d in TriangDists:
129             x = d.rvs()
130
131
132 """ Weibull distribution """
133
134
135 def weibull_parametric():
136
137     for mc in MC:
138         for s_i in S:
139             u = np.random.weibull(C)
140             x = (s_i ** M) * ((u * B) + A)
141
142
143 def weibull_inverse_transform():
144
145     for mc in MC:
146         for s_i in S:
147             u = np.random.random()
```

```
148             f = (B * ((-1 * (np.log(1 - u))) ** (1/C)) + A)
149             x = (s_i ** M) * f
150
151
152 def weibull_parametric_generalised():
153
154     for mc in MC:
155         for d in WeibullDists:
156             x = d.rvs()
157
158
159 """ Burr distribution """
160
161
162 def burr_inverse_transform():
163
164     for mc in MC:
165         for s_i in S:
166             u = np.random.random()
167             f = (B * ((((1 - u) ** (-1./D)) - 1) ** (1./C))) + A
168             x = (s_i ** M) * f
169
170
171 def burr_parametric_generalised():
172
173     for mc in MC:
174         for d in BurrDists:
175             x = d.rvs()
176
177
178 """ Loglogistic distribution """
179
180
181 def loglogistic_inverse_transform():
182
183     for mc in MC:
184         for s_i in S:
185             u = np.random.random()
186             f = (B * (u/(1 - u)) ** (1./C)) + A
```

```
187             x = (s_i ** M) * f
188
189
190 def loglogistic_parametric_generalised():
191
192     for mc in MC:
193         for d in LoglogisticDists:
194             x = d.rvs()
```